Clustering in neutron-rich light nuclei produced in reactions of 9Li beam on LiF target

Vukman, Nikola

Doctoral thesis / Disertacija

2022

University of Zagreb

FACULTY OF SCIENCE

Nikola Vukman

Clustering in neutron-rich light nuclei produced in reactions of ^{9}Li beam on LiF target

DOCTORAL DISSERTATION

Zagreb, 2022

University of Zagreb

FACULTY OF SCIENCE

Nikola Vukman

Clustering in neutron-rich light nuclei produced in reactions of ^{9}Li beam on LiF target

DOCTORAL DISSERTATION

Supervisor: Dr. sc. Neven Soić

Zagreb, 2022

Nikola Vukman

Klasterska građa neutronski bogatih lakih jezgara proizvedenih u reakcijama snopa ^{9}Li na meti LiF

DOKTORSKI RAD

Mentor: Dr. sc. Neven Soić

Zagreb, 2022

Supervisor

Dr. Neven Soić is a Senior Scientist in the Laboratory for Nuclear Physics at the Ruđer Bošković Institute. He obtained his PhD, MSc and BSc degree in experimental nuclear physics at the Faculty of Science, University of Zagreb. He was postdoctoral researcher at the University of Birmingham UK, research assistant at the Paul Scherrer Institute Switzerland and visiting researchers at INFN-LNS, Catania, Italy.

He was leading the H2020 ERA Chair project PaRaDeSEC, the project funded by European Structural and Investment Funds, the FP7 REGPOT project CLUNA, the project in the EuroGENESIS programme of the European Science Foundation, and he was core team member of the FP7 REGPOT project "Particle Detectors", and COST action ChETEC. He was co-proposer and spokesperson of part of the research on two research grants of Croatian Science Foundation, on the National Scientific Centre of Excellence for advanced materials and sensing devices, and on research project funded by Croatian Ministry of Science and Education.

He participated in more than 90 experiments performed in international collaborations at the international accelerator laboratories in Italy, France, Belgium, Australia, Canada, USA and CERN, he was spokesperson of 11 experiments at the international laboratories (IreS Strasbourg, ANU Canberra, GANIL Caen, INFN-LNS Catania, IPN Orsay, INFN-LNL Padova, TRIUMF Vancouver) and co-spokesperson of two experiments (HRIBF ORNL and INFN-LNS Catania). His main research interests are structure of light nuclei, reactions with deformed nuclei, and nuclear reactions important for nuclear astrophysics. According to Web of Science Core Collection, he is author of more than 140 peer-reviewed original scientific papers in international journals cited more than 2380 times, H-index=26. He has been supervisor of five PhD students, five graduate students and three postdoctoral researchers. He was teaching undergraduate course at University of Zagreb and teaches on postgraduate doctoral study of nuclear physics.

Acknowledgements

University of Zagreb

Doctoral Thesis

Faculty of Science

Department of Physics

Clustering in neutron-rich light nuclei produced in reactions of ^{9}Li beam on LiF target

Nikola Vukman

Ruđer Bošković Institute, Zagreb

The results presented in this thesis are based on the analysis of the S1620 experiment performed at TRIUMF, where multi-nucleon and cluster transfer reactions of the ^{9}Li beam of 74.8 MeV on the ≈ 1 mg/cm^2 LiF target were used to populate excited states of neutron-rich light nuclei ^{10}Be, ^{12}Be and ^{13}B. The main motivation behind this work was the need for experimental data to wage on the existence of molecular-like structures in the excited states of these nuclei and to resolve inconsistent observations from the previous measurements. For the latter two nuclei, the use of transfer reactions and resonant particle spectroscopy method to study molecular structures is independent and novel approach to more commonly used resonant elastic scattering and inelastic breakup measurements. Most important results are the first experimental observation of the decays of the ^{12}Be excited states to the ^{6}He+^{6}He* (1.8 MeV, 2^+) channel and the ^{13}B decays to the ^{10}Be+^{3}H and ^{7}Li+^{6}He channels. In the ^{10}Be nucleus, new states were observed in the ^{8}Be+nn decay channel and past results for the ^{4}He+^{6}He* (1.8 MeV, 2^+) channel were confirmed, alongside newly observed states. In both cases only one previous measurement was available. New states were observed in the ^{4}He+^{6}He, ^{4,6}He+^{8,6}He and ^{9}Li+^{4}He decay channels of the ^{10}Be, ^{12}Be and ^{13}B nuclei, respectively. Even though branching ratios were not determined, due to limited resolution of the present data, important spectroscopic information on the cluster structures in these nuclei was obtained, which could be related to the molecular α-Xn-α and α-2n-t-α structure of the ^{10,12}Be and ^{13}B nuclei, respectively.

(184 pages, 125 references, 110 figures, 66 tables, original in English)

Keywords: clustering in neutron-rich light nuclei, nuclear molecules, ^{10}Be, ^{12}Be, ^{13}B, transfer reactions, resonant particle spectroscopy

Prošireni sažetak

U ovom radu proučavana je klasterska građa neutronski bogatih lakih jezgara berilija i bora, s fokusom na izotope ^{10,12}Be i ^{13}B, za koje postoji još mnogo otvorenih pitanja, a koje uz jezgre ugljika i kisika predstavljaju neke od ključnih jezgara za razumijevanje nuklearne strukture, te razvoj i testiranje teorijskih modela [1]. U radu je prikazan temeljit pregled analize i rezultata dobivenih iz S1620 eksperimenta: "Examining the helium cluster decays of the ^{12}Be excites states by triton transfer to the ^{9}Li beam", napravljenog tokom ljeta 2017. godine na akceleratorskom postrojenju ISAC-II, TRIUMF u Vancouveru. U navedenim jezgrama je opažen čitav niz novih stanja i novih kanala raspada, te eksperimentalna potvrda kanala raspada za koje je do sada postojalo samo po jedno mjerenje. Na temelju ostvarenih rezultata značajno je unaprijeđeno znanje o klasteriranju u visokopobuđenim stanjima danih jezgara, a koje se može povezati s α-Xn-α molekulskom građom u izotopima berilija [10, 11, 20] i α-2n-t-α molekulskom građom u jezgri ^{13}B [25]. Navedeni su rezultati bitni za razumijevanje evolucije klasteriranja u (neutronski-bogatim) lakim jezgrama u ovisnosti o broju valentnih nukleona, te razvoja molekulske građe prelaskom s dvo-centralnog klasteriranja u izotopima berilija na tro-centralno klasteriranje u izotopima ugljika, čime je ostvaren važan znanstveni doprinos ovog rada.

Motivacija

Primarna motivacija za izradu ovog rada i predlaganje S1620 eksperimenta (N. Soić, M. Freer), na čijoj se analizi rad temeljio, bila je nedostatak eksperimentalnih podataka za klasterske raspade pobuđenih stanja u jezgri ^{12}Be koji bi potvrdili ili opovrgnuli postojanje rotacijskih vrpci molekulske α-Xn-α strukture, predložene na temelju rezultata iz članka [12, 13]. U kasnijem su eksperimentu navedeni rezultati dovedeni u pitanje [14], jer snažni klasterski raspadi nisu opaženi, iako je korištena ista eksperimentalna metoda. Tek su nedavno na energijama bliskim pragu raspada opažena nova stanja [15], koja idu u prilog postojanju rotacijskih vrpca predloženih od strane [12, 13], no na visokim je energijama i dalje potrebna potvrda u vidu novih eksperimentalnih podataka.

U ovom eksperimentu je stoga korištena potpuno nezavisna metoda proučavanja stru-

kture visokopobuđenih stanja ^{12}Be, a to su višenukleonske reakcije prijenosa, koje su do sada uspješno korištene od strane zagrebačke nuklearne grupe, ali i drugih, za opažanje molekulske strukture jezgre ^{10}Be [16–19]. Kako su reakcije prijenosa osjetljive na strukturu jezgara u ulaznom i izlaznom kanalu, korištenjem neutronski bogatog snopa ^{9}Li na jezgri ^{7}Li, koja ima izraženu podstrukturu α+t, očekuje se pobuđivanje klasterskih struktura niza jezgara u izlaznom kanala, dok se primjerice ^{12}Be mogao proizvesti direktnim prijenosom tritona na snop ^{9}Li. Na sličan se način u direktnim reakcijama, prijenosom protona ili α jezgre mogu proizvesti pobuđena stanja jezgara ^{10}Be i ^{13}B. Osim direktnih procesa, očekuju se i doprinosi složenih mehanizama reakcije koji se odvijaju u više koraka.

Iako je jezgra ^{10}Be znatno više proučavana od ^{10}Be i ^{12}Be, i dalje postoji otvoreno pitanje o postojanju 4^{+} člana rotacijske vrpce osnognog stanja [21] i 6^{+} člana jako deformirane rotacijske vrpce s σ valentnim neutronima [22–24]. U slučaju jezgre ^{13}B, eksperimentalnih podataka gotovo da i nije bilo do nedavnog eksperimenta rezonantnog elastičnog raspršenja snopa ^{9}Li na plinskoj ^{4}He meti, gdje su opažena stanja koja se snažno raspadaju u ^{9}Li+^{4}He kanal, u skladu s teorijskim predviđanjima [2]. No podataka koji bi potvrdili postojanje molekulske α-2n-t-α strukture u visokopobuđenim stanjima ^{13}B uopće nije bilo. Tu je također doprinos nezavisne metode mjerenja, korištenjem reakcija prijenosa od iznimnog značaja za razumijevanje pojave i razvoja klasterske i molekulske strukture u pobuđenim stanjima jezgre^{13}B, koji je u svom osnovnom stanju dobro opisan modelom ljusaka [25].

Klasterska građa lakih jezgara

Klasteriranje se u jezgri pojavljuje kao posljedica optimizacije energije i delikatnog balansa međudjelovanja nukleona kratkodosežnim odbojnim silama, Paulijevog odbijanja nuklearnom silom srednjeg dosega i dugodosežnog kulonskog odbijanja. Pojava klasteriranja je usko povezana s finim detaljima nuklearne sile [5], gdje snažne korelacija među parovima nukleona igraju značajnu ulogu. Utjecaj korelacija te kompeticije jednočestičnih i višenukleonskih aspekata strukture su možda najizraženiji u slabo vezanim, deformiranim strukturama, kao što su nuklearne molekule [28]. Ako uzmemo jezgru ^{10}Be za primjer nuklearne molekule, njena α-2n-α struktura se može opisati pomoću α-α sredice i valentnih neutrona, čije se gibanje oko sredice karakterizira molekulskim σ i π orbitalama.

Za razliku od atomskih orbitala oko jedne od α jezgara, molekulske orbitale karakterizira gibanje oko α-α sredice. Njihovo je proučavanje stoga iznimno bitno za fundamentalno razumijevanje nuklearne sile i bogatog fenomena različitih struktura koje proizlaze iz međudjelovanja nukleona (Slika 1.1).

Zbog postojanja snažnih korelacija među nukleonima, modeli koji dobro opisuju klasterske strukture u lakim jezgrama i reproduciraju eksperimentalne rezultate su oni koji polaze od nukleonskih stupnjeva slobode i realističnih interakcija među njima. Klasični model ljusaka, koji podrazumijeva gibanje svih nukleona nezavisno u efektivnom srednjem potencijalu, stoge ne opisuje klasterske strukture dobro, bez da model proširi izrazito velikim brojem oscilatorskih ljusaka. Povijesno su prvi modeli, kao ACM (Alpha Cluster Model) podrazumijevali postojanje α-klastera a priori, te su individualne interakcije među nukleonima zamijenjene onima među α klasterima [55]. Takav model je dobro opisivao eksperimentalne podateke u tzv. α-konjugiranim jezgram (^{8}Be, ^{12}C, ^{16}O), te uspostavio formalizam koji su mnogi od kasnijih metoda naslijedili. Metode koje se i danas koriste u opisu klasteriranja su GCM (Generator Coordinate Method) i RGM (Resonant Group Method) [36, 58, 60], polaze od mikroskopskog opisa jezgre, no i dalje generaliziraju pristup na postojanje podskupina unutar jezgre radi optimizacije računskog dijela problema, antisimetrizacije valne funkcije, na način da se fermionski stupnjevi slobode nukleona preslikaju na klastere i valentne nukleone [64, 65]. Jedan od takvih modela je i GTCM (Generalized Two-center Cluster Model), koji je uspješno koristen za opis molekulskih struktura u neutronski bogatim izotopima berilija [11, 61]. Metode koje se u potpunosti baziraju na nukleonskim stupnjevima slobode, bez a priori pretpostavke postojanja klastera unutar jezgre, su AMD (Antisymmetrized Molecular Dynamics) [3, 9] i FMD (Fermionic Molecular Dynamics) [70, 71], koje varijacijskim pristupom dolaze do rješenja i ostvaruju realističan opis raznih strukturnih fenomena u jezgri. Ono što je osnova svakog od ovih modela, a time i njihova razlika u pristupu, je odabir hamiltonijana (potencijala interakcije) i valnih funkcija preko kojih se traži rješenje problema. U ovom radu se često referenciraju AMD računi, upravo zbog njihovog dobrog slaganja s eksperimentalnim podacima, ali i dostupnosti računa za jezgre ^{10}Be [20], ^{12}Be [10] i ^{13}B [25]. Zanimljiva je i primjena formalizma nuklearnih energijskih funkcionala gustoće (NEDF) [67, 68], kojim se uspješno opisuje struktura srednje teških i teških jezgara u okviru

samo-konzistentnog srednjeg polja, na opis pojave klasteriranja i molekulskih struktura u lakim jezgrama [5, 45, 69]. S porastom kapaciteta računala, u posljednja dva desetljeća napravljeni su značajni napretci u ab initio opisu jezgre [74] i klasterskih struktura [7, 80, 82]. Takvi su modeli GFMC (Green's function Monte Carlo) [77], NCSM (No-core Shell Model) [78] i NLEFT (Nuclear Lattice Effective Field Theory) [76], koji se zasnivaju na realističnim silama koje proizlaze iz kvantne kromodinamike (QCD) [75]. Navedeni su modeli i njihova primjena na lake jezgre detaljno opisani u Poglavlju 2.

Eksperimentalni postav i analiza podataka

Za mjerenje produkata nuklearnih reakcija snopa ^{9}Li na meti LiF, korišten je LAMP detektorski postav, koji je pokrivao $\sim$ 16-48 stupnjeva u polarnom kutu i gotovo 360 stupnjeva u azimutu. Postav se sastojao od 12 silicijskih detektora oblika klinastog isječka (dizajn YY1, Micron Semiconductor [99]), postavljenih u 6 teleskopa od kojih se svaki sastojao od $\sim$ 70 μm tankog ΔE detektora za mjerenje energijskih gubitaka produkata reakcije i $\sim$ 1.5 mm debelog E detektora u kojem su se produkti u potpunosti zaustavljali. Kako različiti izotopi imaju drugačije gubitke energije po jedinici duljine, ovisno o masi, naboju i ulaznoj energiji, korištena je standardna ΔE-E metoda za identifikaciju produkata reakcije. Za kalibraciju detektora korišten je 3-α izvor (^{239}Pu, ^{241}Am i ^{244}Cm) te elastično raspršenje snopa na meti zlata (Au). Za dodatne detaljne korekcije geometrije korišteno je elastično i neelastično raspršenje na svim konstituentima mete LiF. Svi detalji vezani za eksperimentalni postav, kalibraciju detektora, selekciju podataka, provjeru kvalitete svih koraka u analizi mogu se pronaći u Poglavlju 3.

Kako se u tročestičnim reakcijama zbog prostornog pokrića detektiraju najčešće dvije od tri čestice, potrebne za potpunu rekonstrukciju kinematike tročestičnog događaja, u Poglavlju 3 su opisani svi koraci rekonstrukcije događaja i ispravne selekcije podataka iz kojih su onda dobivene energije pobuđenja jezgara u izlaznom kanalu reakcije. S obzirom da se a priori ne zna koja je od jezgara u izlaznom kanalu u reakciji pobuđena u neko od stanja poviše praga za čestični raspad, a čiji se produkti raspada detektiraju, u dvodimenzionalnim spektrima pobuđenja prikazane su sve kombinacije čestica u izlaznom kanalu kroz čija se pobuđena stanja reakcija mogla odviti. Nakon identificiranja najjačih stanja, ukoliko ih ima, u dvodimenzionalnim spektrima za svaku od jezgara napravljena je

projekcija u kojoj su isključeni doprinosi pobuđenih stanja drugih jezgara. Ukoliko je selekcija podataka bila jednoznačna, bez pozadinskih doprinosa drugih reakcija, ostvaruje se čist jednodimenzionalan spektar pobuđenja jezgre. Navedena metoda se zove rezonantna čestična spektroskopija. Na jednodimenzionalne spektre je tada rađena prilagodba s procijenjenom pozadinom i nizom Gausovih funkcija koje opisuju spektar, kako bi se izvukli položaji vrhova koji su kandidati za prava stanja u jezgri. Rezultati uključuju i račun efikasnosti detekcije, napravljen korištenjem Monte Carlo simulacija [107], koji je koristio kao pomoć u interpretaciji rezultata, ali i za oblik procjenjene pozadine u spektrima. Analiza je rađena, a tako su i rezultati prezentirani, za svaku kombinaciju čestica i elemenata detektorskog postava u izlaznom kanalu zasebno, a objedinjeni su unutar potpoglavlja za svaku jezgru za raspad u dani kanal. Na kraju svakog potpoglavlja, za različite kanale raspada za svaku od jezgara ^{10}Be, ^{12}Be i ^{13}B, dan je najbitniji rezultat, konačna tablica opaženih stanja po kanalima raspada.

Rezultati

Rezultati za raspade visokopobuđenih stanja, poviše praga za dani čestični raspad, u ^{4}He+^{6}He (0^{+}), ^{4}He+^{6}He (1.8 MeV, 2^{+}), ^{9}Be+n i ^{8}Be+nn kanale raspada za jezgru ^{10}Be, ^{6}He+^{6}He (0^{+}), ^{6}He+^{6}He (1.8 MeV, 2^{+}), ^{4}He+^{8}He za jezgru ^{12}Be, i ^{9}Li+^{4}He, ^{7}Li+^{6}He i ^{10}Be+^{3}H za jezgru ^{13}B su prikazani u Poglavlju 4. Raspadi visokopobuđenih stanja u kanale ^{6}He+^{6}He (1.8 MeV, 2^{+}) za ^{12}Be [115] (Tablica 4.26), te ^{7}Li+^{6}He i ^{10}Be+^{3}H za ^{13}B (Tablica 4.52), su prvi put opaženi u ovim eksperimentalnim podacima. Za ^{10}Be, u ^{4}He+^{6}He (1.8 MeV, 2^{+}) (Tablica 4.17) i ^{8}Be+nn (Tablica 4.20) kanalima raspada do sada je postojalo samo po jedno mjerenje, stoga su u prvom slučaju potvrđena opažanja zagrebačke grupe za raspade u pobuđeno stanje jezgre ^{6}He na 1.8 MeV [18], dok su u drugom slučaju opažena nova stanja koja se raspadaju u osnovno stanje jezgre ^{8}Be, koja daju potpuniju sliku ovog kanala raspada i ne slažu se u potpunosti s interpretacijom rezultata iznesenom u [21]. Detalji o pojedinim stanjima su diskutirani u vidu klasterske i molekulske strukture jezgara ^{10}Be, ^{12}Be i ^{13}B u Poglavlju 5, gdje su također dane pregledne tablice svih opaženih stanja.

U svim su promatranim kanalima raspada pronađena nova stanja, čime su uz novoopažene kanale raspade dobivene bitne spektroskopske informacije za strukturu pobuđenih stanja

navedenih jezgara. Uspješnom primjenom nezavisne eksperimentalne metode mjerenja, višenukleonskih reakcija prijenosa, za proučavanje strukture pobuđenih stanja jezgara ^{12}Be i ^{13}B ostvareni su važni rezultati, koji sugeriraju postojanje molekulske α-4n-α strukture u ^{12}Be i α-2n-t-α strukture u ^{13}B, u skladu s prijašnjim rezultatima [2, 12, 13, 15] i teorijskim predviđanjima [10, 25], te koji otvaraju put primjeni reakcija prijenosa za proučavanje i drugih neutronski bogatih lakih jezgara.

Ključne riječi: klasteriranje u neutronski bogatim lakim jezgrama, nuklearne molekule, ^{10}Be, ^{12}Be, ^{13}B, reakcije prijenosa nukleona, rezonantna čestična spektroskopija

Contents

1   Introduction

The work presented in this thesis is based on the results from the data analysis of the S1620 experiment: "Examining the helium cluster decays of the ^{12}Be excites states by triton transfer to the ^{9}Li beam" (N. Soić, M. Freer), performed at ISAC-II accelerator facility at TRIUMF, Vancouver, Canada during the three weeks experimental campaign in the summer of 2017. While many interesting decay channels and cluster states were populated in wide variety of light nuclei, main focus here is given to neutron-rich beryllium and boron isotopes, specifically ^{10,12}Be and ^{13}B, for which structure there are still a lot of open questions [1] and in the case of the ^{13}B experimental data was almost non-existent until recently [2]. These nuclei, together with some carbon and oxygen isotopes present the key nuclei to benchmark and constrain the theoretical models [3–7]. Since the nucleus is rather complex many-body nuclear system with rich and varying structural phenomena (Fig. 1.1), it has become increasingly important for these models to be able to realistically describe both aspects of the nuclear structure, namely the single particle dynamics (shell-like) and collective behavior (cluster and molecular-like) within the same framework [8]. Obtaining high-quality experimental data for weakly bound and exotic key light nuclei, crucial to benchmark the theoretical models, is quite a challenging task which was nevertheless tackled in the study presented here.

Motivation for the present study

The main motivation to perform an experiment to study the helium clustering and examine proposed molecular α-4n-α structure in the excited states of neutron-rich ^{12}Be nuclei [10, 11], came from the question weather strong clustering built on the α-α core persist in neutron-rich beryllium isotopes and subsequently in neutron-rich light nuclei in general,
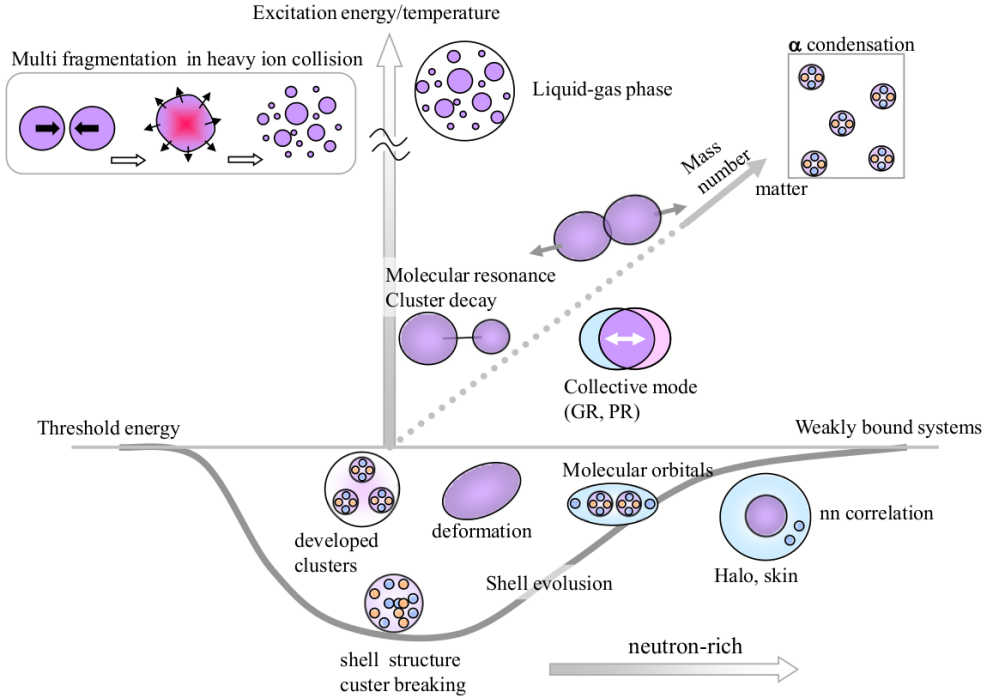
Figure 1.1: Schematic representation of rich structural phenomena emerging in nuclei depending on the mass number, excitation energy and isospin asymmetry. Taken from [9].

especially with the increase of the spin-orbit force [1]. Molecular rotational bands built on the ^{6}He+^{6}He and ^{4}He+^{8}He clustering were proposed to exist in the early work by Freer et al. [12, 13], but the consistency of the obtained results was questioned in the later experiment [14], which had used the same experimental method, the ^{12}Be beam inelastic breakup on the CH$_2$ target. Only later came the experiment by Yang et al. [15], where the states near the corresponding particle decay threshold were observed and in the small energy range where two experiments overlap, found agreement with early results by Freer et al.[12, 13]. These results still need strong experimental confirmation, especially in the higher excitation energy region, as the latter experiment had very low statistics, while the former two had large influences of unresolved background due to inability to completely separate reactions from the constituents of the CH$_2$ target. Thus came the motivation to use complementary experimental method, independent of the previous measurements and novel to the study of the ^{12}Be helium-helium cluster decays, the many-body and cluster transfer reactions with resonant particle spectroscopy method.

This approach was successfully utilized in the study of the α-2n-α molecular structure in lighter ^{10}Be nuclei, in the seminal work by Zagreb group [16–19], where the 2^+ and 4^+ members of highly deformed band built on the molecular σ-orbit [20] of valence neutrons

were found. Still, there is a doubt weather the 4^+ member of the ground state rotational band exists [21] and there is an active search, with inconsistent results [22–24], for the 6^+ member of aforementioned σ molecular band. To establish the nuclear molecule as a general type of structure in the neutron-rich light nuclei, it is essential to experimentally confirm it in heavier beryllium nuclei, particularly in the ^{12}Be nucleus in which four valence neutrons may occupy shell model orbitals, atomic-like orbitals around individual α-core or molecular-like orbitals around both α-cores.

In the case of much less studied neutron-rich boron isotopes and specifically ^{13}B presented in this thesis, many cluster states with well developed ^{9}Li+^{4}He structure were proposed to exist at high excitation energies, alongside quasi-molecular three-center α+Xn+α+t structures [25]. Experimental data on α-clustering in ^{13}B were really scarce [26, 27] until recently, where in the measurement of the ^{9}Li resonant elastic scattering on the ^{4}He gas target [2], a number of resonances in that channel were observed.

Evolution of the clustering with addition of neutrons in neutron-rich beryllium isotopes and the role that additional proton has in boron isotopes, provide benchmark studies both experimentally and theoretically for understanding of the evolution and emergence of the α-clustering and two- and three-center molecular-like structures in neutron-rich light nuclei. Here the ^{13}B could present itself as a gateway nuclei to understand the crossing from two-center α-α clustering found in beryllium isotopes to three-center α-α-α clustering in carbon isotopes, where four valence neutrons and a proton can result in rich and varying structural phenomena.

Outline and organization of the thesis

The thesis is organized as follows. In Chapter 2 an introduction to cluster and molecular-like structure of key neutron-rich light nuclei is given, with brief overview of the theoretical models which have been successful in describing clustering aspects of the structure of light nuclei, including recent developments towards ab initio models and generalization of the theory of nuclear structure. Finally the overview of transfer reactions and resonant particle spectroscopy technique is given. In Chapter 3 details of the experimental setup, calibration process, hit and event reconstruction, alongside crucial quality control checkpoints are given. In Chapter 4, obtained results for every applicable combination of the

telescope elements and particle combinations in the reaction exit channel are presented, with relevant data selection, excitation energy and correlation spectra. Most importantly, final results are presented in the form of fitted one-dimensional spectra with corresponding tables and detection efficiency calculation. At the end of every section for particular decay channel of corresponding nuclei, the summary table of the observed states is given with indicated confidence of the observed peak. As it will be shown, comprehensive analysis was carried out to obtain the results for the ^{10}Be decays to the ^{4}He+^{6}He, ^{4}He+^{6}He* (1.8 MeV, 2^{+}), ^{9}Be+n and ^{8}Be+nn, the ^{12}Be decays to the ^{6}He+^{6}He, ^{6}He+^{6}He* (1.8 MeV, 2^{+}) and ^{4}He+^{8}He and the ^{13}B decays to the ^{9}Li+^{4}He, ^{9}Li*+^{4}He, ^{7}Li+^{6}He and ^{10}Be+^{3}H. In Chapter 5, these results are discussed in detail for every decay channel and key state observed, in terms of underlying structure indicated and in context of the previous measurements if they are available. Results are summarized and final remarks on the cluster and molecular structures of the ^{10,12}Be and ^{13}B are given, with outlook for the future studies in Chapter 6.

2 Structure of neutron-rich light nuclei

2.1 Cluster and molecular structures in light nuclei

Clustering in nuclei emerges from a delicate balance among repulsive short-range force, Pauli blocking effects, attractive medium-range nuclear force and long-range Coulomb repulsion among protons [1]. As such, due to strong nn, np and pp correlations among nucleons, emergence of the clustering phenomena is closely related to the fine details of the nuclear force [5], which is most evident in deformed structures found in weakly bound systems, such as nuclear molecules, where interaction between valence nucleons and clustered core (covalent exchange on neutrons among among two of more centers) plays an important role and can compete with mean-field aspects of the nuclear force [28].

The premise of strong clustering in $N\alpha$ (^{8}Be, ^{12}C, ^{16}O ...) conjugate systems has been around more than 50 years and is best presented by the famous Ikeda diagram [29], where it is proposed that the dominating effects of clustering are expected to emerge near the corresponding particle-decay thresholds [28]. The relevance of this proposition was found true [30, 31] for one of the most important [32] and still intensively studied [7] structure in nuclear physics, the 3α structure of 0_2^+ state in ^{12}C - the Hoyle state, whose astrophysical importance for the 3α capture process is unutterable [33].

The ^{8}Be is perfect example of pure α-α clustering [34] with it's unbound ground state 92 keV above the $\alpha - \alpha$ decay threshold and rotational band built on that state with 2^+ member at 3.06 MeV ($\Gamma \approx$1.5 MeV) and 4^+ at 11.35 MeV ($\Gamma \approx$3.5 MeV) with large moment of inertia [1], making it almost the perfect (rigid) rotor. Additional neutron in ^{9}Be bounds the structure and makes the simplest example of nuclear molecule, where α-α

core is orbited by covalently exchanged valence neutron, in either σ or π orbital. The π orbital is associated with the ground state and it's rotational $K^\pi = 3/2^-$ band. Due to the motion of orbiting neutron perpendicular to the node containing the α-α core, the π orbit leads to more compact structure of the nucleus. The σ orbital, associated with the $K^\pi = 1/2^+$ band, on the other hand contains the node along the α-α core, making the two α's more separated and consequently the structure more deformed [9]. Similarly, in ^{10}Be and ^{12}Be two and four valence neutrons, respectively, can be arranged in π, σ or combination of orbitals ($\sigma\pi$) making wide variety of exotic structures (Fig. 2.1) appear in the excitation energy spectra [10, 20]. It's quite remarkable that the molecular band built on the ^{10}Be ground state [35] has almost the same moment of inertia as the ^{8}Be ground state band, meaning that the α-α core still largely persist with addition of the neutrons [20, 36]. Question is weather, and in what conditions, can strong two-center clustering withstand dissociation by spin-orbit force at large momenta of nuclei. Although this is still being tackled experimentally, there is no firm agreement on the existence of the 4^+ member of the 0^+ ground state band [21]. There is also ongoing search, with inconsistent results [22, 24], for the 6^+ member of the largely deformed (α-α separation almost the double of that from the ground state band) 0_2^+ band built on arrangement of the valence neutrons in σ orbitals.

In the case of the ^{12}Be nucleus, proposed existence of the molecular bands built on the ^{6}He-^{6}He and ^{4}He-^{8}He clustering [12, 13] was contradicted by later experiment [14], where strong structures corresponding to aforementioned decay channels were not found. Interestingly enough, resonant elastic scattering experiment [37] from the same main authors didn't produce better results and for example in 2n transfer reaction [38], authors didn't manage to obtain any results to support the proposed clustering in ^{12}Be nuclei. More recently, [15] had performed high-resolution inelastic breakup experiment with zero-degree detector and, apart from finding two states near corresponding decay threshold, have found agreement with [12, 13], in small energy range where two experiments overlap, indicating well developed α-4n-α structure in ^{12}Be. This goes to say that experimental search for helium-helium clustering in ^{12}Be has proved itself to be quite a challenging task with mixed success and there is still a need for strong experimental confirmation of the result by [12, 13] and [15], especially in the higher excitation energy range.

In both ^{10}Be and ^{12}Be there is still a burning question weather the strong α-α clustering

persist with increase in spin-orbit force and what role do the valence neutrons play in stabilization of the cluster structure. On the other hand, to grasp the prevailing importance of the clustering in (neutron-rich) light nuclei, there is more and more evidence on the cluster-like features even in the ground states of wide range of nuclei, coexisting with the mean-field aspects of nuclear structure, influencing the ground and low-lying states properties and in the case of the ^{12}Be for example, is the most plausible reason for breaking of the N=8 shell closure [9, 39].
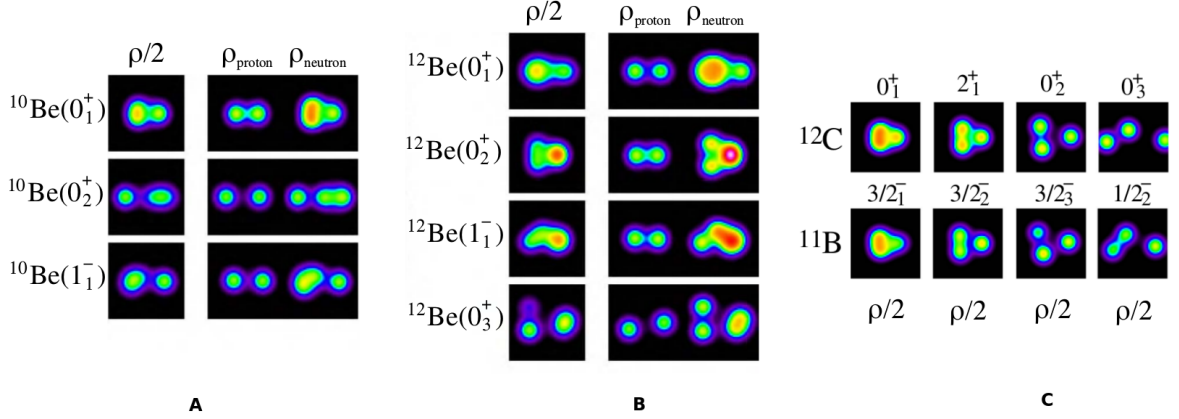
Figure 2.1: Density distributions of the intrinsic states for the band-head states of ^{10}Be (A) and ^{12}Be (C) obtained by AMD-VAP [10, 20]. Density distributions of intrinsic states for the ground and excited states of ^{11}B and ^{12}C (C) calculated by AMD-VAP [40, 41]. The integrated densities of matter are presented in all nuclei, while proton and neutron densities are presented only for A and B. Taken from [9].

The three-center clustering is even more complex and experimentally very hard to directly observe. The measurements and consequently the methods developed in the study of direct 3α decays of the ^{12}C excited states can guide future studies [1, 32, 33]. Here, the boron isotopes could be of prime importance (see the results from [42, 43] for example), as in the ^{11}B nuclei, an analog to the Hoyle state was proposed [44], near the corresponding particle decay threshold, suggesting that apart from the better studied ^{7}Li+α two-center clustering, triton (^{8}Be+t) could play a similar role to the "third" α (^{8}Be+α) in ^{12}C three-center model, specially for triaxially deformed states (Fig. 2.1). Just like the evolution of clustering with addition of neutrons in carbon isotopes is benchmark for theoretical models [45], with proposed molecular-like structure of ^{14}C [46], an intriguing parallel can be made to the evolution of clustering in the neutron-rich boron isotopes. Besides strong lithium-helium clustering, also a molecular-like three-center structures were proposed to exist at higher excitation energies in ^{13}B [25]. With only one experimental study of

the ^{9}Li-α clustering in ^{13}B carried out [2], present experimental results are much needed to understand the ^{13}B structure, as well as to propel both experimental and theoretical study of the neutron-rich boron isotopes.

2.2   Overview of theoretical models

A nucleus is complex many-body quantum system with rich and varying structural phenomena often competing and coexisting within the same nucleus. The dominance of one aspect of the structure over the other is ever-changing, depending on the mass number, isospin asymmetry, excitation energy and binding energy of the ground state, just to name a few. In the light nuclei, the interplay between the collective and single-particle aspect of structure becomes even more evident as it reveals the fine details of the interaction between the nucleons. Small number of important degrees of freedom enables the theoretical models to realistically model the nuclei starting from the two- and three-body interactions with remarkable results [1]. The effect of strong correlations among nucleons is perhaps best seen in helium isotopes. The ^{4}He is strongly bound with one of the largest binding energy per nucleon in the whole chart, having the first excited state at 20.21 MeV [47]. This strongly bound and stable structure causes the formation of α sub-systems on which the cluster structures in more complex systems reside, from Nα clustering in α-conjugate nuclei (^{8}Be, ^{12}C, ^{16}O ...) to α-Xn-α molecular structure in beryllium isotopes. Unlike the ^{5}He and ^{7}He nuclei, which are unbound, the ^{6}He and ^{8}He nuclei are stable and show Borromean structure with large neutron halo. In the case of the latter two, even number of neutrons results in strong nn correlations which stabilize the structure [48]. From the clustering standpoint, this evolution is best seen in beryllium isotopes, where valence neutrons added to the unbound ^{8}Be nuclei stabilize the structure and results in the appearance of molecular-like α-Xn-α structure in neutron-rich beryllium nuclei. It's evident that classical shell model, based on the assumption of free motion of nucleons in effective mean-field potential generated by all other nucleons [49], cannot account for these kind of structure, where fine details of interaction among nucleons and strong correlations play a dominating role. The so-called exotic nuclei offer unprecedented view at the most important aspects of various components of the nuclear force, in particular cases when theoretical descriptions are confronted with experimental data and provide a

driving force for the evolution of the modern shell model [50, 51].

2.2.1 Microscopic clustering models and Mean-field approach

It was discovered in the early days of nuclear physics that nuclei with even, and equal, number of protons and neutrons, so-called α-conjugate nuclei: ^{12}C, ^{16}O ..., are particularly stable having large binding energy per nucleon, compared to it's neighbors. This is valid even for the ^{8}Be, even though it's ground state is unstable for the α-α decay. The binding energy of such systems can be described by the number of bonds between α particles with the linear dependency: N(BE$_\alpha$) + N$\times$ B$_{\alpha\alpha}$, where BE$_\alpha$ is the binding energy of the α-particle and B$_{\alpha\alpha}$ is the energy associated with the α-α interaction [52]. Later, it was realized that the cluster structure does not manifest itself in the ground-state, but emerges as the internal energy of the system is increased and the threshold for the decay to constituent clusters is approached [29]. Modern theoretical approaches reveal that existence of strong clustering in the nucleus influences the ground state properties [35, 39]. Underlying symmetries influence the geometrical arrangement of the α-particles and models based on the deformed harmonic oscillator found that for axial deformations of $(\omega_\perp : \omega_z)$ 2:1 and 3:1 deformed magic numbers occur. Interesting feature that the spherical magic numbers (2, 6, 12, 20...) are repeated twice at the deformation of 2:1 and three times at 3:1. These symmetries have been explored [53, 54] to identify particular cluster partitions and show that at the deformation of 2:1 super-deformed cluster states should be found in ^{8}Be $(\alpha-\alpha)$, ^{20}Ne $(^{16}$O$+\alpha)$ ... and at 3:1 deformation, speculated hyper-deformation is proposed to exist in ^{12}C $(\alpha-\alpha-\alpha)$, ^{24}Mg $(\alpha-^{16}$O$-\alpha)$ ... What is interesting, underlying symmetries that are associated with the arrangements of the α-particles are found to be present in deformed harmonic oscillator model, even if the α-particles are not explicitly assumed within nucleus [54]. There is a direct link between the appearance of shell structures in deformed HO and configurations found in Alpha Cluster Model ([55] and ref. therein). Here the α is preassumed and constructed from the quartet (2p+2n) of particles in 0s$_{1/2}$ orbital and the collection of such quartets may be treated in harmonic oscillator framework. The total wave function of the system is antisymmetrized to account for fermionic degrees of freedom and is created using a Slater determinant. Hamiltonian of a system is proportional to center-of-mass energy, $\alpha-\alpha$ interaction effective potential and Coulomb interaction. The optimal arrangement of the

α-particles is derived variationally, where the parameters which are being optimized are the locations and size of the α-particles. In the limit where the separation of the α particles tends to zero, corresponding harmonic oscillator configurations are found. On the other hand, the model doesn't account for the class of states where the α separation is large enough so that the internal structure of the α particle is not so important and behavior of the system resembles that of a "free α-particle gas", nuclear Bose-Einstein condensate. These concepts were particularly important for the description of the 3-α Hoyle state [1]. To account for condensate-like behaviors the α-particles system THSR wave-function was formulated [56, 57]. In the limit where the separation of the α-particles tends to infinity a free α-particle gas is obtained, mathematically represented by the product of the Gaussian wave functions, while for the small separation antisymmetrization operator takes over and accounts for the internal fermionic degrees of freedom. Even though the mentioned models briefly described here had a great success in describing the experimental properties of Nα systems, true degrees of freedom are those of constituent nucleons and potentials based on realistic NN and NNN interactions. Still, the ingredients for more realistic and complex variational models are established in a similar manner, namely the choice of the Hamiltonian with effective NN interactions and the basis (wave functions) in which the solutions are obtained.

The shortcomings of Alpha Cluster Model were addressed within the generator coordinate method (GCM) [58] and resonating group method (RGM) [59], both of which span the development of many different microscopic approaches to describe the cluster and molecular-like structures in nuclei, as for e.g. very successful microscopic calculations of the ^{9,10,11}Be structure by [60] based on the $\alpha + \alpha +$Xn constituents. Within the RGM formalism the wave-function describing the A nucleons is separated into two clusters [48]:

$$\psi(\mathbf{r}_1, \mathbf{r}_1, ..., \mathbf{r}_1) = \mathrm{F}(\mathbf{R}_{\mathrm{CM}})\hat{\mathbf{A}}\{\phi_1(\xi_1)\phi_2(\xi_2)\mathbf{g}(\mathbf{R})\} \tag{2.1}$$

where $\mathrm{F}(\mathbf{R}_{\mathrm{CM}})$ describes the motion of the center of mass of the nucleus, $\hat{\mathbf{A}}$ is the antisymmetrization operator which exchanges nucleons between the two clusters, $\phi(\xi)_i$ are antisymmetrized internal states of the two clusters and $\mathbf{g}(\mathbf{R})$ describes relative motion of two clusters. The great advantage of this approach is the fact that the constituents of the clusters are fully antisymmetrized and the excitations of the cluster core can be taken into account in multi-channel approach.

On these basis generalized two-center cluster model (GTCM) was formed, which can treat covalent, ionic and atomic configurations in general systems with two inert cores plus valence nucleons [61] In this model, the covalent configurations constructed by the molecular orbital (MO) method and the atomic (or ionic) configuration obtained by the valence bonding (VB) method can be handled in a consistent manner. This model was successfully applied to study the neutron-rich systems ^{10,12}Be $= \alpha + \alpha +$ Xn (X = 2, 4), where different configurations were established. These include molecular states in which the valence neutrons are covalently exchanged among α cores and ionic $\alpha+^{6}$He and ^{4,5,6}He$+^{8,7,6}$He configuration, in which the neutrons are localized on one of the cores. Similarly, in the GTCM calculation by [11] it was shown that in unbound region above particle-decay thresholds, the ionic configurations appear as the molecular resonances of the ^{4,5,6}He$+^{8,7,6}$He cluster configurations. Other models like four-cluster model with RGM method [36] or stochastic variational method [62] and GCM with Real-time Evolution Method (REM) [63] have been used to study neutron-rich beryllium isotopes.

In the nuclei with excess of neutrons, the cluster cores are surrounded by the valence neutrons which play a glue-like role among the weakly coupled cluster cores. There is an energy gain due to interactions between clusters and the neutron, while the kinetic energy between clusters is reduced. The glue-like effect of valence neutrons causes the lowering of the corresponding energy levels and the appearance of so-called intruder states, which have well developed cluster structure in the lower bound region [61]. For this reason molecular orbit model has been successful in describing the low-lying states of light neutron-rich nuclei, particularly Be [64, 65] and B [66] isotopes, built on α-α core plus valence nucleons structure.

Another interesting development in the nuclear structure theory in the last two decades, is the application of self-consistent mean-field approach, within the energy density functional (EDF) theory [67, 68], to describe the emergence of cluster and molecular-like structures in the light nuclei [5, 45, 69]. The great benefit of this approach is quite accurate description of wide variety of structural phenomena across the whole nuclear chart within the single framework, with the use of global effective interactions adjusted to reproduce empirical properties of both symmetric and asymmetric nuclear matter and bulk properties of simple, spherical and stable nuclei [68]. While the approach has successfully been utilized to study nuclei in medium to heavy and super-heavy mass region, it's recent application

to light nuclei (Be, B and C isotopes) [5, 45, 69] has yielded quite remarkable results in description of clustering aspects of nuclei, for such generalized approach. The persistence of α-α core clustering with addition of neutrons is found for the neutron-rich beryllium isotopes, molecular-like α-Xn-α structure is to large extent correctly reproduced, as the effect of the clustering are seen even in the properties of the ground states, although the model over-binds the structure. The appearance of strong α-α clustering is predicted to emerge in ^{13}B and the shell-like, triaxially deformed and chain structures are found in ^{12}C [69]. What is perhaps more important, are the general remarks on the emergence of clustering, where the localization of the wave-functions is directly connected with the depth of the effective potential, thus the emergence of the clustering is strongly influenced by the fine details of the nuclear force [5]. Another important remark is the influence of the σ valence neutrons on the stabilization of the chain $\alpha - \alpha - \alpha$ structure in neutron-rich carbon isotopes [45]. These results could perhaps guide the search for chain structure in the form of ^{10}Be* $(\sigma)+$ $^{4+Xn}$He molecular resonances. Precise experimental results on weakly-bound and exotic structures are quite important benchmark for the application of these (and other) models to light nuclei.

2.2.2 Antisymmetrized molecular dynamics (AMD) and Fermionic molecular dynamics (FMD)

Antisymetrized molecular dynamics (AMD) is microscopic model based on the nucleonic degrees of freedom and realistic NN interactions, which can be applied to study both mean-field and clustering aspects of nuclei [3]. Great advantage of the AMD approach, compared to aforementioned microscopic clustering models, is that the existence of clusters or inert cores is not a priori assumed or imposed, and it can be used to study both nuclear structure and reactions [9]. In the AMD wave-function, all single nucleons are treated independently as localized Gaussians (φ_i), antisymmetrized via Slater determinant:

$$\Phi_{\mathrm{AMD}}(\mathbf{Z}) = \frac{1}{\sqrt{A!}}\hat{\mathbf{A}}\{\phi_1, \phi_2, ..., \phi_A\} \tag{2.2}$$

where nucleon wave-function ϕ_i contains the spatial (φ_i), spin (ξ_i) and isospin (τ_i) part: $\phi_i = \varphi_i \xi_i \tau_i$ and $\mathbf{Z}$ is complex set of variational parameters describing the spin and geometry of the wave-function [3]. The wave-function of the system is obtained as linear combination

of AMD wave functions and the energy of the system is computed, variationally, utilizing an effective nucleon-nucleon interaction. Accordingly, corresponding cluster and shell-model like structures naturally emerge, as positions of the Gaussian wave-packages are being variationally treated. For the comparison with the experimental data, intrinsic wave function are projected to the total-angular-momentum eigenstates and expectation values of operators are calculated. In that sense, two approaches are differentiated: energy variation after the parity projection but before projection (VBP) with respect to the total-angular momentum and energy variation after the spin-parity projection (VAP). AMD has been successfully applied to wide variety of light nuclei, with beryllium, boron and carbon isotopes being of particular interest in the thesis [9, 10, 20, 25].

Fermionic molecular dynamics (FMD) describes a system of fermions by an antisymmetrized many-body state ("fermionic" property), built from single-particle wave-packets of gaussian shape localized in the phase-space ("molecular" property). Each single-particle state is parametrized by its mean spatial position, mean momentum, two angles for the spin direction and a complex width parameter [70]. For a chosen parametrization of the trial state the equations of motion for the parameters are derived from the time-dependent quantum variational principle ("dynamic" approach). Since there is a unique mapping of the parameter set on the quantum trial state, dynamics of the parameters is actually the representation of the dynamics of the quantum many-body state [71]. The choice of the parametrized antisymmetric trial state determines which physical phenomena are being described and is closely related to the choice of the interaction potential [71].

The features of FMD calculations coincide with those of AMD, but variable Gaussian complex width parameter should in principle allow for better description of shell-model like and also weakly bound states. On the other hand, AMD method is very adaptive and in combination with other microscopic clustering models can be applied to wide variety of nuclear structure and dynamics phenomena [1]. An example of these derivatives are AMD+GCM [72] and AMD+3α GCM [73], where 3α-GCM wave function is found to be equivalent to single THSR wave-function [1] and in that sense can almost be seen as AMD+THSR combination.

2.2.3   Ab-initio type models

With the evolution of the microscopic description of the rich structural phenomena found in wide variety of both light and heavy nuclei, naturally comes the question on how do these structures emerge from the basic principles and realistic nucleon-nucleon interaction without any preconceived assumptions or the usage of effective interactions. In the last two decades many advances in modern ab initio theories have been achieved [74], to the point where realistic description of emerging structural phenomena in complex many-body quantum systems, which nuclei are, can be achieved. The use of realistic NN, with inclusion of NNN, interactions provide rather stunning insights in the structure of nuclei and the emergence of various structures from the basic properties of the nuclear force, derived from QCD [75]. Interaction is usually formulated in terms of various types of exchange processes in chiral effective field theory, which in LO (leading order) include pion exchange, in NLO (next-to leading order) two-pion exchange, as well as one pion absorption and emission by a single nucleon, which interacts with a second via pion exchange (called normalization of one pion exchange), N3LO (next to, next to, next to leading order) which amongst other components includes three-pion exchange components and even in some cases N4LO [75, 76].

Modern ab initio models like Green's function Monte Carlo (GFMC) [77], No-core Shell model (NCSM) [78] and Nuclear lattice Effective field theory (NLEFT) [76] all rely on the use of realistic NN interactions with usual inclusion of zero-range NNN interactions for realistic description of the basic properties of nuclei (see [79] for e.g.). Advancements in these theories caused the revitalization and revision of description of the key features of the key light nuclei, like the $\alpha - \alpha$ ground state of ^{8}Be [34] and the existence of rotational bands in Be isotopes [80], structure of the ground and the Hoyle state in ^{12}C [6, 81], phase transitions and α clustering in light nuclei [7, 82], to name a few.

2.3   Structure of the ^{10,12}Be and ^{13}B nuclei

The molecular-like α-Xn-α structure of the neutron-rich beryllium isotopes, and its evolution with addition of neutrons, is an important benchmarks for the development and hands-on test of the theoretical models. As such, description of cluster and molecular-like phenomena had been revisited many times as these models have been developing. These

include detailed study of the ^{10}Be structure in microscopic $\alpha+\alpha+n+n$ model [36, 62, 83], MO model [64], microscopic three-cluster hyperspherical harmonics approach [84], AMD [20, 85], GTCM [61], REM+GCM [63], THSR approach [86] and NCSM [80]. Similarly, the ^{12}Be structure has been studied with AMD [10], MCC+AMD [87], GTCM [11, 61], hyperspherical adiabatic expansion method [88], THSR [39] and NCSM [80]. In Fig. 2.1, the structure of the band head states in both ^{10}Be and ^{12}Be was shown, while on Fig. 2.2 unified schematic representation of the same states in ^{10}Be was given in terms of di-cluster, total and single-particle AMD wave-function distributions.

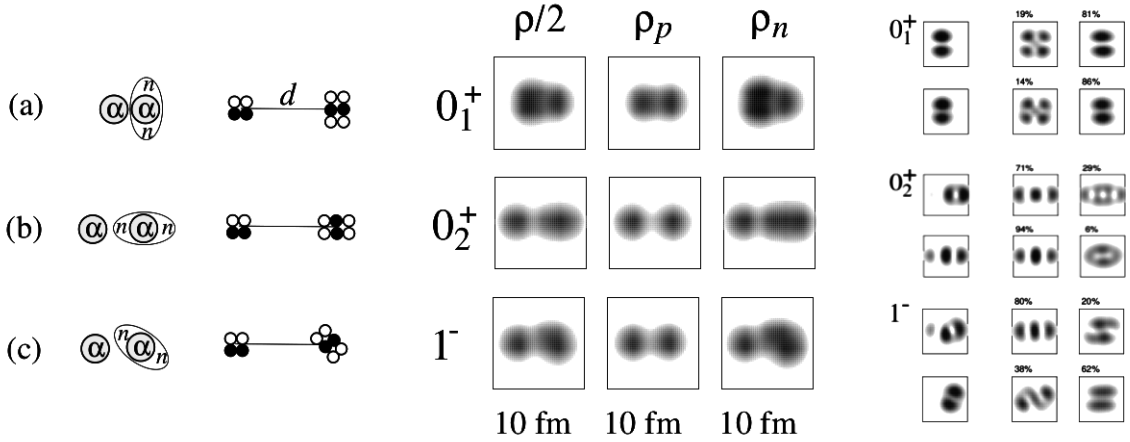Figure 2.2: Unified schematic representation of the intrinsic structure of the ^{10}Be band heads: a) $0_1{}^+$ (ground state, MO: π), b) 0_2^+ (exp: 6.18 MeV, MO: σ) and c) 1^- (exp. 9.56 MeV, MO: $\pi\sigma$). Left side of the figure presents di-cluster $\alpha+^6$He representation, middle presents density distributions of proton, neutron and total wave-functions, while the right side presents single particle wave functions for the same set of states. Taken from AMD study [20].

The ^{13}B and neutron-rich boron isotopes in general have been much less studied, both theoretically and experimentally. These studies are usually focused on lighter ^{10,11}B in three-center MO model [66], or generalized to neutron-rich boron isotopes in MO [89] and AMD [90] approaches, with only one dedicated study of ^{13}B structure in AMD formalism [25]. The ground state of ^{13}B exhibits shell-like features, due to the restoration of the N=8 shell closure, compared to ^{12}Be in which the shell closure is broken due to the intruder configuration of the ^{11}Be ground state. In the higher excitation energy region, number of excited states having strong ^{9}Li+α and three-center molecular-like (α-2n)-t-α structures are proposed to exist, with corresponding rotational bands built on these structures [25]. Although ^{10}Be+t configuration is not found explicitly in the study, it is proposed to co-exist with the pronounced α clustered states. As the ^{10}Be nucleus has strong α-α core clustering "built-in", the observation of these states could be correlated to the three-

center quasi molecular-like structures in the ^{13}B, built on α-2n-t-α clustering, similarly to molecular α-2n-α-α structure in the ^{14}C. As discussed in the introduction (Section 2.1) in more details, boron isotopes and the ^{13}B in particular could provide a gateway in the understanding of the evolution of molecular α-Xn-α two-center clustering, found in neutron-rich beryllium isotopes, to molecular-like α-Xn-α-α three-center clustering found in neutron-rich carbon isotopes. On the other hand, structure like ^{12}Be+p is expected to exist with excitations on both the valence proton and neutrons inside the core [25]. Proposed rich structural phenomena [25] in N=8 shell nucleus ^{13}B, recent experimental observation of the number of the ^{9}Li+α resonances existing in the 15-20 MeV excitation energy range [2], and the results presented in this thesis should motivate future detailed studies of the ^{13}B nucleus.

The details on particular states and proposed rotational bands built on molecular-like structure of ^{10,12}Be and ^{13}B can be found in Chapter 5, where the results from the present experiment are discussed.

2.4   Experimental approach

In the present experiment, many-nucleon and cluster transfer reactions of the ^{9}Li beam on LiF target were used to populate the cluster and molecular-like structures of the excited states of the neutron-rich beryllium and boron isotopes, which are than studied via the so-called resonant particle spectroscopy method [91, 92].

2.4.1   Transfer reactions

The cluster transfer reactions of the ^{7}Li beam on the ^{7}Li target were successfully used to study the molecular structure of the ^{10}Be excited states in seminal work by Zagreb group [16, 18] and to study the Li+He and Be+H clustering in the ^{10,11,12}B [43]. In simplified view of the direct reaction mechanism, excited states of the Be and B nuclei could have been produced in t or α transfer, respectively, from either the ^{7}Li target or the beam. It is reasonable to expect that, from the point of view of the direct reactions, the t or α transfer to the neutron-rich ^{9}Li beam would provide a mechanism to populate the molecular and cluster structures in the ^{12}Be and ^{13}B nuclei. Additionally, for the products in the ground states, both of these reaction proceed with large and positive Q-values. It is important to

mention that this is quite a novel approach to study these two nuclei, as all of the results from the previous measurements were obtained through more commonly used resonant elastic scattering and inelastic breakup measurements [2, 12–15, 93]. Similarly, the ^{10}Be excited states could have been produced via the p/t transfer from/to ^{7}Li target. Of course, complex many-step processes like two-step transfer or incomplete fusion followed by the sequential decay cannot be ruled out at energies of few MeV per nucleon and do play an important role in population of cluster states [94]. Experimental data obtained in the transfer reactions are usually compared to the theoretical calculations within the DWBA (Distorted Wave Born Approximation) [95] and CDCC (Coupled Discretized Continuum Channels) [94] frameworks. As will be addressed in detail mostly in the discussion of the ^{10}Be and ^{12}Be results, transfer reactions are very sensitive to the structure of the nuclei in the entrance channel and the total energy available in the reaction [94, 96], valid also for the breakup reactions, which led to some underwhelming results in the past [14, 38] in attempt to study the cluster structure of the ^{12}Be nuclei.

2.4.2 Resonant particle spectroscopy

For the resonant particle spectroscopy measurements [91, 92] wide angular coverage detector arrays are much needed, as the coincident detection of the two out of three and three out of four reaction products, necessary to reconstruct the full kinematics of the event, greatly reduces the available phase space. For this reason large silicon strip detector array has to be used and usually the standard ΔE-E technique is used to identify the reaction products. Exit channels are identified and selected by imposing linear or graphical cuts on the Q-value spectra, Catania plot [97] and additional correlation spectra if needed. Once the exit channel is identified, relative energy for every pair of the reaction products is reconstructed and after excluding the contributions from the prominent states in other two combinations, excitation energy spectrum (projection) for particular combination of particles from sequential decay of mother nuclei is obtained. The spectra are than fitted on top of the estimated background, taking the geometrical efficiency, obtained from the realistic Monte Carlo simulations, and possible sources of remaining background contributions into account.

Great advantage of these kind of measurements is the ability to directly observe particular decay channel of given nucleus which, due to structural overlap, tends to select states with

large partial decay widths for the decay to that channel. Knowing the partial widths for every decay channel is desirable, as the dominating partial width is indicative of the underlying structure of the decaying nucleus.

3 Nuclear reactions of ^{9}Li beam on LiF target

3.1 Experimental setup

In this section, the experimental conditions under which the experiment was performed are explained, from the accelerator facility itself and the production of the radioactive ion beam, to the detector setup and the targets used.

3.1.1 ISAC-II accelerator facility and production of the ^{9}Li beam

The TRIUMF Isotope Separator and Accelerator (ISAC) facility, shown in Fig. 3.1., uses the isotope separation on-line (ISOL) technique to produce rare-isotope beams (RIB) [98]. The ISOL system consists of a 520 MeV Cyclotron, used for the production of the primary high-energy proton beam which is then, depending on the needs, focused onto one of four main beam lines, as it can be used for RIB production, irradiation of the materials, proton treatment for cancer and production of medical isotopes. The proton beam is accelerated through high-frequency alternating electric field and a massive six-sector magnet is used to confine the beam onto a heavy production target. The rare isotopes produced during the interaction of the proton beam with the target nuclei are stopped in the bulk of the target material. They diffuse within the target material matrix to the surface of the grain and then effuse to the ion source where they are ionized to form an ion beam that can be separated by mass, accelerated, and guided to the experimental area. In present case, this was ISAC-II experimental hall and the TUDA chamber, where the LiF target and detector setup were mounted. RIB is delivered in bunches (every 85.5 ns) with a duration $\sim$ 1 ns, which was used to setup the trigger condition, to coincide collection of the data with the arrival of the beam.
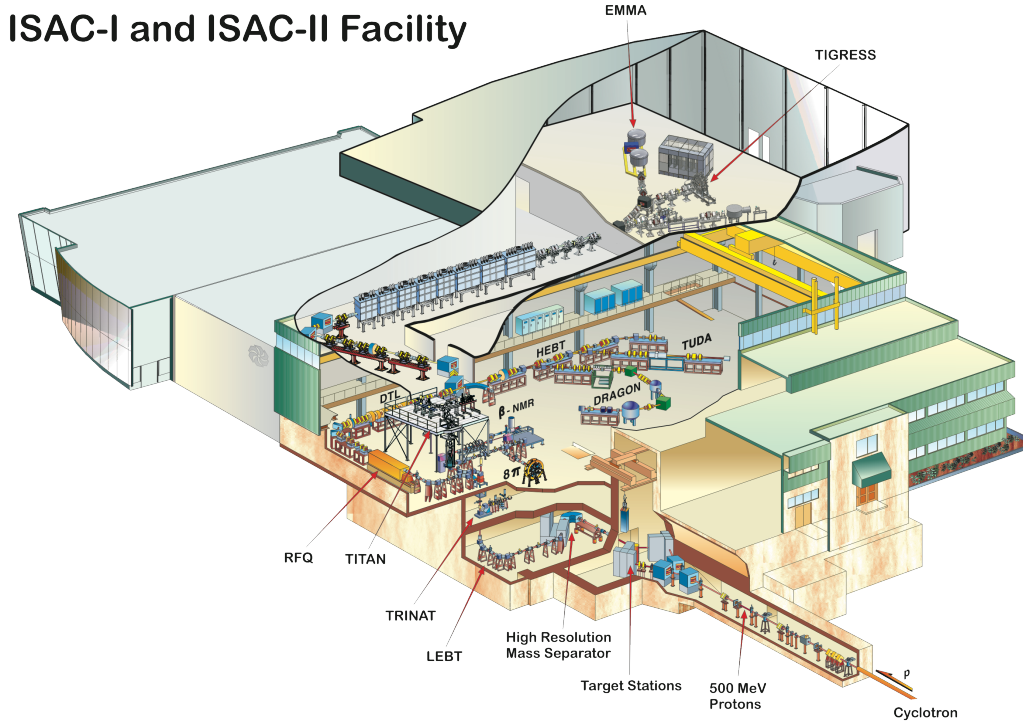
ISAC-I and ISAC-II Facility

Figure 3.1: The TRIUMF Isotope Separator and Accelerator (ISAC) schematic view.

During the experiment average current of the 74.8 MeV ^{9}Li^{3+} beam was of the order $\sim$ 8-10$\times$10^6 pps (4-5 epA), ranging from 16-20$\times$10^6 pps at the beginning to 5-6$\times$10^6 pps at the end of the experiment. The beam was collimated through a 3 mm hole at the beginning of the experiment, ensuring it will not scatter directly of the target frame to the detectors. Due to the feature of the radioactive beams, being much more difficult to produce and to maintain stable, refocusing of the beam spot on the LiF target occurred frequently during the experiment and was taken into account in the analysis procedure to accommodate for the small change in the geometry of the detector setup, which will be explained in the following chapter. Although precautions had been taken, throughout the first half of the experiment a part of the beam has been directly scattering off the collimator frame, effectively entering the detector setup at a different angle. This can be seen in the particle identification spectra as a large enhancement in the presence of spurious "^{11}Li" isotope data, due to the longer path of the ^{9}Li beam in the ΔE detector. As the experiment went through, better focusing of the beam was achieved and this effect was minimized. As a result of condensation on the LiF target, a small amount of hydrogen contamination is present in the data. This was taken into account in the data analysis and is explained in more detail in the results.

3.1.2 LAMP detector setup and the LiF target

Detector setup comprised of six wedge-shaped telescopes, shown in the Fig. 3.2, arranged in the "lampshade" geometry (LAMP), was used for detection of the reaction products. Each telescope contains single sided silicon strip thin ($\sim 70~\mu$m) ΔE detector and thick ($\sim 1500~\mu$m) E detector. Telescope configuration of the each detector set has enabled the use of standard ΔE-E method for the particle identification. Due to the different mass and atomic number (Z, A), each detected isotope of a given total energy, losses different amount of energy in the ΔE detector, with loss being described by Bethe-Bloch formula. Resulting energy-loss curves in the ΔE-E spectra enabled the identification of a given isotope by the use of graphical cuts.
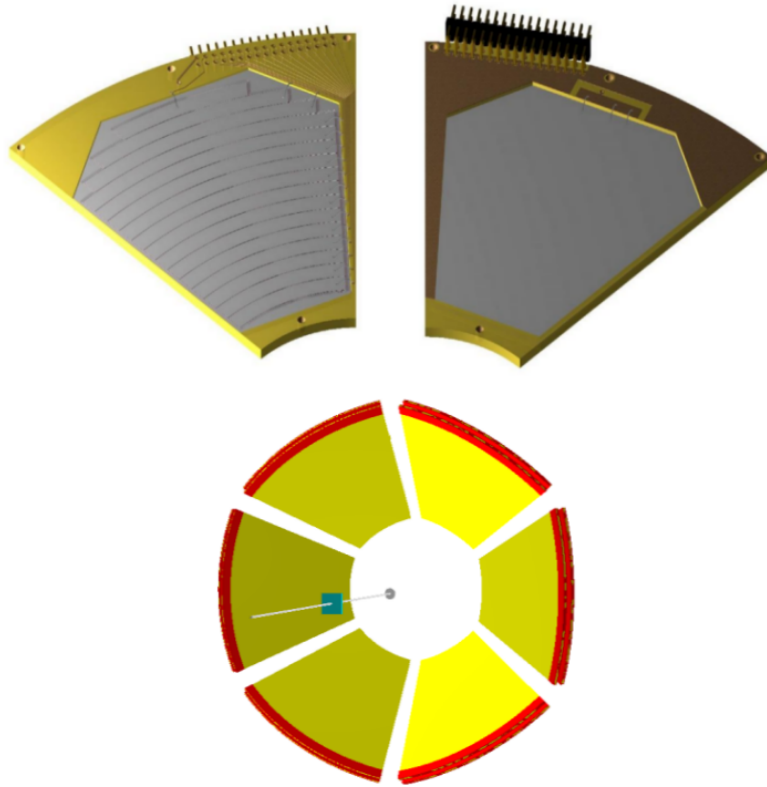
Figure 3.2: LAMP telescope setup consisting of twelve YY1 single-sided silicon strip detectors by Micron Semiconductor Ltd. [99], arranged in the lampshade geometry. Schematic representation is produced in AUSA framework [100].

Wedge shaped YY1 detectors were produced by Micron Semiconductor Ltd. [99] and have 16 strips: 0.1 mm wide inactive gaps separate the active areas (5 mm per strip) covered by electrodes for the individual signal readout. Segmentation of the detector is

seen in the experimental data as a mean θ value of the strip, defined by the position of the center of the strip relative to the target position. Angular coverage of the LAMP setup is defined by the distance of the detector mount from the target and the angular tilt from the detection plane toward the beam line. Each detector has a standard metalization (2M) layer from each side ~ 0.5 μm in thickness, treated as ^{27}Al "dead" layer, which was taken into account in the calibration and analysis procedure. As different isotopes lose different amount of energy in dead layer, this especially affects energy calibration for the lightest and heaviest nuclei. Thickness of the detectors used in the experiment is listed in the Table 3.1.

telescope	#1	#2	#3	#4	#5	#6
ΔE [μm]	65	67	75	71	70	72
E [μm]	1537	1537	1538	1541	989	1537
ϕ	180°	120°	60°	0°	-60°	-120°

Table 3.1: Telescopes used in the experiment, YY1 design from Micron Semiconductor Ltd. [99]. Naming the telescopes was done "counterclockwise", while absolute ϕ=0° is defined by the beam axis (+Z).

Detector setup efficiency was optimized (angular coverage) for the detection of decay products of the ^{12}Be excited states: ^{6}He+^{6}He and ^{4}He+^{8}He, as the ^{12}Be measurement was the main objective of the S1620 experiment. Efficiency optimization was done using Monte Carlo nuclear reactions simulation software AUSALIB (SimX) by Aarhus University Subatomic Physics group [100], varying the distance and tilt angle of the LAMP setup until the best results were obtained. Since the lampshade geometry of the detector setup is symmetrical, nominal angular coverage $\Delta\theta$ of all telescopes was $\sim 16°$-48°, accounting for 2° per strip of E detector and total $\Delta\phi$ range of $\sim 55°$ per telescope. Rough detector mount design was made in FreeCAD software [101], after which it was taken to the technicians at Ruđer Bošković Institute for the final CAD drawing, from which the mount itself was made in-house.

In the final setup detectors were mounted to a metal frame (detector mount) using a plastic screw and 1.2mm thick plastic washers. Plastic was used to insulate the detectors from the mount and to prevent electrical shorts and ground loops between the detector,

electronics and mount together with the chamber. Due to the damage made on one of the detectors in transport, a replacement E detector for telescope 5 was used. Since the motherboard of the replacement detector was slightly different, more plastic washers were used to mount the ΔE_5 detector, pushing it closer to the beam line. For this reason nominal θ_0 for ΔE_5 is a bit smaller compared to the rest of ΔE detectors. Distance of the detector mount from the target center was 164 mm. To calculate the exact position of each strip, detailed measurements of the mounting frame and detectors were taken. Taking into account the slope angle of $44°$ toward the beam line, 2.2 mm thickness of each detector motherboard and the number of plastic washers used, one can calculate the exact position of each strip. Total nominal polar angle coverage, without any corrections to the target center is presented in Table 3.2.

$\Delta\theta_0$ (ΔE_5)	$\Delta\theta_0$ ($\Delta E_{1,2,3,4,6}$)	$\Delta\theta_0$ (E_{1-6})
[15.5°, 50.5°]	[16.4°, 50.2°]	[17.2°, 50°]

Table 3.2: Total nominal $\Delta\theta$ coverage for each detector used, measured from the center of the target prior to any corrections.

Due to the unfortunate misuse prior to experiment, target ladder on which the targets were mounted in the TUDA chamber was bent away from the detectors (Fig. 3.3), changing calculated nominal geometry. For this reasons, correct geometry of the detector setup had to be found in the offline analysis. This was done in great detail using the elastic scattering of the ^{9}Li beam on the ^{197}Au target, and further corrected using elastic and inelastic scattering on the LiF target. All the targets (Table 3.3) used in the present experiment were made at the Target Lab of Istituto Nazionale di Fisica Nucleare - Laboratori Nazionali del Sud (INFN-LNS) by A. Massara. Gold (^{197}Au) target of ~ 250 μg/cm^2 thickness was self-supporting, while LiF targets of ~ 1000 μg/cm^2 were made on a thin ^{27}Al ~ 40 μg/cm^2 backing, both by evaporation technique in clean conditions. Since LiF contains natural lithium it is estimated that the content of the ^{6}Li isotope in the target should be around 7.5 % of total lithium content. Due to the production process of the targets, a small amount of ^{184}W contamination was found, which can only be seen in elastic scattering data. Aforementioned ^{1}H contaminant, which had affected in most parts only ^{4}He+^{6}He and ^{4}He+^{4}He coincidences, was carefully taken into account in the analysis of many-body reactions.
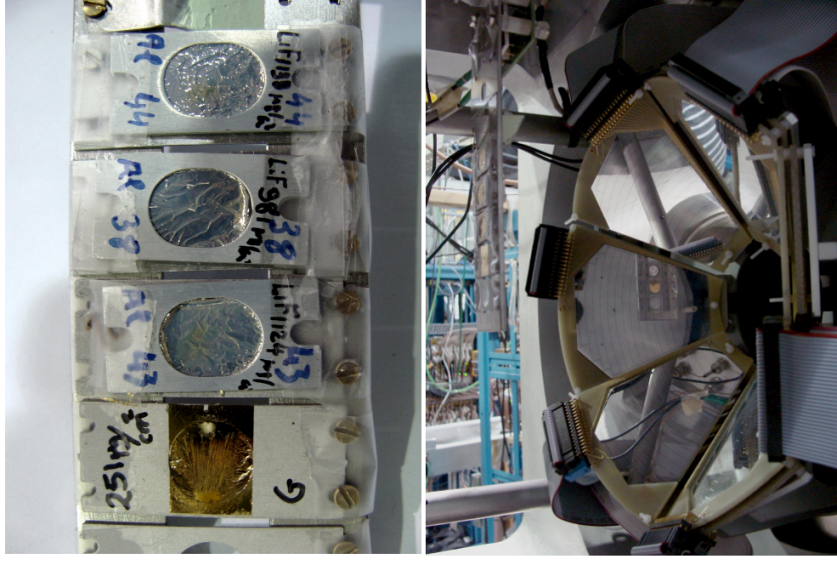
Figure 3.3: Targets used in the experiment and LAMP setup inside the TUDA chamber.

target (backing)	LiF#3(Al)	LiF#4(Al)	LiF#5(Al)	Au
thickness [μg/cm^2]	1124 (43)	981 (38)	1138 (44)	251

Table 3.3: Targets used in the experiment, from top to bottom as seen in Fig. 3.3.

3.1.3 Electronics chain and data acquisition

This section describes the electronics chain, trigger setup, and equipment used in the experiment. General details on semiconductor detectors and common electronics can be found in [102]. Mounted inside the TUDA chamber, twelve YY1 detectors (Table 3.1) by Micron Semiconductor Ltd. [99], were used. The detectors were arranged in six telescopes in the so-called "lampshade" geometry, as shown in Fig. 3.2. Each detector was connected to a separate 16-channel preamplifier, made at Daresbury Laboratory (UK) for the use with the YY1 detectors. The preamplifiers were mounted on two plates inside the TUDA chamber and were cooled with circulating liquid system of 50% water and 50% ethanol at a temperature of $\sim 0°$C to reduce noise level. Each preamplifier had a signal input from the detector with a distribution line for high-voltage (HV), an output to the amplifier, a bias input for the preamplifier, and a pulsar input for test signal. Pulsars were used for the initial setup of the electronics chain and ran throughout the experiment through a distribution grid that provided a constant ~ 4.5 V signal to the preamplifiers to test the stability of the electronics. The high voltage bias for the detectors was controlled by a digital Caen unit via a laptop terminal. The signal cable from the preamplifier is then

connected to two amplifier-shaper units from Daresbury Laboratory, as each amplifier had only 8 channels. The amplifiers have provided also a discriminator unit and an ECL logic signal for each channel, which was also start signal for corresponding TDC. Suitable energy ranges for E and ΔE detectors were selected using resistor jumpers and the shaping time was set to 1 μs. The energy signals from the amplifiers are passed to the 12-bit, 32-channel Silena ADC's for analogue-to-digital conversion, while the logical signals from all E detectors were combined to satisfy the "total OR" condition. This is the so-called "single trigger", i.e. the signal must be above the threshold in at least one detector to generate the trigger signal. In more technical terms (following scheme on Fig. 3.5), the ECL signals from sets of three amplifiers are coupled in "OR" condition. This signal is than converted in dedicated logical unit to the NIM standard output signal, which is than connected to the logical FIFO (fan-in/fan-out) unit. This unit couples logical signals from all detectors in total "OR" condition. The "total OR" signal from all detectors and the delayed logical signal related to the accelerator RF from the beam buncher are summed in the logical "AND" condition, i.e. the real event in the LAMP setup has to coincide with the presence of the beam. This signal went to the SAC unit as a trigger signal to start data conversion in ADC's. The same signal, combined with the signal from SAC indicating that event is accepted, delayed by 100ns has provided a common stop for the TDC's. Whole electronics and triggering chain are schematically presented in Fig. 3.5, while all of the equipment used in this experiment is listed in Table 3.4, with some photos from the experimenal hall shown on Fig. 3.4.

Synchronization of the data converted by the ADC's was done by the command SAC unit. In the case all ADC units were synchronized, a good event was collected in the MIDAS DAQ [103]. Otherwise, the data would be discarded and the buffer cleared for the next event. Triggering of the data was monitored via the ratio of total "OR" of the events in detectors, in "AND" condition with the RF signal, and accepted triggers in the DAQ. The ratio was always high, meaning that the dead time, where DAQ is not accepting new events was kept very low. The collected data were monitored on-line on a SunOS system running the MIDAS DAQ. The data provided by the MIDAS are hexadecimaly encoded files, which were converted off-line in the format suitable for the analysis in the ROOT framework [104].

In the final analysis, the data from TDC units were not used, as it has been confirmed in
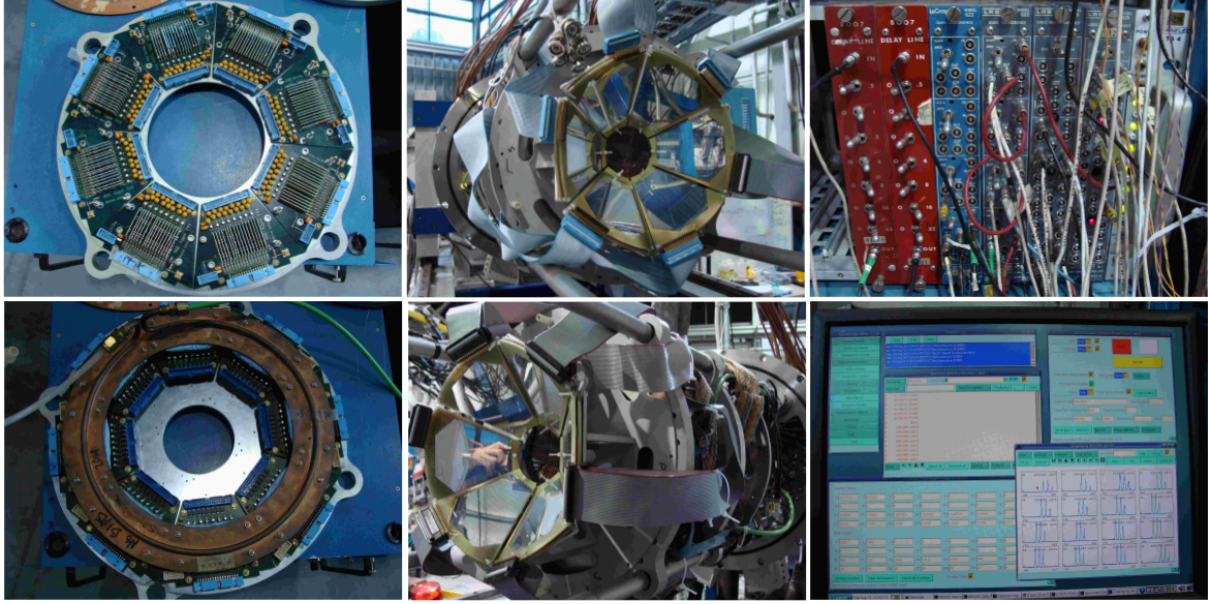
Figure 3.4: Some photos from the ISAC-II experimental area: preamplifier plates with the cooling system (left), LAMP telescope setup (center) and the part of the electronics with the MIDAS DAQ system (right).
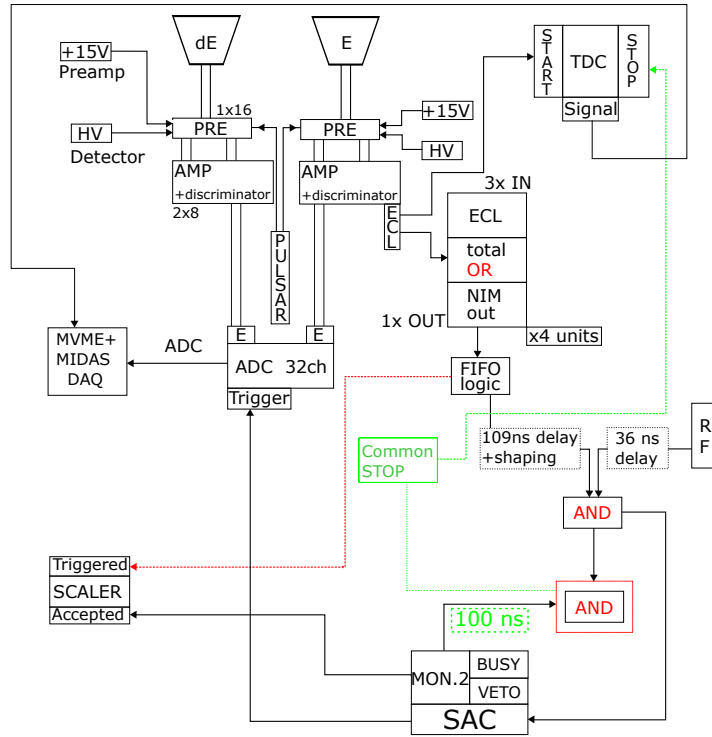
Figure 3.5: Schematic representation of the electronic chain and the trigger setup.

the pre-analysis that only one ^{9}Li beam particle was delivered per bunch in average, two α-particles from the β decay of the beam were not interfering with the physical events, while the noise in the detectors was filtered through the energy and geometry conditions. Imposing additional conditions on the TDC data was shown not to be necessary and

equipment used	manufacture/model
detectors	Micron Semiconductior Ltd., YY1
pre-amplifiers	Daresbury Laboratory
amplifiers	Daresbury Laboratory, Shaping Amplifier Module
HV for detectors	Caen SY403
HV for pre-amplifiers	University of Edinburgh
VME-processor	Motorola MVME 2431
ADC	Silena 9418
TDC	Caen V1190A
scaler	Caen V560, TRIUMF, BO98
FAN-in/FAN-out	LeCroy, LRS 429
quad coincidence	LeCroy, LRS 622
quad discriminator	LeCroy, 821Z
pulsar	Berkeley Nucleonics Corp. BNC mod. PB5
delay	TRIUMF, BO07
ECL-NIM-ECL converter	ESN EC1601
workstation	SUN Microsystems
DAQ	Daresbury Laboratory, MIDAS (32bit)

Table 3.4: List of equipment used in the S1620 experiment.

would only cause a loss of statistics, due to the fact that some of the TDC units ware not always collecting the data.

3.2   Calibration procedure

In this section all of the steps taken in the energy calibration and fine-tuning of the geometry of the detector setup are presented, alongside additional steps taken to test the stability of the electronics.

3.2.1   Pulsar gain check - stability of electronics

To ensure the stability of the electronics throughout the experiment, the signals from the pulsar were fed into the electronic chain throughout the data taking period. Two major runs of the pulsar data were taken, one at the beginning and one at the end of the experiment. Feeding the signals from $2-9$V in 1V increments into the electronic chain ensured that a correction factor could be determined in the case a voltage gain drift had happened. Comparing the average value of the pulsar signal (~ 4.5V) per channel for all runs with the signal value for the single run (Fig. 3.6), it was found that electronic chain was very stable and fluctuations in the pulsar amplitude were less than a few channels. If the pulsar amplitude deviated more than 2σ limit from the average, particular ADC channel was excluded in the analysis for that run, which happened for only a few channels in few runs throughout the experiment.

It is shown in Fig. 3.6 that the electronics gain was very stable throughout the experiment, allowing the raw data to be used for each run without the need to gain-match the data. The pulsar data were used to set up the electronics chain at the beginning of the experiment, to ensure that each channel behaved correctly and were also used to develop the code for the automatic fitting procedure in ROOT framework, which was subsequently used to fit the three alpha and elastic scattering peaks in the energy calibration procedure.

3.2.2   Energy calibration and fine tuning of geometry

The energy calibration was performed separately for each ADC channel corresponding to particular strip of the detector, for both ΔE and E detectors using the simple linear regression formula:

$$E[j] = slope[j] \times peak[j] + offset[j], \tag{3.1}$$
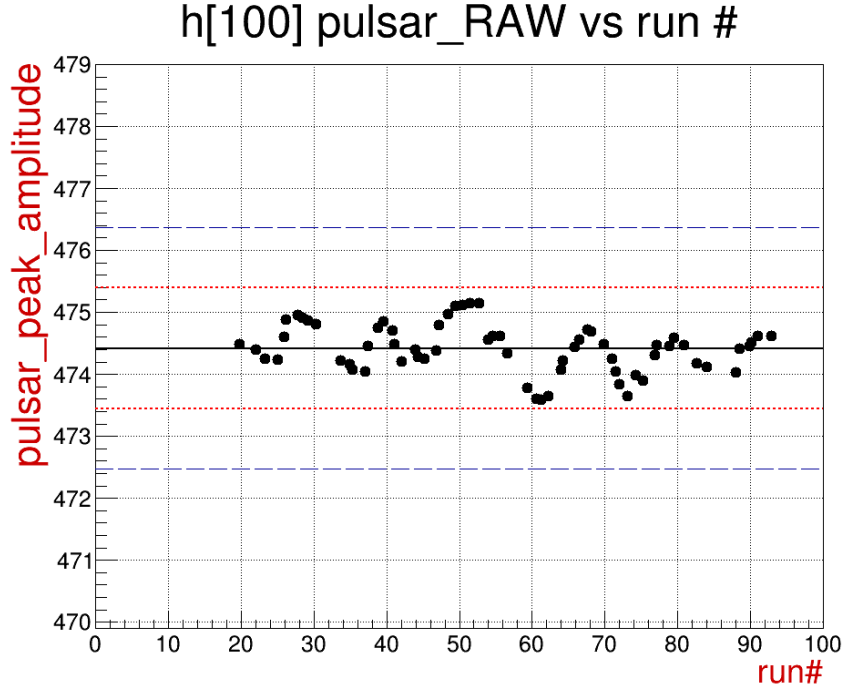
h[100] pulsar_RAW vs run

Figure 3.6: Average values of the pulsar peak for raw data in ADC channel 100 (detector: E1, strip: 1) throughout the experiment. The blue dashed line indicates the 1σ limit, while the red one indicates the 2σ limit from the mean value of the Gaussian fit, represented by the solid black line.

where j indicates ADC channel number (particular strip) and *peak*[*j*] indicates the RAW 12-bit ADC signal amplitude, i.e. the Gaussian peak value measured in channels: 0-4096.

For the low energy region, calibration 3-α source was used, containing the ^{239}Pu, ^{241}Am and ^{244}Cm isotopes, which are emitting alphas with energies of 5.155, 5.486 and 5.805 MeV. Two alpha-calibration runs were taken, at the beginning and at the end of the experiment. When comparing the amplitude difference for each channel and each α peak, it was found that the detectors were stable throughout the experiment, with the relative difference in α peak values generally being less than 1-2 channels. The strip 2 of detector E2 showed an energy drift of ~ 7 channels and was unreliable, smearing the spectra, and was therefore discarded from data analysis. The alpha run at the end of the experiment was used for the final calibration. For the high energy calibration point, the elastic scattering of the ^{9}Li beam on the ^{197}Au target was used. Contrary to α energies with fixed values, the energy of the gold peak varies with θ for each strip, as does the number of events with $\sim 1/\sin^4(\theta/2)$ according to the Rutherford cross-section. Since the geometry of LAMP is symmetric, one should expect the number of events in the corresponding

strips to be the same in each detector, since they should have been on the same nominal θ angle. Due to the fact that the beam position was not centered on the target, this was not the case. Applying Rutherford's scattering law and comparing the number of events in the detectors on opposite sides of the beam (e.g., 1 and 4), one can determine the exact θ, as the deviation from the nominal value: $\theta = \theta_0 \pm \Delta\theta$ using the formula:

$$\eta_{41} = (\frac{(dN/d\Omega)_4}{(dN/d\Omega)_1})_j = \frac{sin^4(\frac{(\theta_0+\Delta\theta)_1}{2})}{sin^4(\frac{(\theta_0-\Delta\theta)_4)}{2})}|_j \tag{3.2}$$

where η_{41} is the difference in the number of events in the same strip, noted with index j, for detectors on opposite sides of the beam. In this case, detectors are 1 ($\phi=180°$) and 4 ($\phi=0°$), and it is assumed that the number of events: $N_4 > N_1$. After the manipulation with the trigonometric formulas and the development into series assuming small $\Delta\theta$, the final relation for $\Delta\theta_{41}$ takes the form:

$$tan(\Delta\theta_j) = \frac{\eta_{41}^{1/4} - 1}{\eta_{41}^{1/4} + 1} tan(\theta_0). \tag{3.3}$$

The calculated $\theta = \theta_0 \pm \Delta\theta$ is used in the kinematic calculations for the exact energy of the gold peak in each strip. The value $\Delta\theta \sim 0.2\text{-}0.6$ ° was usually observed, corresponding to a movement of ~ 0.5 mm of the beam spot from the target center. The beam spot can be seen on Fig. 3.3, having a darker shade on the LiF target.
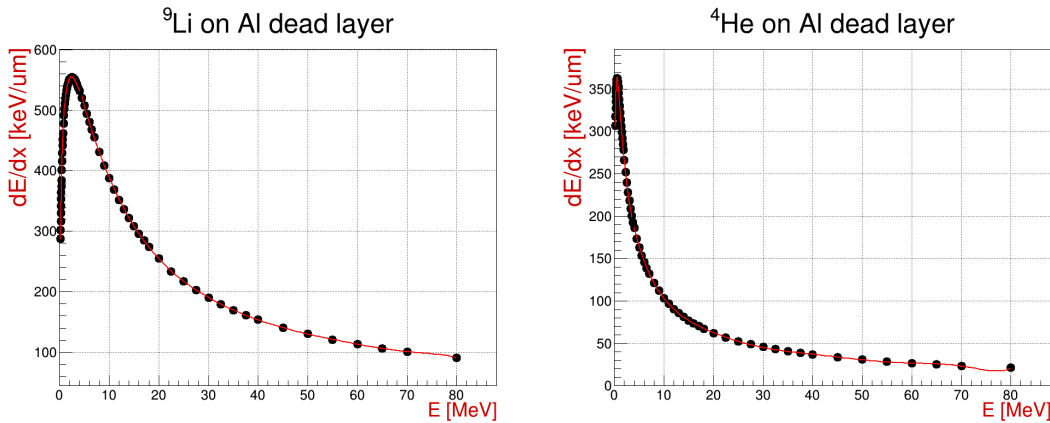

Figure 3.7: Calculation of the energy loss per unit length in SRIM software for ^{9}Li (left) and ^{4}He in ^{27}Al (right), fitted with a parametric function in ROOT framework.

To account for the energy loss of the alphas in the dead layer and the ^{9}Li beam in the target and dead layer, calculations were performed in SRIM software [105] for each isotope and "target" combination. As an example, the energy loss per unit length (dE/dx) of ^{9}Li

and ^{4}He isotopes in ^{27}Al electrodes ("dead layer") is shown in Fig. 3.7. One can also see the difference in energy loss between these relatively close elements. The energy loss data were parameterized with two "pol8" functions (8th degree polynomial), one for the low energy region where the Bragg peak is located and one for the higher, more uniform energy region. Depending on the energy of projectile, one set of parameters is used over the other. Since the energy loss of the elastically scattered ^{9}Li beam in the ΔE detector is $\sim$ 6-6.5 MeV, which is very close to the 3-α peak energies, the elastic scattering data were not used in the calibration of the ΔE detectors. Because of the energy variations in the $\Delta\theta \sim 2°$ range, the peak itself was smeared, making the Gaussian fit rather broad and uncertain. For this reason, it was decided that using only the alpha peaks would provide better calibration of the ΔE detectors. The peak from elastic scattering on the ^{197}Au target is shown for the detector: E1, strip: S1 (ADC channel = 100) in Fig. 3.8.

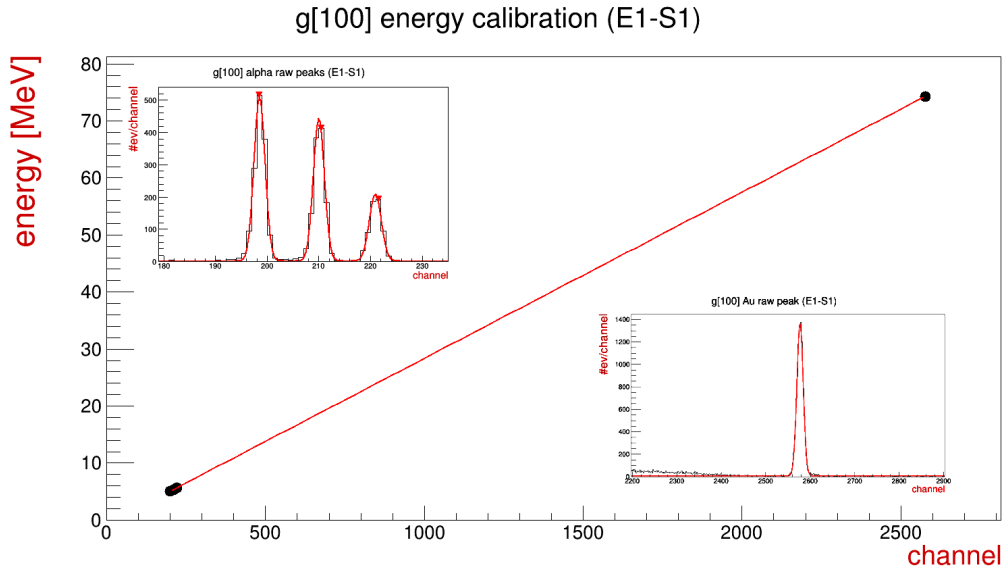Figure 3.8: Energy calibration of detector E1, strip S1 using ^{239}Pu-^{241}Am-^{244}Cm α peaks and ^{9}Li+Au (74.8 MeV) elastic scattering.

It should be noted that due to the lack of data statistics for the elastic scattering in the last $\sim$ 3 strips in all E detectors, they were calibrated using only the 3-α source. This was not a major problem in the analysis, as these strips were detecting mainly light nuclei (H, He) at higher polar angle, for which the α calibration is satisfactory and did not negatively affect the experimental resolution. After the final energy calibration, it's necessary to verify the quality of the obtained calibration. In the simplest form this was first done by examining the elastic scattering of the ^{9}Li beam on the ^{197}Au target, for run 26, where full detection setup, in the form of telescopes (ΔE+E) was used. Using the

formula for the two-body excitation energy for the undetected particle (X) in the reaction T(b,d)X:

$$E_x = E_b + Q_0 - E_d - E_X, \qquad (3.4)$$

leads to the expression:

$$E_x = Q_0 + \frac{M_x - M_b}{M_x} E_b - \frac{M_x + M_d}{M_x} E_d + \frac{2}{M_x}\sqrt{M_b M_d}\sqrt{E_b E_d}\cos\theta_d \qquad (3.5)$$

after applying the conservation of momentum, where T stands for target, b for beam, d for detected and X for undetected nuclei. For elastic scattering ^{197}Au(^{9}Li,^{9}Li)^{197}Au, the Q value is zero and expected excitation energy of undetected ^{197}Au is $E_x = 0$. Since this is true regardless of the θ angle at which ^{9}Li is detected, one must see a straight "line" (locus) around zero in the 2D plot of E_x (^{197}Au) versus θ (^{9}Li) (Fig. 3.9), which represents the elastic scattering.

As mentioned earlier, due to the fact that the target ladder was bent downstream from the target, the nominal geometry did not provide good enough results, so the energy calibration was an iterative process. Once the geometry of the setup was optimized, the energy calculation for the elastic scattering peak of the ^{9}Li beam on the ^{197}Au target (calibration run 18, using only E detectors) was recalculated. Than the excitation energy spectra, such as the one shown in Fig. 3.9, were analysed again. It was found that the target was moved 6.75mm in average, away from the detectors, making the total distance from the detector mount 164+6.75=170.75 mm and the tilt angle of the detector setup toward the beam line 42.5° effectively.

$\Delta\theta_{0'}$ (ΔE$_5$)	$\Delta\theta_{0'}$ (ΔE$_{1,2,3,4,6}$)	$\Delta\theta_{0'}$ (E$_{1-6}$)
[15.0°, 48.2°]	[15.8°, 48.0°]	[16.6°, 47.8°]

Table 3.5: Total nominal $\Delta\theta$ coverage for each detector used, corrected for the offset of the target center.

Once $E_x(^{197}$Au$) \approx 0$ was achieved for all detectors, the procedure of fine-tuning the beam spot on the target was repeated, according to the Equation 3.5, which in the end gave the final calibration points. An example of the calibration for one strip of the E detector is shown in Fig. 3.8.
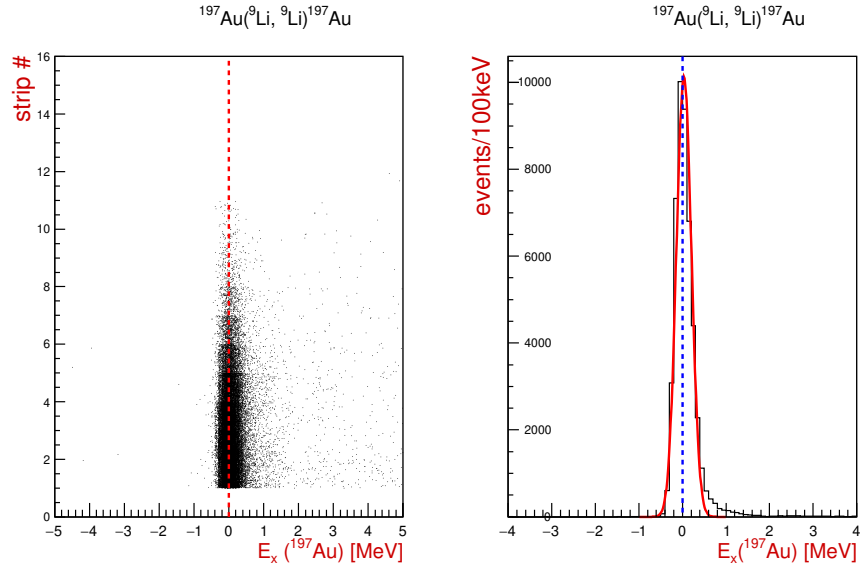
Figure 3.9: Excitation energy of undetected ^{197}Au from the ^{197}Au(^{9}Li,^{9}Li)^{197}Au reaction versus the strip number ($\sim \theta$) of detected ^{9}Li (left) and the projection of the spectra (right). Data are shown for all detectors, with the resulting σ of the Gaussian fit equal to 170 keV.

As an example of the procedure, the results for two detectors on opposite sides of the beam are presented: E1 on the right and E4 on the left side of the beam. Based on the difference in the number of detected events in strips 2+3+4 between these two detectors, one can calculate $\theta_s = \theta_{0'} \pm \Delta\theta$ and, consequently, the position of the beam spot on the target relative to the center of the target: $x_\pm = 0 \pm \Delta x$, where it is $-\Delta x$ if the beam spot is closer to the respective telescope, or $+\Delta x$ if it's farther away. The results are summarized in Table 3.6.

detector	E1 ($\phi = 180°$)	E4 ($\phi = 0°$)
Δx [mm]	+0.66	-0.66
$\Delta\theta$ (active area)	[16.8°, 48.0°]	[16.4°, 47.6°]

Table 3.6: Summary of the effects that the beam position on the target, relative to the center, has on the angular coverage of the detectors and consequently on the experimental resolution.

This type of analysis and fine-tuning of the geometry was performed for all opposite detector combinations: 1-4, 2-5 and 3-6. From the 1D projection of the elastic scattering data, one can estimate the intrinsic experimental resolution of the LAMP setup, which is ~ 150-200 keV, depending on the telescope, represented as σ of the Gaussian fit.

3.3   Data analysis

Once the quality of the energy calibration was ensured and the geometry of the detector setup corrected, next step was the data analysis. All the steps taken to ensure quality of the data, particle identification and hit (defined by good event in telescope) reconstruction procedure are explained in detail. After these steps, an overview of the event reconstruction, exit channel identification and all the steps taken prior to obtaining the final results for the physical case of interest, will be given.

3.3.1   Two-body reaction, run groups and fine tuning of geometry

Due to already mentioned problems with the tilt of the target ladder and position of the beam on the target, it was necessary to fine-tune effective geometry of the detector setup every time there was a change in the experimental conditions. These changes happened due to retuning of the beam, swapping of the LiF targets, starts and stops of the beam due to unexpected conditions such as water leak on main proton line, maintenance of the accelerator, RF problems and others.

For this analysis the elastic and inelastic scattering of the ^{9}Li beam on ^{7}Li and ^{19}F constituents of the LiF target were used, in same manner as was done previously for elastic scattering on the gold target. Every change in experimental condition was treated as a separate analysis for runs and run groups as summarized in Table 3.7.

target	run [start, stop]
LiF#3	$[39, 41], 42, [43, 44], [45, 47], [48, 52], [79, 84], [87, 92]$
LiF#4	$[27, 30], [77, 78]$
LiF#5	$[22, 25], [33, 38], [53, 56], [59, 67], [68, 76]$

Table 3.7: The run groups used for fine tuning of the detection geometry due to changes of the experimental conditions (see text for details).

Since for this analysis it was only needed to identify ^{9}Li from the ΔE-E spectra, the particle identification process is explained in the next section, alongside the hit reconstruction and classification of the data. At this point it is only important to mention that the

cleanest possible data set was chosen for this study: events with only a single hit in one ΔE strip and a single hit in one E strip, which geometrically coincide in the real space. In this way, the events in which signal sharing or two close hits ("double-hits") had happened were neglected.

Excitation energy spectra for both elements of the LiF target were simultaneously studied using the two-body excitation energy formula (Eq. 3.5), where it was ensured that the elastic peak is at: $E_x({}^7Li_{gs}) = 0$ and $E_x({}^{19}F_{gs}) = 0$ for both cases. Also, inelastic excitations of the target constituents should have been seen at exact energies of the known states. In this way it was ensured that the energy calibration and the effective geometry calculations are done correctly before proceeding to more complex physical cases.

Fine tuning of the geometry was done by varying the beam spot on the target, as previously explained. Process was iteratively repeated for all telescopes until the best results were achieved.
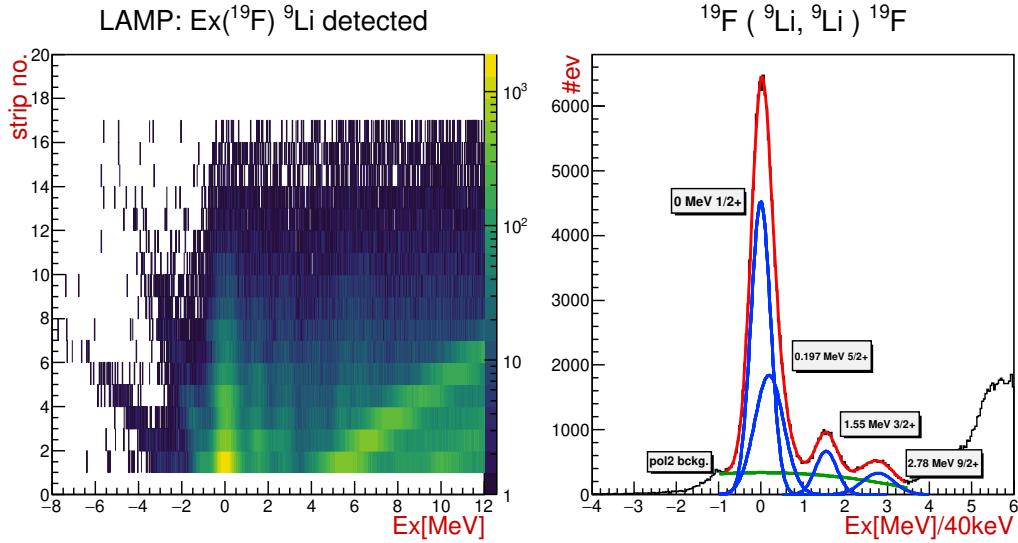

Figure 3.10: The excitation energy of the ^{19}F nucleus from the ^{19}F$(^9$Li,^{9}Li$)^{19}$F reaction versus the strip ($\sim \theta$) of the detected ^{9}Li for all detectors and data from whole experiment. Detailed list of states can be found at [106].

In Fig. 3.10, one can notice that excitation energy of the elastic peak is correctly placed at $E_x(^{19}F) = 0$, and excited states have correct energies. These ^{19}F states show a straight "line" or locus in the 2D spectrum, confirming the quality of energy calibration and analysis done to fine tune the geometry of detection setup. In the case this had not happened, true states would have an offset from the right positions and would bent away from the straight vertical "line" indicating these states. One can also notice the two loci of the

data bent toward the left side of the spectrum and a few bent toward the rights side of the spectrum. These show contributions from the other elements of the target: ^{184}W contaminant, ^{27}Al from the target backing and ^{7}Li as the target material, seen in this order from the left to the right side of the spectrum.
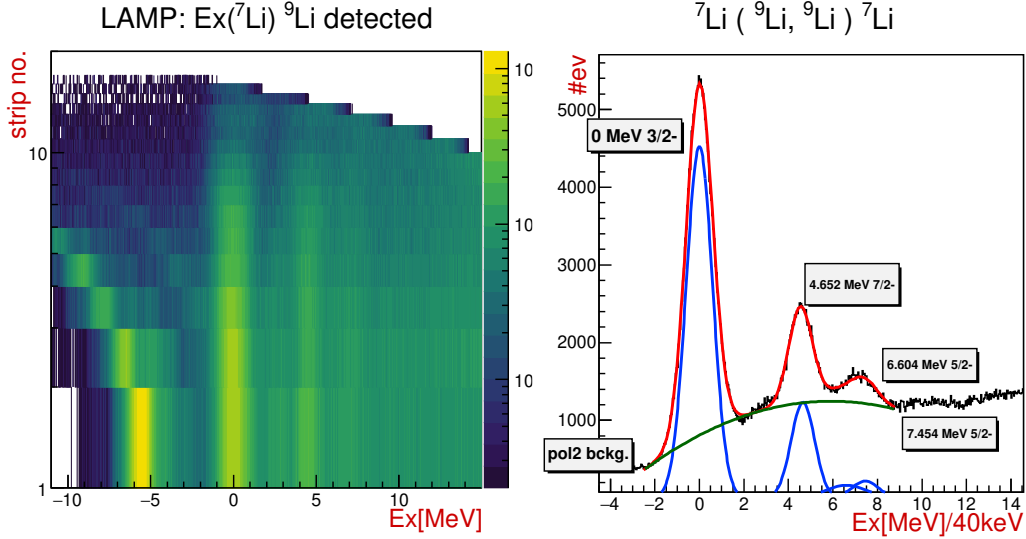

Figure 3.11: Excitation energy of ^{7}Li from ^{7}Li(^{9}Li,^{9}Li)^{7}Li reaction versus the strip ($\sim \theta$) of detected ^{9}Li. Detailed list of states can be found at [106].

A similar observations can be made for Fig. 3.11, with difference that, apart from seeing the mixture of the ground and unresolved first excited states at 0.48 MeV together, alongside other excited states of the ^{7}Li target, a vague locus at ~ 2.7 MeV, coming from the $1/2^-$ first excited state of the ^{9}Li beam, is observed. Same contribution can be expected at 4.65+2.7=7.35 MeV energy, where the 7.45 MeV $5/2^-$ state of ^{7}Li is.

Other two-body spectra for other target constituents were also studied, taking into account full statistics of the experiment with hits reconstructed from energy sharing in ΔE or E detectors. All of these spectra confirm the conclusions about the quality of the calibration and the target composition made here.

3.3.2 Particle identification, event reconstruction and classification

Particle identification was done using the standard ΔE-E method, by making the graphical cuts on 2D spectra around the locus representing the given isotope, as shown in Fig. 3.12. To obtain the cleanest possible particle identification (PID), only the so called "single-hits"

events were used (see Fig. 3.13): [$S_{\Delta E}$, S_E] and [$(S+1)_{\Delta E}$, S_E] combinations. Although [$(S-1)_{\Delta E}$, S_E] combination in principle may had happened, due to the fact that ΔE detector was misplaced by plastic spacers, effectively moving it towards the beam line and taking the tilt angle of the detector setup into account, this combination was not geometrically possible for the single-hits, but was later used in the reconstruction when the signal sharing between adjacent strips had happened. So, PID data include only the hits in the ΔE and E detectors where there are no signals in the neighbouring strips. This method has helped to improve the resolution of the data and to reject the events where signal sharing in either ΔE or E detector had happened.

Prior to making the graphical cuts a cross-check was done, testing that the position of a given isotope had not changed on 2D ΔE-E spectra throughout the experiment. After the results of the analysis on the pulsar data and 3-α calibration peaks were confirmed, one could proceed to make the graphical cuts which are valid for the whole experiment. Separate graphical cuts were made for each isotope in each strip of each telescope. Where it was possible to overlap the data from neighbouring strips, it was done to save the time on making the cuts. Each cut was saved as a separate ROOT object and was read from the memory as a function of a strip in a given telescope. An example of the PID identification spectra is shown in Fig. 3.12, while classification of the single hits is graphically represented in Fig. 3.13.

It is important to mention that a lot of effort went into hit classification and cleaning of the data before the final data selection took place. Due to electrical cross-talk which most likely happened at the amplifier stage, data had to be cleaned before attempting to match the hits between ΔE and E detectors. As one detector was connected to two amplifiers, electrical cross-talk was seen in the raw data as one main signal inducing signals in the rest of channels connected to that amplifier. To avoid putting a large threshold on the input signal, which would cause a lot of good low-energy events to be rejected, cleaning was done in the following way. If the multiplicity of the events in one detector was larger than four, a large threshold was set to be sure that only good events are taken into account. If the multiplicity of the event in detector was between two and four (for e.g., one single hit together with two hits coming from sharing or double-hit in that detector) threshold was set to reject the low-level noise and cross-talk signal, usually of order $\sim$ 0.5-0.7 MeV. On the contrary, if only one good hit in the detector was read, geometrically matched between
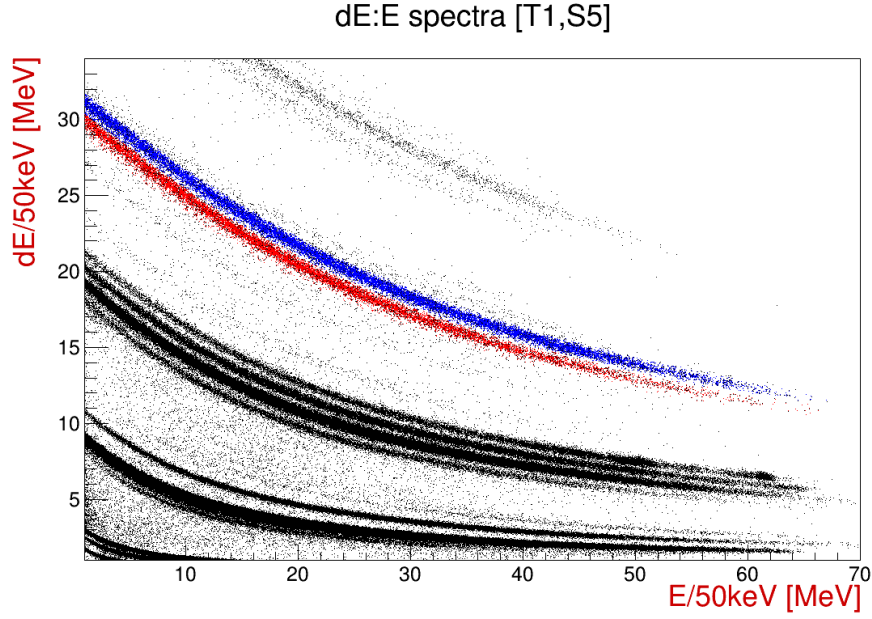
Figure 3.12: An example of the PID ΔE-E spectra for [T1, S5] for runs: 60-90. The graphical cuts, represented by the colored markers, are shown and were made to separate the ^{9}Be (red) and ^{10}Be (blue) isotopes as an example. Spectrum is zoomed to improve visability, and identified isotopes starting form bottom to the top include: ^{1,2,3}H, ^{3,4,6,8}He, $^{6,7,8,9,"11"}$Li, ^{7,9,10,11,12}Be and ^{10,11,12}B.
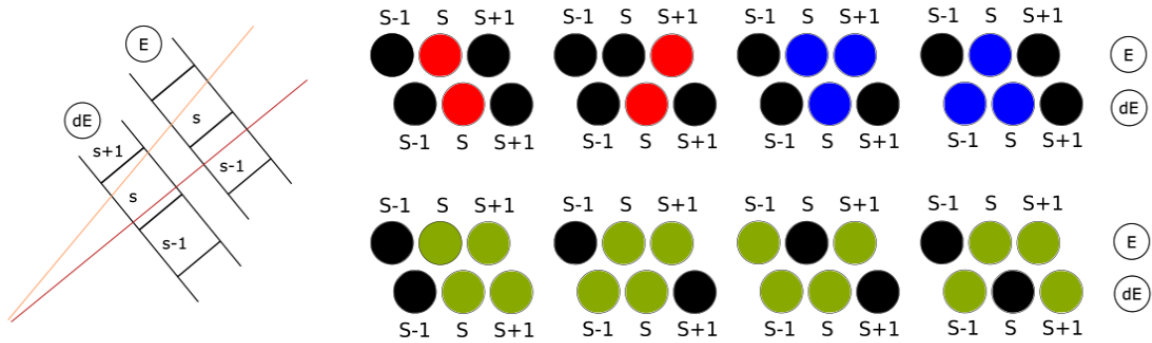

Figure 3.13: Schematic representation of the trajectory through ΔE and E detector and corresponding classification of the observed hits in the telescopes: single-hits (RED), signal sharing (BLUE) and double-hits (GREEN). See text for details.

ΔE and E, one could go as low as $\sim$ 100 keV in signal amplitude to reconstruct the hit, prolonging the ΔE-E "banana" to very low energies, which would be rejected otherwise. If the event in the detector geometrically coincides with possible physical event, after the initial cleaning step was done, raw data would be written into matrices of 16 strips for both ΔE and E detector.

At this point the cleanest PID spectra were produced, hit classification and reconstruction

in the case of signal sharing and/or the double-hits were done, thus it was possible to proceed to make the final data structure as a ROOT tree. Conditions were made on "IF-ELSE IF-ELSE" principle, looping the data of physical event for each strip of E detector, looking for the corresponding hits in ΔE detector. Simplest events were single-hits (IF), after which signal sharing or double hits (ELSE IF) evens were searched for and if no match was found between $\sim$ 11 possible event classifications in the telescope (ELSE), looping would continue to the next strip (or group of strips), repeating the procedure. Also, care was taken not to double count any strip or event.

variable	description
hitN	number of good hit in the event
pid[ ]	numerical particle (isotope) identifier
dE[ ],E[ ]	calibrated energy signal
T[ ]	telescope number
strip[ ]	strip number
θ[ ]	polar angle of the hit
N-pid [pid]	number of times particular isotope was detected
type[ ], geo [ ]	geometry and type of the hit
btype[ ]	basic hit identification: single-hit (0), sharing (1) and double-hit (2)

Table 3.8: List of the most important variables in the final structure of the data.

All of the more complex hits were compared to the cleanest ΔE-E spectra (see Fig. 3.14. for reference) and the quality check of energy and angle reconstruction was done using the two-body excitation energy formula (Eq. 3.5). One interesting example would have been the energy sharing in E detector, which is the one defining the θ angle, where the signal weight between two strips was used to calculate the effective θ angle of the hit as: $\frac{E_1\theta_1+E_2\theta_2}{E_1+E_2}$. Events were written in a ROOT tree structure of size equal to the number of total hits detected, with experimental variables summarized in Table 3.8.

When analysing the data one has to take into account the energy losses of the reaction products in the metalization layers of E and ΔE detectors, as well as the energy loss at the exit of the target, both corrected for the angle of the trajectory through the material, as schematically shown in Fig. 3.15. Energy loss of the beam in the first half of the LiF target and ^{27}Al backing was also taken into account.
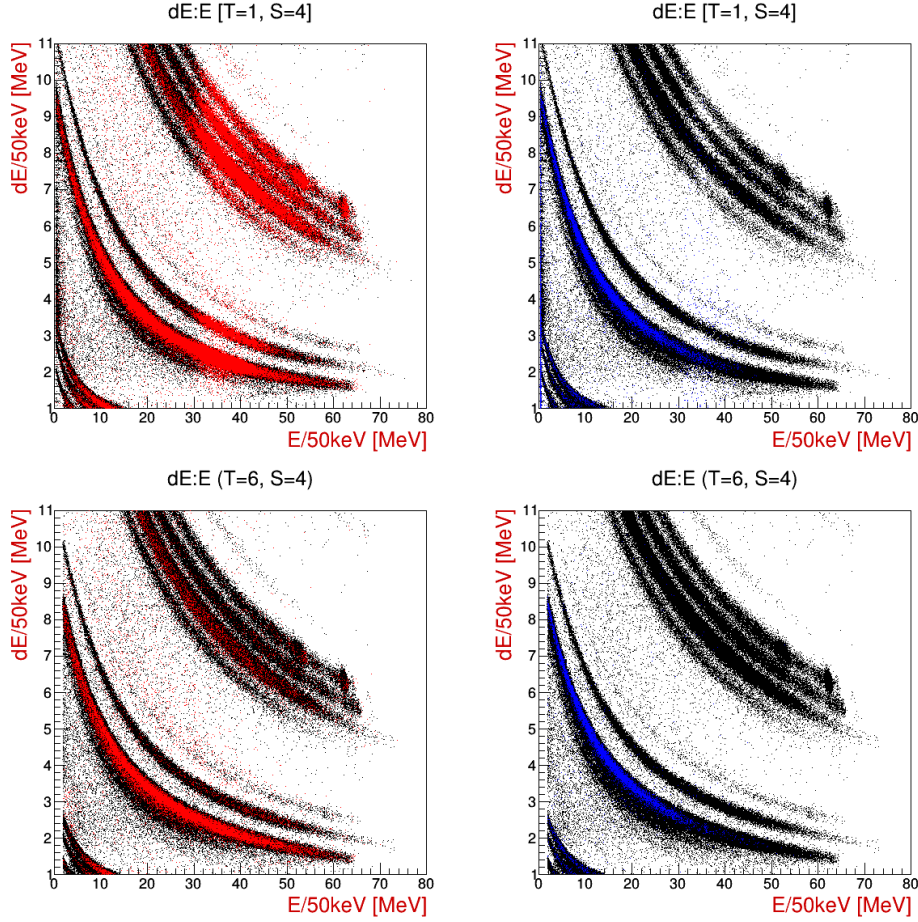
Figure 3.14: The ΔE-E spectra for [T1, S4] (top) and [T6, S4] (bottom), where the black dots represent only the cleanest single-hit data, while colored dots represent reconstructed hits: red for signal sharing and blue for double-hits.

Addition of the energy loss to the total energy, was done iteratively in a two step process, to account for the fact that the reaction product has slightly larger energy than measured, due to the loss in metalization layer. If the example of energy loss in the metalization layer of E detector is taken, the two-step iteration: $\Delta E_1^{calc.}=\Delta E_1(E+\Delta E_1^{calc.})$ was found to be enough to get the exact result. The reason of such good agreement lies in the fact that the energies of reaction products are far from the Bragg peak, as can be seen in Fig. 3.7. Total energy of the reaction product is then a sum of all contributions (see Fig. 3.15):

$$E_{\text{particle}}^{tot.} = [E + \Delta E_1^{calc.}]_{E-det} + [\Delta E_2^{calc.} + dE + \Delta E_3^{calc.}]_{dE-det} + [\Delta E_4^{calc.}]_{\frac{1}{2}LiF} \qquad (3.6)$$

and

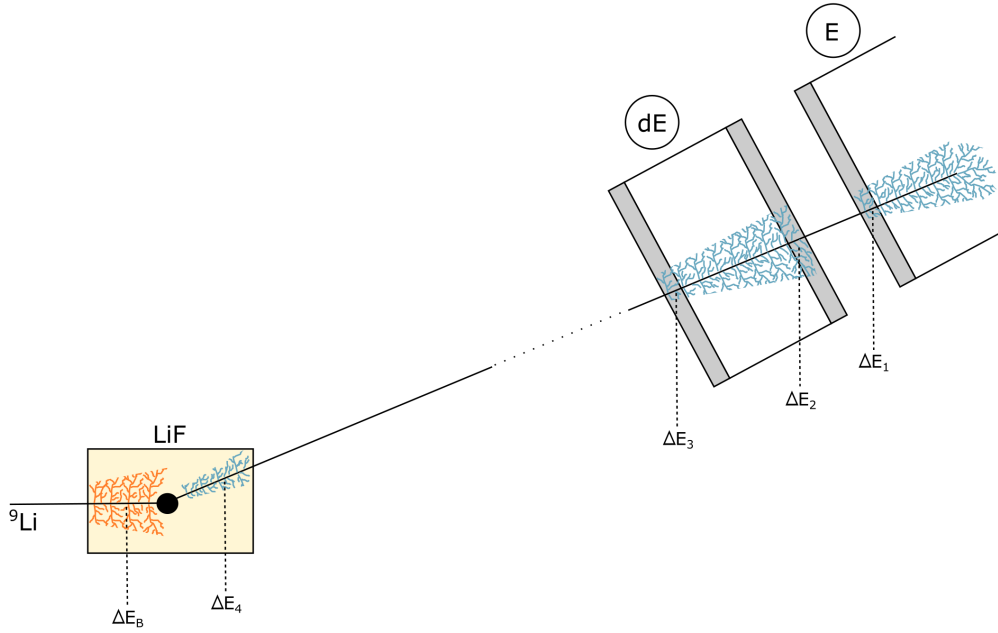$$E_{\text{beam}} = E_{beam} - [\Delta E_B^{calc.}]_{\frac{1}{2}LiF} \qquad (3.7)$$

Figure 3.15: Schematic representation of the energy losses taken into account in the total energy calculation. See Equations 3.6 and 3.7 for reference on how the total energy in the reaction of the reaction products and the beam was calculated.

3.3.3 Quality control of the hit reconstruction and composition of the target

As it was mentioned before, the best way to test the quality of the hit reconstruction, the total energy of detected isotope and the angle at which it is detected, is to analyse the two-body reactions on the constituent elements of the target. In this way one can see how hits, reconstructed from signal sharing in either ΔE or E detector contribute to the total statistics of the experiment, without affecting the resolution in a negative way. For this example elastic and inelastic scattering on the ^{7}Li and ^{19}F were used (Fig. 3.16), while the elastic scattering on the ^{27}Al target backing and ^{184}W contaminant, as well as ^{1}H(^{9}Li, ^{4}He^{6}He) reaction on the ^{1}H contaminant, with Q value of 12.22 MeV, were also studied. All of these yield expected physical results for the respective channels, but together with the other interesting physical cases studied are omitted here to focus on the main part of the thesis subject.

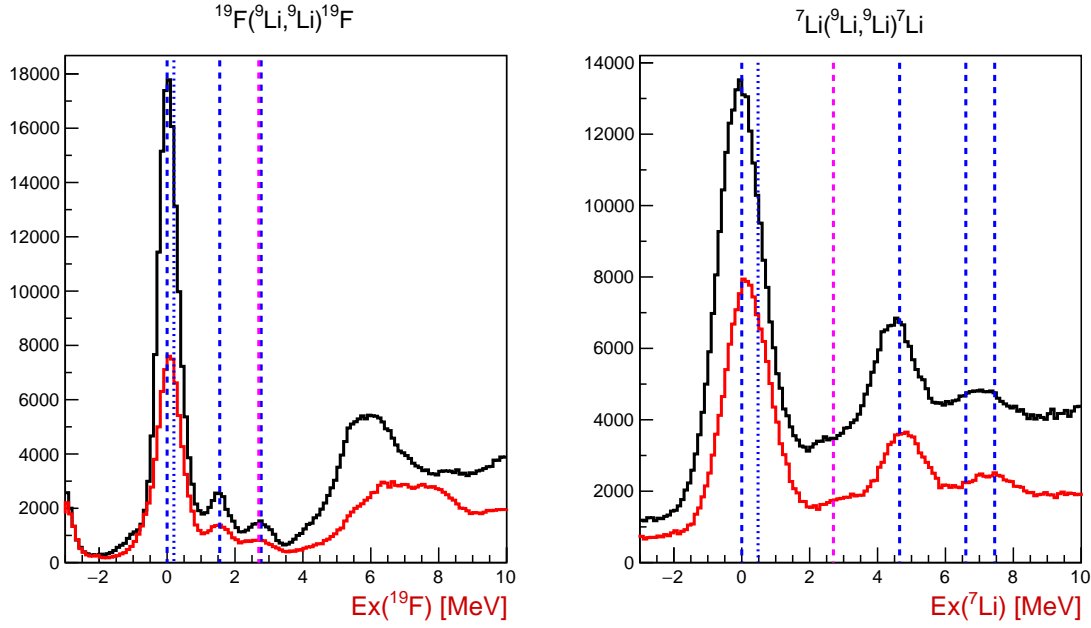Another important quality assurance test is the position of the ^{8}Be ground state obtained

Figure 3.16: The excitation energy spectra of the ^{19}F (left) and ^{7}Li (right) for the two-body reactions of the ^{9}Li beam on LiF target. Black lines represent btype=0 data (single-hits), while red lines represent btype=1 data (hits reconstructed from sharing and cross-talk). Results from the Figures 3.10 and 3.11 are well reproduced here. Blue dashed lines indicate states in ^{19}F at 0 MeV, (0.2 MeV), 1.55 MeV and 2.78 MeV, and in ^{7}Li at 0 MeV, (0.48 MeV), 4.65 MeV, 6.6+7.5 MeV. Pink dashed line indicates possible contribution from the ^{9}Li excited state at 2.69 MeV. Detailed list of states can be found at [106].

from double-hits in the same telescope, using the Equations [3.8, 3.9, 3.10], for the ^{8}Be$_{g.s.}$ $\rightarrow$ ^{4}He + ^{4}He decay:

$$E_{^8Be} = E_{\alpha 1} + E_{\alpha 2} - |E_{^8Be \rightarrow \alpha 1 + \alpha 2}| \tag{3.8}$$

$$\theta_{^8Be} = \cos^{-1}\left(\frac{\sqrt{E_{\alpha 1}}\cos(\theta_{\alpha 1}) + \sqrt{E_{\alpha 2}}\cos(\theta_{\alpha 2})}{2E_{^8Be}}\right) \tag{3.9}$$

$$\phi(^8Be) = \sin^{-1}\left(\frac{\sqrt{E_{\alpha 1}}\sin(\theta_{\alpha 1})\sin(\phi_{\alpha 1}) + \sqrt{E_{\alpha 2}}\sin(\theta_{\alpha 2})\sin(\phi_{\alpha 2})}{\sin(\theta_{^8Be})} \times \sqrt{2E_{^8Be}}\right) \tag{3.10}$$

Since the LAMP setup is symmetrical, only the relative azimuthal angle is important. For the $\alpha+\alpha$ pair, detected in the same telescope, it can only be assumed that $\Delta\phi_{\alpha 1 - \alpha 2}=0°$, due to the lack of experimental resolution, resulting in $\phi_{^8Be}=\phi_{\alpha 1, \alpha 2}$. The term $|E_{^8Be \rightarrow \alpha 1 + \alpha 2}|$ is the excitation energy of the ^{8}Be ground state at 92.4 keV.

To check the quality of the double-hit reconstruction the btype = 0 data (clean selection), coming from two α hits in the same detector, separated with at least one strip and btyle = 2 data (double-hits), coming from the hits in the neighbouring strips, are compared in Fig. 3.17, to show the effect of the reconstruction on the ground state peak resolution.
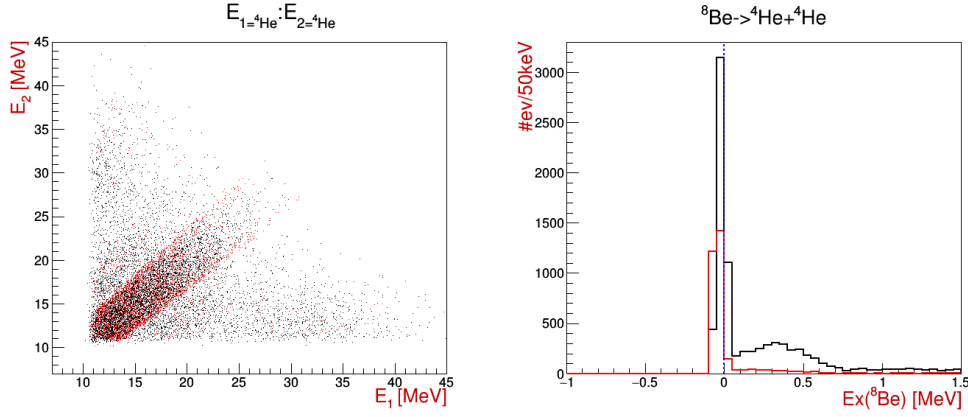

Figure 3.17: Signature of the α-α decay in $E_{\alpha 1}$ vs. $E_{\alpha 2}$ spectrum (left) and reconstructed ^{8}Be ground state energy (right) from the single-hits (btype=0, black) and double-hits (btype=2, red) events in the same detector (dT=0). Data from the coincident detection of ^{4}He+^{4}He+^{6}He isotopes was used.

As one can see in Fig. 3.17, obtained resolution in both cases is almost the same and around 100 keV FWHM, indicating that the complex double-hit patterns seen in Fig. 3.13 are correctly identified and classified. In many-body reactions, when the ^{8}Be ground state is reconstructed, double-hit data can safely be used without further corrections,

3.3.4 Three-body reactions: exit channel identification and full kinematics reconstruction

In this section a detailed description of the most important parts of the three-body reaction analysis [91, 92, 97] are given: identification of the exit channel of the reaction and full kinematical reconstruction of the event.

The three-body reaction has typical representation as p + t $\rightarrow$ 1 + 2 + 3 or t(p,12)3, where p is projectile (beam), t is target, 1 and 2 are the detected reaction products, while 3 is undetected one. As particularly convenient example the ^{7}Li(^{9}Li,^{6}He^{6}He)^{4}He reaction is considered, with Q value of 2.24 MeV, which is important for the study of the helium cluster decays of the ^{10,12}Be excited states. Schematic representation of the three-body event is shown in Fig. 3.18, with all relevant kinematics variables: E_i, $\vec{p}_i$, θ_i, ϕ_i, where i is index for a given particle. By the definition the Q value of the reaction is:
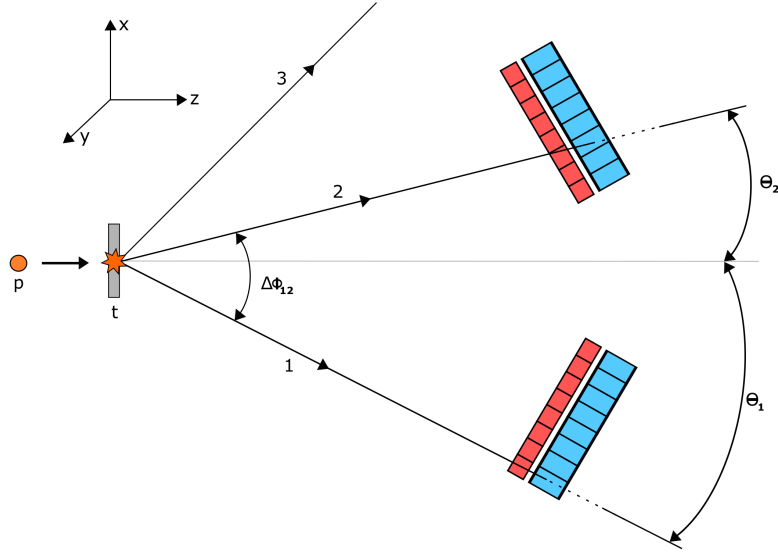
Figure 3.18: Schematic representation of the t(p,12)3 reaction, with relevant kinematics variables and side-view of the LAMP detector setup.

$$Q = (m_p + m_t - m_1 - m_2 - m_3)c^2 \tag{3.11}$$

which contributes to the total energy available to the system as:

$$E_p + Q = E_1 + E_2 + E_3 \tag{3.12}$$

while conservation of the momentum gives the relation:

$$\vec{p_p} = \vec{p_1} + \vec{p_2} + \vec{p_3} \tag{3.13}$$

Since the reaction product 1 and 2 are detected, one has to identify the third, undetected particle and the Q value of the reaction, which define the exit channel, as the products can be in either ground or excited state. The detected product can only be detected in the excited states which are stable to particle decay, while undetected product can also be in particle unstable states. An improved way for the unambiguous identification of the exit channel of the reaction is to correlate momentum $|\vec{p_3}|$ and energy E_3 in the so-called Catania plot [97].

From Equation 3.12 the energy variable can be defined as:

$$\tilde{E} = E_3 - Q = E_p - E_1 - E_2, \tag{3.14}$$

and from Equation 3.13 the momentum variable is defined as:

$$\tilde{P} = \frac{p_3^2}{2m_u} \tag{3.15}$$

where $m_u = 931.5$ MeV/c^2 is atomic mass unit. By plotting the events in the $[\tilde{P}, \tilde{E}]$ correlation plane, called Catania plot, events from the specific reaction gather in a locus around the line defined by relation:

$$\tilde{E} = \frac{1}{A_3}\tilde{P} - Q \tag{3.16}$$

where one can read -Q value on the ordinate axis when $P_3 = 0$, while the data follows $1/A_3$ slope. The momentum P_3 is calculated from the conservation law.

At this point it is important to take the resolution in the ϕ azimuthal angle of the detector setup into account. Since each detector is segmented by the 16 strips only in the polar angle (θ), there is large uncertainty in the azimuthal angle (ϕ). For a hit in a given strip, one can only attribute that hit to the center of the strip, which accounts for $\Delta\theta_{strip}$ uncertainty of $\sim 2°$ and $\Delta\phi_{strip}$ uncertainty of $\sim 55°$. For the symmetrical LAMP setup, only the relative $\Delta\phi$ angle between detected reaction products is relevant in the kinematic calculations for (p_3, E_3, Q) and the excitation energy ($E_{r12} \sim \cos\Delta\phi_{12}$) of the decaying nucleus X, given by equation:

$$E_{x,ij} = E_{rij} + E_{th,X\rightarrow i+j}, \tag{3.17}$$

where ij are pairs of particles 12, 13 and 23, E_{rij} is the relative energy of the pair and $E_{th,X\rightarrow i+j}$ is the threshold energy for the nucleus X to decay into particular ij pair. Due to the symmetry of the LAMP setup, one can always choose particle 1 as the "origin" of the system: $\phi = 0°$, setting $\phi_2 = \Delta\phi_{12}$ relative to ϕ_1. As an example, if two particles are detected in the same telescope, one can only say $\Delta\phi_{12}=0°$ and similarly if they are detected in the neighbouring detectors $\Delta\phi_{12}=60°$. Relation for the nominal $\Delta\phi_{12}$ angle is deduced as:

$$\Delta\phi_{12}^{nom.} = dT \times 60°, \tag{3.18}$$

where dT = 0,1,2,3 for the particles detected in the same detector, neighbouring, separated by one and in the opposite telescopes. Table 3.9 summarizes the uncertainty of the $\Delta\phi_{12}^{nom.}$ (nom. = nominal) angle.

dT	$\Delta\phi_{12}^{nom.}$	$\Delta\phi_{12}^{real}$
0	0°	[0°, 55°]
1	60°	[5°, 115°]
2	120°	[65°, 175°]
3	180°	[125°, 180°]

Table 3.9: Nominal values of the azimuth angle $\Delta\phi_{12}^{nom.}$, compared to the possible realistic physical value deduced from the geometrical coverage of the detector setup.

This large $\Delta\phi$ uncertainty predominantly affects reconstruction of the momentum of the third particle $\vec{p_3}$, making the exit channel identification by means of the Q value and/or Catania plot more difficult and sometimes not even possible, especially for the dT=1 and dT=2 cases when close grouping of the channels separated by a small Q value difference is present. The dT=3 case is the "best case scenario", since the $\Delta\phi$ uncertainty is not as large as in the dT=1 and dT=2 cases and clean selection of the data is always possible. The same can be said for the dT=0 case, where near threshold cluster decays usually are detected, even though extra caution has to be taken due to the edge of the phase space effects and unresolved contributions from other reaction channels.

To account for this problem many extra steps were taken in the analysis to make cleanest data selection possible. Once the selection of the data in particular exit channel is made, it is possible to calculate the relative azimuthal angle $\Delta\phi_{12}^{reconstructed}$, by the use of the conservation of the momentum and energy, assuming the channel identification is correct. To present the scale of this effect and the way reconstruction of the full kinematics of the event was done, the triple coincidence events from the three-body reaction with the ^{4}He+^{6}He+^{6}He in the exit channel is shown here. Since the triple coincidence events and the data from the Monte Carlo simulations are available [107], these present controlled conditions in which one can study the behaviour of the data with different telescope (dT)

and particle combinations in the exit channel.

The first step is to take a look at the reconstruction of the momentum of the third undetected reaction product:

$$p_3^z = \sqrt{2}(\sqrt{m_p E_p} - \sqrt{m_1 E_1}\cos\theta_1 - \sqrt{m_2 E_2}\cos\theta_2) \tag{3.19}$$

$$p_3^\phi = (2m_1 E_1 \sin^2\theta_1 + 2m_2 E_2 \sin^2\theta_2 + 2\sqrt{2m_1 E_1 2m_2 E_2}\sin\theta_1 \sin\theta_2 \cos\Delta\phi_{12})^{\frac{1}{2}} \tag{3.20}$$

$$p_3 = \sqrt{(p_3^z)^2 + (p_3^\phi)^2} \tag{3.21}$$

where the symmetry was taken into account making $\phi_1 = 0°$, $\phi_2 = \Delta\phi_{12}$, $\phi_3 = \Delta\phi_{13}$. The term $\cos\Delta\phi_{12}$ can be calculated as a function of $\cos\Delta\phi_{12}(m_1, m_2, m_3, E_1, E_2, \theta_1, \theta_2, E_p, Q)$ using the equation:

$$\cos\Delta\phi_{12}^{reco.} = \frac{E_p(m_3 - m_b) - E_1(m_1 + m_3) - E_2(m_2 + m_3) + m_3 Q}{2\sqrt{m_1 m_2 E_1 E_2}\sin\theta_1 \sin\theta_2} - \frac{2\sqrt{m_1 m_2 E_1 E_2}\cos\theta_1 \cos\theta_2 - \sqrt{m_2 m_b E_2 E_b}\cos\theta_2}{\sqrt{m_1 m_2 E_1 E_2}\sin\theta_1 \sin\theta_2} \tag{3.22}$$

where the indices are same as the schematic representation of the three-body reaction in Fig. 3.18. Since the $\Delta\phi_{12}^{reco.}$ is dependent on the m$_3$ and the Q value ($\sim$ p$_3^2$/2m$_3$), the first step is to identify the exit channel of the reaction, to use the kinematical reconstruction of the $\Delta\phi$ angle. This was done by placing cuts, either simple or graphical, on the Q value spectrum and/or Catania plot, both constructed using the nominal angle $\Delta\phi = $ dT $\times 60°$, not to bring the assumption of the exit channel in the calculation. Once the exit channel is identified, one can use $\Delta\phi_{12}^{\text{reco.}}$ relation from Eq. 3.22 to substitute the nominal $\Delta\phi_{12}^{\text{nom.}}$ angle. This procedure greatly restores the resolution in the excitation energy of decaying nuclei. The $\Delta\phi_{12}^{\text{reco.}}$ angle was used for further cleaning of the data in cases were overlaps between the data from the reactions on the ^{19}F and ^{7}Li targets were present, by placing simple conditions on realistic physical values of the relative $\Delta\phi$ angle as listed in Table 3.9. It should be mentioned that separation in $\Delta\phi$, as a cleaning condition, is not

sensitive enough to separate the closely excited states ($\Delta E_x \sim$ 2-3 MeV) of the detected (1 and 2) or undetected (3) nuclei in the exit channel.

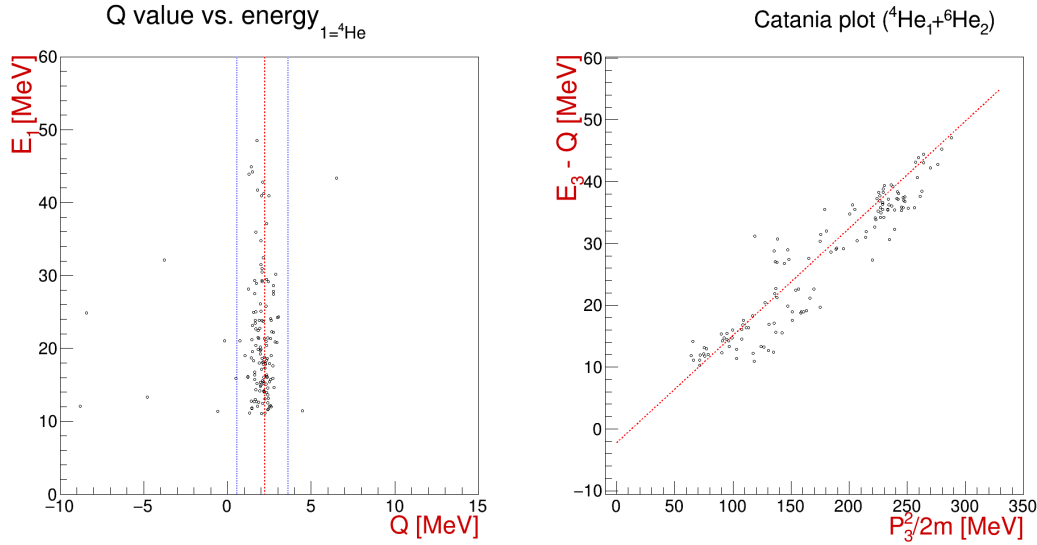Figure 3.19: The Q value spectrum (left) for the triple coincidence events from the ^{7}Li(^{9}Li, ^{4}He^{6}He^{6}He) reaction. The red line indicates real Q value of the reaction at 2.24 MeV, while the blue lines indicates data selection used in the analysis. The Catania plot (right) is constructed using only particles 1=^{4}He and 2=^{6}He, from the data selected within blue lines on the Q value spectrum, as if the particle 3=^{6}He was not detected, just to show the effect of the $\Delta\phi_{12}^{nom.}$ on the resolution of the reconstructed momentum and energy of the third particle.

The 1D projection of the data shown in Fig. 3.19 yields Q value of Q = 2.1 MeV with σ_Q = 0.4 MeV from the Gaussian fit, making the total energy offset <150 keV. This is quite satisfactory considering the total energy available in the reaction is $\sim$ 80 MeV, making the error less than 0.2% of the total scale. As all three particles in the exit channel were detected, this should be considered as the "best case scenario" considering the simplicity of identification and resolution obtained. For the case when two out of three particles were detected, the resolution is varying and mostly depends on the $\Delta\phi_{12}^{\text{nom.}}$ and the number of closely spaced exit channel observed. The offsets of $\sim$ 200-500 keV are usually observed in the Q value spectra for the dT=3 case, one of the reasons being that $\Delta\phi_{12}^{\text{nom.}}$=180° is assumed, while the real $\Delta\phi$ distribution usually peaks slightly below ($\sim$ 160 °), depending on the case. The $\Delta\phi_{12}$ distribution for ^{7}Li(^{9}Li, ^{4}He^{6}He^{6}He) reaction is shown in Fig. 3.21. These small systematical offsets are always taken into account when making the data selection and are compensated for in the excitation energy calculation, by using the real Q value of the identified reaction. A small discrepancies in the obtained geometrical efficiency curves from MC simulations can also arise, as MC generated data
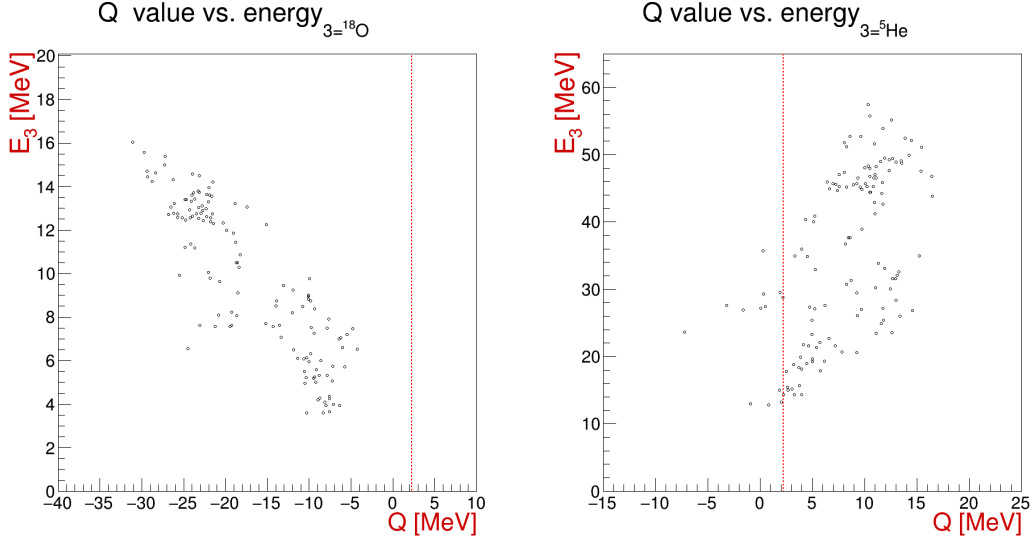
does not have the exact same offsets.

Figure 3.20: The Q value spectra (same data as in Fig. 3.19) for the ^{7}Li(^{9}Li, ^{4}He^{6}He^{6}He) data. The correct reaction on ^{7}Li is indicated with the red line at Q=2.24 MeV. The data loci are bent toward the sides, due to purposefully wrong assumption of the exit channel, with the undetected particle being ^{18}O (left) from the reaction on ^{19}F (Q=4.23 MeV) and ^{5}He (right) from the reaction on ^{6}Li (Q=7.63 MeV).

The standard test for the correct identification of the exit channel is to consider the plot of calculated Q value versus the energy of the third undetected particle, for all target constituents: ^{6,7}Li, ^{19}F. Since the Q value of the reaction is a constant, the data locus should appear as a straight line in the 2D Q value spectrum, as shown in Fig. 3.19. In case of wrong assumption of the exit channel, as it was purposefully done on Fig. 3.20, the data is bent away from the straight line around the expected Q value. By simultaneously cross-checking the data for all combinations of targets it is possible to make correct selection of the exit channel.

In the case of dT=1 and dT=2 data, due to large uncertainty in $\Delta\phi_{12}$, one can only make very rough selection of the data, but can make further cleaning by imposing additional cuts on the momentum of the third particle or $\Delta\phi_{12}^{\text{reco.}}$ range as an example. The use of correlations of kinematical variables, calculated with different equations using either nominal or reconstructed $\Delta\phi$ angle and examination of these variables in 2D correlation plots can also be very useful to identify the reaction exit channel. Further explanation of the steps taken in the analysis are given in Section 4, where the final results are shown, as the selection of the events was guided by differences in specific cases. As an example of the event selection, simulated data for full excitation energy range of the ^{10}Be $\rightarrow$ ^{4}He+^{6}He
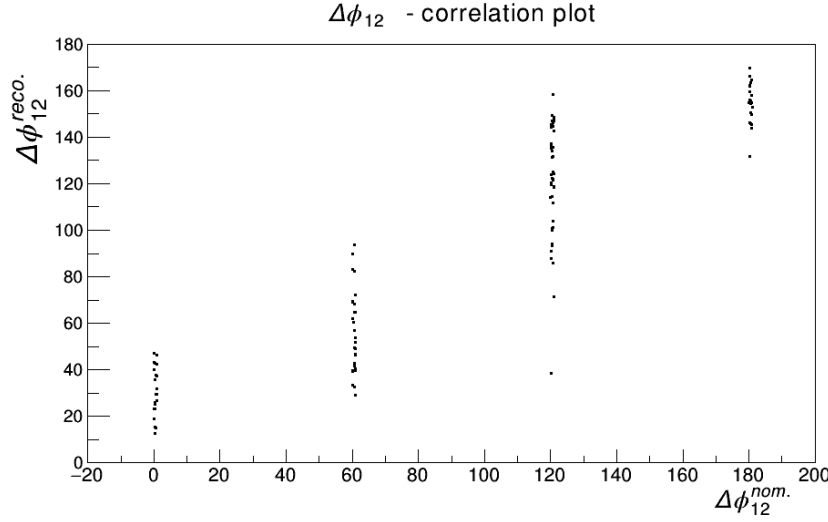
Figure 3.21: The $\Delta\phi_{12}^{\mathrm{reco.}}$ versus $\Delta\phi_{12}^{\mathrm{nom.}}$ distribution for the data selection shown in Fig. 3.19, for the ^{7}Li(^{9}Li, ^{4}He^{6}He^{6}He) reaction.

decay is presented here, with the same conditions as for the real data. Although it may seem that lot of events are being cut off, these selections were made taking the presence of the 1.8 MeV excited state of the undetected ^{6}He* into account, as well as the reaction on the ^{19}F target, which are not shown in the simulated data. Due to the large spread of data in the Q value (Fig. 3.22) and $[\tilde{P}, \tilde{E}]$ pairs in Catania plot (Fig. 3.23), the dT = 1,2 cases were omitted from the final analysis.
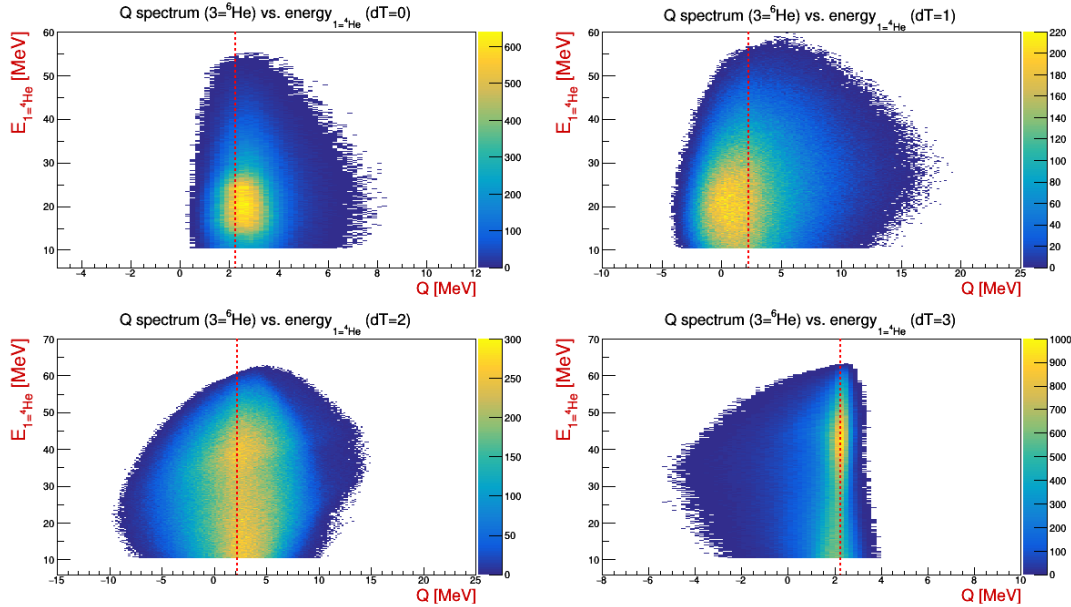

Figure 3.22: The simulated Q value spectra for the ^{7}Li(^{9}Li, ^{4}He^{6}He)^{6}He reaction for dT=0, 1, 2, 3 telescope combinations respectively. The Q value is plotted against the energy of detected ^{4}He and red dashed line indicates the real Q value of the reaction at 2.24 MeV. Please note that dT=1 and dT=2 cases were not used in the final analysis due to inability to distinguish reaction channels (see text for details).
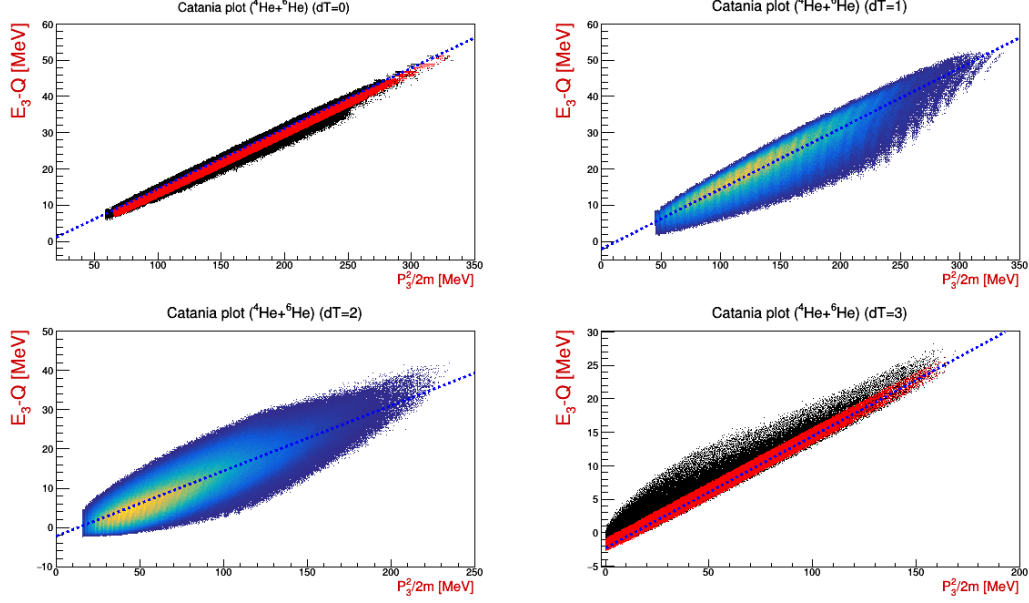
Figure 3.23: The simulated Catania plots for the ^{7}Li(^{9}Li, ^{4}He^{6}He)^{6}He reaction for dT=0, 1, 2, 3 telescope combinations respectively, with the data selection used in the analysis of the real data indicated with red markers. Blue dashed line indicates the real Q value of the reaction at 2.24 MeV, with the slope $\frac{1}{A} = \frac{1}{6}$ corresponding to undetected ^{6}He nuclei. Please note that dT=1 and dT=2 cases were not used in the final analysis due to inability to distinguish reaction channels (see text for details).

3.3.5 Three-body reactions: relative energies and excitation energy spectra

Having explained the methods for exit channel identification, this subsection explains the methodology behind the three-body reaction analysis: reconstruction of the excitation energy spectra, identification of the excited states of a given nucleus and the correlation spectra used for further separation and interpretation of the data. These considerations were made having the typical three-body event in mind, where two (1 and 2) out of three particles are detected. Relative energy between two detected particles, independent on the frame of reference, is given by the relation:

$$E_{r12} = \frac{\mu_{12}}{2}(\vec{v_1} - \vec{v_2})^2$$

$$E_{r12} = \frac{\mu_{12}}{2}(v_1^2 + v_2^2 - 2v_1 v_2 \cos\Theta_{12}) \tag{3.23}$$

$$E_{r12} = \mu_{12}(\frac{E_1}{m_1} + \frac{E_2}{m_2} - 2\sqrt{\frac{E_1 E_2}{m_1 m_2}}\cos\Theta_{12})$$

where $\cos\Theta_{12}$ is defined as:

$$\cos\Theta_{12} = \cos\theta_1\cos\theta_2 + \sin\theta_1\sin\theta_2\cos\Delta\phi_{12}. \tag{3.24}$$

These relations show the role of the relative angle $\Delta\phi_{12}$ in the excitation energy of the decaying nucleus X→1+2, defined by Eq. 3.17. It can be noticed that one has the option to use either $\Delta\phi_{12}^{\text{nom.}}$ (Eq. 3.18) or $\Delta\phi_{12}^{\text{reco.}}$ (Eq. 3.22) to calculate the excitation energy. Since the dT=0 and dT=3 cases have acceptable uncertainty in the $\Delta\phi_{12}^{\text{nom.}}$ value, it is possible to correlate the two calculations, where expected locus lies on the diagonal line in the [$\text{E}_{x12}(\Delta\phi_{12}^{\text{nom.}})$, $\text{E}_{x12}(\Delta\phi_{12}^{\text{reco.}})$] plane. For the dT=1 and dT=2 cases, where $\Delta\phi_{12}^{\text{nom.}}$ uncertainty is too large, it can be expected that $\text{E}_{x12}(\Delta\phi_{12}^{\text{nom.}})$ has broad range ($\sim$ 2-4 MeV) of values for a given real excitation energy, while the $\text{E}_{x12}(\Delta\phi_{12}^{\text{reco.}})$ gathers the data around the locus defined by the real excitation energy. To demonstrate this phenomena, and to improve understanding of the data, the MC calculations for the ^{7}Li(^{9}Li, ^{4}He^{6}He)^{6}He reaction are shown in Figure 3.24. These data, as well as all the simulated data used in the analysis, were produced using UNISim software framework for the MC simulation, developed by D. Dell'Aquila for the RBI Nuclear physics group [107].

Next, the excitation energy relations for the combinations of one detected and one undetected particle (E_{r13} and E_{r23}) are presented. Total energy available to the system is given by the relation:

$$E_{tot}^{CM} = Q + \frac{m_t}{m_t + m_p}E_p, \tag{3.25}$$

and the relation:

$$E_{tot}^{CM} = E_{1-23} + E_{23} = E_{2-13} + E_{13} \tag{3.26}$$

if two particle sub-systems are considered. In the center-of-mass system it is valid:

$$|\vec{p_1^{CM}}| = |\vec{p_{1-23}}|. \tag{3.27}$$
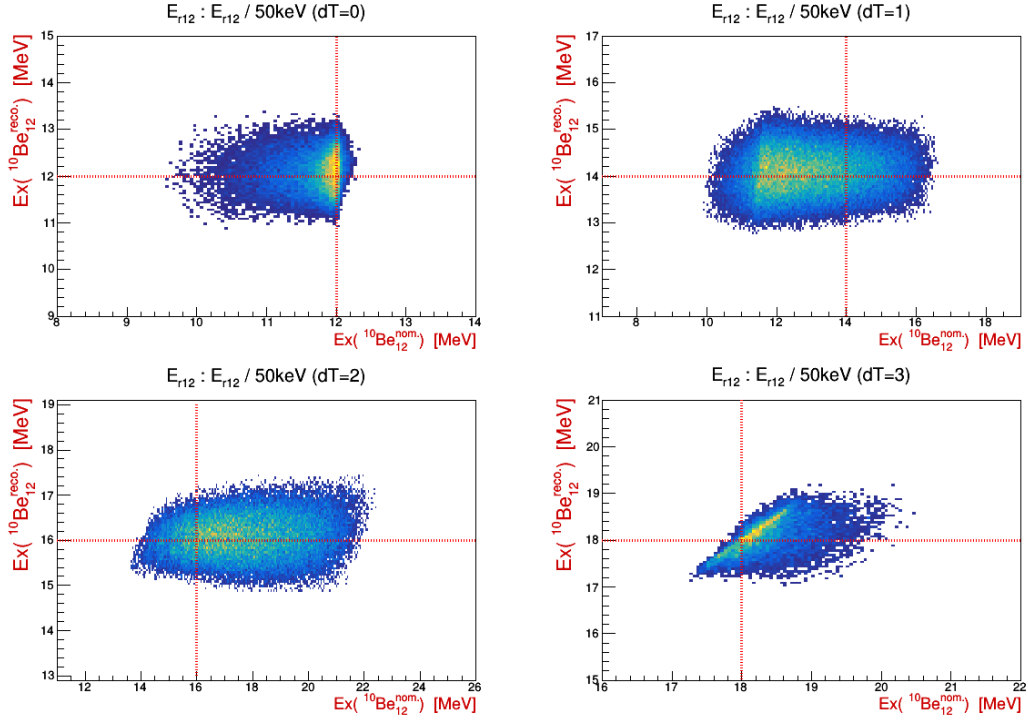
From the Equation 3.27 and the definition of reduced mass:

Figure 3.24: The ^{10}Be excitation energy comparison spectra for the values calculated using $\Delta\phi_{12}^{\text{reco.}}$ (Y axis) versus $\Delta\phi_{12}^{\text{nom.}}$ (X axis) for the ^{7}Li(^{9}Li, ^{4}He^{6}He)^{6}He reaction simulated data. Included cases are: E$_x$(^{10}Be) = 12 MeV (dT = 0, top left), E$_x$(^{10}Be) = 14 MeV (dT = 1, top right), E$_x$(^{10}Be) = 16 MeV (dT = 2, bottom left) and E$_x$(^{10}Be) = 18 MeV (dT = 3, bottom right).

$$\mu_{1-23} = \frac{m_1}{m_1 + m_2 + m_3}(m_2 + m_3) \tag{3.28}$$

follows the relation:

$$E_{1-23} = \frac{m_1 + m_2 + m_3}{m_2 + m_3} E_1^{CM}. \tag{3.29}$$

Using the Equations 3.26 and 3.29 one can write:

$$E_{r23} = E_{tot}^{CM} - \frac{m_1 + m_2 + m_3}{m_2 + m_3} E_1^{CM}, \tag{3.30}$$

which combined with the Equation 3.25, gives the final expession for the relative energy E$_{r23}$:

$$E_{r23} = Q + \frac{m_t}{m_t + m_p} E_p - \frac{m_1 + m_2 + m_3}{m_2 + m_3} E_1^{CM} \tag{3.31}$$

and relative energy E$_{r13}$:

$$E_{r13} = Q + \frac{m_t}{m_t + m_p} E_p - \frac{m_1 + m_2 + m_3}{m_1 + m_3} E_2^{CM} \tag{3.32}$$

Center-of-mass energies are given by the relation:

$$E_i^{CM} = E_i^L + \frac{m_i m_p}{(m_p + m_t)^2} E_p - 2 \frac{\sqrt{m_p E_p}}{m_p + m_t} \sqrt{m_i E_i^L} \cos\theta_i^L \tag{3.33}$$

where index i denotes the particle number. From Equations 3.31 and 3.32, it can be seen that the relative energies E_{r13} and E_{r23} depend only on the energy and the θ angle of the detected particles, as well as the Q value of the reaction. One can also use the "two-body" excitation energy from Equation 3.5 to calculate the same relative energies. This fact was also used in the data analysis to cross-check the data selection as the discrepancies between two spectra would indicate contaminations in the data, coming from the exit channel identification procedure.

An example of the excitation energy spectra for the simulated decay of ^{10}Be $\rightarrow$ ^{4}He+^{6}He, detected in dT=3, from the reaction on the ^{7}Li is shown in Fig. 3.25. One can notice characteristic behaviour of the excitation energy of E_{r12} combination: vertical locus in the E_{r12} - E_{r13} and E_{r12} - E_{r23} combinations, and off-diagonal locus in the E_{r13} - E_{r23} combination. In present analysis, these spectra are always shown with the threshold energy for the respective decay channel added.

From the MC simulations it can be deduced that σ of the Gaussian peak from the projection shown on Fig. 3.25 is 0.35 MeV, which corresponds to the value observed in the physical data for this channel really well and gives an estimate of expected experimental resolution. The offset of $\sim$ 100 keV is to be expected, considering the contribution of all uncertainties: $\Delta\phi_{12}^{\text{reco.}}$, $\theta_{1,2}$ and $E_{1,2}$ from calibration and energy loss calculations. This is taken into account in the interpretation of the results and will be further explained in the following subsection.

3.3.6 Three-body reactions: interpretation of the data

In this subsection, the problem of low resolution and small statistics observed in most spectra from the present experimental data will be addressed.
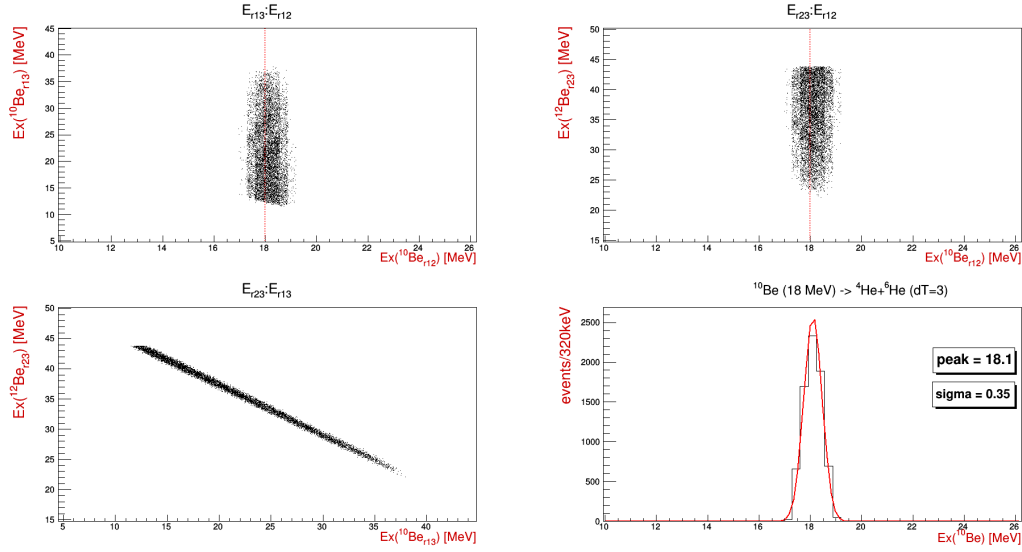
Figure 3.25: An example of the excitation energy spectra for all combinations of the particles from the ^{7}Li(^{9}Li,^{4}He^{6}He)^{6}He reaction, for the simulated excitation energy of ^{10}Be* of 18 MeV for the ^{4}He+^{6}He (12 combination) detected in the opposite detectors (dT=3).

Main sources of uncertainty

One of the main causes of the energy uncertainty is the $\sim$ 1mg/cm^2 thickness of the LiF target, which is reflected in the energy uncertainty of the ^{9}Li beam of $\pm$ 200 keV. If the ^{9}Li is detected nucleus in the reaction exit channel, addition $\pm$ 200-500 keV of energy uncertainty is added, depending on the initial energy in the reaction and the angle of detection, as the exact position of the reaction inside the target is not know (see Section 3.3.7 for details). This uncertainty is smaller for the lighter particles, as they loose less energy at the exit of the target. Another major, if not the biggest, cause of the uncertainty, which reflects in all parts of data analysis is the lack of segmentation in azimuth angle of the LAMP setup (Fig. 3.2). As the result, for the initial data selection the $\Delta\phi_{12}^{\text{nom.}} = \text{dT} \times 60°$ azimuthal angle is used (example: Fig. 3.19 for the data, Fig. 3.22 and 3.23 for MC simulations). Once the data is selected, the $\Delta\phi_{12}^{\text{reco.}}$ value, reconstructed from kinematic variables of detected particles, can be calculated (Eq. 3.22) to extract more realistic value of relative azimuthal angle (example: Fig. 3.21), to be used in the excitation energy calculation (Eq. 3.23), if the correct reaction exit channel is identified (example: Fig. 3.25 and 3.24). This procedure helps to restore the resolution in the excitation energy, but has two major drawbacks inherently. The first one is that uncertainties in the kinematic variables (E$_i$, P$_i$, θ_i) are reflected in the systematic uncertainty of reconstructed $\Delta\phi_{12}^{\text{reco.}}$ value, which is different for different nuclei and telescope combinations in the exit channel,

as the latter scans different excitation energy regions, which are dependent on the opening angle of nuclei from the particular decay. This is seen on the example of the MC data presented on Fig. 3.25. The second one is that misidentified data from other reaction exit channels results in wrong calculation of the $\Delta\phi_{12}^{\text{reco.}}$ value and hence the excitation energy, which brings additional uncertainty and affects the resolution.

Spectra binning and fitting procedure

The consequences of these uncertainties are low resolution and systematic uncertainty of ~ 350 keV in the excitation energy spectra. For this reason the binning was adjusted to observe well known states in wide range of nuclei as a single peak in corresponding spectra, resulting in 320 keV/bin scale used. Thus, it is common for the position of the peak, extracted with Gaussian fit on a smooth background, to be observed ± 1 bin, lower of higher, in the spectrum. Additional contribution to the uncertainty of the Gaussian fit, reflected in extracted position, norm and width of the peak, is the background estimate. Thus the background was always estimated by smooth, usually polynomial, function which describes the general shape of the data and/or detection efficiency curves, on top of which the Gaussians are fitted. These Gaussian peaks are not considered to be real states a priori, but the candidates for states, due to the resolution and statistics obtained for these peaks. A part of the Gaussian peaks are added to better describe the background, usually at very high excitation energies. Because the kinematic variables were used in the calculation of the $\Delta\phi_{12}^{\text{reco.}}$ value, both in the data and MC simulations, which have slightly different uncertainties, an offset of ~ 350 keV (1 bin) can sometimes be observed in the shape of detection efficiency curve. This was taken into account in the data analysis and the interpretation of the results.

Important note on the interpretation of the data

It is important to note that any single spectrum, with corresponding fit and peaks which are candidates for real states, was not used by it's own to derive the conclusion on the existence of the real states in corresponding decay channel. This was done by simultaneously considering all of excitation energy spectra obtained, for different data sets, together with the fits to the data, for all particle and telescope combinations in the reaction exit channel. The only exception being the channels for which only single data set was avail-

able. The peaks which were strongly observed in one spectrum, and the key states which are known to decay strongly to the examined decay channel, were used as a guidance for the fitting procedure in spectra with very low statistics.

Layout of the results and summary tables of the observed states

To take into the consideration large systematic and statistical uncertainties of present experimental data, results (Chapter 4) are systematically presented for each case studied, as they were thoroughly analysed, with the most important result, the summary table of the observed states presented at the end of each decay channel studied. The obtained results are than discussed (Chapter 5) in the context of previous measurements and theoretical studies, with the focus on the cluster and molecular-like structures in the excited states of the ^{10}Be, ^{12}Be and ^{13}B nuclei. The states and decay channels which are for the first time observed in present experimental data are discussed from the clustering standpoint.

3.3.7 Monte Carlo simulations: width of the states

In this subsection, a detailed overview of the methods used to deduce the FWHM of the states observed in the excitation spectra will be given. Total experimental resolution is given by the relation:

$$\sigma^2_{\text{tot.}} = \sigma^2_{\text{state}} + \sigma^2_{exp.} \tag{3.34}$$

where σ_{state} is the intrinsic width of the state and $\sigma_{\text{exp.}}$ is the experimental resolution for a given reaction channel at given excitation energy, which is estimated with the help of the MC simulation and input from the SRIM software for the energy loss uncertainty calculations. The FWHM of the state is related to the σ of the Gaussian fit to the data with the relation: FWHM = 2.355 $\times \sigma$. From Equation 3.34 it follows:

$$FWHM_{state} = 2.355 \times \sqrt{\sigma^2_{\text{tot.}} - \sigma^2_{exp.}} \tag{3.35}$$

One major contribution to the total uncertainty in the FWHM estimate is the $\sigma_{tot.}$, which is deduced from the Gaussian fit to the data. While the fits were performed using free parameters, guided by the initial manual fit, the background estimate certainly plays a major role in the uncertainty of the fit, and to reduce systematic uncertainties, background

was usually modelled after the geometrical efficiency and/or was guided by the shape of the two-dimensional excitation energy spectra for a given projection.

For the experimental resolution estimate (MC simulations), detailed discussion based on the analysis of the 13.5 MeV excited state of ^{13}B nuclei, undergoing the ^{9}Li+^{4}He decay, is given here. Starting with the "perfect conditions" in the MC simulations, beam positioned at the center of infinitesimally thin target, exact θ and ϕ angles (deduced from the x,y,z coordinates of the hit inside the detector and exact energies (without energy straggling uncertainty) yields the $\sigma_{exp.}$ of 20 keV for estimated experimental resolution. This is a good checkpoint as the input equals to the output (finite width due to the binning of the histogram). When realistic polar angle (θ) uncertainty of $\sim 2°$ per strip is introduced, based on the corrected nominal geometry of the LAMP setup (Table 3.5), keeping all other parameters the same $\sigma_{exp.}$ yields 260 keV. In the next step, uncertainty in the beam energy, due to the uncertainty of the reaction position inside the target, is introduced. For the ^{9}Li beam of 74.8 MeV, energy loss throughout the whole LiF target (average thickness was taken to be ~ 1.1 mg/cm^2, see Table 3.3) is ~ 400 keV. For the assumption that the reaction had happened at the center of the target, energy loss up to that point is ~ 200 keV, thus the uncertainty in the reaction position inside the target was taken into account by uniformly randomizing the energy of the beam within +/- 200 keV from the target center using the formula:

$$E'_{beam} = E_{beam} - \Delta E(\frac{d}{2} \times LiF) + rnd(\frac{d}{2} \times LiF). \tag{3.36}$$

where $rnd()$ is uniform randomizer function inside ROOT framework. Introduction of the uncertainty in the beam energy yields $\sigma_{exp.}$ of 290 keV.

In the next step uncertainty of the beam position (angle straggling) on the target was introduced in the MC simulations by introducing the Gaussian uncertainty of 3 mm from the target center, which should generally be a realistic estimate for the radioactive beams. Also, Gaussian uncertainty of 100 keV was introduced to the input beam energy. Please keep in mind that these Gaussian uncertainty distributions have far less of an impact compared to the uniform random function. With these additions, $\sigma_{exp.}$ yields 375 MeV.

In the final step, uncertainty in the energy loss of the reaction products inside the target was taken into account. The path of the reaction product inside the target is d$'/\cos\theta$,

where θ is the angle at which the product is detected and d' is the length of the target from the reaction point to the exit of the target. Following the same principle as for the beam energy uncertainty (Eq. 3.36), energies of the products were varied by uniform random value to account for the uncertainty of the reaction position inside the target. Due to the wide range of energies of the detected reaction products, different uncertainties for the energy losses inside the target, calculated by the SRIM software for each isotope, were taken for different energy groups. Usually there were four to five groups for every five to ten MeV difference in the detected energy. For each group the average (due to the different detection angles) energy loss per whole detector was taken into account. The same process was applied to each detected reaction product individually. The final $\sigma_{exp.}$, experimental resolution estimate, for the 13.5 MeV excited state of ^{13}B, undergoing decay to the ^{9}Li+^{4}He channel ("1-2" combination, Eq. 3.23), was deduced to be 385 MeV.

To conclude, deduced FWHM for this state, based on the analysis presented here and the experimental data presented on Fig. 4.64, is deduced to be ~ 330 keV, which is in good agreement with the only published width estimate of < 320 keV for ^{13}B excited state at 13.6 MeV decaying to the ^{9}Li+^{4}He channel [27]. The more detailed discussion is presented in Section 5.3. The method presented here is used throughout the analysis, whenever the FWHM estimate is presented, taking different energy loss uncertainty distributions for isotopes in question.

4   Experimental results

In the following subsections, obtained experimental results for the ^{10}Be decays (to the ^{4}He+^{6}He and ^{4}He+^{6}He*(1.8 MeV, 2^+) in Tables 4.16-4.17, ^{9}Be+n and ^{8}Be+nn in Table 4.20), the ^{12}Be decays (to the ^{6}He+^{6}He and ^{6}He+^{6}He*(1.8 MeV, 2^+) in Tables 4.25-4.26, ^{4}He+^{8}He in Table 4.38) and the ^{13}B decays (to the ^{9}Li+^{4}He and ^{9}Li*+^{4}He in Table 4.46, ^{7}Li+^{6}He and ^{10}Be+t in Table 4.52) will be presented.

With the aim to present the results as clearly as possible, they are always shown in the same order: data selection and exit channel identification spectra are shown first, followed by two-dimensional excitation energy spectra for all combinations of reaction products in the reaction exit channel and one-dimensional projections with calculated detection efficiency. The projections are than fitted with combination of the Gaussian functions on top of the estimated background, with the results presented in the corresponding tables. Due to large systematic uncertainty, low resolution and statistics obtained in most spectra (see Section 3.3.6 for details), fitted peaks are considered to be the candidates for the real states, with () indicating low quality of the candidate peak. The tables contain the parameters of the Gaussian fit: centroid (Ex), standard deviation (σ) and the norm (N), and the function used to describe the background for each spectrum, which is written in abbreviated form: "polX" for the polynomial of Xth degree, "exp" for the exponential function, and "gaus(E)" for the broad Gaussian function centered at the excitation energy value E. The background was modeled as a smoothly varying function to match the general shape of the data, taking the detection efficiency into account. If the rise in background contribution was observed at higher excitation energies in two-dimensional spectra, a broad Gaussian was added to account for the rise of the background. These Gaussians are labeled with $^{\otimes}$ in the tables, while the ones indicated with * require further

examination in the text.

Since the data was analyzed separately for every pair of telescopes and combination of the reaction products in the exit channel, presented data selection spectra will vary for different cases to make them as informative as possible. The Q value spectra presented will contain the colored markers to indicate the final selection of the data used in the results, as well as the Catania plot, with addition of colored dashed lines to indicate the loci of particular reaction exit channel. In some cases, the excitation energy correlation spectra will be presented, like the ones shown previously in Fig. 3.24, where the excitation energies of the detected pairs of nuclei (Eq. 3.23), calculated with either kinematically reconstructed $\Delta\phi_{12}^{\mathrm{reco.}}$ (Eq. 3.22) or nominal $\Delta\phi_{12}^{\mathrm{nom.}}$ (Eq. 3.18) relative azimuth angle, are being compared. Since the $\Delta\phi_{12}^{\mathrm{reco.}}$ (Eq. 3.22) is reconstructed after the initial identification, or under the assumption, of the reaction exit channel (Q, E_3, P_3), while the $\Delta\phi_{12}^{\mathrm{nom.}}$ is of fixed value, the loci of the data from different exit channels can be separated in the $\mathrm{Ex}(\Delta\phi_{12}^{reco.})$-$\mathrm{Ex}(\Delta\phi_{12}^{\mathrm{nom.}})$ correlation plane. The difference in loci is usually sufficient to separate the contributions from the reactions on different elements of the target, but not the excited states of nuclei in the same exit channel.

It has to be mentioned that the fit to the data was performed to describe the excitation energy spectra and to extract the peaks position and width, from the corresponding particle decay threshold up to $\sim$ 15-20 MeV in relative energy, after which unresolved background contributions dominate. The results of the fit are shown in the tables which, in the text, appear after the excitation energy spectrum. At the end of each section, i.e. dedicated case study for particular decay channel, a summary table of the observed states is presented, on the basis of aforementioned fits, which also indicates a level of confidence for the corresponding state. Only if the peak is observed clearly in more than two independent data sets, it is taken as a real state, otherwise a tentative assignment is made.

Due to the large uncertainty in the nominal relative $\Delta\phi_{12}^{\mathrm{nom.}}$ angle, which affects the reconstruction of the energy and momentum of the undetected particle and hence the obtained Catania plot and Q-value spectra, data selection may seem odd at times due to small systematic offsets introduced by the initial use of the $\Delta\phi_{12}^{\mathrm{nom.}}$ value, as previously seen on Fig. 3.22 and 3.23. In many cases where unambiguous data selection was not

possible many iterations with additional conditions were made to ensure cleanest possible data selection for the particular exit channel and telescope combination. If unambiguous data selection was not achieved, particular reaction exit channel is omitted from the final results. All case studies for particular combination of the detected particles are presented, starting with the reactions on the ^{7}Li target, followed by the reactions on the ^{19}F and ^{6}Li targets, respecting the ordering of the telescope combinations from dT=3 to dT=0. The reaction channel is always labeled as: t(p,12)3, where "t" and "p" are target and projectile respectively, the particles "1" and "2" are the detected ones, while the "3" is undetected. Finally, the results presented in the following subsections are discussed, and compared with the theory and previous measurements in Chapter 5.

4.1 Decays of the ^{10}Be excited states

In this section, the obtained experimental results for the ^{4}He+^{6}He, ^{4}He+^{6}He* (1.8 MeV, 2^{+}), ^{9}Be+n and ^{8}Be+nn decays of the ^{10}Be excited states are presented. These are obtained through three dedicated case studies of the ^{4}He+^{6}He+^{6}He, ^{4}He+^{6}He and ^{6}He+^{6}He coincidences for helium decays, and ^{9}Be+^{6}He and ^{8}Be+^{6}He for one- and two-neutron decay in all telescope combinations. Although the focus of this thesis is on the cluster and molecular structure of the ^{10}Be excited states, the observed neutron decays are a valuable part of the interpretation of the results and are therefore presented here.

4.1.1 ^{4}He+^{6}He decay channel

^{7}Li(^{9}Li, ^{4}He^{6}He^{6}He) reaction

The coincident detection of all three particles in the exit channel of the ^{9}Li+^{7}Li reaction, represents the cleanest data available for the study of the ^{10}Be helium cluster decays. Although the detection efficiency and consequently the obtained statistics are very low in this case, due to the clean data selection, these results represent the reference case for the observed helium cluster decays in the low excitation energy region, close to the particle decay threshold at 7.41 MeV. Since the ^{10}Be decays are accessed through both "1-3" and "2-3" combination of the particles in the exit channel, the results shown in Fig. 4.3, are presented as a sum of the two aforementioned excitation energy spectra.

Having all reaction products in the exit channel detected, provides an opportunity for
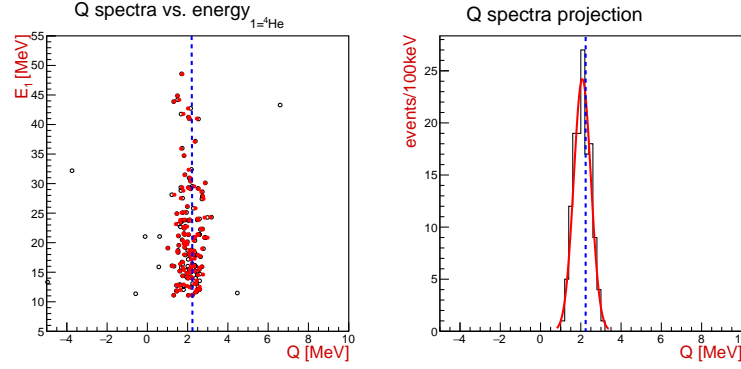
Figure 4.1: The Q value spectrum for the ^{7}Li(^{9}Li, ^{4}He^{6}He^{6}He) reaction versus the energy of detected ^{4}He (left), and the projection of the same spectrum (right). Blue dashed line indicates correct Q value for this reaction at 2.24 MeV, while the red line indicates resulting Gaussian fit: [N = 242, Q = 2.1 MeV, σ = 0.4 MeV].

the comparison of the relative energy spectra obtained by treating every combination of particles as "1-2", i.e. the detected pair (Eq. 3.23) or "1-3"/"2-3", i.e. the combinations of one detected and one undetected reaction product (Eq. 3.32 and 3.31 respectively), effectively testing the consistency of the excitation energy calculation and validity of the $\Delta\phi_{12}^{\mathrm{reco.}}$ reconstruction (Eq. 3.22). As the results are consistent, the use of $\Delta\phi_{12}^{\mathrm{reco.}}$ is justified for the relative energy calculation in the cases where the clean data selection is possible. This being the case, for the results presented here all particle combinations in the exit channel were treated as the detected pairs.
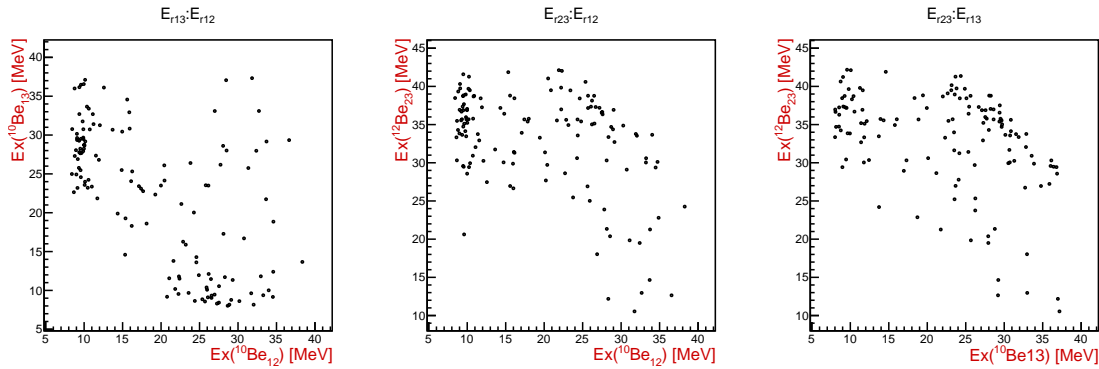

Figure 4.2: Excitation energy spectra for the ^{10}Be$_{12}$, ^{10}Be$_{13}$ and ^{12}Be$_{23}$, from the ^{7}Li(^{9}Li, ^{4}He^{6}He^{6}He) reaction.

Systematic offset of $\sim$ - 100 keV is observed, both in the Q value and in the excitation energy. The offset in the Q value spectrum is attributed solely to the total energy statistical error, as the Q values is calculated using only the energies of the detected particles. The offset observed in the excitation energy (Table 4.1), compared to the known states at 9.6, 10.2 and 11.8 MeV [106], is likely the combination of the energy and the angle
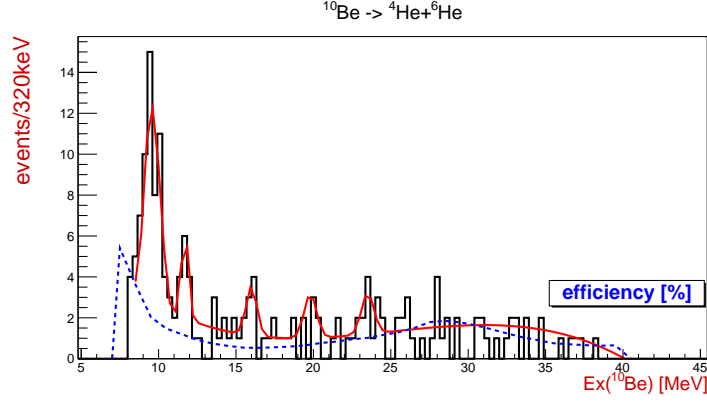
Figure 4.3: Excitation energy spectrum for the sum of ^{10}Be$_{12}$ and ^{10}Be$_{13}$, with the calculated detection efficiency in blue and the fit to the data in red. The results of the fit are shown in Table 4.1.

uncertainties.

Ex [MeV]	9.5	10.1	11.7	(16.0)	(19.8)	(23.4)	background
σ [MeV]	0.4	0.3	0.25	(0.35)	(0.4)	(0.4)	pol3

Table 4.1: Results of the fit for the ^{10}Be excited states from the ^{7}Li(^{9}Li, ^{4}He^{6}He^{6}He) reaction.

^{7}Li(^{9}Li, ^{4}He^{6}He)^{6}He reaction

The ^{4}He+^{6}He coincidences, being the first case study of two out of three particles detected in the three-body reactions shown in this chapter, are presented here with a more comprehensive overview of the exit channel identification process and quality control of the data selection for the obtained results. For the dT=3 case, Catania plot (Fig. 4.4) and Q value spectra (Fig. 4.5) are shown separately for the demonstration of the exit channel identification, and the Ex(^{10}Be$_{12}^{\mathrm{reco.}}$) vs. Ex(^{10}Be$_{12}^{\mathrm{nom.}}$) excitation energy correlation spectra (Fig. 4.6) is shown to justify the reasoning for the selection of the main contributions to the results, omitting the less pronounced channels such as the reactions on ^{19}F target with undetected ^{18}O nucleus in the excited state. All of the observed exit channels for all telescope combinations, together with the color coding used throughout this section, are presented in Table 4.2. Due to inability to exclude minor contributions from the excited states of ^{18}O nucleus, which are expected to contribute to the data no more than 5-10 %, these events were treated as the background contamination.

As for all cases, Catania plot and Q value spectra are calculated using the nominal $\Delta\phi$ angle, and the relative energy of the particles "1-2", i.e. the detected pair, is calculated

reaction	$^7\text{Li}(^9\text{Li}, {}^4\text{He}{}^6\text{He})^6\text{He}$	$^7\text{Li}(^9\text{Li}, {}^4\text{He}{}^6\text{He})^6\text{He}^*_{1.8}$	$^{19}\text{F}(^9\text{Li}, {}^4\text{He}{}^6\text{He})^{18}\text{O}$
Q [MeV]	2.24	0.44	4.23
color	red	blue	pink
	$^{19}\text{F}(^9\text{Li}, {}^4\text{He}{}^6\text{He})^{18}\text{O}^*_{1.98}$	$^{19}\text{F}(^9\text{Li}, {}^4\text{He}{}^6\text{He})^{18}\text{O}^{**}_{\sim 3.7}$	$^6\text{Li}(^9\text{Li}, {}^4\text{He}{}^6\text{He})^5\text{He}$
	2.25	0.53	7.63
	green	gray	orange

Table 4.2: The Q values and color coding for the three-body reaction channels observed in the data from the $^4\text{He}+^6\text{He}$ coincident events in all detector combinations.

using the reconstructed $\Delta\phi_{12}^{\text{reco.}}$ value (Eq. 3.22), if not stated otherwise. Due to the proximity of the 1.8 MeV excitation of the undetected ^6He nucleus to the ground state and poor resolution in the Catania plot and the Q value spectra, caused by the uncertainty in the $\Delta\phi_{12}^{\text{nom.}}$, these contributions were not separated in the analysis of the dT=1 and dT=2 cases, resulting in these two cases being omitted from the final results. Therefore, for the reaction on the ^7Li target, only the dT=3 and dT=0 cases are presented.
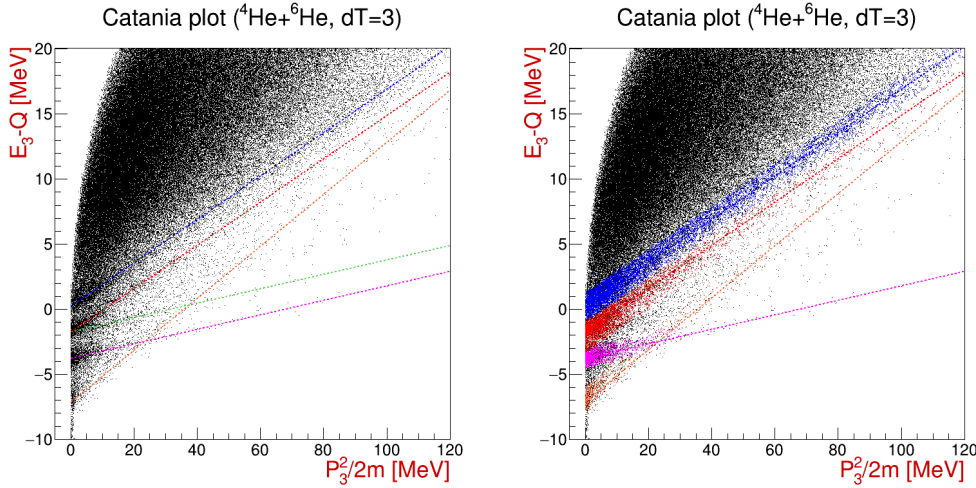

Figure 4.4: Catania plot for the $^4\text{He}+^6\text{He}$ coincident events detected in the dT=3 combination. Dashed lines indicate expected Q values, as listed in Table 4.2, taking offsets ($\sim$ -500 keV) into the account, and represent the locus of the data for most prominent exit channels. The undetected particles are: ^6He (red) and $^6\text{He}^*$ (blue) from the reaction on the ^7Li, ^{18}O (pink) and $^{18}\text{O}^*$ (green) from the reaction on the ^{19}F, and ^5He (orange) from the reaction on the ^6Li target. Not fully seen in spectra is the data locus from the two-body data from the reaction on ^1H contaminant, with the Q value of 12.22 MeV.

It is interesting to note how $\Delta\phi_{12}^{\text{reco.}}$ shifts the data for different exit channels in the ^{10}Be excitation energy comparison spectra, shown in the Fig. 4.6. Taking the $^7\text{Li}(^9\text{Li},$
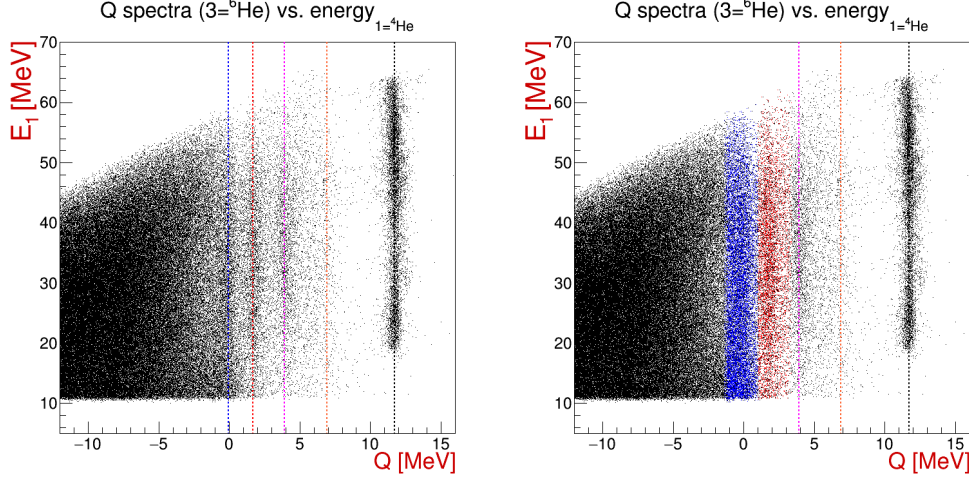
Figure 4.5: The Q value spectra for the ^{7}Li(^{9}Li, ^{4}He^{6}He)$_{dT=3}$^{6}He reaction versus the energy of detected ^{4}He. Dashed lines indicate expected Q values for different exit channels, as listed in Table 4.2, taking offsets into the account, while the colored markers indicate final data selection with same color coding used. Unselected data on the right side of the spectra (black dashed line) comes from the two-body reaction on ^{1}H contaminant with the Q value of 12.22 MeV, while the rest of the data is coming from the reaction on ^{19}F, ^{6}Li and many-body exit channels. Since the assumption of the third particle was made in the calculations (P$_3$, E$_3$), data for channels which are not coming from the ^{7}Li target doesn't have the correct Q value, but are still presented here to understand contributions to the spectra.

^{4}He^{6}He)$_{dT=3}$^{6}He* reaction as an example (blue markers), one can notice the data from the mentioned reaction aligned along the diagonal line representing expected locus of the data. A small offset is also observed, as in the Catania plots and the Q value spectra. Above the line reaction with larger Q value appear: ^{7}Li(^{9}Li, ^{4}He^{6}He)^{6}He at 2.24 MeV, ^{19}F(^{9}Li, ^{4}He^{6}He)^{18}O at 4.23 MeV and ^{6}Li(^{9}Li, ^{4}He^{6}He)^{5}He at 7.63 MeV, while the many-body reactions appear beneath, mirroring the Q value spectrum, without showing any structure (locus) in the spectra. These considerations ensure that if there are contribution from the unresolved channels in the data, these are small and should not affect the final results, apart from the contribution to the background.

Helium cluster decays of the ^{10}Be excited states, produced in the ^{7}Li(^{9}Li, ^{4}He^{6}He)^{6}He reaction can be accessed through "1-2" and "1-3" combination of the particles in the exit channel. Having only dT=3 and dT=0 cases resolved, it is important to note that "1-3" combination of the dT=3 case covers similar phase space as the "1-2" combination in the dT=0 case. This is an important cross-check of the data and should be kept in mind when comparing these two results. The same is true for the "1-2" combination in the dT=3 case, which covers the same or a similar phase space as the dT=3 and dT=2 combinations for the reactions on the ^{19}F and ^{6}Li targets.
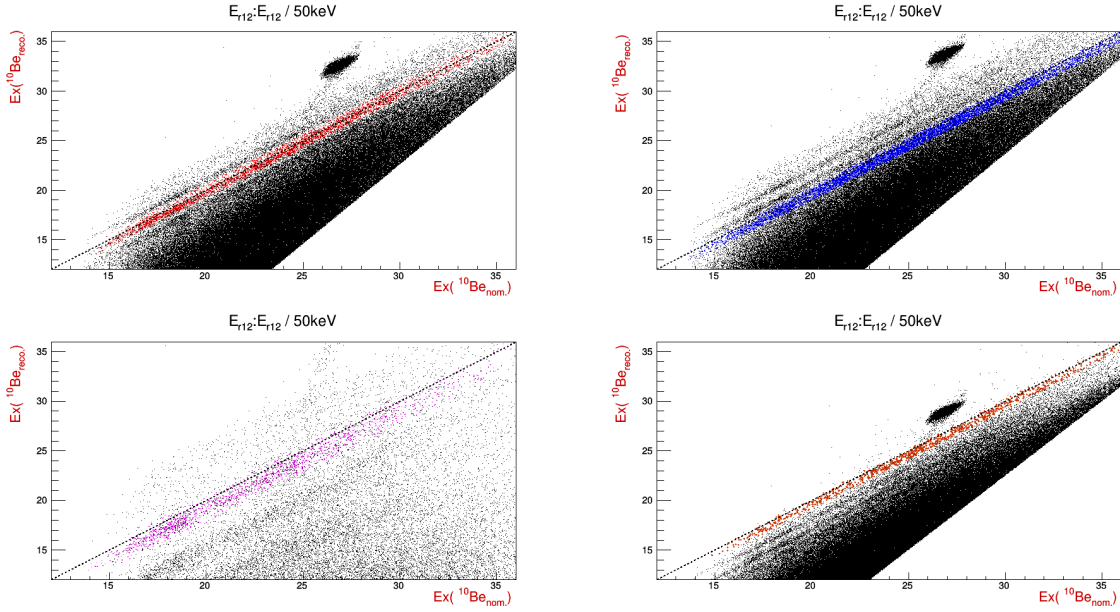
Figure 4.6: The ^{10}Be excitation energy comparison spectra for the LiF(^{9}Li, ^{4}He^{6}He)$_{dT=3}$X reaction. The excitation energies are calculated using nominal $\Delta\phi_{12}^{nom.}=180°$ value, shown on the abscissa, and reconstructed $\Delta\phi_{12}^{reco.}$ (Eq. 3.22) value, shown on the ordinate axis. Black dashed lines represents the expected loci (along the diagonal line) for the particular exit channel, while the color coding of reactions is as listed in Table 4.2: ^{7}Li(^{9}Li, ^{4}He^{6}He)^{6}He (red, top left), ^{7}Li(^{9}Li, ^{4}He^{6}He)^{6}He* (blue, top right), ^{19}F(^{9}Li, ^{4}He^{6}He)^{18}O (pink, bottom left) and ^{6}Li(^{9}Li, ^{4}He^{6}He)^{5}He (orange, bottom right). The strong circular locus is coming from the two-body reaction on the ^{1}H in the target.

Ex [MeV]	16.8	18.2	21.1	23.3	25.0*	background
σ [MeV]	0.5	0.7	0.3	0.8	2.4	pol4-gaus(20.5)*

Table 4.3: Results of the fit for the ^{10}Be$_{12}$ excited states from the ^{7}Li(^{9}Li, ^{4}He^{6}He)$_{dT=3}$^{6}He reaction, presented on the left side of Fig. 4.8. See text for * explanation.

In Table 4.3 the broad peak at 25.0 MeV is likely a part of the background, as it was not observed in other spectra. The background was modeled to describe the general shape of the data presented in Fig. 4.8 (left), hence the broad Gaussian at 20.5 MeV with negative amplitude was used. In the consistency cross-check procedure, same peaks were obtained from the fit with different background used, which was modeled after detection efficiency curve with the sum of three broad Gaussians.

Ex [MeV]	9.9*	11.6	14.1*	16.6	18.5	19.7	22.3	background
σ [MeV]	0.6	0.7	0.8	0.5	0.4	0.3	0.5	pol2+gaus(28.9)

Table 4.4: Results of the fit for the ^{10}Be$_{13}$ excited states from the ^{7}Li(^{9}Li, ^{4}He^{6}He)$_{dT=3}$^{6}He reaction, presented on the right side of Fig. 4.8. See text for * explanation.
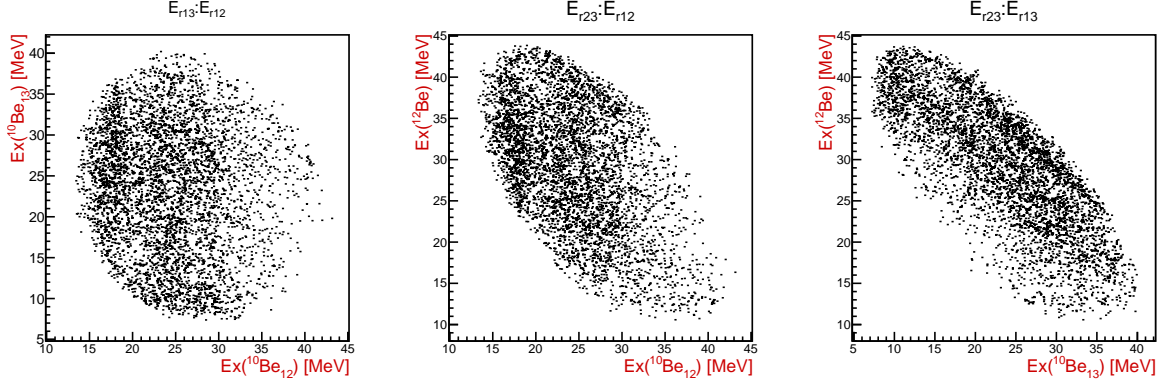
Figure 4.7: Excitation energy spectra for the ^{10}Be$_{12}$, ^{10}Be$_{13}$ and ^{12}Be, from the ^{7}Li(^{9}Li, ^{4}He^{6}He)^{6}He reaction. The ^{4}He+^{6}He pair was detected in dT=3 case, while undetected ^{6}He is in the ground state (0^+).
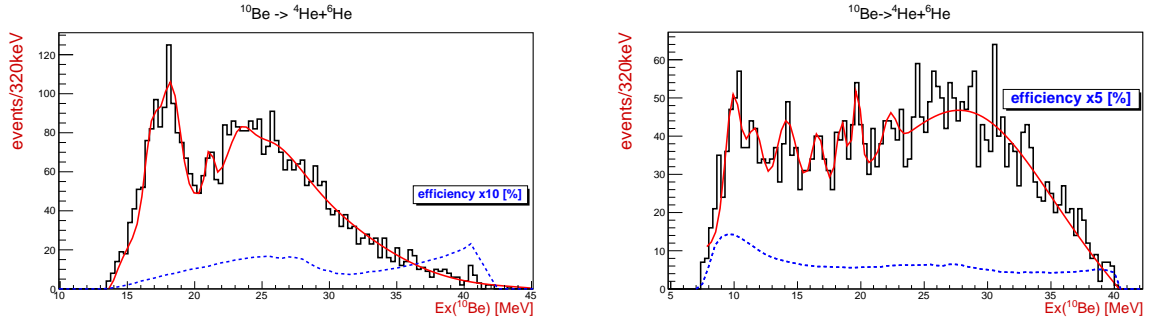

Figure 4.8: Excitation energy spectra for the ^{10}Be$_{12}$ (left) and ^{10}Be$_{13}$ (right), from the ^{7}Li(^{9}Li, ^{4}He^{6}He)^{6}He reaction. The ^{4}He+^{6}He pair was detected in dT=3 case, while undetected ^{6}He is in the ground state (0^+). Blue dashed line represents the detection efficiency curve, while the red line represents the results of the fit, with states listed in Table 4.3 for the "1-2" and Table 4.4 for the "1-3" combinations, respectively.

In Table 4.4, the peak at 9.9 MeV likely corresponds to two known states, the dominating one at 10.2 MeV and contributing state at 9.6 MeV. Due to the experimental resolution of at least ~ 500 keV close to particle decay threshold, these two states cannot be separated. Since the peak at 14.1 MeV is observed only in the spectrum in Fig. 4.8 (right), it is likely not a real state, but an unresolved background contribution from the ^{19}F(^{9}Li, ^{4}He^{6}He)^{18}O* reaction, which has almost the same Q value as the ^{7}Li(^{9}Li, ^{4}He^{6}He)^{6}He reaction.

For the ^{7}Li(^{9}Li, ^{4}He^{6}He)^{6}He* reaction it's important to note that "1-3" combination of the particles in the exit channel shows the decay of the ^{10}Be excited states to the 1.8 MeV (2^+) excited state of the ^{6}He nucleus, while the "1-2" combination shows the decay to the ^{6}He ground state. The latter combination should be directly compared with the states observed in the "1-2" combination for the ^{7}Li(^{9}Li, ^{4}He^{6}He)^{6}He reaction (Table 4.3), as they cover the same excitation energy range with similar kinematic phase space.

The excited state of ^{6}He nucleus will always be noted with a subscript "1.8" or using a superscript "$*$", when it is referred to in the spectra.
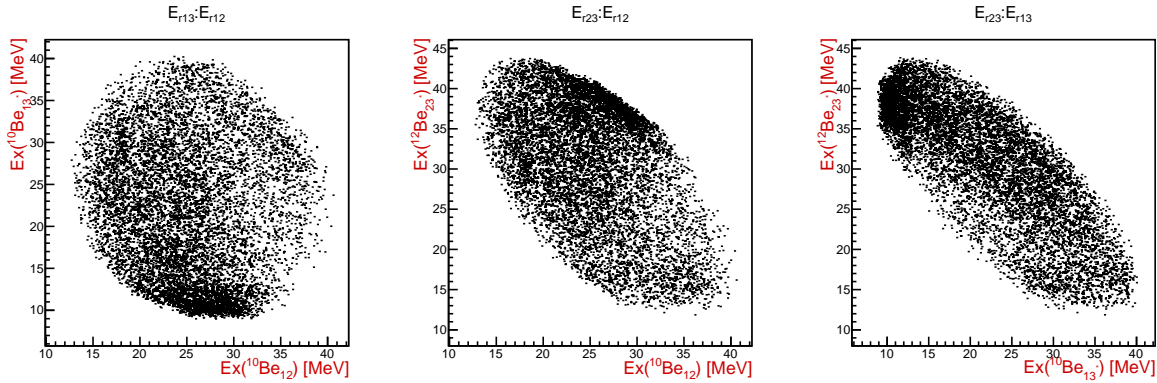

Figure 4.9: Excitation energy spectra for the ^{10}Be$_{12}$, ^{10}Be$_{13*}$ and ^{12}Be$_{23*}$, from the ^{7}Li(^{9}Li, ^{4}He^{6}He)^{6}He* reaction. The ^{4}He+^{6}He pair was detected in dT=3 combination, while undetected ^{6}He* is in the 1.8 MeV (2^+) excited state.
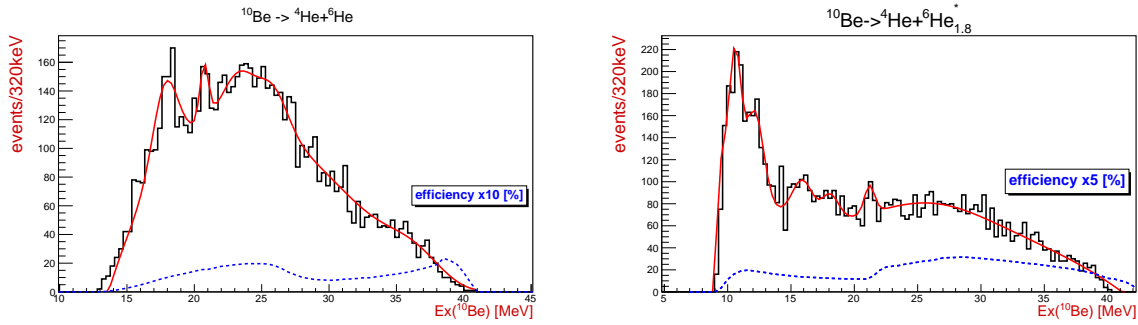

Figure 4.10: Excitation energy spectra for the ^{10}Be$_{12}$ (left) and ^{10}Be$_{13*}$ (right), from the ^{7}Li(^{9}Li, ^{4}He^{6}He)$_{dT=3}$^{6}He* reaction. Blue dashed line represents the detection efficiency curve, while the red line represents the results of the fit, with the states listed in Tables 4.5 and 4.6 respectively.

In Tables 4.5 and 4.6, a broad Gaussian functions were added to the background in the high excitation energy region to account for the rise of the background contribution, while the sharp Gaussian at 8.8 MeV was subtracted just to describe the data behavior at the particle decay threshold. The ^{10}Be$_{13*}$ excited states have an offset of $\sim$ 400 keV from the known states at 9.6, 10.2 and 11.8 MeV [18] and the first peak observed is likely the combination of both 9.6 and 10.2 MeV states.

Ex [MeV]	17.8	20.7	23.3	25.8$^\otimes$	background
σ [MeV]	0.9	0.3	1.1	1.1	pol4+gaus(36.4)

Table 4.5: Results of the fit for the ^{10}Be$_{12}$ excited states from the ^{7}Li(^{9}Li, ^{4}He^{6}He)$^6_{dT=3}$He* reaction, presented on the left side of Fig. 4.10.

Ex [MeV]	10.6	12.2	15.9	18.0	21.2	background
σ [MeV]	0.4	0.7	0.8	0.7	0.4	pol6+gaus(25.9)-gaus(8.8)

Table 4.6: Results of the fit for the ^{10}Be$_{13*}$ excited states decaying to the ^{6}He*, from the ^{7}Li(^{9}Li, ^{4}He^{6}He)$^{6}_{\mathrm{dT}=3}$He* reaction, presented on the right side of Fig. 4.10.

An example of auxiliary spectra for the ^{7}Li(^{9}Li, ^{4}He^{6}He)^{6}He and ^{7}Li(^{9}Li, ^{4}He^{6}He)^{6}He* reactions are shown in Figures 4.11 and 4.12, where one can see additional steps taken in the evaluation of the results presented. From these spectra it can be concluded that the calculated excitation energy has systematical uncertainty of ~ 400 keV, or $\sim$1 bin in the spectra, which also holds true for the rest of the obtained results, and it's taken into account when compiling the final table of the observed states for particular decay channel for each nuclei studied in this experiment. For the consistency test, excitation energy of the "1-3" pair for both reactions was calculated using the "three-body" (Eq. 3.31) or the "two-body" (Eq. 3.5) formulas. For the correct exit channel identification, the results should be in a good agreement, as they are here. The use of $\Delta\phi_{12}^{\mathrm{nom.}}$ in the excitation energy formula for the detected pair introduces a systematic offset, as the real $\Delta\phi$ has a particular value between $125° - 180°$ for each pair of particles, while the $\Delta\phi_{12}^{\mathrm{nom.}}$ is fixed at $180°$ in this case.
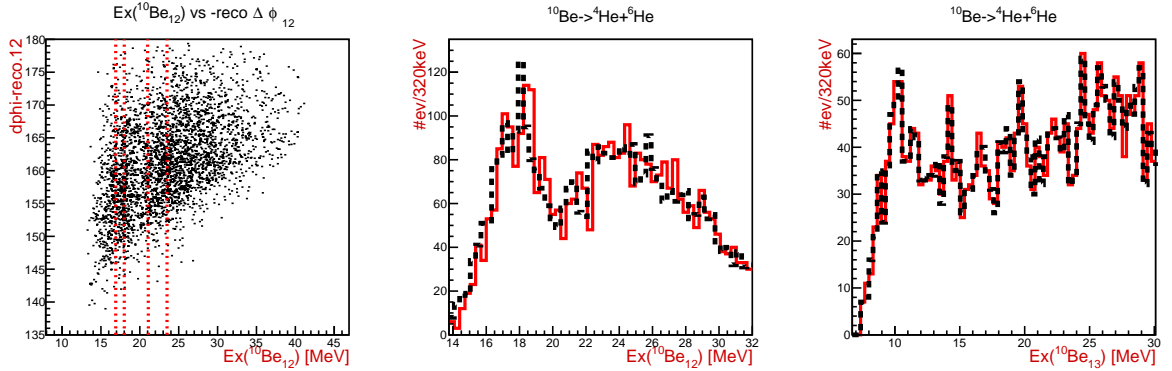

Figure 4.11: An example of auxiliary spectra for the ^{7}Li(^{9}Li, ^{4}He^{6}He)$_{\mathrm{dT}=3}$^{6}He$_{\mathrm{g.s.}}$ reaction. Figure on the left shows the ^{10}Be excitation energy versus the value of the reconstructed $\Delta\phi_{12}^{\mathrm{reco.}}$ angle; center one shows ^{10}Be excitation energy comparison spectrum for the value calculated using the "standard" $\Delta\phi_{12}^{\mathrm{reco.}}$ (black) or $\Delta\phi_{12}^{\mathrm{nom.}}$ (red); the figure on the right compares calculated excitation energy spectrum of the "1-3" particle pair (in this case ^{10}Be$_{13}$) using the "three-body" (Eq. 3.31) and "two-body" (Eq. 3.5) excitation energy formulas.

For the dT=0 case, a clean separation between the reactions on the ^{7}Li and ^{19}F targets was achieved by imposing the graphical cuts on the Catania plot, while additional Q value cuts were made to separate the ground and excited states of undetected ^{6}He and
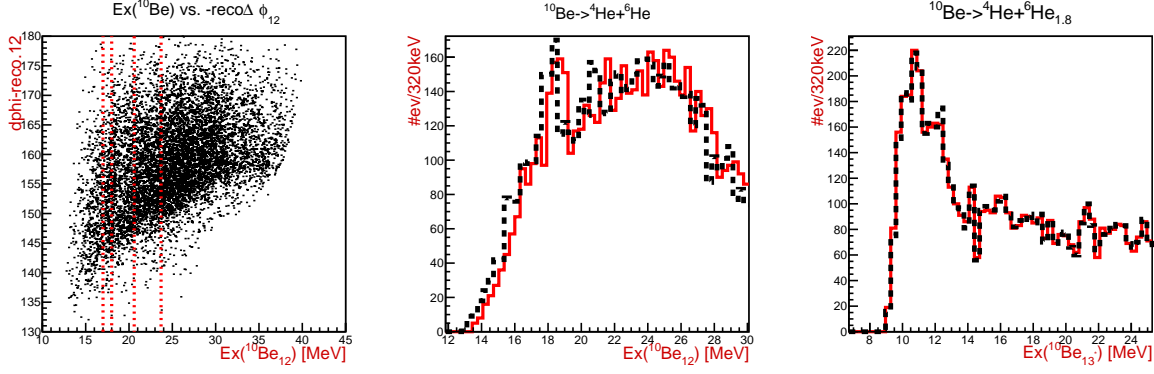
Figure 4.12: An example of auxiliary spectra for the ^{7}Li(^{9}Li, ^{4}He^{6}He)$_{dT=3}$^{6}He* reaction. Figure on the left shows the ^{10}Be excitation energy versus the value of the reconstructed $\Delta\phi_{12}^{\text{reco.}}$ value; center one shows the ^{10}Be excitation energy comparison spectrum for the value calculated using the "standard" $\Delta\phi_{12}^{\text{reco.}}$ (black) or $\Delta\phi_{12}^{\text{nom.}}$ (red); the figure on the right compares calculated excitation energy spectrum of the "1-3*" particle pair (in this case ^{10}Be$_{13*}$) using the "three-body" (Eq. 3.31) and "two-body" (Eq. 3.5) excitation energy formulas.

^{18}O nuclei respectively. For the reaction on the ^{7}Li target, although clean identification of the ground state of undetected ^{6}He was achieved, there are unresolved contributions to the ^{6}He excited state channel, from many-body reactions with ^{5}He+n and ^{4}He+nn in the exit channel. These contributions are best seen in Catania plot on Fig. 4.13, above the blue dashed line for the ^{6}He* channel. To confirm these considerations, the excitation energy of the ^{10}Be for the ^{6}He* data was additionally calculated using the $\Delta\phi_{12}^{\text{nom.}} = 0°$ value, which does not require the knowledge of the exit channel. When compared to the excitation energy calculated using the standard $\Delta\phi_{12}^{\text{reco.}}$ value presented on Fig. 4.15, the peak at $\sim$ 9 MeV is not observed, while the peak at $\sim$ 9.9 MeV remains, which corresponds to the mixture of 9.6 and 10.2 MeV states. This means that only the part of the data is coming from the ^{6}He* in the exit channel, and that the same states are produced in many-body reactions, but $\Delta\phi_{12}^{\text{reco.}}$ and consequently excitation energy is not correctly reconstructed for these events. A more comprehensive overview is given in Discussion 5.1, where the experimental data and Monte Carlo simulations are compared.

In the excitation energy spectra for the ^{7}Li(^{9}Li, ^{4}He^{6}He)^{6}He and ^{7}Li(^{9}Li, ^{4}He^{6}He)^{6}He* reactions, shown on Fig. 4.14, in the lower energy region the dominance of the 9.6 MeV state can be seen. Although the 10.2 MeV state is not as prominent as in "1-3" combination in the dT=3 case, shown on Fig. 4.8, it's presence can clearly be seen, especially in the spectra on the left and center, where ^{6}He ground state channel is presented. The inclusion of this peak improves the fits presented in Table 4.7. Due to unresolved many-body contributions, for the ^{6}He* excited state channel, obtained spectrum has poor resolution
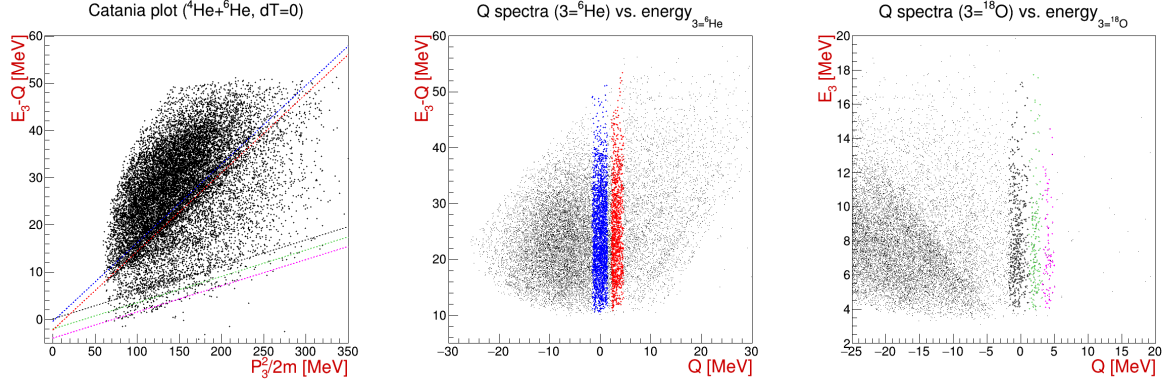
Figure 4.13: Catania plot and Q value spectra for the ^{4}He+^{6}He coincident events in the dT=0 combination, with identified exit channels from the reactions on ^{7}Li and ^{19}F targets, color coded as in Table 4.2. Contributions of the unresolved mix of higher excitation energy states centered around ~ 3.75 MeV (3.55 4+, 3.63 0+ and 3.92 2+) of ^{18}O, from the reaction on the ^{19}F target are shown in gray.
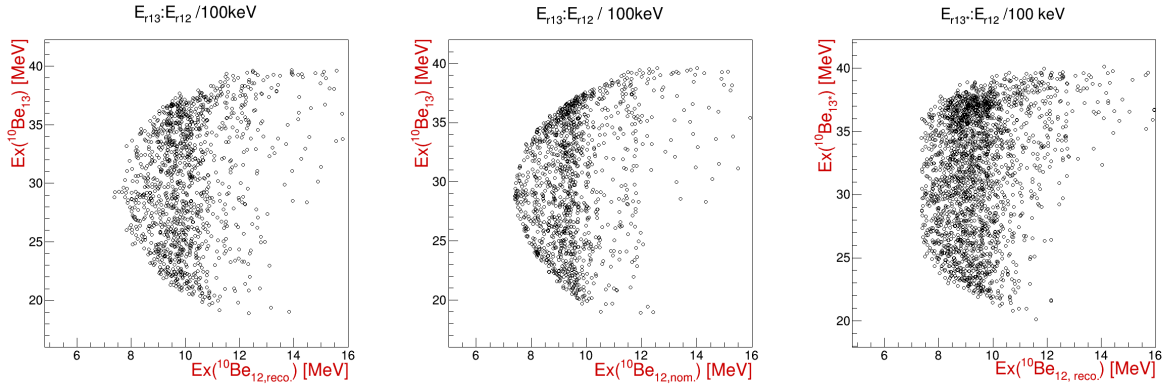

Figure 4.14: Excitation energy spectra for ^{10}Be$_{12}$ versus the ^{10}Be$_{13}$ and ^{10}Be$_{13*}$ combinations from the ^{7}Li(^{9}Li, ^{4}He^{6}He)^{6}He (left, center) and ^{7}Li(^{9}Li, ^{4}He^{6}He)^{6}He* (right) reactions, respectively. The ^{4}He+^{6}He pair was detected in the dT=0 combination, while undetected ^{6}He is either in the ground (left, center) or 1.8 MeV (2^+) excited state (right). Excitation energy of the ^{10}Be is calculated using the reconstructed $\Delta\phi_{12}^{\text{reco.}}$ (left, right) or the nominal $\Delta\phi = 0°$ (center) value.

and two states are observed as one peak at ~ 9.9 MeV. If the dependence of the excitation energy on the $\Delta\phi_{12}^{\text{reco.}}$ is considered, the state at 10.2 MeV is well separated and contributes more to the final spectrum above $\sim 30°$, as the opening angle between the decay products is slightly increased in that region.

Ex [MeV]	9.6	10.2	11.8	[9.0]*	[9.9]*	[11.7]	background
σ [MeV]	0.4	0.4	0.6	[0.6]	[0.6]	[0.4]	expo

Table 4.7: Results of the fit for the ^{10}Be$_{12}$ excited states from the ^{7}Li(^{9}Li, ^{4}He^{6}He)$_{\text{dT}=0}$^{6}He and ^{7}Li(^{9}Li, ^{4}He^{6}He)$_{\text{dT}=0}$^{6}He* ([] brackets) reactions, presented on Fig. 4.15. See the text for * explanation.
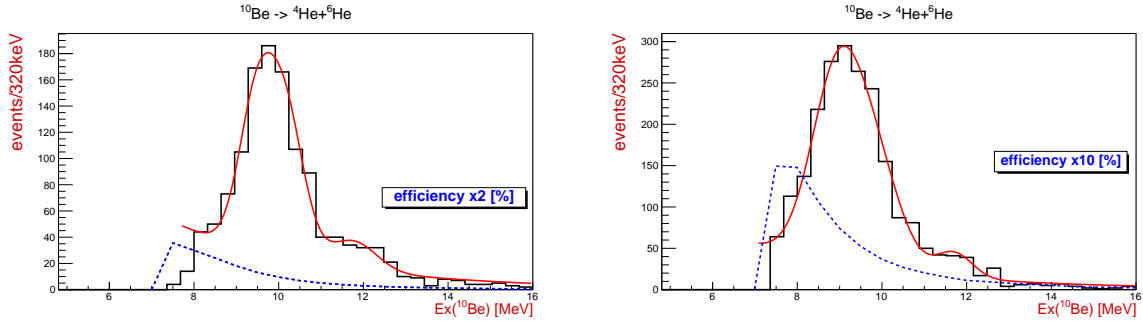
Figure 4.15: Excitation energy spectra of $^{10}\text{Be}_{12}$ from the $^{7}\text{Li}(^{9}\text{Li}, ^{4}\text{He}^{6}\text{He})_{\text{dT}=0}{}^{6}\text{He}$ and $^{7}\text{Li}(^{9}\text{Li}, ^{4}\text{He}^{6}\text{He})_{\text{dT}=0}{}^{6}\text{He}^{*}$ reactions respectively. The results of the fit for both cases are listed in Table 4.7.

$^{19}\text{F}(^{9}\text{Li}, ^{4}\text{He}^{6}\text{He})^{18}\text{O}$ reaction

Due to different kinematics of the three-body reactions on the ^{19}F from the ^{7}Li target, affecting the data selection for the heavier recoil ^{18}O, satisfactory exit channel identification was achieved in previously omitted dT=1 and dT=2 cases. Although separation between the ground and the excited states of the undetected ^{18}O was not completely achieved, due to the effects of $\Delta\phi_{12}^{\text{nom.}}$ uncertainty, these reactions are well separated from the reactions on the ^{7}Li target, as seen in the data selection spectra on Fig. 4.18 for the dT=2 and Fig. 4.20 for the dT=1 cases. For the dT=3 and dT=0 cases, exit channel identification was clear and unambiguous as seen previously in Figures 4.4 and 4.13, respectively. Results are presented starting from dT=3 up to dT=0 case.
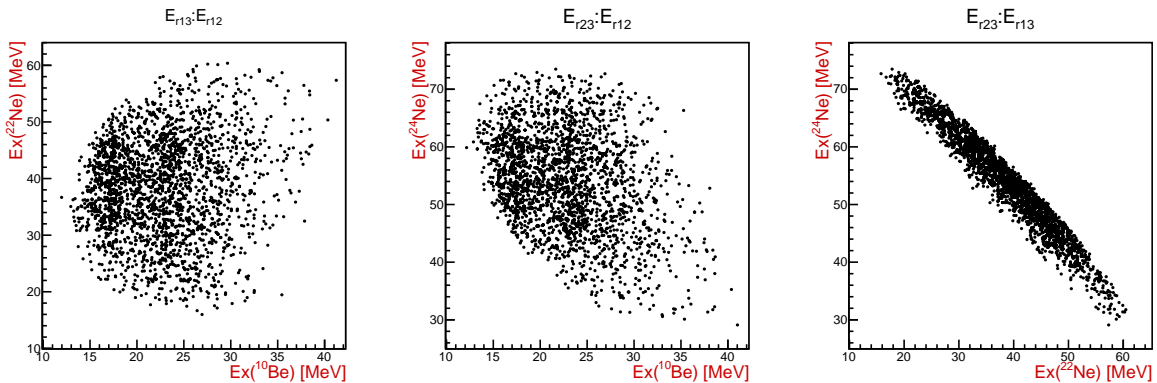

Figure 4.16: Excitation energy spectra for the $^{10}\text{Be}_{12}$, $^{22}\text{Ne}_{13}$ and $^{24}\text{Ne}_{23}$, from the $^{19}\text{F}(^{9}\text{Li}, ^{4}\text{He}^{6}\text{He})_{\text{dT}=3}{}^{18}\text{O}$ reaction.

Obtained results for the $^{4}\text{He}+^{6}\text{He}$ decays of the ^{10}Be excited states, for the dT=3 (Table 4.8) and dT=2 (Tables 4.9 and 4.10) cases, from the reaction on the ^{19}F target, should be directly compared to the results on the ^{7}Li target in the dT=3 case (Table 4.3 and 4.5), as they cover the same range of excitations in the ^{10}Be nuclei. On the other hand results
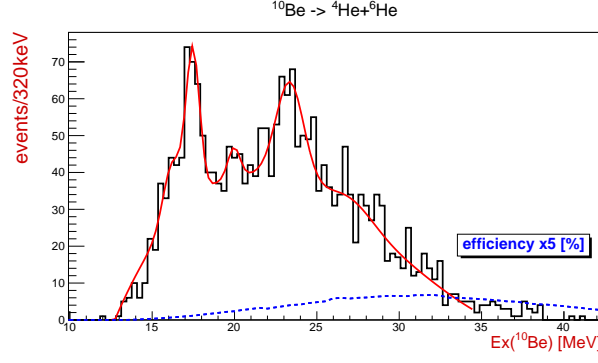
Figure 4.17: Excitation energy spectrum for the ^{10}Be$_{12}$ from the ^{19}F(^{9}Li, ^{4}He^{6}He)$_{dT=3}$^{18}O reaction. The results of the fit are listed in Table 4.8.

Ex [MeV]	16.2	17.5	20.0	23.4	background
σ [MeV]	0.5	0.4	0.4	0.8	pol3+gaus(27.1)

Table 4.8: Results of the fit for the ^{10}Be$_{12}$ excited states from the ^{19}F(^{9}Li, ^{4}He^{6}He)$_{dT=3}$^{18}O reaction, presented on Fig. 4.17.
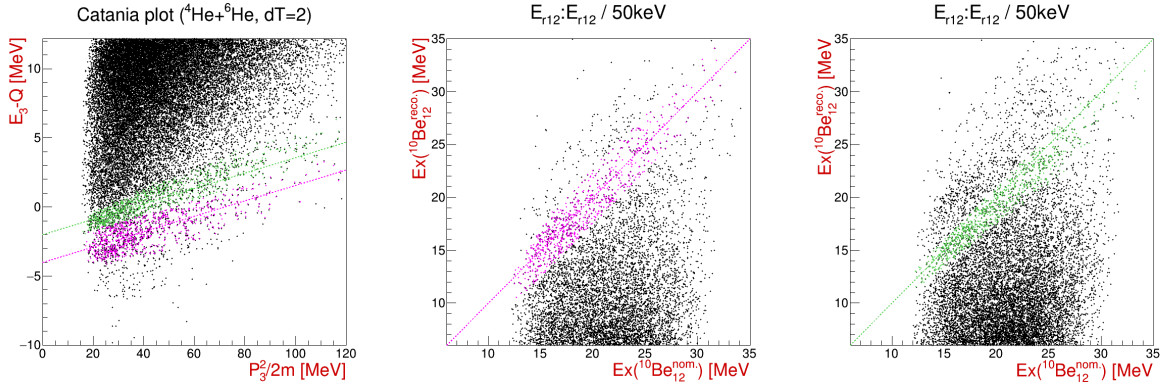

Figure 4.18: Catania plot for the ^{4}He+^{6}He coincident events in the dT=2 combination, with identified exit channels of reactions on the ^{19}F target. Color coding as in Table 4.2: undetected ^{18}O$_{g.s.}$ recoil is shown in pink, while ^{18}O$_{1.98}$ is shown in green. To confirm the data selection, the ^{10}Be excitation energy comparison spectra are shown, where ^{10}Be$_{12}^{nom.}$ is calculated using $\Delta\phi_{12}^{nom.} = 120°$ value, while ^{10}Be$_{12}^{reco.}$ is calculated using $\Delta\phi_{12}^{reco.}$ value (Eq. 3.22).

Ex [MeV]	(15.0)	16.7	18.3	19.8	background
σ [MeV]	(0.6)	0.7	0.5	0.4	pol3+gaus(12.0)+gaus(25.1)

Table 4.9: Results of the fit for the ^{10}Be$_{12}$ excited states from the ^{19}F(^{9}Li, ^{4}He^{6}He)$_{dT=2}$^{18}O reaction, presented on the left side of Fig. 4.19.

for the dT=1 and dT=0 cases, from the reactions on the ^{19}F target are supplementary to the "1-3" combination of particles for the dT=3 (Table 4.4) case and "1-2" combination for the dT=0 case (Table 4.7) from the reaction on the ^{7}Li target. Detailed overview of
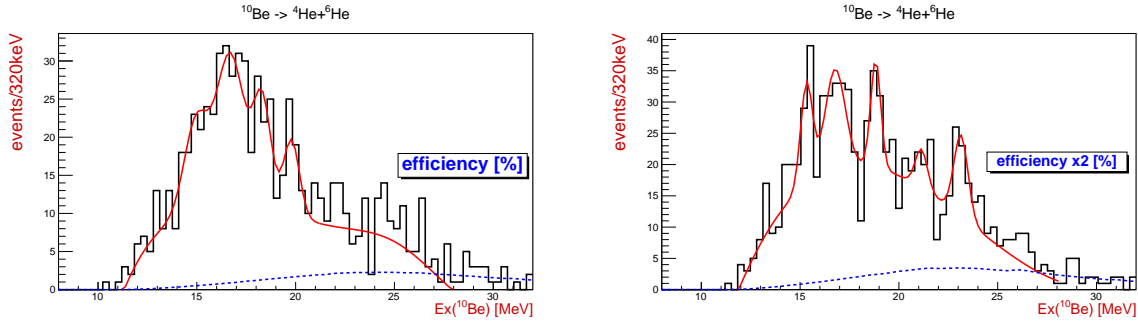
Figure 4.19: Excitation energy spectra for $^{10}\text{Be}_{12}$ from the $^{19}\text{F}(^9\text{Li}, \, ^4\text{He}^6\text{He})_{\text{dT}=2}{}^{18}\text{O}$ and $^{19}\text{F}(^9\text{Li}, \, ^4\text{He}^6\text{He})_{\text{dT}=2}{}^{18}\text{O}^*$ reactions, respectively. The results of the fit are listed in Table 4.9 for the ^{18}O recoil in the ground state and Table 4.10 for ^{18}O in the 1.98 MeV (2^+) excited state, respectively.

Ex [MeV]	15.3	16.8	18.8	21.1	23.1	background
σ [MeV]	0.3	0.5	0.3	0.3	0.4	pol3

Table 4.10: Results of the fit for the $^{10}\text{Be}_{12}$ excited states from the $^{19}\text{F}(^9\text{Li}, \, ^4\text{He}^6\text{He})_{\text{dT}=2}{}^{18}\text{O}^*{}_{1.98}$ reaction, presented on the right side of Fig. 4.19.

the obtained results for two targets will be given in Discussion 5.1, while the summary Table 4.16 can be found at the end of this subsection, with all of the observed states listed clearly for the comparison.
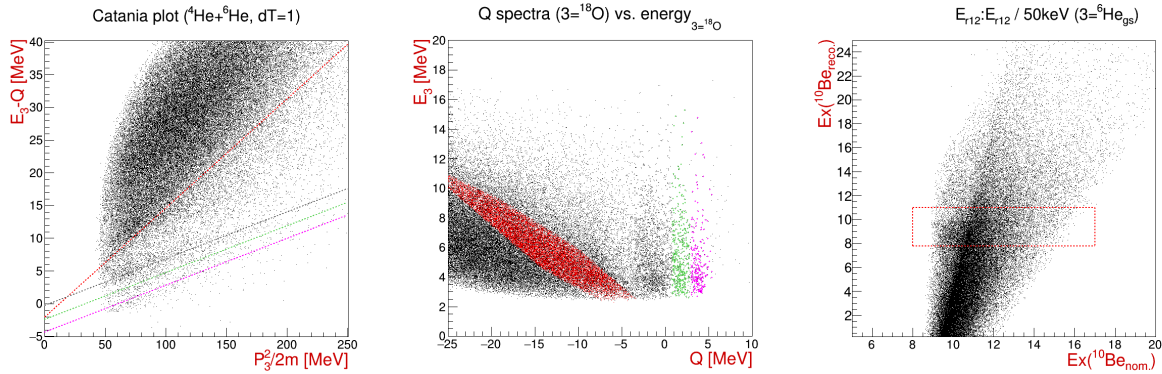

Figure 4.20: Catania plot and Q value spectrum for the $^4\text{He}+^6\text{He}$ coincident events in the dT=1 combination, with identified exit channels of the reactions on ^{19}F and ^7Li targets (rough selection for $^6\text{He}_{\text{g.s.}}$ data). The same color coding as listed in Table 4.2, with addition of unresolved mix of the higher excitation energy states centered around ~ 3.7 MeV (3.55 4+, 3.63 0+ and 3.92 2+) of the ^{18}O shown in gray. On the right side of the figure, ^{10}Be excitation energy comparison spectrum is shown for the reaction on the ^7Li target, with $^6\text{He}_{\text{g.s.}}$ (in the red dotted box) assumed as the undetected particle.

For the dT=1 case, data selected in Fig. 4.20 for the unresolved mix of the higher excitation energy states centered around ~ 3.7 MeV of the ^{18}O were not used, as the achieved resolution in the excitation energy was not satisfactory. The ^{10}Be excitation energy comparison spectrum, shown on the right side of Fig. 4.20, for the assumed

reaction on the ^{7}Li target, with ^{6}He ground state contributions marked inside the red dotted box, shows the effect of the $\Delta\phi_{12}$ uncertainty on the separation of the states. Although a locus is present around the area of expected ^{10}Be excitations at 9.6 MeV and 10.2 MeV, it is hard to tell weather this data is coming from the ^{6}He recoil in the ground or excited state, which affects the reconstruction of the $\Delta\phi_{12}$ used to calculate the excitation energy. Still, the visual confirmation of the presence of this states in the spectrum serves as a valid consistency test for the dT=1 data.
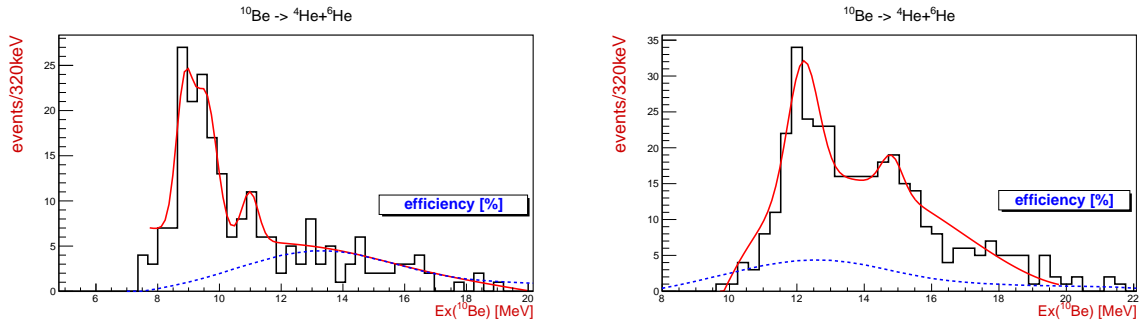

Figure 4.21: Excitation energy spectra for the ^{10}Be$_{12}$, from the ^{19}F(^{9}Li, ^{4}He^{6}He)$_{dT=1}$^{18}O and ^{19}F(^{9}Li, ^{4}He^{6}He)$_{dT=1}$^{18}O*$_{1.98}$ reactions, respectively. The results of the fit are listed in Table 4.11 for both cases. See the text for discussion on the observed offsets.

Ex [MeV]	8.9*	9.5*	11.0*	[12.2]*	[14.8]*	background
σ [MeV]	0.3	0.4	0.3	[0.5]	[0.3]	pol1+gaus(13.5)/[pol3]

Table 4.11: Results of the fit for the ^{10}Be$_{12}$ excited states from the ^{19}F(^{9}Li, ^{4}He^{6}He)$_{dT=1}$^{18}O and ^{19}F(^{9}Li, ^{4}He^{6}He)$_{dT=1}$^{18}O*$_{1.98}$ ([] brackets) reactions, presented on Fig. 4.21. See the text for discussion on the observed offsets (*).

Note that the ^{18}O$_{g.s.}$ and ^{18}O$_{1.98}$ data for the dT=1 case, presented in Table 4.11, have an offset of $\sim$ -750 keV and $\sim$ +400 keV respectively, from the expected states in the ^{10}Be nucleus if the known state at 11.8 MeV is taken as a reference. Results for the latter, the ^{18}O$_{1.98}$ data, should also be taken with a caution, as subtracting $\sim$ 2 MeV of the ^{18}O excitation energy would reproduce the results from Table 4.11, the known states at 10.2 and 11.8 MeV, indicating that these data could be just the ^{18}O ground state data, systematically shifted by the excitation energy of the undetected nuclei. Due to the large uncertainty in the dT=1 case, additional tests did not provide a clear answer.

The results for the dT=0 case are not presented here, due to low resolution of the obtained peaks, but similarly to the results from the reactions on the ^{7}Li target (Fig. 4.15), an

indications for the peaks at 9.6, 10.2 and 11.8 MeV are observed in all three cases, where undetected ^{18}O recoil was in the ground, 1.98 MeV and ~ 3.7 MeV excited states.

^{6}Li(^{9}Li, ^{4}He^{6}He)^{5}He reaction

The last part of the case study of the coincidences of the ^{4}He+^{6}He pairs is the reaction on the ^{6}Li target, present in the LiF target as a part of the natural lithium ($\sim 7.5\%$). Due to the small concentration of the ^{6}Li as a target element, only the dT=3 case had sufficient statistics and resolution to be included in the final results, serving as an important complementary spectra for the results on the ^{7}Li and ^{19}F targets.
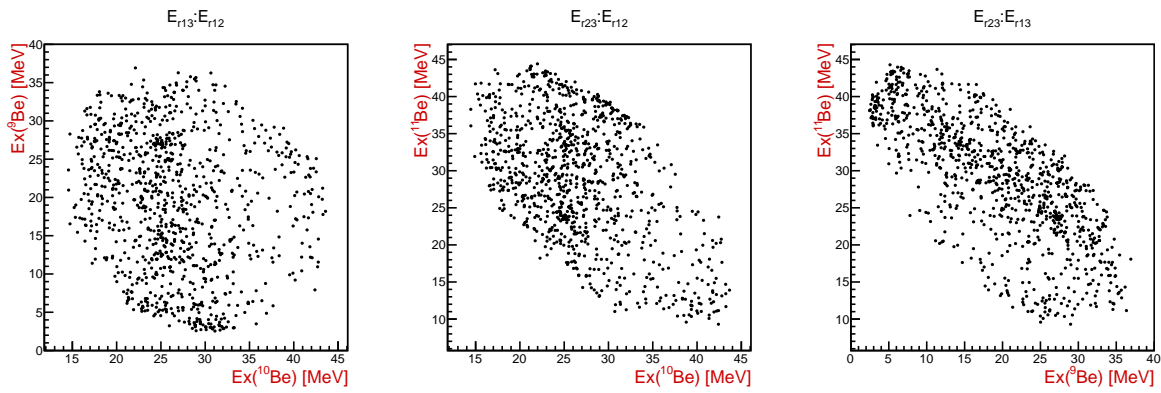
Figure 4.22: Excitation energy spectra for the ^{10}Be$_{12}$, ^{9}Be$_{13}$ and ^{11}Be$_{23}$, from the ^{6}Li(^{9}Li, ^{4}He^{6}He)$_{dT=3}$^{5}He reaction.
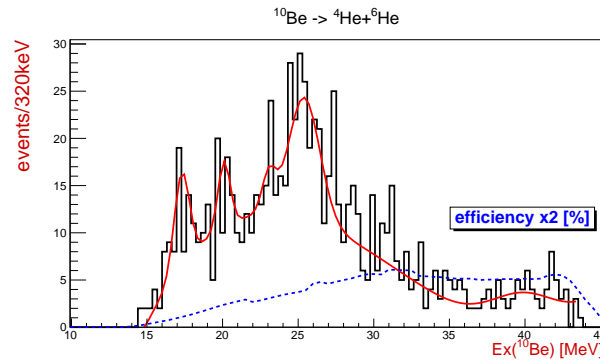
Figure 4.23: Excitation energy spectrum for the ^{10}Be$_{12}$, from the ^{7}Li(^{9}Li, ^{4}He^{6}He)$_{dT=3}$^{5}He reaction. The results of the fit are listed in Table 4.12.

Taking the systematical uncertainty of ~ 500 keV into consideration, the peaks observed in Table 4.12 correspond very well to the peaks previously observed for the reactions on the ^{7}Li target. The peak observed at 25.4 MeV, although has been observed as a part of the background in the ^{7}Li(^{9}Li, ^{4}He^{6}He)$_{dT=3}$^{6}He reaction, is unlikely to be a real state in the presented spectrum. Close inspection of the detection efficiency curve in Fig. 4.23

reveals a sudden change, which may cause the rise of statistics in that region and the appearance of a false peak. Weak contributions from the excited states of ^{9}Be and ^{11}Be nuclei were excluded from the projection of the ^{10}Be excited states, as in all other cases.

Ex [MeV]	17.3	20.1	(23.1)	25.4*	background
σ [MeV]	0.5	0.4	0.5	1.0	pol3+gaus(39.9)

Table 4.12: Results of the fit for the ^{10}Be$_{12}$ excited states from the ^{7}Li(^{9}Li, ^{4}He^{6}He)$_{\mathrm{dT}=3}$^{5}He reaction, presented in Fig. 4.23. See the text for discussion on *.

^{7}Li(^{9}Li, ^{6}He^{6}He)^{4}He reaction

The ^{6}He+^{6}He coincidences present a cleaner data set compared to the ^{4}He+^{6}He coincidences. Due to the large Q value difference between the reaction on the ^{7}Li target from the reactions on the ^{19}F and ^{6}Li targets, as shown in Table 4.13, exit channels are easily separated and identified in the analysis. As the ^{4}He is one of the most stable nuclei on the nuclear chart, having the first excited state at 20.21 MeV, and ^{6}He has no bound excited states, there is only contribution of the ground states for the reaction on the ^{7}Li target. This altogether enables broad data selection conditions, especially important for the dT=1 and dT=2 cases, where the influence of the uncertainty in the $\Delta\phi_{12}^{\mathrm{nom.}}$ is the largest. Since the ^{10}Be excited states are accessed through both "1-3" and "2-3" combination of particles in the ^{6}He+^{6}He coincidences, only the dT=3 and dT=2 data will have a significant contribution and the detection efficiency to observe the ^{10}Be helium cluster decays. The dT=1 and dT=0 data will contribute only to the study of the ^{12}Be excited states, near the particle decay thresholds, and will be presented in Section 4.2.1.

reaction	^{7}Li(^{9}Li, ^{6}He^{6}He)^{4}He	^{19}F(^{9}Li, ^{6}He^{6}He)^{16}O	^{6}Li(^{9}Li, ^{6}He^{6}He)^{3}He
Q [MeV]	2.24	-6.99	-11.09
color	red	blue	gray

Table 4.13: The Q values and color coding used for the three-body reaction channels from the ^{6}He+^{6}He coincident events in all telescope combinations.

Due to the large uncertainty in the nominal $\Delta\phi_{12}^{\mathrm{nom.}} = 120°$ value for the dT=2 case, contributions from the reaction on the ^{19}F target cannot be fully separated from the reaction on the ^{7}Li target. For this reason, all of the data shown with red markers on Fig.
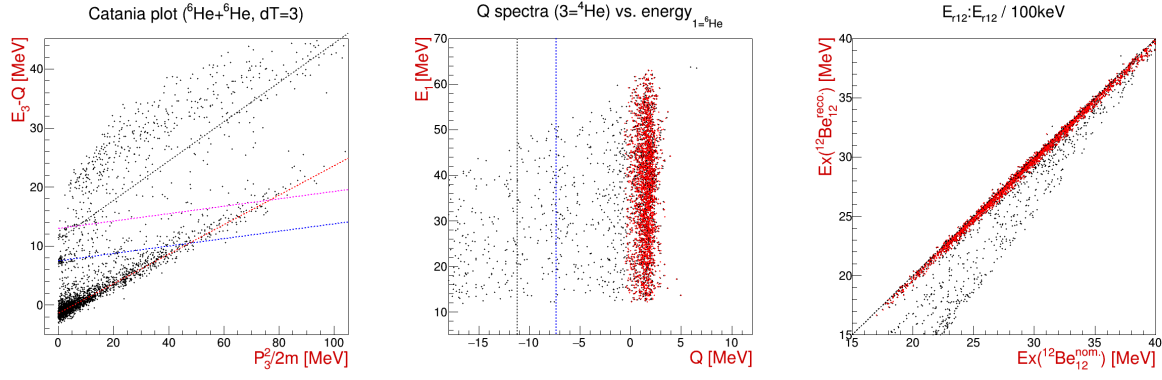
Figure 4.24: Catania plot and Q value spectrum for coincident detection of the ^{6}He+^{6}He pairs in the dT=3 combination, with identified exit channel from the reactions on ^{7}Li shown with red markers, where ^{4}He is undetected particle, as listed in Table 4.13. Not contributing to the results, but having a slight contribution to the data is the excited state of undetected ^{16}O, from the reaction on the ^{19}F target, labeled with the pink dashed line, while the ground state of ^{16}O is labeled with blue. Data locus from the reaction on the ^{6}Li target is labeled in gray. On the right side of the figure, ^{12}Be excitation energy comparison spectrum is shown, calculated using $\Delta\phi_{12}^{reco.}$ and $\Delta\phi_{12}^{nom.} = 180°$ values, as evidence of the clean data selection, seen as the alignment of the data locus along the diagonal line.
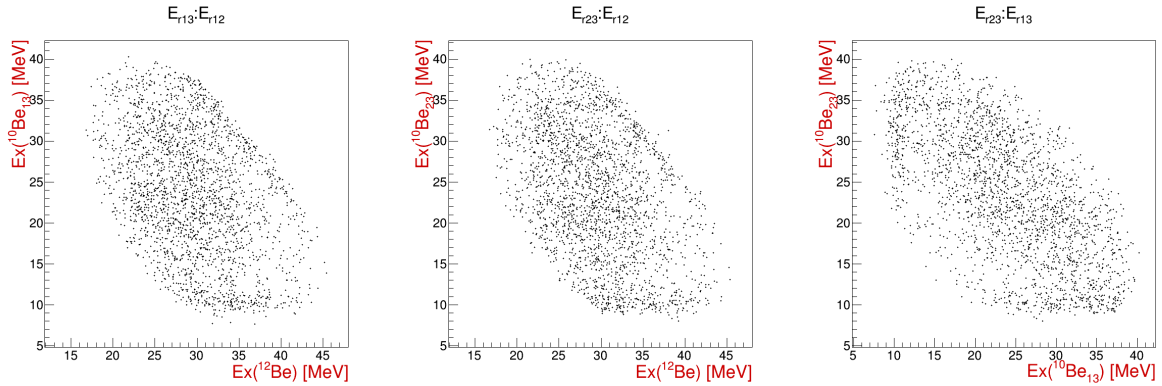
Figure 4.25: Excitation energy spectra for the ^{12}Be$_{12}$, ^{10}Be$_{13}$ and ^{10}Be$_{23}$, from the ^{7}Li(^{9}Li, ^{6}He^{6}He)$_{dT=3}$^{4}He reaction.

4.26 was treated as coming from the reaction on the ^{7}Li target, and the events coming from the reaction on the ^{19}F target were treated as the background and are expected to contribute no more than $\sim$ 15-20 % to the excitation energy spectrum of ^{10}Be. This selection was based on the reference dT=3 case, which has better separation of the reaction exit channels in the data selection spectra, shown on Fig. 4.24, where the dominance of the events on the ^{7}Li target can be seen.

For the final results it was chosen to present the sum of one-dimensional projections for the "1-3" and "2-3" combinations, together with the fit and the detection efficiency calculation, after the relevant cut was made on "1-2" (^{12}Be) excited states. As the detected pair of particles are identical in mass, the "1-3" and "2-3" combinations (^{10}Be states) are occupying
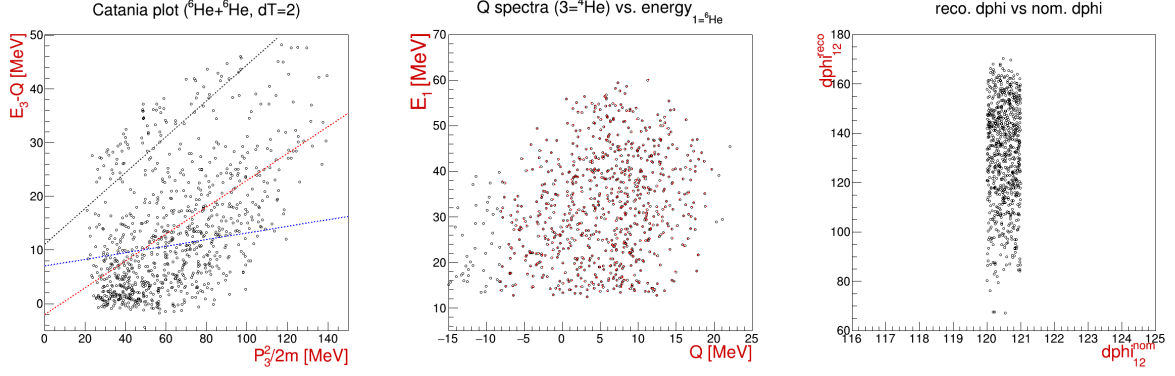
Figure 4.26: Catania plot and Q value spectrum for coincident detection of the ^{6}He+^{6}He pair in dT=2 combination, with exit channels identified and labeled as listed in Table 4.13. Data for the reaction on the ^{7}Li target is shown with red markers. On the right side of the figure, calculated $\Delta\phi_{12}^{\mathrm{reco.}}$ (Eq. 3.22) is plotted against the nominal $\Delta\phi_{12}^{\mathrm{nom.}} = 120°$ value. Although $\Delta\phi_{12}^{\mathrm{reco.}}$ is showing a wide spread in relative azimuthal angle between detected particles, it's inside the physical limitations of detectors, indication a good selection of the data.

the same kinematic phase space. Since it's totally arbitrary which of the detected ^{6}He is "1" and which is "2", summing both projections enhances the statistics at the potential expense of broadening of the peaks, which was found to be marginal compared to the gain in the statistics.
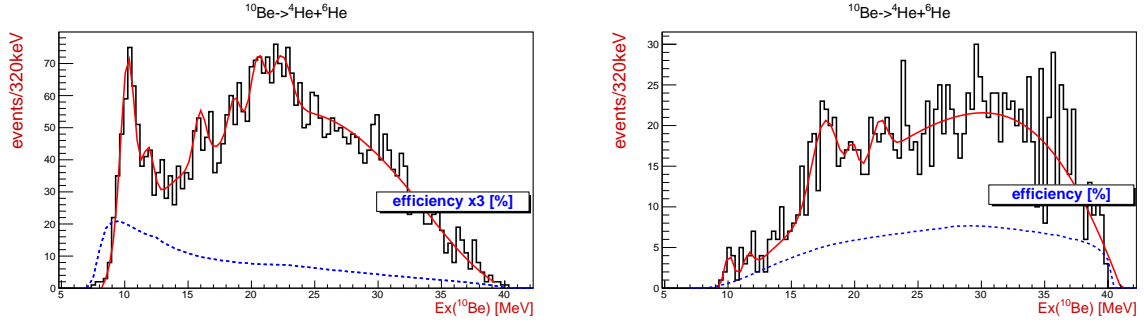

Figure 4.27: Excitation energy spectra for the ^{10}Be$_{13}$ and ^{10}Be$_{23}$ sum, from the ^{7}Li(^{9}Li, ^{6}He^{6}He)^{4}He reaction. The ^{6}He+^{6}He pair was detected in either dT=3 (left) or dT=2 (right) combination. The results of the fit are listed in Table 4.14 for the dT=3 and Table 4.15 for the dT=2 case.

Ex [MeV]	10.2	11.8	16.0	18.6	20.5	22.3	background
σ [MeV]	0.6	0.4	0.5	0.5	0.5	0.8	pol6 + gaus(33.3)

Table 4.14: Results of the fit for the ^{10}Be$_{13+23}$ excited states from the ^{7}Li(^{9}Li, ^{6}He^{6}He)$_{\mathrm{dT=3}}^4$He reaction, presented on the left side of Fig. 4.27.

Due to the clean selection of the data for the dT=3 case and the gain in statistics obtained by summing both projections for the ^{10}Be excited states, this result serves as a reference for

Ex [MeV]	(10.0)	(11.6)	17.6*	(19.8)	22.0	background
σ [MeV]	0.4	0.4	1.0	0.4	0.6	pol4 + gaus(36.3)

Table 4.15: Results of the fit for the $^{10}\text{Be}_{13+23}$ excited states from the $^7\text{Li}(^9\text{Li},\,^6\text{He}^6\text{He})_{\text{dT}=2}{}^4\text{He}$ reaction, presented on the right side of Fig. 4.27. See text for * explaination.

the observation of the $^4\text{He}+^6\text{He}$ cluster decays in the whole excitation energy range. If one compares the tables for dT=2 and dT=3 combinations, the same peaks can be observed within large systematic experimental uncertainty. Thus, it is likely that observed peak at $\sim$ 17.6 MeV in dT=2 case (Table 4.15) corresponds to the sum of the 16.0+18.6 MeV peaks, observed in dT=3 case (Table 4.14). This is also indicated by the large width of the peak.

Summary table of the observed states: $^{10}\text{Be}\rightarrow{}^4\text{He}+^6\text{He}$

$^4\text{He} + {}^6\text{He} \downarrow$ || Ex (^{10}Be)[MeV] $\rightarrow$	9.6	10.2	11.8	16.5	18.5	20.5	22.3
$^7\text{Li}(^9\text{Li},\,^4\text{He}^6\text{He}^6\text{He})$ (12+13)	●	●	●	○			
$^7\text{Li}(^9\text{Li},\,^4\text{He}^6\text{He})_{\text{dT}=3}{}^6\text{He}$ (12)				○	●	●	●
$^7\text{Li}(^9\text{Li},\,^4\text{He}^6\text{He})_{\text{dT}=3}{}^6\text{He}^*$ (12)				○	●	●	○
$^7\text{Li}(^9\text{Li},\,^4\text{He}^6\text{He})_{\text{dT}=0}{}^6\text{He}$ (12)	●	○	●				
$^7\text{Li}(^9\text{Li},\,^4\text{He}^6\text{He})_{\text{dT}=0}{}^6\text{He}^*$ (12)	●	○	●				
$^7\text{Li}(^9\text{Li},\,^4\text{He}^6\text{He})_{\text{dT}=3}{}^6\text{He}$ (13)	○	●	●	●	○	○	○
$^7\text{Li}(^9\text{Li},\,^6\text{He}^6\text{He})_{\text{dT}=3}{}^4\text{He}$ (13+23)	×	●	●	●	○	●	○
$^7\text{Li}(^9\text{Li},\,^6\text{He}^6\text{He})_{\text{dT}=2}{}^4\text{He}$ (13+23)	×	●	●	○	●	●	○
$^6\text{Li}(^9\text{Li},\,^4\text{He}^6\text{He})_{\text{dT}=3}{}^5\text{He}$ (12)					○	○	○
$^{19}\text{F}(^9\text{Li},\,^4\text{He}^6\text{He})_{\text{dT}=3}{}^{18}\text{O}$ (12)				○	●	●	●
$^{19}\text{F}(^9\text{Li},\,^4\text{He}^6\text{He})_{\text{dT}=2}{}^{18}\text{O}$ (12)				●	○	○	×
$^{19}\text{F}(^9\text{Li},\,^4\text{He}^6\text{He})_{\text{dT}=2}{}^{18}\text{O}^*$ (12)				●	●	●	●
$^{19}\text{F}(^9\text{Li},\,^4\text{He}^6\text{He})_{\text{dT}=1,0}{}^{18}\text{O}^{\text{gs},*}$ (12)	○	○	○				

Table 4.16: Results for the $^4\text{He}+^6\text{He}$ decay of the $^{10}\textbf{Be}$ **excited states** from the observed reactions on the **LiF target**. Clear peaks with good statistics are shown with ● symbol, while peaks with lower statistics and/or background interference are shown with ○ symbol. Low quality peaks observed in other datasets, but not seen clearly and/or are at the edge of the phase space are shown with × symbol.

^{4}He + ^{6}He* ↓ ‖ Ex (^{10}Be)[MeV] →	9.6	10.2	11.8	(16.0)	(21.2)
^{7}Li(^{9}Li, ^{4}He^{6}He)$_{dT=3}$^{6}He* (13) ‖	○	●	●	○	○

Table 4.17: Results for the ^{4}He+^{6}He* decay of the ^{10}**Be excited states** from the observed reaction on the ^{7}**Li target**. Clear peaks with good statistics are shown with ● symbol, while peaks with lower statistics and/or background interference are shown with ○ symbol. Low quality peaks observed in other datasets, but not seen clearly and/or are at the edge of the phase space are shown with × symbol.

4.1.2 ^{9}Be+n decay channel

To round up comprehensive study of the ^{10}Be excited states neutron decays are considered here, as the ^{9}Be+n decay is closely related to the single-particle structure of the excited states. The two-neutron decays are presented in Section 4.1.3.

^{7}Li(^{9}Li, ^{9}Be^{6}He)n reaction

Since the LAMP setup, comprised of silicon detectors, is only intended for the detection of charged particles, to observe the neutron decays one has to study the ^{9}Be+^{6}He coincidences from the reaction on the ^{7}Li target, where neutron is undetected reaction product and the ^{10}Be excited states are accessed through the "1-3" combination of the particles in the exit channel. In the data selection spectra, shown on Fig. 4.28, one can see clean and unambiguous selection of the events from the reaction on the ^{7}Li target in dT=3 telescope combination, where resolution and statistics are the best. The Q value for the ^{7}Li(^{9}Li, ^{9}Be^{6}He)n reaction is 2.85 MeV.
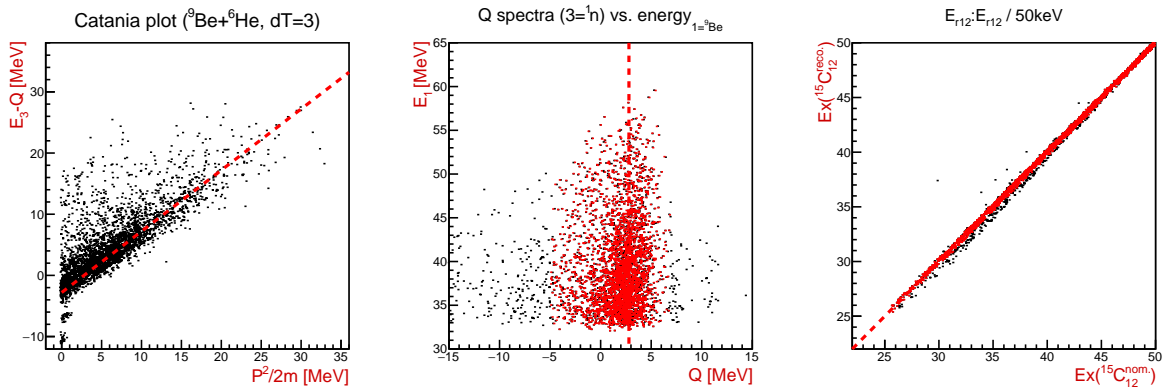

Figure 4.28: Data selection spectra for the ^{9}Be+^{6}He coincident events in dT=3 combination. Identified and selected events from the reaction on the ^{7}Li target are shown with red markers. On the right side of the figure, the ^{15}C excitation energy comparison spectrum is shown, indicating a clean selection of the reaction exit channel.
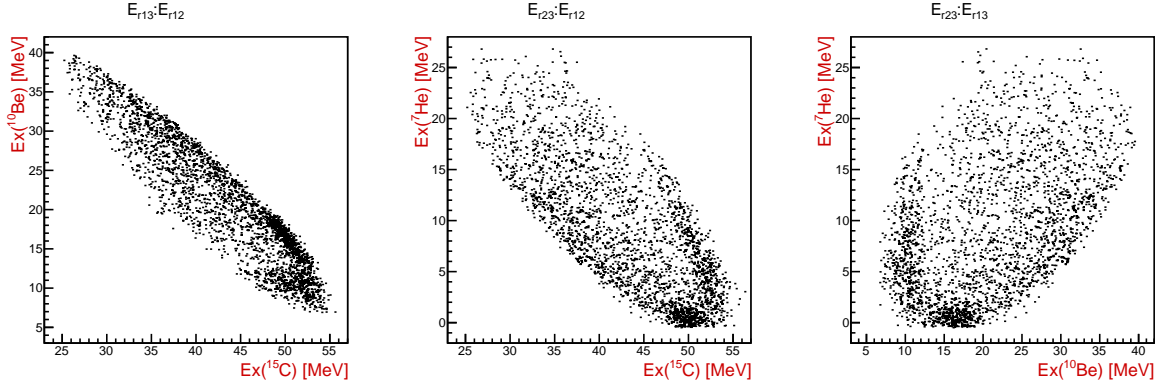
Figure 4.29: Excitation energy spectra for the $^{15}C_{12}$, $^{10}Be_{13}$ and $^{7}He_{23}$, from the $^{7}Li(^{9}Li,$ $^{9}Be^{6}He)_{dT=3}n$ reaction.

Unlike all the other cases, where linear cuts in the relative energy spectra were used, to exclude relevant contributions from the excited states of the other nuclei in the spectra, this time a graphical cut was used to exclude the ground state of the ^{7}He nucleus. Since this state was constrained in a small phase space on the spectra (see Fig. 4.29), graphical cut was used to preserve as much statistics as possible for the neutron decays of the ^{10}Be excited states.
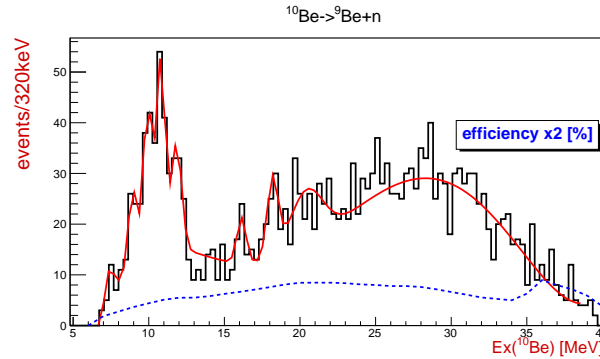
Figure 4.30: Excitation energy spectrum for the ^{10}Be decay to the $^{9}Be+n$, from the $^{7}Li(^{9}Li,$ $^{9}Be^{6}He)_{dT=3}n$ reaction. The results of the fit are listed in Table 4.18.

Ex [MeV]	7.4	8.9*	9.9*	10.8*	11.8	16.1	18.2	20.4*	background
σ [MeV]	0.3	0.3	0.3	0.3	0.3	0.3	0.4	1.1	pol5

Table 4.18: Results of the fit for the ^{10}Be excited states from the $^{7}Li(^{9}Li, {}^{9}Be^{6}He)_{dT=3}n$ reaction, presented in Fig. 4.30. See the text for discussion on *.

The states in Table 4.18 have a systematic uncertainty of ~ 320 keV in the spectrum, thus the observed peaks at 7.4, 8.9 and 10.8 MeV are most likely corresponding to the tabulated states at 7.4, 9.3 and 10.6 MeV which exclusively or dominantly undergo neutron decay

compared to the α decay. The observed peak at 9.9 MeV likely corresponds to the 9.6 MeV state, which also decays through neutron. The peak at 20.4 MeV, due to large uncertainty is likely to be a part of the background. For the consistency check, it is important to notice that the 10.2 MeV state, considered to have α-2n-α molecular structure, is as expected not observed here. The observed states are discussed in the context of the helium cluster decays in Discussion 5.1 and they are summarized along with the ^{8}Be+nn decay channel in summary Table 4.20.

4.1.3 ^{8}Be+nn decay channel

The ^{8}Be+nn decay includes sequential decay through ^{9}Be excited states, but also a possible direct 2n decay. In both cases, in molecular picture, it represents decay of 2π neutron states, as the structure with the σ neutrons can not decay to the ^{8}Be ground state.

^{7}Li(^{9}Li, ^{8}Be^{6}He)nn reaction

Since only indirect measurement of the neutron decay channels is possible with the LAMP setup, coincident detection of the ^{4}He+^{4}He+^{6}He pairs was studied. In the first step of this analysis a condition was made for two ^{4}He to be detected in the same detector (dT=0 case). For these events ^{8}Be ground state was reconstructed, as seen in Fig. 4.31, and the cut was made to treat these events in the next step of the analysis as a one particle (^{8}Be).
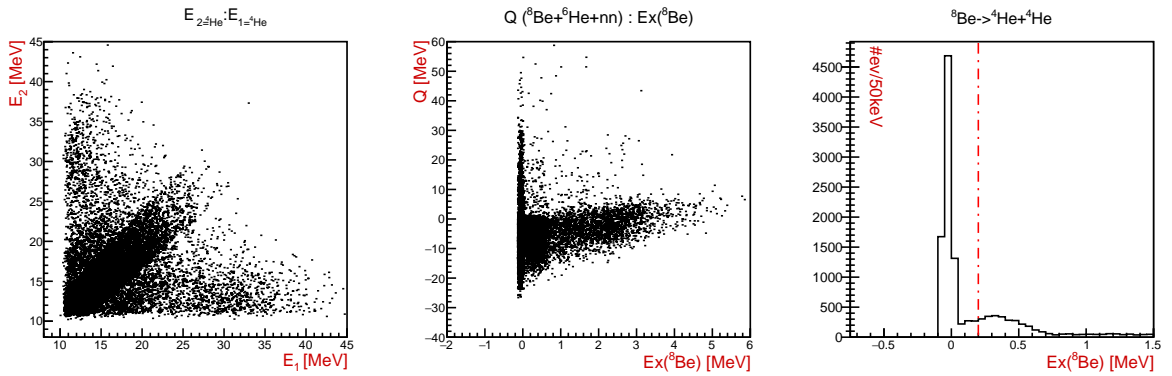
Figure 4.31: The ^{8}Be ground state reconstruction (center, right) for the ^{4}He+^{4}He pairs detected in the same telescope (dT=0 combinations), and the energy-energy spectrum of two detected α particles (left). Data are for the ^{4}He+^{4}He+^{6}He coincident events.

In the next step, condition that ^{8}Be and ^{6}He were detected on the opposite sides of the setup (dT=3 case) was made and, for the reaction on the ^{7}Li target, undetected two neutrons were treated as one particle in the data selection process, shown on Fig. 4.32.

Since for the full kinematic reconstruction of the four-body event one needs at least three out of four particles detected, this assumption was a workaround used to select the data for the exit channel on the ^{7}Li target as one would do in a three-body event.
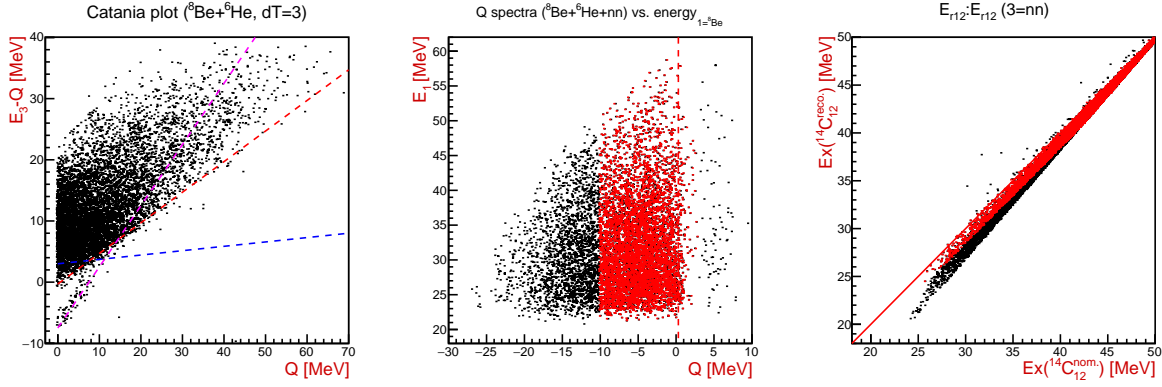
Figure 4.32: Data selection spectra for the ^{8}Be+^{6}He coincident events in dT=3 combination. Identified and selected events from the reaction on the ^{7}Li target are shown with red markers. In the kinematic calculations two neutrons were treated as one particle (see text for details).

The reaction on the ^{6}Li target, labeled in pink on Fig. 4.32, with neutron as undetected particle, show the quality of the data reconstruction, as the data locus fall exactly on the expected kinematic line in the Catania plot. No evidence of events belonging to the reaction on the ^{19}F target, labeled in blue on Fig. 4.32, was found.
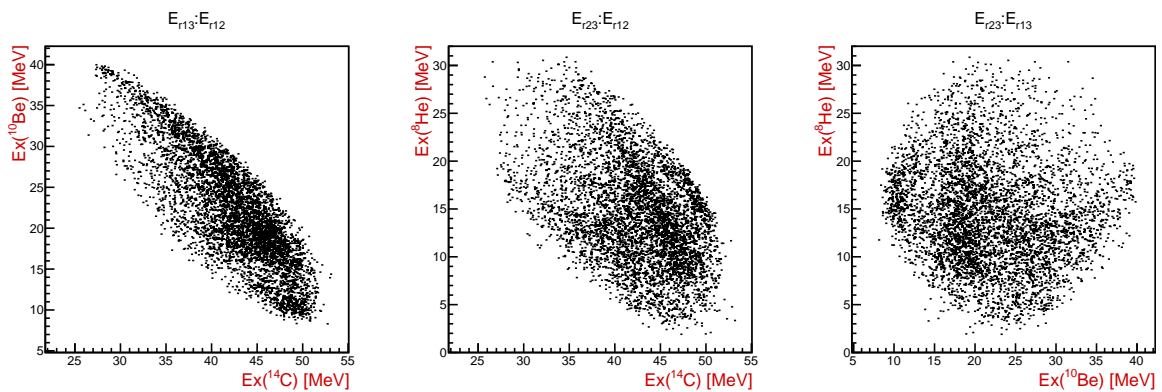
Figure 4.33: Excitation energy spectra for $^{14}C_{12}$, $^{10}Be_{13}$ and $^8He_{23}$, from the ^{7}Li(^{9}Li, ^{8}Be^{6}He)$_{dT=3}$nn reaction.

In following Chapter 5.1, peaks observed in Table 4.19 will be discussed and compared to the only available experimental measurement for this decay channel.
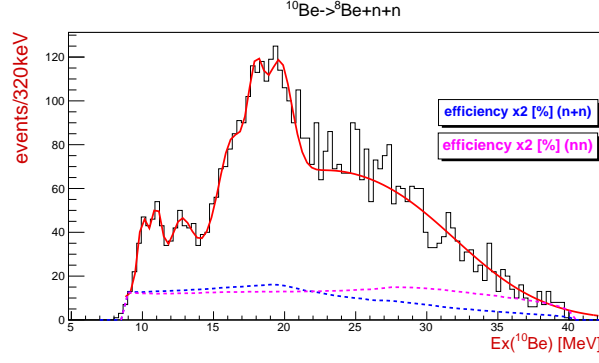
Figure 4.34: Excitation energy spectrum for the ^{10}Be decay to the ^{8}Be+nn from the ^{7}Li(^{9}Li, ^{8}Be^{6}He)$_{dT=3}$nn reaction. The results of the fit are listed in Table 4.19.

Ex [MeV]	10.6	12.7	16.3	18.0	19.6	background
σ [MeV]	0.7	0.7	0.9	0.6	0.9	gaus(16.0)+gaus(19.5)+gaus(26.5)

Table 4.19: Results of the fit for the ^{10}Be excited states from the ^{7}Li(^{9}Li, ^{8}Be^{6}He)$_{dT=3}$nn reaction, presented in Fig. 4.34.

Summary table of the observed states: ^{10}Be$\rightarrow$^{9}Be+n,^{8}Be+nn

^{9}Be + n $_\downarrow$ ‖ Ex (^{10}Be)[MeV] $\rightarrow$	(7.4)	(9.3)	9.6	10.6	11.8	(16.1)	(18.1)
^{7}Li(^{9}Li, ^{9}Be^{6}He)$_{dT=3}$n (13)	○	○	●	●	●	○	○
^{8}Be + nn $_\downarrow$ ‖ Ex (^{10}Be)[MeV] $\rightarrow$				10.6	12.7	(16.3)	(19.6)
^{7}Li(^{9}Li, ^{8}Be^{6}He)$_{dT=3}$nn (13)				●	●	○	○

Table 4.20: Results for the ^{9}Be+n and ^{8}Be+nn decays of the ^{10}**Be excited states** from the observed reactions on the ^{7}**Li target**. Clear peaks with good statistics are shown with ● symbol, while peaks with lower statistics and/or background interference are shown with ○ symbol.

4.2   Decays of the ^{12}Be excited states

4.2.1 ^{6}He+^{6}He decay channel

One way of observing the helium cluster decays of the ^{12}Be excited states to the ^{6}He+^{6}He and ^{6}He+^{6}He* (1.8 MeV, 2*) pairs is through the analysis of the ^{7}Li(^{9}Li, ^{4}He^{6}He)^{6}He and ^{7}Li(^{9}Li, ^{4}He^{6}He)^{6}He* reactions, where the ^{12}Be decays are observed as the "2-3" combination of the particles in the exit channel, where the particle "3" labels undetected reaction product. The other way of observing the ^{6}He+^{6}He decays, is through the analysis of the ^{6}He+^{6}He coincidences from the reaction on constituents of the LiF target. In this case, the ^{12}Be excited states are observed through "1-2" combination of particles.

In the study of the ^{12}Be excited states through ^{4}He+^{6}He coincidences, as already seen with "1-3" and "2-3" combinations for the ^{10}Be excited states from the ^{7}Li(^{9}Li, ^{6}He^{6}He)^{4}He reaction (Section 4.1.1), the only relevant cases, having sufficient statistics and efficiency, are the dT=3 and dT=2 cases. This is due to the kinematic phase space which particles "1-2" cover when detected with large relative $\Delta\phi$ angle, meaning one can either observe the decays of the highly excited states in the "1-2" combination, or the low lying excitations in the "1-3" or "2-3" combinations, where one detected particle is combined with the undetected one. A similar phase space to the latter is covered, when the "1-2" particle combination, the ^{6}He+^{6}He in this case, is detected in the dT=0 and dT=1 combinations.

Concerning the coincident detection of all particles in the exit channel, from the reaction on the ^{7}Li target, presented previously in Section 4.1.1, there is not enough statistics obtained to observe the ^{12}Be excited states. Only a few events centered around $\sim$ 13 MeV in excitation energy of the ^{12}Be can be seen in the relative energy spectra on Fig. 4.2.

^{7}Li(^{9}Li, ^{4}He^{6}He)^{6}He reaction

As previously mentioned, the ^{4}He+^{6}He coincidences contribute significantly to the decays of the ^{12}Be excited states only in the dT=3 and dT=2 cases. Due to the small difference in the Q values and large $\Delta\phi_{12}^{\mathrm{nom.}}$ uncertainty, separation of the undetected ^{6}He ground (0^{+})

and 1.8 MeV (2^+) excited state was not achieved for the dT=2 telescope combination, thus these results are not presented here. For the dT=3 case, data selection was shown in Figures 4.4 and 4.5, and the relative energies in Figures 4.7 and 4.9 for the ground and 1.8 MeV excited state, respectively. The contributions of the ^{10}Be excited states are excluded from the projections, i.e., the excitation energy of the ^{12}Be nucleus. The Q value for the reaction on the ^{7}Li target, with all reaction products in the ground state, is 2.24 MeV.
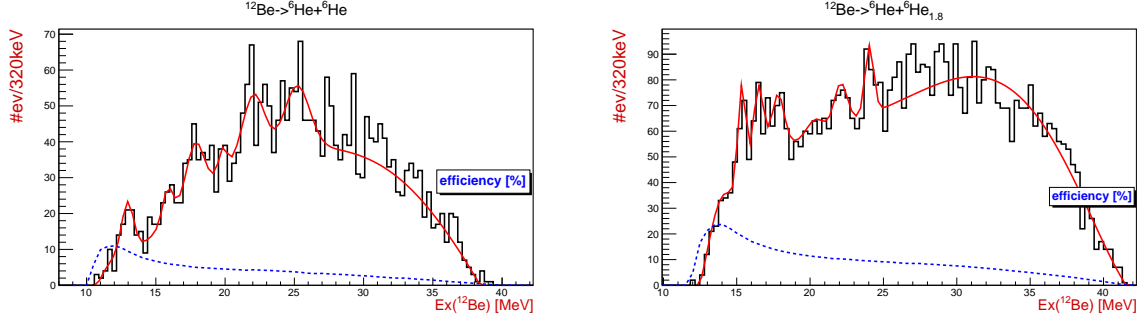
Figure 4.35: Excitation energy spectra for the ^{12}Be$_{23}$ and ^{12}Be$_{23*}$, from the data of the ^{7}Li(^{9}Li, ^{4}He^{6}He)^{6}He and ^{7}Li(^{9}Li, ^{4}He^{6}He)^{6}He* reactions respectively. The ^{4}He+^{6}He pair was detected in dT=3 combination, while undetected ^{6}He is either in the ground (0^+) state, shown on the left side of the figure, or 1.8 MeV (2^+) excited state, shown on the right side of the figure. Blue dashed lines represents the detection efficiency curve, while the red lines represent the results of the fit, with the states listed in Tables 4.21 and 4.22 respectively.

Ex [MeV]	12.9	15.9	17.9	19.8	22.2	25.3	background
norm [events]	12.3	9.0	16.2	8.0	18.0	17.4	
σ [MeV]	0.7	0.5	0.6	0.3	0.9	0.7	pol3

Table 4.21: Results of the fit for the ^{12}Be$_{23}$ excited states from the ^{7}Li(^{9}Li, ^{4}He^{6}He)$_{dT=3}$^{6}He$_{g.s.}$ reaction, presented on the left side of Fig. 4.35.

peak [MeV]	13.8	15.4	16.5	17.8	20.3	22.1	24.0	background
norm [events]	14.4	41.4	33.3	23.2	5.6	16.2	26.7	
σ [MeV]	0.7	0.3	0.4	0.4	0.5	0.4	0.3	pol6 + gaus (36.3)

Table 4.22: Results of the fit for the ^{12}Be$_{23*}$ excited states decaying to the ^{6}He*, from the ^{7}Li(^{9}Li, ^{4}He^{6}He)$_{dT=3}$^{6}He* reaction, presented on the right side of Fig. 4.35.

^{7}Li(^{9}Li, ^{6}He^{6}He)^{4}He reaction

Having already shown the data selection (Fig. 4.24 and 4.26), and the relative energy spectra (Fig. 4.25), for all particle combinations in the exit channel for the dT=3 and

dT=2 cases in Section 4.1.1, only the one-dimensional excitation energy spectra are shown here (Fig. 4.36). These include also the detection efficiency calculation and the fit to the data. As with all projections, these were made after applying the cuts on the relevant excitation energy range in the ^{10}Be nuclei, to exclude the contributions of the dominating excited states. For the dT=1 and dT=0 cases, data selection spectra (Fig. 4.37 and 4.38) are shown here. Results are presented starting from dT=3 and dT=2 cases, followed by the dT=1 and dT=0 cases for the reaction of the ^{7}Li target, followed by the results on the ^{19}F target. The Q values and the color coding, used to label the exit channels, are listed in Table 4.13.
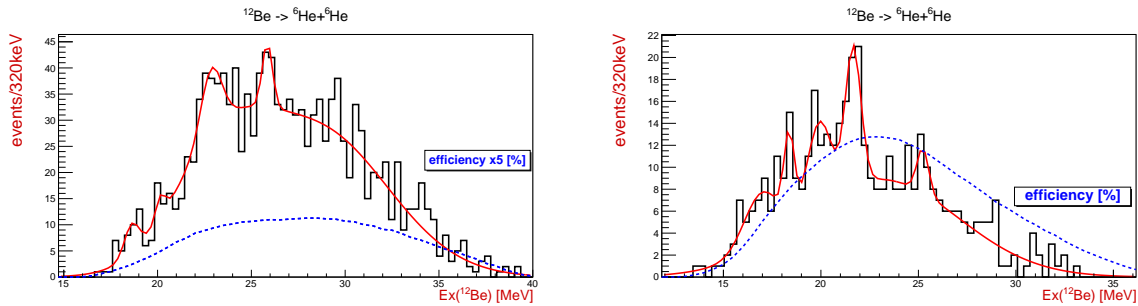
Figure 4.36: Excitation energy spectra of the ^{12}Be, from the ^{7}Li(^{9}Li, ^{6}He^{6}He)^{4}He reaction. The ^{6}He+^{6}He pair were detected in either the dT=3 (left) or dT=2 (right) telescope combination. The results of the fit are listed in Table 4.23 for both cases.

In the ^{12}Be excitation energy spectrum for the coincident detection of the ^{6}He+^{6}He pairs in dT=2 combination, shown on the right side of Fig. 4.36, evident dip in the statistics is seen in the $\sim$ 22-27 MeV range, compared to the dT=3 combination, shown on the right side of the same figure. This dip most likely comes from strict cuts applied to the data selection (Fig. 4.26) and two-dimensional relative energy spectra, imposed to remove as much contributions from the reactions on the other target constituents as possible, as well as background contributions from the ^{10}Be excited states. As one would expect to see the same states in both dT=3 and dT=2 cases, where the phase space overlaps, this is likely the reason why peak at $\sim$ 21.7 MeV is seen at lower energy (part of the peak is missing from the spectra) compared to the dT=3 case, where it is seen at 22.9 MeV and why peak at $\sim$ 25.2 has such low statistics in the dT=2 case.

For the dT=1 and dT=0 cases, as they are appearing for the first time in the text, data selection spectra are also presented here.

As seen on the ^{12}Be excitation energy comparison spectrum, shown on the right side of Fig. 4.37, values of the ^{12}Be$_{12}^{\text{nom.}}$ excitation energy are dispersed over a broad range, due to

Ex [MeV]	[16.9]	18.6/[18.4]	20.1/[19.9]	22.9/[21.7]	25.9/[25.2]	bg.
norm [ev.]	[4.8]	5.7/[7.3]	4.2/[7.5]	12.2/[12.6]	12.4/[4.1]	[gaus(23)]
σ [MeV]	0.9	0.4/[0.3]	0.3/[0.6]	0.6/[0.4]	0.3/[0.3]	pol5+gaus(30)

Table 4.23: Results of the fit for the ^{12}Be excited states from the ^{7}Li(^{9}Li, ^{6}He^{6}He)^{4}He reaction, for the dT=3 and dT=2 ([] brackets) cases, presented on Fig. 4.36.

Figure 4.37: Catania plot and Q value spectrum for the ^{6}He+^{6}He coincident events in the dT=1 combination, with identified exit channels from the reactions on ^{7}Li (red), ^{19}F (blue) and ^{6}Li (gray) targets, as listed in Table 4.13. Final data selected for the reaction on ^{7}Li target are shown with red markers. On the right side of the figure, ^{12}Be excitation energy comparison spectrum is shown, calculated using $\Delta\phi_{12}^{\text{reco.}}$ (ordinate) and $\Delta\phi_{12}^{\text{nom.}}$ (abscissa), as an indication of the observation of the same states seen on Fig. 4.39.

the use of the $\Delta\phi_{12}^{\text{nom.}}$ angle. When correct $\Delta\phi_{12}^{\text{reco.}}$ is reconstructed from the kinematics calculation, these values "gather" in horizontal locus on the ^{12}Be$_{12}^{\text{reco.}}$ (ordinate) axis, representing the real states in the ^{12}Be nuclei. This behaviour of the data is due to the large uncertainty in the $\Delta\phi_{12}$ value, where a nominal value of $60°$ is assumed for the dT=1 case, with the estimated error of $+/- 55°$, for which $\Delta\phi_{12}^{\text{reco.}}$ is compensating. Since for this case there are no significant contributions from the other reaction channels, reconstruction works nicely restoring the resolution in the observation of the ^{6}He+^{6}He decays of the ^{12}Be excited states. The ^{12}Be excitation energy comparison spectrum is also shown for the dT=0 case in Fig. 4.38. Although the statistics observed is fairly low, data locus from the ^{7}Li target is aligned along the diagonal line, indicating a clean data selection.

In the data selection spectra on Fig. 4.38 it can be seen that only a small portion of the observed coincidences in the same detector yield the data with the correct Q value of 2.24 MeV, for the reaction on the ^{7}Li target. The ^{12}Be excitation energy comparison spectrum, presented on the right side of Fig. 4.38, shows how background contributions
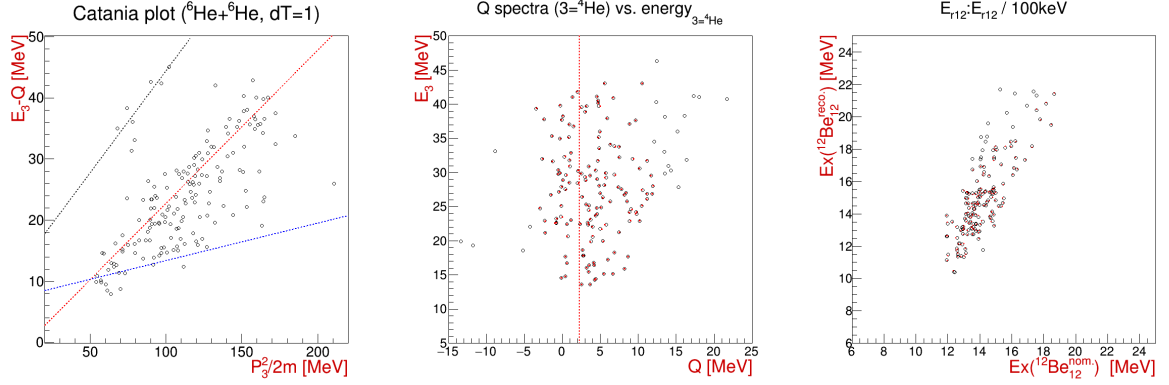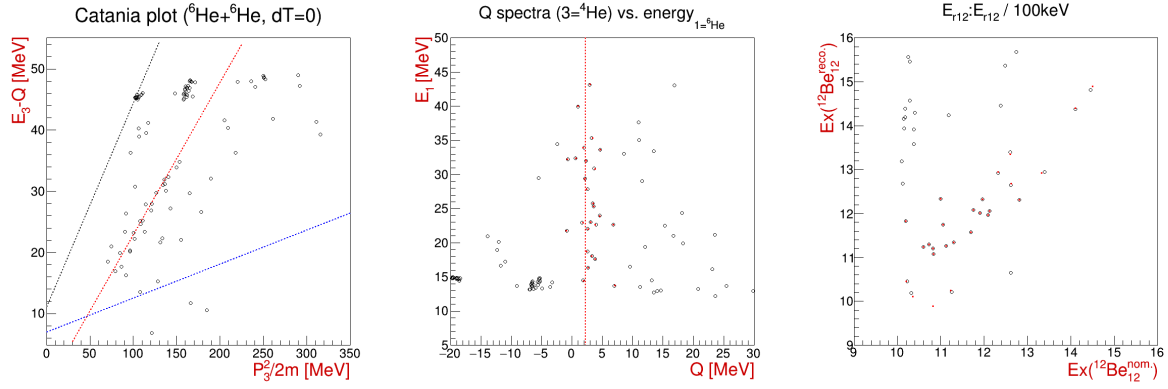
Figure 4.38: Catania plot and Q value spectrum for the ^{6}He+^{6}He coincident events in the dT=0 combination, with identified and labelled exit channels from the reactions on ^{7}Li (red), ^{19}F (blue) and ^{6}Li (gray) targets, as listed in Table 4.13. On the right side of the figure ^{12}Be excitation energy comparison spectrum is shown.

seen in the data selection spectra were discarded, and the clean selection for the final excitation energy spectrum (Fig. 4.39) was obtained.
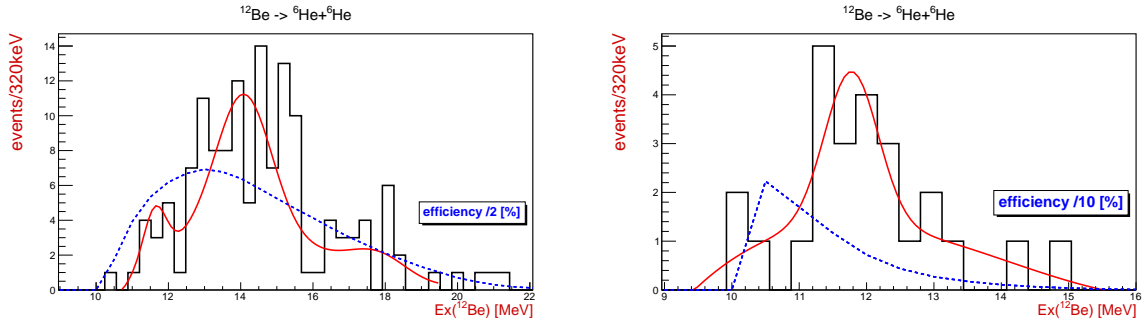
Figure 4.39: Excitation energy spectra for the ^{12}Be from the ^{7}Li(^{9}Li, ^{6}He^{6}He)^{4}He reaction. The ^{6}He+^{6}He pair was detected in either dT=1 (left) or dT=0 (right) combination. The results of the fit are listed in Table 4.24 for both cases.

Ex [MeV]	11.6/[11.8]	14.1	background
norm [events]	3.0/[3.1]	8.0	[pol3]
σ [MeV]	0.3/[0.4]	0.8	pol3 + gaus (17.8)

Table 4.24: Results of the fit for the ^{12}Be excited states from the ^{7}Li(^{9}Li, ^{6}He^{6}He)^{4}He reaction, for the dT=1 and dT=0 ([] brackets) cases, presented on Fig. 4.39.

A comprehensive overview of the observed states is given in Discussion 5.2, while the states are listed in the summary Table 4.25, where a confidence level for state observation is also indicated.

^{19}F(^{9}Li, ^{6}He^{6}He)^{16}O reaction

For the observation of the ^{6}He+^{6}He decays of the ^{12}Be excited states, from the reaction on the ^{19}F target, only the dT=3 case had enough statistics to be clearly separated from the reaction on ^{7}Li target, as seen in data selection spectra on Fig. 4.24. Because of large negative Q value of $\sim$ -7 MeV, the three-body reactions on the ^{19}F target are expected to be dominated by the reaction on the ^{7}Li target, which has positive Q value of 2.24 MeV. Due to low resolution and statistics result are not presented here, even though an indication of the peak at 18.7 MeV was observed in the excitation energy spectra.

Summary table of the observed states: ^{12}Be$\to$ ^{6}He+^{6}He

^{6}He+^{6}He $_\downarrow$ $\parallel$ Ex [MeV] $_\rightarrow$	(11.7)	13.5	(16.5)	18.5	(20.0)	22.5	25.4
^{7}Li(^{9}Li, ^{4}He^{6}He)$_{dT=3}$^{6}He (23)	×	●	○	●	○	●	●
^{7}Li(^{9}Li, ^{6}He^{6}He)$_{dT=3}$^{4}He (12)				●	○	●	●
^{7}Li(^{9}Li, ^{6}He^{6}He)$_{dT=2}$^{4}He (12)			○	●	●	●	○
^{7}Li(^{9}Li, ^{6}He^{6}He)$_{dT=1}$^{4}He (12)	○	●	×				
^{7}Li(^{9}Li, ^{6}He^{6}He)$_{dT=0}$^{4}He (12)	●						
^{19}F(^{9}Li, ^{6}He^{6}He)$_{dT=3}$^{16}O (12)			×	○	×*	×*	×

Table 4.25: Results for the ^{6}He+^{6}He decay of the ^{12}Be excited states from the observed reactions on the LiF target. Clear peaks with good statistics are shown with ● symbol, while peaks with lower statistics and/or background interference are shown with ○ symbol. Low quality peaks observed in other data sets, but not seen clearly and/or are at the edge of the phase space are shown with × symbol. Two states indicated with * symbol are observed as a one peak in corresponding spectrum.

^{6}He+^{6}He* $_\downarrow$ $\parallel$ Ex [MeV] $_\rightarrow$	15.4	16.5	17.8	22.1	24.0
^{7}Li(^{9}Li, ^{4}He^{6}He)$_{dT=3}$^{6}He (23)	●	●	●	●	●

Table 4.26: Results for the ^{6}He+^{6}He* decay of the ^{12}Be excited states from the observed reactions on the ^{7}Li target. Clear peaks with good statistics are shown with ● symbol, while peaks with lower statistics and/or background interference are shown with ○ symbol.

4.2.2 ^{4}He+^{8}He decay channel

Similarly to the ^{6}He+^{6}He coincidences, large Q value differences for the reactions on different elements of the LiF target (Table 4.27), enable clear data selection for the coincident detection of the ^{4}He+^{8}He pairs and reduce the risk of channels interfering in the final results. The results will be presented starting from the reactions on the ^{7}Li target, followed by the reactions on the ^{19}F and ^{6}Li targets, for the cases with sufficient data statistics.

reaction	^{7}Li(^{9}Li, ^{4}He^{8}He)^{4}He	^{19}F(^{9}Li, ^{4}He^{8}He)^{16}O	^{6}Li(^{9}Li, ^{4}He^{8}He)^{3}He
Q [MeV]	3.40	-5.83	-9.92
color	red	blue	pink

Table 4.27: The Q values and color coding used for the three-body reaction channels observed in the ^{4}He+^{8}He coincident events in all telescope combinations.

Another way of observing the ^{4}He+^{8}He decay of the ^{12}Be excited states is the reaction on the ^{7}Li target, where the ^{4}He+^{4}He pair was detected in either dT=3 or dT=2 telescope combinations. As the ^{12}Be excited states can be accessed both through "1-3" and "2-3" combinations of the reaction products, final results (projections) will be presented as the sum of these combination, after the relevant cuts to exclude the dominating ^{8}Be excited states are made.

^{7}Li(^{9}Li, ^{4}He^{8}He)^{4}He reaction

Coincident detection of the ^{4}He+^{8}He pairs from the reaction on the ^{7}Li target has a great advantage that decays of the ^{12}Be excited states can be observed both through "1-2" and "2-3" combination of the particles in the exit channel. This is specially important in the dT=3 case, where the experimental resolution is best, due to the smallest uncertainty in the relative $\Delta\phi_{12}$ angle between detected particles. The "1-2" combination will contribute to the detection of the higher energy excitations, while the "2-3" combination will be dominantly populating low lying excitations, close to the particle decay threshold of 9 MeV. Due to the overlaps in the excitation energy covered, "1-2" case will serve as a cross-check for the states observed in the dT=2 combination, while the latter ("2-3") case will serve as a cross-check for the dT=0 and dT=1 cases and partially for the dT=2 case in lower excitation energy region. This also holds true for the "1-2" combination from the

observed reactions on the ^{19}F and ^{6}Li targets. It is important to mention that the relative energy spectra are largely dominated by the ^{8}Be excited states, all up to $\sim$ 18-20 MeV in excitation energy. To obtain clean spectra for the ^{12}Be projection, cuts were made to exclude the data largely affected by the ^{8}Be contributions: g.s. (0^+), 3.03 MeV (2^+), 11.35 MeV (4^+), 16.63+16.92 MeV (2^+) and mix of states at 19.86 MeV (4^+), 20.1 MeV (2^+) and 20.2 MeV (0^+), resulting in a large decrease of the efficiency and thus statistics for observation of the ^{12}Be excited states. Keeping this in mind one should always go back and forth with the two-dimensional relative energy spectra and one-dimensional projections, as some states in ^{12}Be could have been affected in sense of loosing a sensible amount of the observed events.
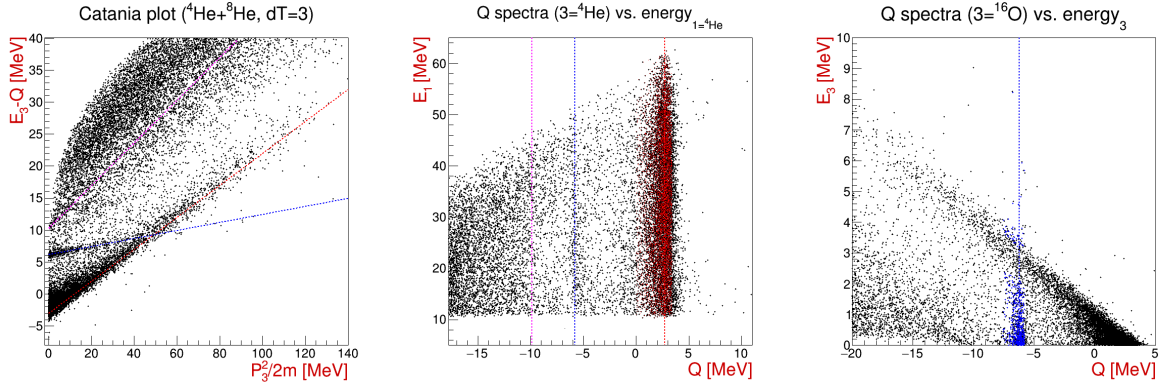
Figure 4.40: Catania plot and Q value spectrum for the ^{4}He+^{8}He coincident events in the dT=3 combination, with identified exit channels from the reactions on ^{7}Li (red), ^{19}F (blue) and ^{6}Li (pink) targets, as listed in Table 4.27.
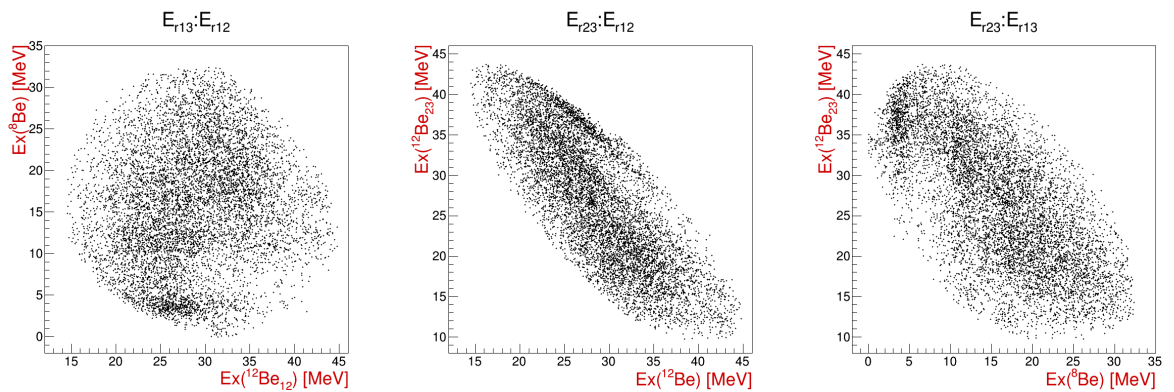
Figure 4.41: Excitation energy spectra for the ^{12}Be$_{12}$, ^{8}Be$_{13}$ and ^{12}Be$_{23}$, from the ^{7}Li(^{9}Li, ^{4}He^{8}He)$_{dT=3}$^{4}He reaction.

In the excitation (relative) energy spectra for all of the particle combinations in the exit channel of the ^{7}Li(^{9}Li, ^{4}He^{8}He)^{4}He reaction (Fig. 4.41), a strong dominance of the ^{8}Be excited states can be seen. A cut was made above 15 MeV in the excitation energy of

the ^{8}Be to exclude the contributions from the ground (0^+), 3.03 MeV (2^+) and 11.35 MeV (4^+) states dominating the spectra. Less prominent contributions from the states at 16.63 and 16.92 MeV states (2^+) were left in both "1-2" and "2-3" projections and treated as a background in those spectra, as a way to achieve a compromise between the final statistics and the quality of the data selection for the projections.
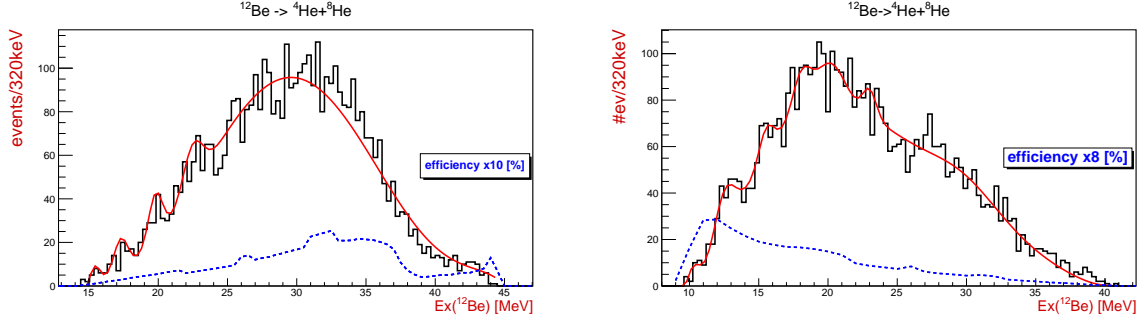
Figure 4.42: Excitation energy spectra for the ^{12}Be$_{12}$ (left) and ^{12}Be$_{23}$ (right), from the ^{7}Li(^{9}Li, ^{4}He^{8}He)$_{dT=3}$^{4}He reaction. The results of the fit are listed in Table 4.28 for the "1-2" and Table 4.29 for the "2-3" combination of the ^{12}Be excited states.

Ex [MeV]	15.4	17.3	19.8	22.5	background
norm [events]	10.0	15.0	22.0	20.0	
σ [MeV]	0.4	0.5	0.5	0.7	pol6

Table 4.28: Results of the fit for the ^{12}Be$_{12}$ excited states from the ^{7}Li(^{9}Li, ^{4}He^{8}He)$_{dT=3}$^{4}He reaction, presented on the left side of Fig. 4.42.

The peak at 12.5 MeV (center of distribution at $\sim$ 13 MeV), seen on the right side of Fig. 4.42, may correspond to the sum of two peaks, the dominating one centered at $\sim$ 13.8 MeV and the smaller one at $\sim$ 12.1 MeV. The shape of the peak indicates so, if the shift of $\sim$ 350-400 keV ($\sim$ one bin in spectrum) towards lower excitation energy is accounted for. While comprehensive overview and systematization of the observed peaks will be given in Discussion 5.2, it is important to note that detailed survey on each fitted peak was made in order to compile the final table of the observed states, listed in Table 4.38, for the ^{12}Be decays to the ^{4}He+^{8}He.

As it can be seen on the data selection spectra for the dT=2 case (Fig. 4.43), due to the large uncertainty in the relative $\Delta\phi_{12}^{\text{nom.}}$ angle, affecting the reconstruction of the energy and momentum of the undetected particle, data is showing a large spread in the Catania plot and the Q value spectrum. This behavior is expected for the dT=2 case and can be

Ex [MeV]	10.2	12.5*	15.5	18.0	20.1	23.0	background
norm [events]	14.0	21.3	12.9	17.1	18.0	11.7	
σ [MeV]	0.6	0.8	0.5	0.7	1.1	0.5	pol6 + gaus(28.8)

Table 4.29: Results of the fit for the ^{12}Be$_{23}$ excited states from the ^{7}Li(^{9}Li, ^{4}He^{8}He)$_{\text{dT}=3}$^{4}He reaction, presented on the right side of Fig. 4.42. See the text for the discussion on the peak at 12.5 MeV.

reproduced in the Monte Carlo simulations. Final data selection for the reaction on the ^{19}F target, shown in blue markers on the ^{12}Be excitation energy comparison spectrum, is less affected by the uncertainty in the $\Delta\phi_{12}^{\text{nom.}}$ angle and consequently shows how data selection for the ^{7}Li target is not interfering in the selection, resulting in satisfactory separation between two exit channels.

Figure 4.43: Catania plot and Q value spectrum for the ^{4}He+^{8}He coincident events in the dT=2 combination, with identified and labeled exit channels from the reactions as listed in Table 4.27. Right side of the figure shows ^{12}Be excitation energy comparison spectrum for the assumption of the reaction on the ^{19}F target.

In the relative energy spectra for the dT=2 case (Fig. 4.44 - left), one can notice a strong contributions from the 16.63 MeV and 16.92 MeV states (2^+), as well as the lower excitation energy states of the ^{8}Be nuclei. To obtain a clean projection for both ^{12}Be$_{12}$ and ^{12}Be$_{23}$ excitation energies, a cut was made to exclude all events below 20 MeV in ^{8}Be excitation. Even a stronger cut at 22 MeV in ^{8}Be was made for the dT=1 case, shown on Fig. 4.44 in center. Both of these cuts were made to exclude the contributions from the states centered around $\sim$ 20 MeV in ^{8}Be: 19.9 MeV (4^+), 20.1 MeV (2^+) and 20.2 MeV (0^+). Such strong cuts consequently reduce the observed statistics of the ^{12}Be excited states, but are necessary to avoid the appearance of false peaks.

For the dT=1 and dT=0 cases, due to the smaller value of the relative $\Delta\phi_{12}^{\text{nom.}}$ angle
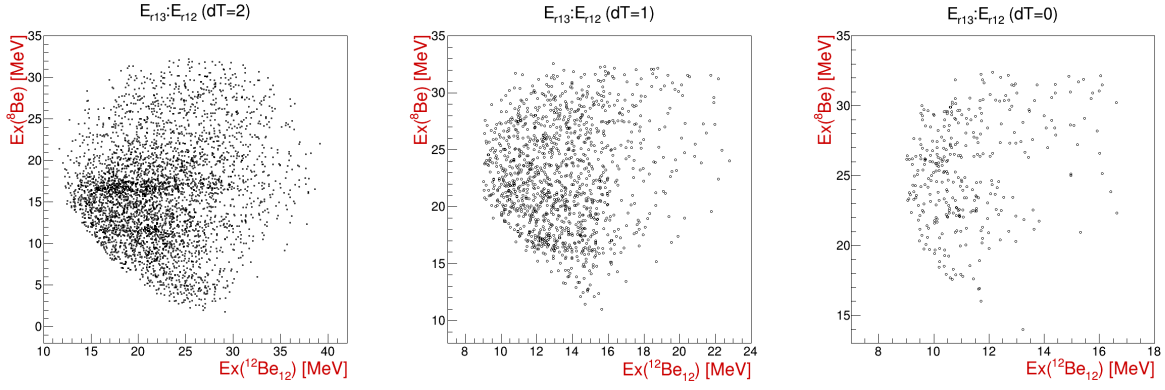
Figure 4.44: Excitation energy spectra for the ^{12}Be$_{12}$ and ^{8}Be$_{13}$, from the ^{7}Li(^{9}Li, ^{4}He^{8}He)^{4}He reaction, for dT=2 (left), dT=1 (center) and dT=0 (right) telescope combinations.
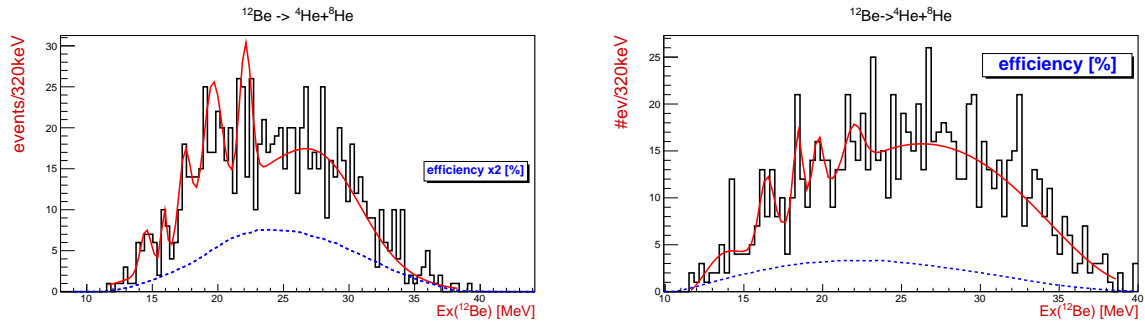
Figure 4.45: Excitation energy spectra for the ^{12}Be$_{12}$ (left) and ^{12}Be$_{23}$ (right), from the ^{7}Li(^{9}Li, ^{4}He^{8}He)$_{\text{dT}=2}$^{4}He reaction. The results of the fit are listed in Tables 4.30 for the "1-2" and Table 4.31 for the "2-3" combination.

Ex [MeV]	14.5	15.9	17.5	19.6	22.1	background
norm [events]	5.0	6.0	11.0	16.0	17.0	
σ [MeV]	0.4	0.2	0.5	0.7	0.5	gaus(24.2)+gaus(27.6)

Table 4.30: Results of the fit for the ^{12}Be$_{12}$ excited states from the ^{7}Li(^{9}Li, ^{4}He^{8}He)$_{\text{dT}=2}$^{4}He reaction, presented on the left side of Fig. 4.45.

Ex [MeV]	13.6	16.4	18.4	19.7	21.9	background
norm [events]	3.3	7.2	8.8	6.3	4.5	
σ [MeV]	1.2	0.5	0.3	0.3	0.6	pol4 + gaus(32.8)

Table 4.31: Results of the fit for the ^{12}Be$_{23}$ excited states from the ^{7}Li(^{9}Li, ^{4}He^{8}He)$_{\text{dT}=2}$^{4}He reaction, presented on the right side of Fig. 4.45.

between the detected particles, only the "1-2" combination of the particles remains relevant for the observation of the ^{4}He+^{8}He decays of the ^{12}Be excited states. On the data selection spectra for the dT=1 case, shown on Fig. 4.46, a small contribution from the reaction on

the ^{6}Li target can be seen, while the efficiency and the observed statistics for the reaction on the ^{19}F decreases. Due to the large Q value differences, the reaction on the ^{7}Li is well separated and the obtained result are expected to have little or almost none of the contributions from other channels.
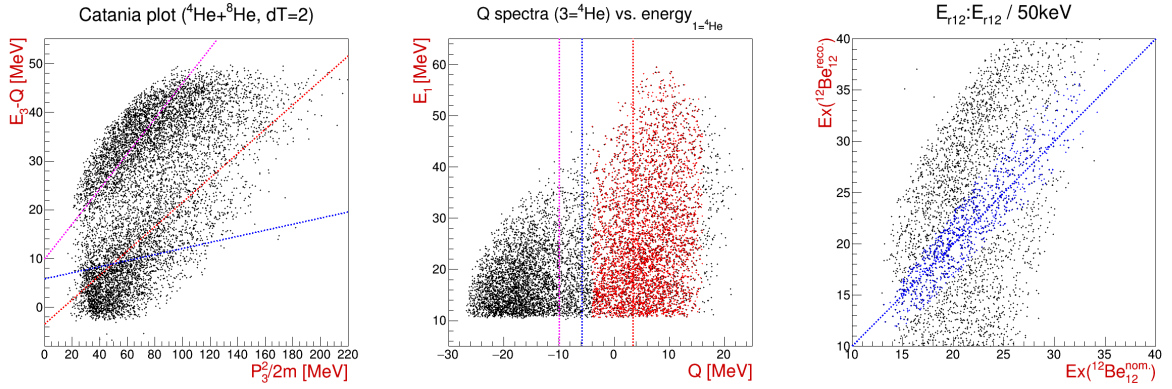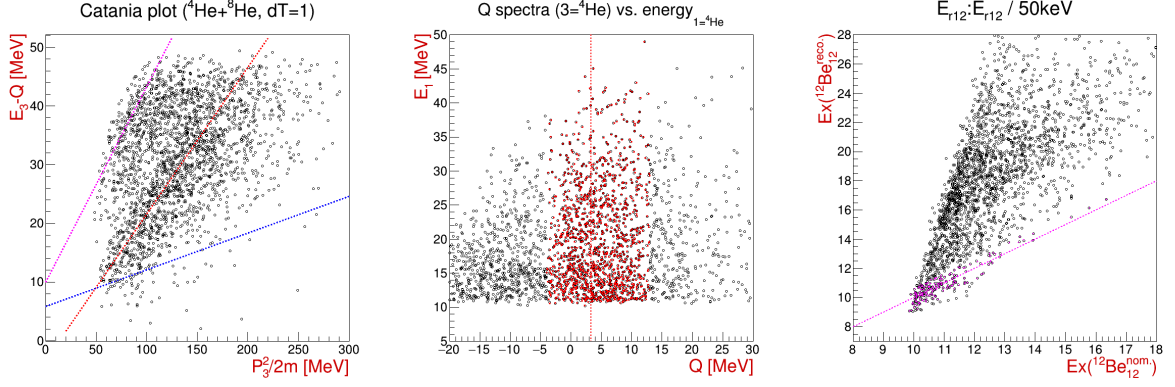

Figure 4.46: Catania plot and Q value spectrum for the ^{4}He+^{8}He coincident events in the dT=1 combination, with identified and labeled exit channels as listed in Table 4.27. Selected data for the reaction on the ^{7}Li target are shown in red markers, while the data selected for the ^{6}Li reaction is shown in pink. Right side of the figure shows ^{12}Be excitation energy comparison spectrum with the assumption of the reaction on the ^{6}Li target.
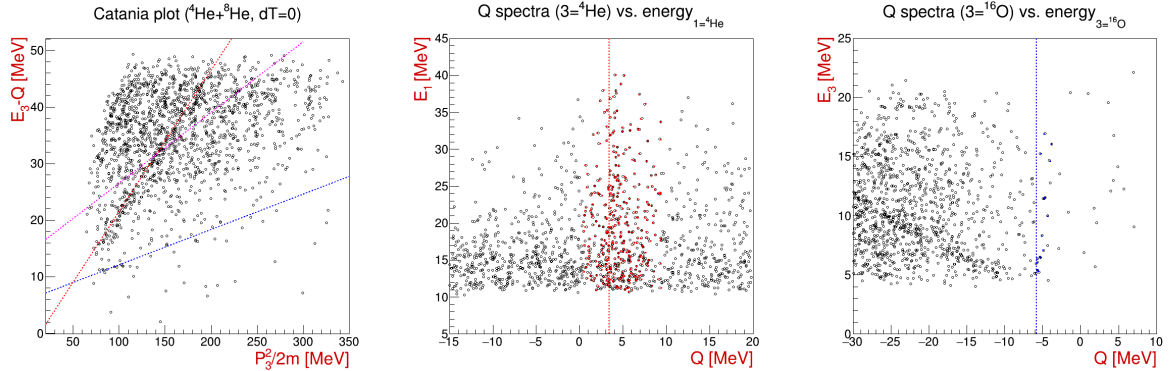
Figure 4.47: Catania plot and Q value spectrum for the ^{4}He+^{8}He coincident events in the dT=0 combination, with identified exit channels as listed in Table 4.27. Data selected for the reaction on the ^{7}Li target is shown in red markers, while low statistics data selection for the ^{19}F reaction is shown in blue, just to show that these cases are well separated.

Ex [MeV]	10.8/[10.6]	12.7/[12.6]	14.4	15.8	17.8	background
norm [events]	9.8/[2.6]	6.0/[5.2]	6.4	12.3	3.4	[expo]
σ [MeV]	0.3/[0.6]	0.5/[0.6]	0.5	0.3	0.5	pol4

Table 4.32: Results of the fit for the ^{12}Be$_{12}$ excited states from the ^{7}Li(^{9}Li, ^{4}He^{8}He)^{4}He reaction presented on Fig. 4.48, where the ^{4}He^{8}He pair was detected in either dT=1 or dT=0 ([] brackets) combination.
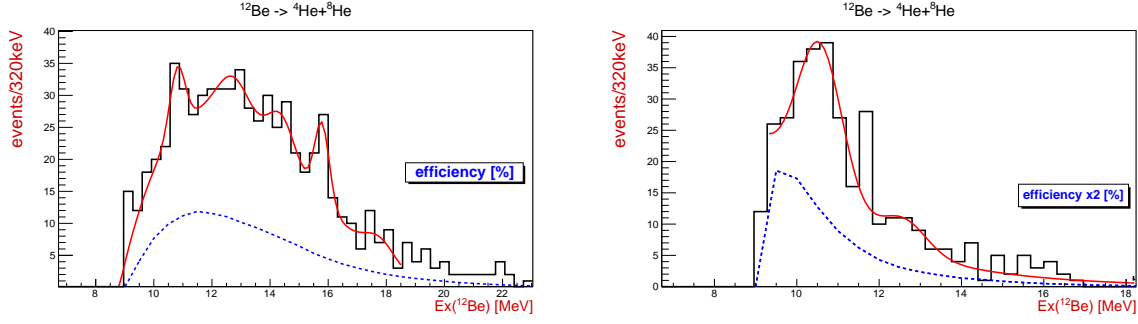
Figure 4.48: Excitation energy spectra for the $^{12}Be_{12}$, from the $^7Li(^9Li, {}^4He^8He)^4He$ reaction. The $^4He+^8He$ pair was detected in either dT=1 (left) or dT=0 (right) combination. The results of the fit are listed in Table 4.32 for both cases.

$^{19}F(^9Li, {}^4He^8He)^{16}O$ reaction

For the coincident detection of the $^4He+^8He$ pairs from the reaction on the ^{19}F target, helium cluster decays of the ^{12}Be excited states can be observed through "1-2" combination of the particles (the detected pair). Having the best resolution, due to the smallest uncertainty in the $\Delta\phi_{12}^{nom.}$ and hence the cleanest exit channel identification, the dT=3 case should serve as a reference for the comparison with the dT=2 case and the results obtained from the ^7Li target. As the detection efficiency and the observed statistics decrease drastically for the dT=1 and dT=0 cases, these should be considered more as an auxiliary spectra for the results on the ^7Li target, to confirm the observed peaks and the behavior of the data. Since the data selection spectra were shown in the previous section, only the excitation energy spectra, both the two-dimensional plots and the projections, will be shown here, together with the efficiency calculation and the results of the fit. Data selection spectra for the dT=3 and dT=2 cases are shown in Figures 4.40 and 4.40 respectively.
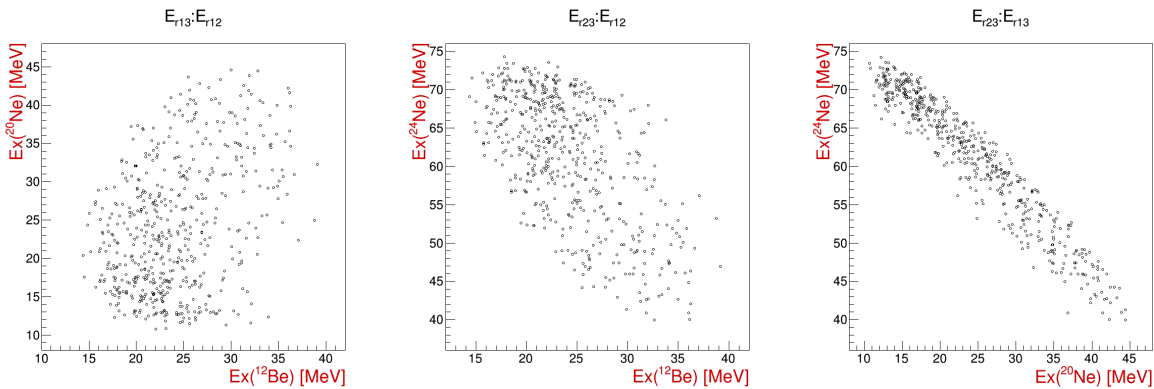
Figure 4.49: Excitation energy spectra for the $^{12}Be_{12}$, $^{20}Ne_{13}$ and $^{24}Ne_{23}$, from the $^{19}F(^9Li, {}^4He^8He)_{dT=3}^{16}O$ reaction.

It is important to mention that no cuts were made on the excited states of the ^{20}Ne for the ^{12}Be projection. Many of closely spaced excited states of the ^{20}Ne that α decay in the relevant excitation energy range, did not seem to have a prominent effect on the ^{12}Be excitation spectra. As it can be seen in the two-dimensional relative (excitation) energy spectra, shown on Fig. 4.49, a vertical loci, which are an indication of possible states, of the ^{12}Be data is prolonged into probably the only relevant contribution from the ^{20}Ne around ~ 12 and ~ 16 MeV. Similarly, for the dT=2 case, contribution from the ^{20}Ne excited states was observed around ~ 15 MeV. Not excluding these set of states introduces a background in the projection for the ^{12}Be excitation energy spectrum, shown on Fig. 4.50. As always, careful inspection of the two-dimensional excitation energy spectra is important in the interpretation of the results.
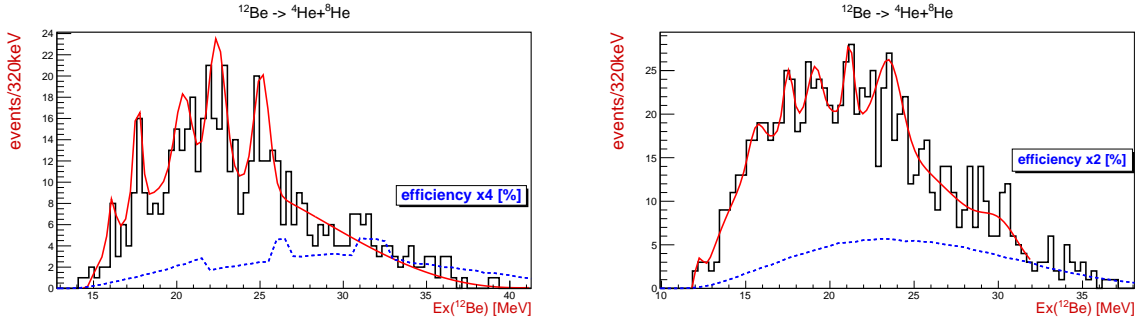
Figure 4.50: Excitation energy spectra for the ^{12}Be$_{12}$, from the ^{19}F(^{9}Li, ^{4}He^{8}He)^{16}O reaction. The ^{4}He+^{8}He pair was detected in dT=3 (left) or dT=2 (right) combination, while undetected particle is ^{16}O. The results of the fit are listed in Table 4.33 for the dT=3 and Table 4.34 for the dT=2 combination.

Close inspection of the excitation energy spectrum for the ^{12}Be decay to ^{4}He+^{8}He pairs in dT=3 combination, presented on the left side of Fig. 4.50, reveals step changes in the detection efficiency, specially in ~ 25 MeV and ~ 31 MeV range, resulting in the appearance of two false peaks at these energies. Since the MC data were analysed in same manner as the experimental one, with same data selection cuts, one can conclude that fitted peak at ~ 25 MeV (see Table 4.33) is product of the rise in the efficiency, while the peak at ~ 31 MeV was not considered in the fitting procedure due to lack of structure in two-dimensional spectra and high background content at these energies in all spectra. Also, one can notice the small systematical shift between the position of the false peaks and steep rise in the detection efficiency, which happens due to the differences in energy and angle reconstruction procedure: MC simulations for detection efficiency don't take into account the energy straggling in the target and dead layer of detectors. This affects

the initial energy and momentum reconstruction, which inherently yields systematical offsets in the position of the Q value peak in the data selection spectra, and later a small difference in the $\Delta\phi^{\mathrm{reco}}$ value which affects the excitation energy spectrum, where the small difference is observed.

Ex [MeV]	(16.1)	17.7	20.4	22.4	25.1*	background
norm [events]	4.0	10.0	8.0	13.0	11.0	
σ [MeV]	0.2	0.3	0.5	0.5	0.5	pol4

Table 4.33: Results of the fit for the $^{12}\mathrm{Be}_{12}$ excited states from the $^{19}\mathrm{F}(^{9}\mathrm{Li}, {}^{4}\mathrm{He}{}^{8}\mathrm{He})_{\mathrm{dT}=3}{}^{16}\mathrm{O}$ reaction, presented on the left side of Fig. 4.50. See text for the discussion on the *.

On the other hand, for the dT=2 case, a strong interference of closely spaced excited states in $^{20}\mathrm{Ne}$ is obstructing the inspection of the $^{12}\mathrm{Be}$ excited states, specially in the Ex > 20 MeV region, where in the case of the $^{7}\mathrm{Li}$ target the state at $\sim$ 22.5 MeV is seen. Thus, it is likely that these peaks are artifacts of $^{20}\mathrm{Ne}$ states boosted in statistics as the detection efficiency rises in this region.

Ex [MeV]	(12.1)	15.6	17.5	19.1	21.2*	23.5*	background
norm [events]	4.2	3.9	6.3	5.4	8.3	9.0	
σ [MeV]	0.3	0.4	0.3	0.4	0.3	0.7	pol4 + gaus(30.1)

Table 4.34: Results of the fit for the $^{12}\mathrm{Be}_{12}$ excited states from the $^{19}\mathrm{F}(^{9}\mathrm{Li}, {}^{4}\mathrm{He}{}^{8}\mathrm{He})_{\mathrm{dT}=2}{}^{16}\mathrm{O}$ reaction, presented on the right side of Fig. 4.50. See text for the discussion on the *.

Due to large drop in the observed statistics of the $^{4}\mathrm{He}+^{8}\mathrm{He}$ coincident events from the reaction on $^{19}\mathrm{F}$ target in dT=1 and dT=0 telescope combinations, these spectra are not presented here. Despite very low statistics, these still indicate the existence of the same states observed at $\sim$ 10.5 MeV (dT=0), $\sim$ 12 MeV (dT=0,1), $\sim$ 13.5-14 MeV (dT=1) and $\sim$ 15.5 MeV (dT=1) seen in the results for the $^{7}\mathrm{Li}$ target (Table 4.38).

^{6}Li(^{9}Li, ^{4}He^{8}He)^{3}He reaction

Due to low concentration of the ^{6}Li isotope in natural lithium (7.5 %) used in the LiF target, and very negative Q value of -9.92 MeV (see Table 4.27) for the ^{6}Li(^{9}Li, ^{4}He^{8}He)^{3}He reaction, only usable data with enough statistics and resolution was the one for the dT=1 case. As it can be seen from the ^{12}Be excitation energy comparison spectrum, shown on the right side of Fig. 4.46, the data selection for the final results for the dT=1 case for reaction on the ^{6}Li is well separated from the reactions on ^{7}Li and ^{19}F. Although the data were analysed for the other telescope combinations for the detected ^{4}He+^{8}He pairs, it was largely dominated by the observed states in the ^{7}Be nuclei in the dT=3 case, low resolution in the dT=2 case and low statistics in the dT=0 case. For this reasons, only the dT=1 case is presented here, supporting the observation of the low lying ^{12}Be excited state, near the particle decay trashold for the ^{4}He decay at 9.0 MeV.
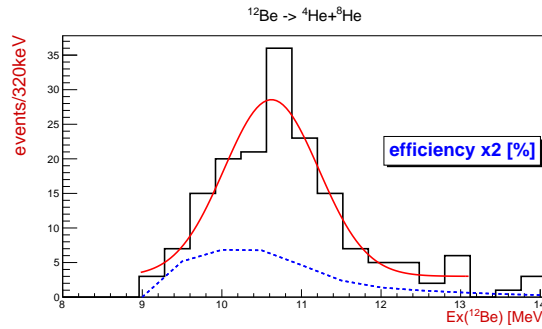
Figure 4.51: Excitation energy spectrum of the ^{12}Be$_{12}$, from the ^{6}Li(^{9}Li, ^{4}He^{8}He)$_{dT=1}$^{3}He reaction. The Gaussian peak fitted at at 10.6 MeV (σ=0.6 MeV) is discussed in the text.

The shape of the spectrum presented on Fig. 4.51 seems to be dominated by the detection efficiency curve, which describes the general shape of the data very well. As the peak around $\sim$ 10.5 MeV was observed in other datasets, it was fitted here in the search for possible contributions from the ^{6}Li target. For this reason presented spectrum should be considered as an auxiliary one for the reaction on the ^{7}Li target.

^{7}Li(^{9}Li, ^{4}He^{4}He)^{8}He reaction

Moving on to the final case study for the helium cluster decays of the ^{12}Be excited states to the ^{4}He+^{8}He pair, the ^{4}He+^{4}He coincidences are presented here. As with the ^{6}He+^{6}He and ^{4}He+^{8}He coincidences, large Q value differences between the reactions on different elements of the target (Table 4.35) enables, in principle, use of wider data selection cuts

for the respective exit channel, with intent to include as much statistics as the data would allow. Having two α particles detected in the exit channel complicates the analysis, as many of α-conjugate nuclei, accessible in the experiment, can undergo α decay leading to many-body exit channels. Large efforts were made to isolate the exit channel of interest, the reaction on the ^{7}Li target: ^{7}Li(^{9}Li, ^{4}He^{4}He)^{8}He, where the ^{12}Be excited states could've been produced and observed through "1-3" and "2-3" combination of the particles in the exit channel. Since these combinations occupy the same kinematical phase space, the final results are presented as the sum of one-dimensional projections for these combinations, separately for the dT=3 and dT=2 cases.

reaction	^{7}Li(^{9}Li, ^{4}He^{4}He)^{8}He	^{19}F(^{9}Li, ^{4}He^{4}He)^{20}O	^{1}H(^{9}Li, ^{4}He^{4}He)nn
Q [MeV]	3.40	14.82	11.25
color	red	blue	black

Table 4.35: The Q values and color coding used for the three-body reaction channels observed in the data for the ^{4}He+^{4}He coincident events in all detector combinations. Additional exit channel from the reaction on the ^{19}F target is observed in the data, with undetected ^{20}O in the 2^+ excited state at 1.67 MeV, color coded in pink. The kinematic line from the reaction on the ^{6}Li target with Q value of 8.08 MeV is labeled in orange.

On the data selection spectra for the ^{4}He+^{4}He coincidences, in the dT=3 telescope combination (Fig. 4.52), a strong contribution from the three-body reaction on the ^{1}H contaminant in the target can be seen, with strong locus in the Catania plot and Q value spectrum corresponding to the undetected two neutrons. To avoid this data affecting the exit channel on the ^{7}Li target, a graphical cut on the Catania plot was made to select the data from the reaction on the ^{7}Li target. This selection was confirmed by the expected behaviour of the data locus (along the diagonal line) in the ^{8}Be excitation energy comparison spectrum and the Q value spectrum, as shown in Fig. 4.52.

In the excitation energy spectra (Fig. 4.53) for all particle combinations in the exit channel for the dT=3 case, one has to mention that ^{8}Be excitation energy was calculated using nominal $\Delta\phi_{12}^{\mathrm{nom.}} = 180°$ value. Due to the large contribution from the many-body reactions, such as undetected ^{7}He+n, ^{6}He+n+n, ^{5}He+n+n+n and ^{4}He+n+n+n+n, a clean data selection was hard to achieve, as these contributions are smeared all over the Q value spectra, thus naturally ending up in the final data selection as well. By comparison with the ^{8}Be excitation energy calculated using reconstructed $\Delta\phi_{12}^{\mathrm{reco.}}$ (Eq. 3.22), one

Figure 4.52: Catania plot and Q value spectrum for the ^{4}He+^{4}He coincident events in the dT=3 telescope combination, with identified and indicated exit channels as listed in Table 4.35. Data selected for the reaction on the ^{7}Li target is shown with red markers. Right side of the figure shows ^{8}Be excitation energy comparison spectrum with the assumption of the reaction on the ^{7}Li target.
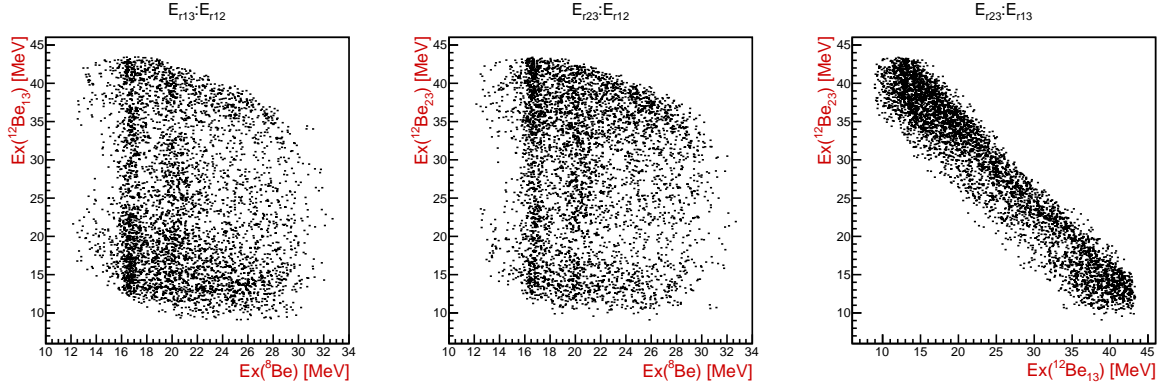
Figure 4.53: Excitation energy spectra for the ^{8}Be$_{12}^{\text{nom.}}$, ^{12}Be$_{13}$ and ^{12}Be$_{23}$, from the ^{7}Li(^{9}Li, ^{4}He^{4}He)$_{\text{dT}=3}$^{8}He reaction. Note that ^{8}Be$_{12}$ excitation energy is calculated using nominal $\Delta\phi_{12}^{\text{nom.}} = 180°$ value.

comes to conclusion that dominantly the ^{8}Be reconstruction is affected, as these events proceed through the ^{8}Be excited states. This was best seen in the observation of the prominent states in the ^{8}Be: mix of 16.63 MeV (2^+) and 16.92 MeV (2^+) states, and 19.86 MeV (4^+), 20.1 MeV (0^+) and 20.2 MeV (2^+). Using $\Delta\phi_{12}^{\text{nom.}} = 180°$ resulted in much cleaner spectrum, compared to $\Delta\phi_{12}^{\text{reco.}}$, due to the fact that a part of the data is not only three-body (decays of undetected ^{8}He for example) and yields incorrectly reconstructed $\Delta\phi_{12}^{\text{reco.}}$ value, while $\Delta\phi_{12}^{\text{nom.}}$ is unaffected by the assumption on the exit channel, thus reproducing the observed states better. The ^{12}Be states remained largely unaffected by change in the reconstruction method, especially since the cut on ^{8}Be$_{12}^{\text{nom.}}$ was introduced to exclude all events below 21 MeV in ^{8}Be excitation energy. Consequently the final efficiency for the ^{12}Be excitations (Fig. 4.55) is lowered due to the cut, but a

cleaner spectrum is obtained, so the final result is obtained through careful consideration of both the two-dimensional excitation energy spectra and one-dimensional projections for all combinations.
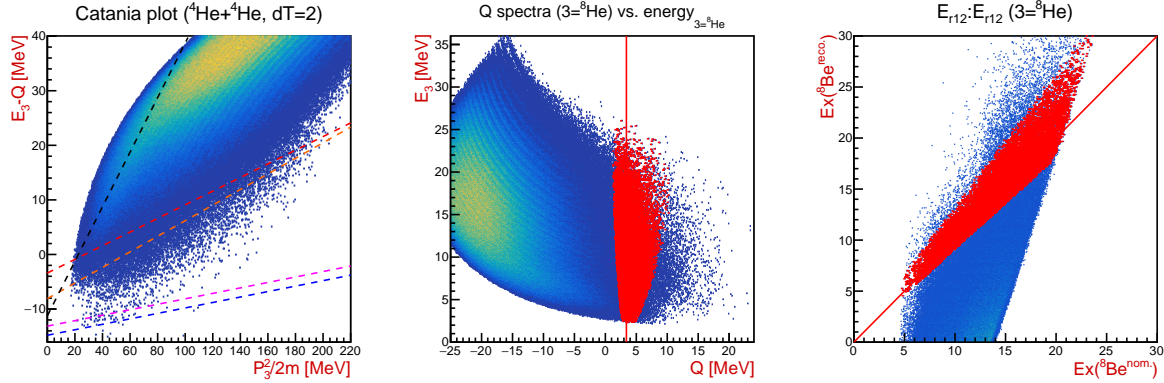
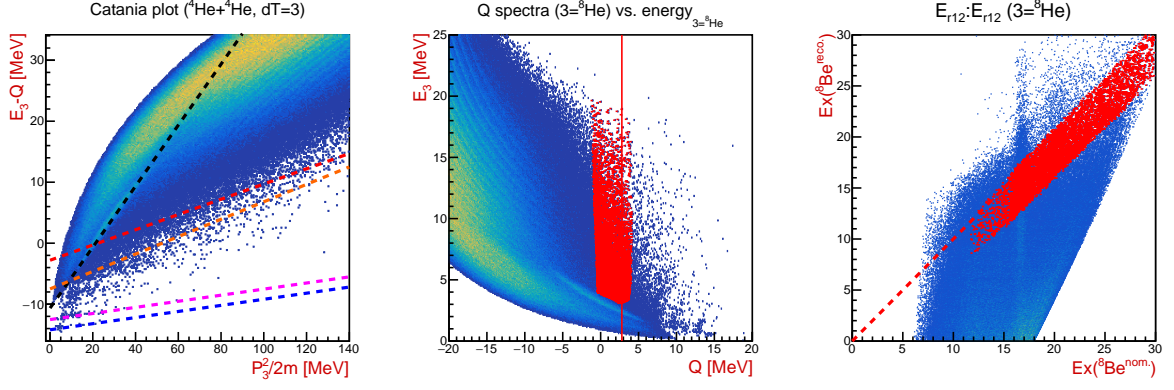

Figure 4.54: Catania plot and Q value spectrum for the ^{4}He+^{4}He coincident events in the dT=2 telescope combination, with identified and indicated exit channels as listed in Table 4.35. Data selected for the reaction on the ^{7}Li target are shown with red markers. Right side of the figure shows ^{8}Be excitation energy comparison spectrum with the assumption of the reaction on the ^{7}Li target.

For the dT=2 case, data selection for the reaction on the ^{7}Li target (Fig. 4.54) was made using a wide Q value cut tailored by the requirement that $\Delta\phi_{12}^{\text{reco.}}$ is constrained by the physically possible range of the relative angle: $[65°, 175°]$. As with previous case, large contribution to the background is coming from the many-body reactions, as well as from reaction on the ^{1}H target. Since these contributions couldn't be excluded, they are expected to deteriorate the resolution, but are not expected to introduce any prominent fake peak. The relative $\Delta\phi_{12}^{\text{reco.}}$ value was used to calculate the excitation energy of the ^{8}Be, and the cut was made for events up to 20 MeV in the ^{8}Be excitation for the ^{12}Be excitation energy projection spectrum (Fig. 4.55), to exclude the contribution of the states at 16.63 MeV (2^+) and 16.92 MeV (2^+), and a wide peak at 11.35 MeV (4^+).

Despite the mentioned difficulties in obtaining the final results, it's clearly seen that the results of the fit for the dT=2 (Table 4.37) and dT=3 (Table 4.36) cases do agree and indicate that the same states in the energy range below 17 MeV in dT=3 and below 21 MeV in dT=2 combination are observed, as in the ^{4}He+^{8}He coincidences, presented previously and summarized in Table 4.38. In the excitation energy spectra, presented on Fig. 4.55, one can see noticeable difference in the behaviour of the data and calculated geometrical efficiency, which happens due to the increase in the background from the interference of the states in ^{8}Be nuclei, even though strongest contributions from the

states up to ~ 20 MeV are excluded in both cases. Since the excited states below $\sim 17\text{-}18$ MeV are not affected as much by the ^{8}Be contributions, these results are observed clearly and do agree very well with previously presented spectra from the reaction on the ^{7}Li target.
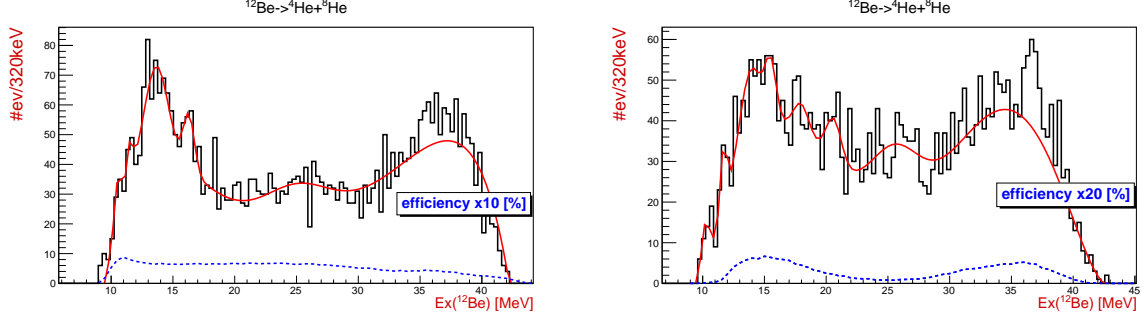
Figure 4.55: Excitation energy spectra for the sum of ^{12}Be$_{13}$ and ^{12}Be$_{23}$, from the ^{7}Li(^{9}Li, ^{4}He^{4}He)^{8}He reaction. The ^{4}He+^{4}He pair was detected in either dT=3 (left) or dT=2 (right) combination, while undetected particle is ^{8}He. The results of the fit are listed Table 4.36 for the dT=3 and Table 4.37 for the dT=2 case.

Ex [MeV]	10.6	11.5	13.7	16.2	background
norm [events]	14.4	12.5	30.4	18.9	
σ [MeV]	0.3	0.3	0.9	0.4	pol6 + gaus(25.0)

Table 4.36: Results of the fit for the sum of ^{12}Be$_{13}$ and ^{12}Be$_{23}$ excitations from the ^{7}Li(^{9}Li, ^{4}He^{4}He)$_{\mathrm{dT}=3}$^{8}He reaction, presented on the left side of Fig. 4.55.

Ex [MeV]	10.2	11.7	13.8	15.5	18.0	20.6	background
norm [events]	13.6	16.7	19.8	14.4	7.2	11.1	
σ [MeV]	0.4	0.3	0.9	0.5	0.6	0.6	pol6 + gaus(25.5)

Table 4.37: Results of the fit for the sum of ^{12}Be$_{13}$ and ^{12}Be$_{23}$ excitations from the ^{7}Li(^{9}Li, ^{4}He^{4}He)$_{\mathrm{dT}=2}$^{8}He reaction, presented on the right side of Fig. 4.55.

Summary table of the observed states: $^{12}\text{Be} \to {}^4\text{He} + {}^8\text{He}$

$^4\text{He}+{}^8\text{He}$ ↓ ‖ Ex [MeV] →	10.3	(12.1)	13.8	15.6	17.5	(19.8)	(22.3)
$^7\text{Li}({}^9\text{Li}, {}^4\text{He}{}^8\text{He})_{dT=3}{}^4\text{He}$ (23)	×	×	●	○	○	○	○
$^7\text{Li}({}^9\text{Li}, {}^4\text{He}{}^8\text{He})_{dT=2}{}^4\text{He}$ (23)			○	●	●	●	○
$^7\text{Li}({}^9\text{Li}, {}^4\text{He}{}^8\text{He})_{dT=3}{}^4\text{He}$ (12)				○	●	○	○
$^7\text{Li}({}^9\text{Li}, {}^4\text{He}{}^8\text{He})_{dT=2}{}^4\text{He}$ (12)				○	○	○	○
$^7\text{Li}({}^9\text{Li}, {}^4\text{He}{}^8\text{He})_{dT=1}{}^4\text{He}$ (12)	●	○	○	●	○		
$^7\text{Li}({}^9\text{Li}, {}^4\text{He}{}^8\text{He})_{dT=0}{}^4\text{He}$ (12)	●	○					
$^7\text{Li}({}^9\text{Li}, {}^4\text{He}{}^4\text{He})_{dT=3}{}^8\text{He}$ (13+23)	○	○	●	●	×	×	×
$^7\text{Li}({}^9\text{Li}, {}^4\text{He}{}^4\text{He})_{dT=2}{}^8\text{He}$ (13+23)	○	○	○	○	●	○	×
$^{19}\text{F}({}^9\text{Li}, {}^4\text{He}{}^8\text{He})_{dT=3}{}^{16}\text{O}$ (12)				○	●	○	○
$^{19}\text{F}({}^9\text{Li}, {}^4\text{He}{}^8\text{He})_{dT=2}{}^{16}\text{O}$ (12)			×	○	○	×	×
$^{19}\text{F}({}^9\text{Li}, {}^4\text{He}{}^8\text{He})_{dT=1,0}{}^{16}\text{O}$ (12)	○	○	○				
$^6\text{Li}({}^9\text{Li}, {}^4\text{He}{}^8\text{He})_{dT=1}{}^3\text{He}$ (12)	●						

Table 4.38: Results for the $^4\text{He}+{}^8\text{He}$ decay of the ^{12}Be excited states from the observed reactions on the LiF target. Clear peaks with good statistics are shown with ● symbol, while peaks with lower statistics and/or background interference are shown with ○ symbol. Low quality peaks observed in other data sets, but not seen clearly and/or are at the edge of the phase space are shown with × symbol.

4.3 Decays of the ^{13}B excited states

4.3.1 ^{9}Li+^{4}He decay channel

The decay of the ^{13}B excited states to the ^{9}Li+^{4}He pair is observed through the analysis of the ^{7}Li(^{9}Li, ^{9}Li^{4}He)^{3}H and ^{19}F(^{9}Li, ^{9}Li^{4}He)^{15}N reactions, where the "1-2" combination of the particles in the reaction exit channel corresponds to the ^{13}B states. Detected ^{9}Li can be observed in either ground ($3/2^-$) or 2.69 MeV ($1/2^-$) excited state. This is best seen in the analysis of the dT=3 case from the reaction on the ^{7}Li target (Fig. 4.56) and was confirmed in the Catania plot and Q value spectra for the case where all three of the particles in the exit channel were detected. Due to the limited kinematic phase space, and because the results were only indicating observation of the well known states in the ^{7}Li nuclei, this case is not presented. The same goes for the results of the analysis for the coincident detection of the ^{9}Li+^{3}H and ^{4}He+^{3}H pairs in the dT=3 and dT=2 combinations, from the reaction on the ^{7}Li target, where the states in the ^{13}B are expected to be observed through the "1-3" combination of the particles. Due to the kinematic phase space covered in these cases for the Ex(^{13}B)$> \sim 25$ MeV, the ^{13}B states were not observed in those data sets. Concerning the reaction on the ^{19}F target, undetected ^{15}N nucleus is observed in either the ground ($1/2^-$) or 6.32 MeV excited ($3/2^-$) state, which for the ^{13}B states studied here is important only in the data selection process and the reconstruction of the relative $\Delta\phi_{12}^{\text{reco.}}$ angle (Eq. 3.22). Although the 6.32 MeV state is the third excited state in ^{15}N nuclei, coming after 5.27 ($5/2^+$) and 5.30 ($1/2^+$) MeV states, it was concluded from the relative Q value difference from the ^{15}N ground state that it's the one contributing to the observed data (Fig. 4.56). No significant contribution from the ^{6}Li target is observed, and can be expected that this data contributes to the background in the spectra for the reactions on ^{7}Li target no more than ~ 5 %. Color coding to show the data selection and the expected Q values for the observed reactions are listed in Table 4.39.

As with all of the case studies presented so far, when the excited states of the particular nuclei, in this case the ^{13}B, are observed through the "1-2" combination of the particles in the exit channel, different "dT" cases provide sampling of the relative energy intervals: from the highest exitations observed in the dT=3 and dT=2 cases, to excitations near

reaction	^{7}Li(^{9}Li, ^{9}Li^{4}He)^{3}H	^{19}F(^{9}Li, ^{9}Li^{4}He)^{15}N	^{6}Li(^{9}Li, ^{9}Li^{4}He)^{2}H
Q [MeV]	-2.46	-4.01	-1.48
color	red	purple	no color

Table 4.39: The Q values and color coding used for the three-body reaction channels observed in the data for the ^{9}Li+^{4}He coincident events in all detector combinations. Since there was no contribution to the data from the reaction on the ^{6}Li target it wasn't labeled. The excited 2.69 MeV (1/2$^-$) state of the detected ^{9}Li from the reaction on the ^{7}Li target (Q = -5.15 MeV) is labeled in blue, while the excited 6.32 MeV (3/2$^-$) state of the undetected ^{15}N from the reaction on the ^{19}F target (Q = - 10.33 MeV) is labeled in pink.

the particle decay threshold in the dT=1 and dT=0 cases. The treshold for the decay of the ^{13}B excited states to the ^{9}Li+^{4}He pair is at 10.82 MeV. Results are presented starting from the reactions on the ^{7}Li target, followed by the ^{19}F target and respecting dT=3 to dT=0 ordering.

^{7}Li(^{9}Li, ^{9}Li^{4}He)^{3}H reaction

In the data analysis process and the interpretation of the results for the ^{9}Li+^{4}He decays of the ^{13}B excited states, produced in the reaction on the ^{7}Li target, an additional precaution has to be taken, as the detected ^{9}Li could have been detected in either the ground or excited state. For the dT=3 case, where the best resolution is expected, presence of the ^{9}Li excited state can clearly be seen in the data selection spectra presented on Fig. 4.56. By iteratively treating the width of the Q value data selection cut, the mixing of these two states was minimized in the final results and quality of the cut was confirmed in the MC simulations. By treating the ground state data as the excited state ones, a systematic shift of ~ 3 MeV was observed for the states presented on the left side of Fig. 4.59 showing the ground state data. Vice versa, using the simulated MC spectra for the decay of the ^{13}B excited states to the excited state of the ^{9}Li, a systematic shift of $\sim$ -3 MeV was observed in the data, when it was treated as a ground state data. This fact should be taken into account when comparing the results of the fit for the ground and the excited state of the detected ^{9}Li for the dT=3 case, presented on Fig. 4.59. This will be further explained in the text.

For both of the ^{13}B excitation energy projections, shown on Fig. 4.59, a cut at 9 MeV in ^{7}Li excitation energy was made to exclude the contributions from the 4.65 MeV (7/2$^-$), 6.60 MeV (5/2$^-$) and 7.45 MeV (7/2$^-$) states [106], and to obtain the clean spectra for
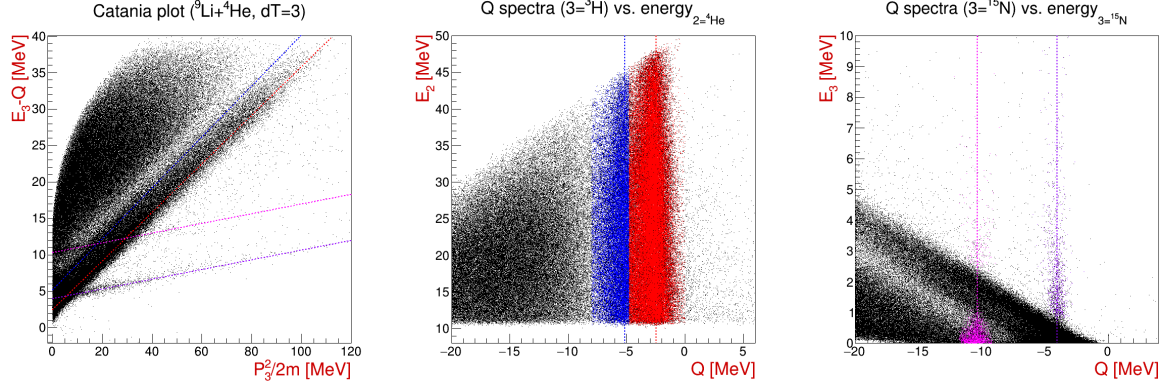
Figure 4.56: Catania plot and Q value spectra for the ^{9}Li+^{4}He coincident events in the dT=3 combination, with identified and labeled exit channels for the reactions on the ^{7}Li and ^{19}F targets. Data selected for the reaction on the ^{7}Li target is shown with red markers for the ^{9}Li detected in the ground state, while the blue markers indicate ^{9}Li detected in the 2.69 MeV excited state. For the reaction on ^{19}F target, purple markers indicate the ground state of the undetected ^{15}N, while the pink markers indicate the 6.32 MeV excited state of the ^{15}N.
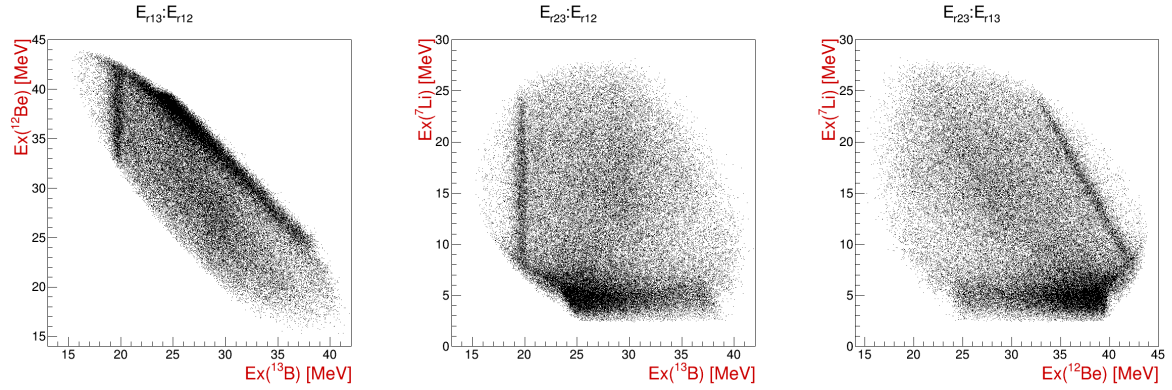
Figure 4.57: Excitation energy spectra for the ^{13}B$_{12}$, ^{12}Be$_{13}$ and ^{7}Li$_{23}$, from the ^{7}Li(^{9}Li, ^{9}Li^{4}He)$_{dT=3}$^{3}H reaction.
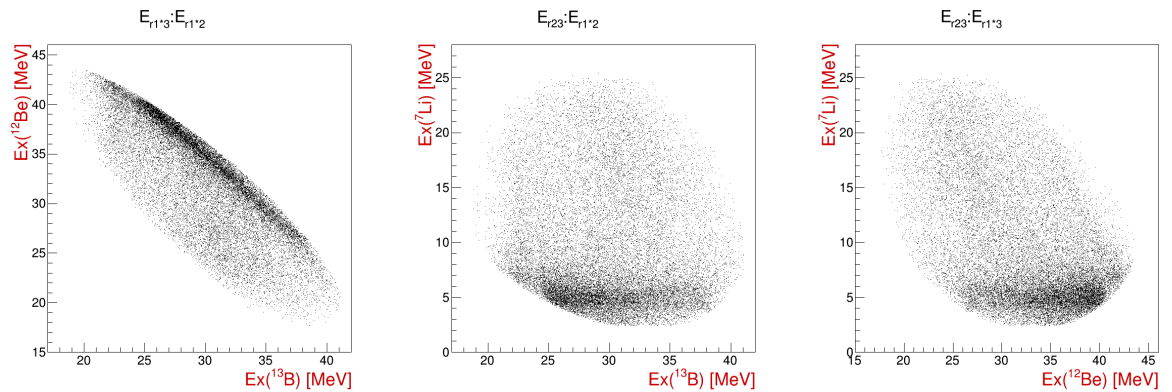
Figure 4.58: Excitation energy spectra for the ^{13}B$_{1*2}$, ^{12}Be$_{1*3}$ and ^{7}Li$_{23}$, from the ^{7}Li(^{9}Li, ^{9}Li$_{2.69}$^{4}He)$_{dT=3}$^{3}H reaction.

the ^{13}B excitations.

Comparing the results of the fit for the ^{13}B decay to the ground (Table 4.40) and excited

111
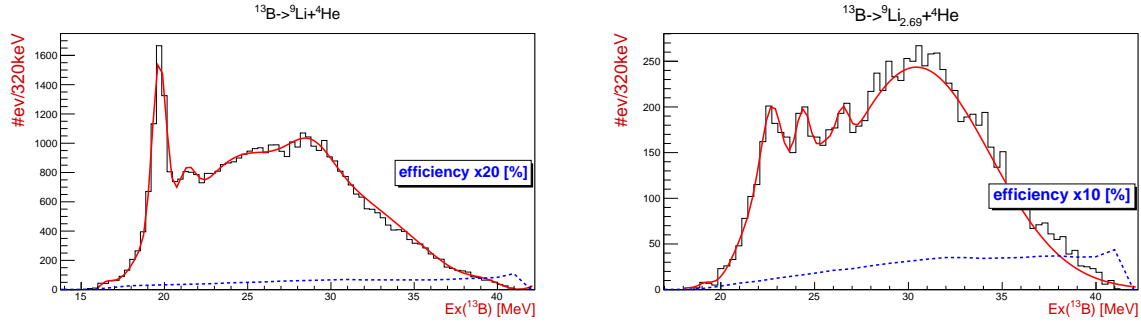
Figure 4.59: Excitation energy spectra for the $^{13}B_{12}$ and $^{13}B_{1*2}$, from the $^7Li(^9Li, {}^9Li^4He)_{dT=3}{}^3H$ reaction, where the detected ^9Li was in either ground (left) or 2.69 MeV excited state (right), respectively. Blue dashed lines represents the efficiency curve, while the red lines represent the results of the fit, which are listed in Tables 4.40 for "1-2" and 4.41 for "1*-2" combinations.

(Table 4.41) state of the ^9Li, it seems that most of the states in Table 4.41 can be reproduced by adding ~ 3 MeV to the values from Table 4.40, showing the results of the fit for the decay to the ground state. The peak observed at 26.5 MeV, being the only exception, can be considered as a candidate state for the ^{13}B decay to the excited state of the ^9Li, even though the unresolved wide peak ($\sigma = 2$ MeV) at ~ 24 MeV can be found in the ground state data. Because of the large width ($\sigma = 2$ MeV), the peak at ~ 24 MeV is more likely to be a part of the background. Apart from the candidate state at 26.5 MeV, from the behaviour of the rest of the data, it seems that the $^9Li^*$ contributed dominantly as a recoil particle in the reactions where the well known states in the ^7Li nuclei (4.65 MeV $(7/2^-)$, 6.60 MeV $(5/2^-)$ and 7.45 MeV $(5/2^-)$ were produced. Following this conclusion and expected much smaller contribution from the ^9Li excited states, for the dT=2 case all of the data were treated as the ground state data, as well as for dT=1 and dT=0 cases where the contributions from the ^9Li excited states are expected to be minor.

Ex [MeV]	(16.3)	(18.5)	19.7	21.3	(24.0)	(28.8)	background
norm [events]	(78)	(50)	1228	274	(130)	(162)	pol4
σ [MeV]	(0.5)	(0.4)	0.4	0.5	(2.0)	(2.0)	

Table 4.40: Results of the fit for the $^{13}B_{12}$ excited states from the $^7Li(^9Li, {}^9Li^4He)_{dT=3}{}^3H$ reaction, presented on the left side of Fig. 4.59. The detected ^9Li is in the ground $(3/2^-)$ state. The values in the brackets label ambiguous peaks, unresolved from the background.

In the ^{13}B excitation energy comparison spectra for the dT=2 case, presented on the right side of Fig. 4.60, it can be seen how the values of the $^{13}B_{12}^{nom.}$, dispersed due to the large uncertainty of the $\Delta\phi_{12}^{nom.}$, are gathered around the real value in the $^{13}B_{12}^{reco.}$ when the

Ex [MeV]	(19.2)	21.3*	22.7*	24.35*	26.5	background
norm [events]	(3.6)	40.5	159	114	49.5	gaus(25.5) + gaus(30.43)
σ [MeV]	(0.3)	0.7	0.7	0.5	0.4	

Table 4.41: Results of the fit for the ^{13}B$_{1*2}$ excited states from the ^{7}Li(^{9}Li, ^{9}Li$_{2.69}$^{4}He)$_{dT=3}$^{3}H reaction, presented on the right side of Fig. 4.59. The detected ^{9}Li is in the excited $(1/2^-)$ state. See text for the discussion on *.

Figure 4.60: Catania plot and Q value spectrum for the ^{9}Li+^{4}He coincident events in the dT=2 combination, with identified and labeled exit channels from the reactions on the ^{7}Li and ^{19}F targets. Data selected for the reaction on the ^{7}Li target are shown with red markers, for the ^{9}Li detected in the ground state. On the ^{13}B excitation energy comparison spectrum red dashed line indicates ideal case correlation between $\Delta\phi_{12}^{\text{reco.}}$ and $\Delta\phi_{12}^{\text{nom.}}$ cases, while the slope of the data is expected and can be reproduced in the MC simulations for the dT=2 case.

$\Delta\phi_{12}^{\text{reco.}}$ (Eq. 3.22) is used to calculate the excitation energy. The strong state at $\sim$ 19.6 is observed in both dT=3 and dT=2 cases. The slope of the data locus, coming from the reaction on the ^{7}Li target, can be reproduced in the MC simulations and is the result of the reconstruction of the relative $\Delta\phi_{12}$ angle, which has the largest uncertainty for the dT=2 case.

Looking at the relative (excitation) energy spectra for all of the particle combinations in the exit channel of the ^{7}Li(^{9}Li, ^{9}Li^{4}He)^{4}H reaction in dT=2 case (Fig. 4.61), noticeable smearing of the data can be observed, especially in the part of the phase space where Ex(^{7}Li) < 15 MeV. This behaviour was reproduced in the MC simulations when the simulated ^{13}B state $\sim$ 20 MeV, produced in the reaction on the ^{19}F target, was treated as belonging to the ^{7}Li data. Due to the large uncertainty in the $\Delta\phi_{12}^{\text{nom.}}$ for the dT=2 case, better separation could not be achieved without loosing a fair amount of statistics, especially in the critical range below 20 MeV in the excitation of ^{13}B. This effect was taken into account in the results, as a background in the projection shown on the left side
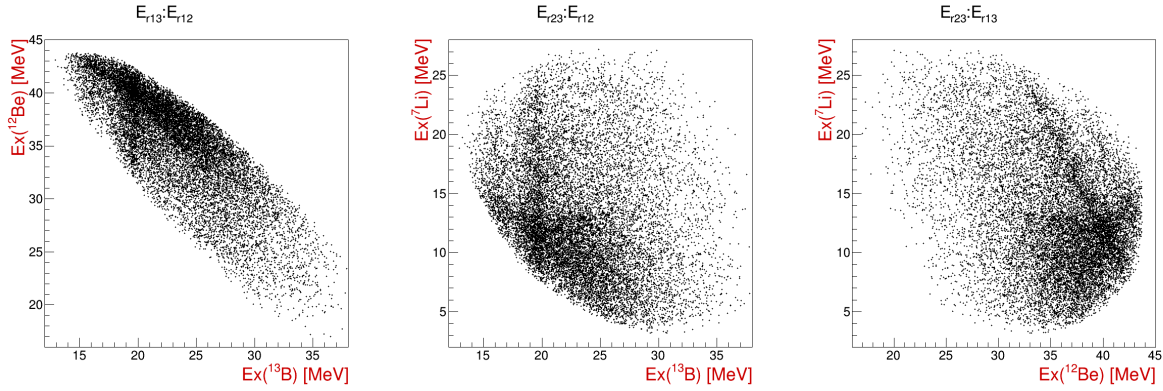
Figure 4.61: Excitation energy spectra for the ^{13}B$_{12}$, ^{12}Be$_{13}$ and ^{7}Li$_{23}$, from the ^{7}Li(^{9}Li, ^{9}Li^{4}He)$_{dT=2}$^{4}H reaction.

of Fig. 4.64. Detection efficiency calculation and the fit were done on the full projection of the excitation energy spectra for the ^{13}B, shown in Fig. 4.61, as a large amount of the statistics is coming from the affected range of energies. To confirm that this procedure does not introduce false peaks in the full projection, two extra projections were made. First one was made by making a cut at 10 MeV in the excitation energy of the ^{7}Li for the projection, to exclude possible contributions of the three well know states, mentioned in the text above, and a possible contribution from the group of wide states at 8.75 MeV $(3/2^{-})$, 9.09 MeV $(1/2^{-})$ and 9.57 MeV $(7/2^{-})$. For the second projection cut was placed at 15 MeV to exclude also the background events coming from the reaction on the ^{19}F target. As seen on the left side of Fig. 4.64, where two extra projections are shown with dashed black lines, these projections are much cleaner, but affected in the obtained statistics for the real peaks, which are listed in Table 4.42. To conclude, neither the states of ^{7}Li, nor the background events coming from the reaction on the ^{19}F target, are introducing fake peaks, thus the fit was preformed on the full spectrum (Fig. 4.61), taking the background into account.

Following the same reasoning for the dT=1 case, as for the dT=2 case, a strong contribution of the 13.7 MeV state (seen in Fig. 4.63) is observed by the characteristic behaviour of a real state in the ^{13}B excitation energy comparison spectrum, presented on the right side of the data selection spectra on Fig. 4.62.

The experimental resolution and the shape of the efficiency curve peaking at $\sim$ 12 MeV shift the excitation energy spectrum for the dT=1 case, shown on Fig. 4.64, at lower excitations, but indication for the possible state candidate at $\sim$ 12 MeV are present. This state is not included in the results of the fit, shown in Table 4.42, as the background
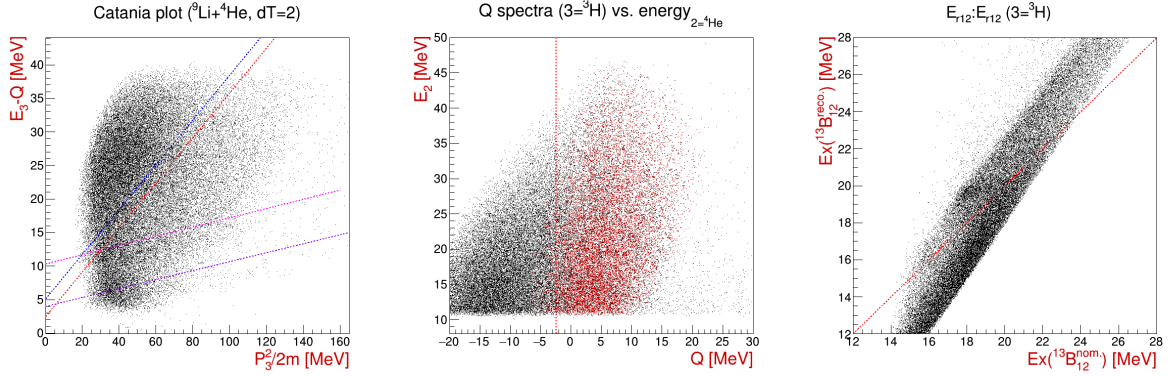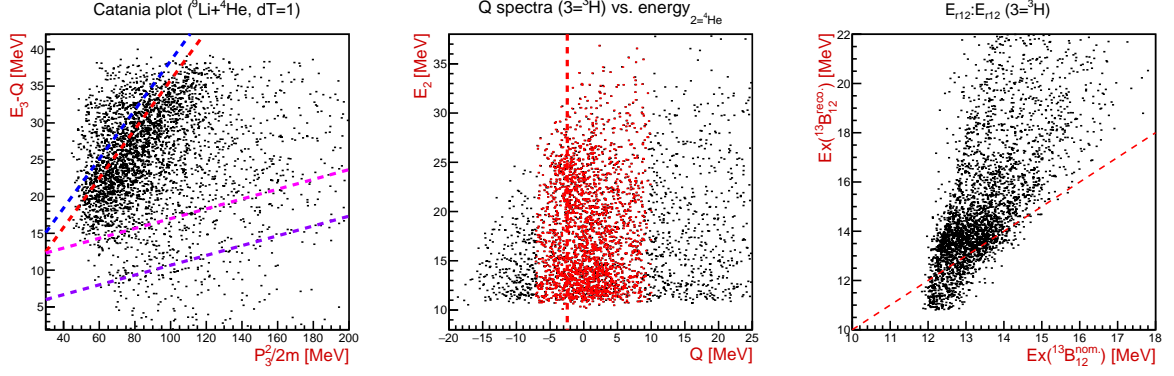
Figure 4.62: Catania plot and Q value spectrum for the ^{9}Li+^{4}He coincident events in the dT=1 combination, with identified and labeled exit channels for the reactions on the ^{7}Li and ^{19}F targets, as in Table 4.39. On the ^{13}B excitation energy comparison spectrum red dashed line indicates ideal case correlation between $\Delta\phi_{12}^{\text{reco.}}$ and $\Delta\phi_{12}^{\text{nom.}}$ cases.
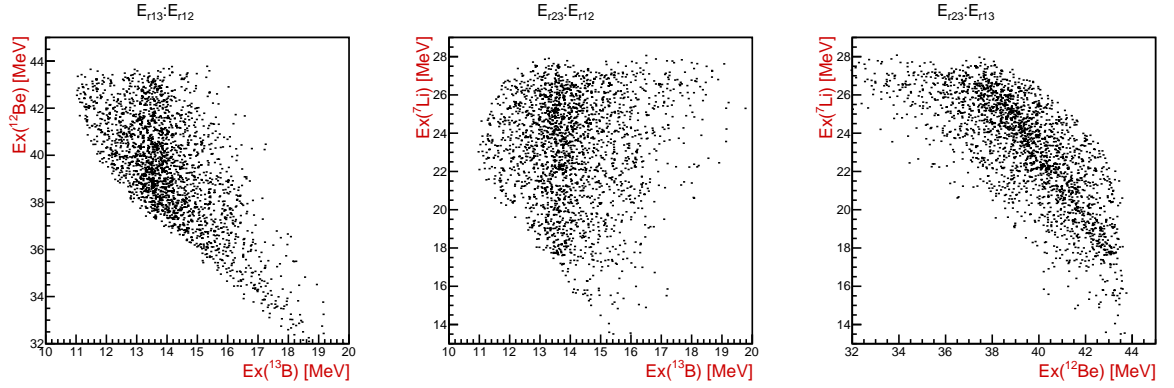
Figure 4.63: Excitation energy spectra for the ^{13}B$_{12}$, ^{12}Be$_{13}$ and ^{7}Li$_{23}$, from the ^{7}Li(^{9}Li, ^{9}Li^{4}He)$_{dT=1}$^{4}He reaction.
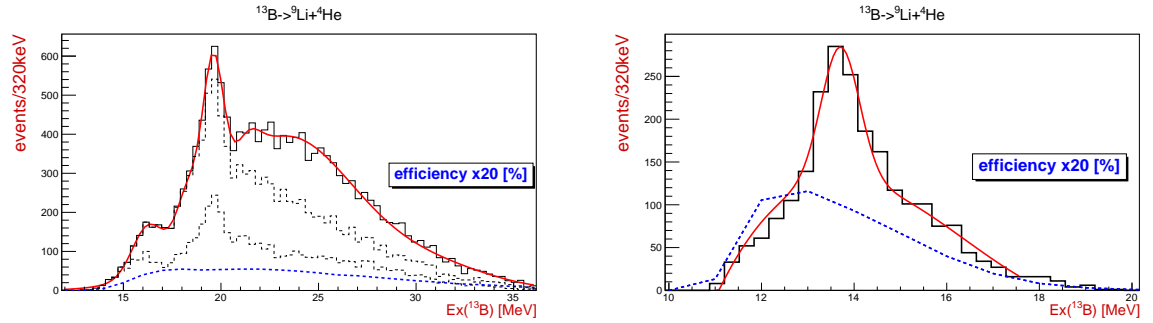
Figure 4.64: Excitation energy spectra for the ^{13}B$_{12}$ from the ^{7}Li(^{9}Li, ^{9}Li^{4}He)^{3}H reaction, for the dT=2 (left) and dT=1 (right) cases. Detected ^{9}Li was (dominantly) in the ground $(3/2^-)$ state. The results of the fit are listed in Table 4.42 for both cases. Two extra projections for the dT=2 case, which differ in the applied cut on the ^{7}Li excitation energy (see text for details), are shown with black dashed lines.

modeled to match the efficiency curve and one Gaussian peak were sufficient to describe the shape of the spectrum.

For the dT=0 case, due to the low statistics for the identified exit channels from the

Ex [MeV]	[13.7]	16.2	(18.3)	19.6	(21.4)	background
norm [events]	[155]	111	(133)	373	(68)	gaus(23.3) + gaus(31.0)
σ [MeV]	[0.4]	0.8	(0.5)	0.5	(0.6)	[pol3]

Table 4.42: Results of the fit for the $^{13}B_{12}$ excited states from the $^{7}Li(^{9}Li, \, ^{9}Li^{4}He)^{3}H$ reaction, for the dT=2 and dT=1 ([] brackets) cases, presented on Fig. 4.64, respectively. The detected ^{9}Li was in the ground $(3/2^{-})$ state.

reactions on the ^{7}Li and ^{19}F target, relative energies spectra are not shown. Instead, the ^{13}B excitation energy comparison spectrum is shown (Fig. 4.66), with only a small part of the data coming from the $^{7}Li(^{9}Li, \, ^{9}Li^{4}He)^{3}H$ reaction. Other data is coming in part from the reactions on the ^{19}F target, while the rest are coming from many-body contributions, such as $^{2}H+n$ or $^{1}H+n+n$ as a recoil. Since the ^{13}B excitation energy, calculated using $\Delta\phi_{12}^{\mathrm{nom.}} = 0°$ is unaffected by the exit channel identification, as there are no assumptions in the calculation, one can see both identified and unidentified data contributions to the excitation energy spectrum.
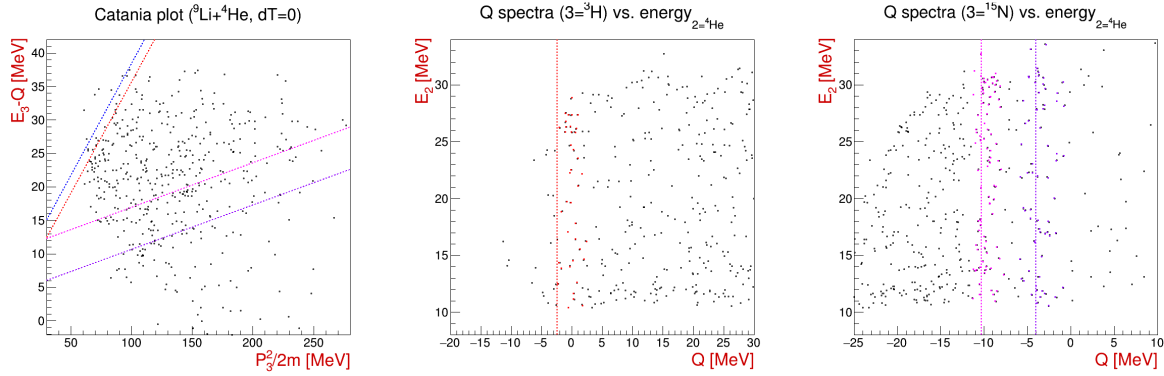
Figure 4.65: Catania plot and Q value spectrum for the $^{9}Li+^{4}He$ coincident events in the dT=0 combination, with identified and labeled exit channels for the reactions on ^{7}Li (red) and ^{19}F (purple, pink) targets, color coded as in Table 4.39.

If these considerations are taken into account, a possible indication of the ^{13}B excited state at ~ 12 MeV can be weakly observed, especially taking the unidentified contributions coming from the many-body exit channels from the reaction on the ^{7}Li and ^{19}F. Note that the observed states have a systematic shift of a $\sim$ -500 keV compared to the values obtained for the previously observed state at ~ 13.5 MeV, which is more clearly seen in this spectrum also.
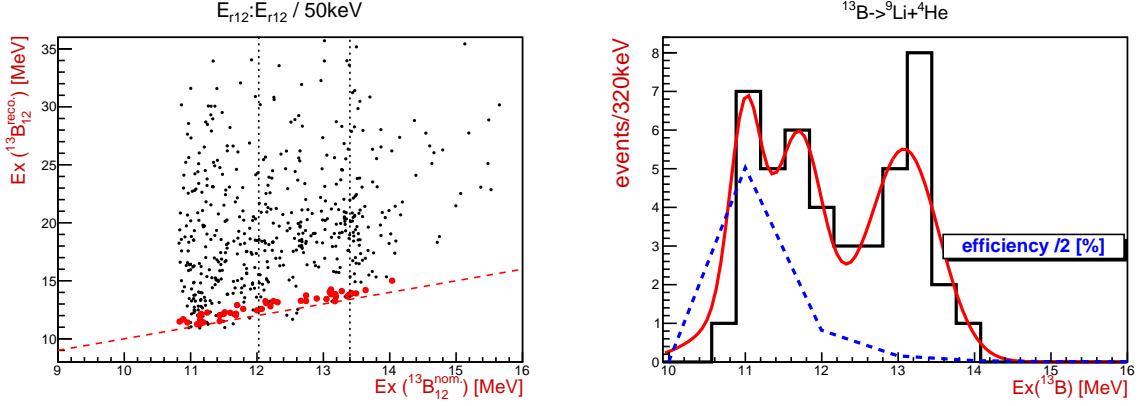
Figure 4.66: Excitation energy comparison spectrum for the ^{13}B$_{12}$ (left), calculated using $\Delta\phi_{12}^{\text{reco.}}$ (ordinate) and $\Delta\phi_{12}^{\text{nom.}} = 0°$ (abscissa) values, and ^{13}B excitation energy spectrum (right) for the ^{7}Li(^{9}Li, ^{9}Li^{4}He)$_{\text{dT}=0}$^{3}H reaction.

Ex [MeV]	(11.7)	13.1	background
norm [events]	(4.1)	5.4	gaus(11.0) + gaus(11.4)
σ [MeV]	(0.3)	0.5	

Table 4.43: Results of the fit for the ^{13}B$_{12}$ excited states from the ^{7}Li(^{9}Li, ^{9}Li^{4}He)$_{\text{dT}=0}$^{3}H reaction, presented in Fig. 4.66. The shape of the background mirrors the detection efficiency curve. The observed peaks have a systematic shift of a $\sim$ -500 keV compared to the values from the previous datasets.

^{19}F(^{9}Li, ^{9}Li^{4}He)^{15}N reaction

Continuing with the ^{9}Li+^{4}He coincident events study, results for decays of the ^{13}B excited states, produced in the reactions on the ^{19}F target: ^{19}F(^{9}Li, ^{9}Li^{4}He)^{15}N and ^{19}F(^{9}Li, ^{9}Li^{4}He)^{15}N$_{6.32}$ are presented. As mentioned in the introduction to this section, undetected ^{15}N nucleus was detected in either the ground or the 6.32 MeV excited state, as observed by the relative difference in the Q value spectrum for the best resolution dT=3 case (Fig. 4.56). From ^{13}B observation standpoint, ^{15}N is viewed as a recoil particle, thus affects only the data selection for the particular exit channel and the real Q value which serves as input parameter in the relative $\Delta\phi_{12}^{\text{reco.}}$ angle reconstruction. Results are presented starting from dT=3 to dT=0 case, while the data selection spectra are presented in previous subsection. As noticed in relative energy spectra for the dT=2 case (Fig. 4.61) presented in the ^{7}Li section (Sec. 4.3.1), due to the large uncertainty in the relative $\Delta\phi_{12}^{\text{nom.}}$ angle, contributions from these two targets were not completely separated. This led to the blurring of the data and low resolution in one part of that spectra, most likely

due to the strong contribution of the 19.7 MeV state in ^{13}B, produced in the reaction on the ^{19}F target.
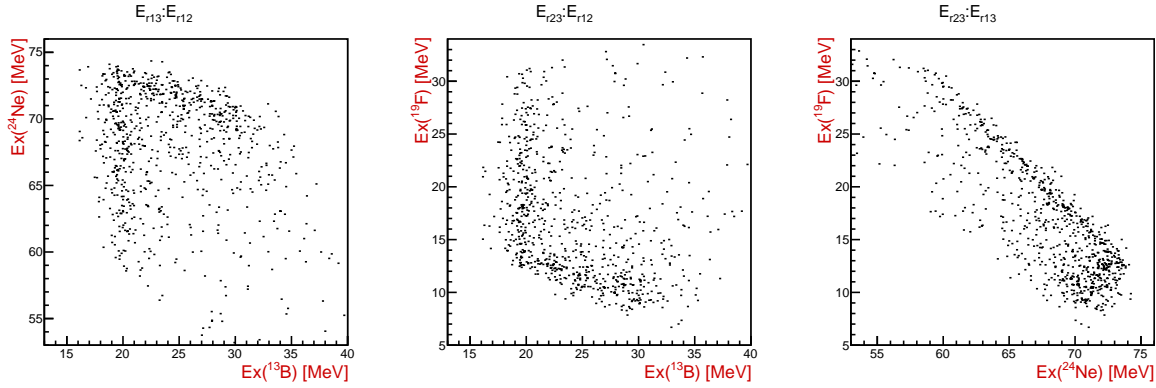
Figure 4.67: Excitation energy spectra for the ^{13}B$_{12}$, ^{24}Ne$_{13}$ and ^{19}F$_{23}$, from the ^{19}F(^{9}Li, ^{9}Li^{4}He)$_{dT=3}$^{15}N reaction. The undetected ^{15}N is in the ground $(1/2^-)$ state.
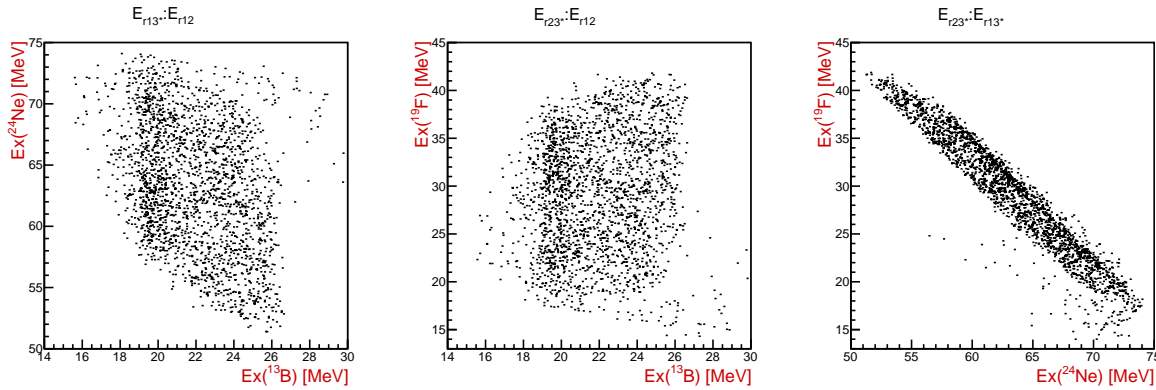
Figure 4.68: Excitation energy spectra for the ^{13}B$_{12}$, ^{24}Ne$_{13*}$ and ^{19}F$_{23*}$, from the ^{19}F(^{9}Li, ^{9}Li^{4}He)$_{dT=3}$^{15}N$_{6.32}$ reaction. The undetected ^{15}N is in the 6.32 MeV $(3/2^-)$ excited state.
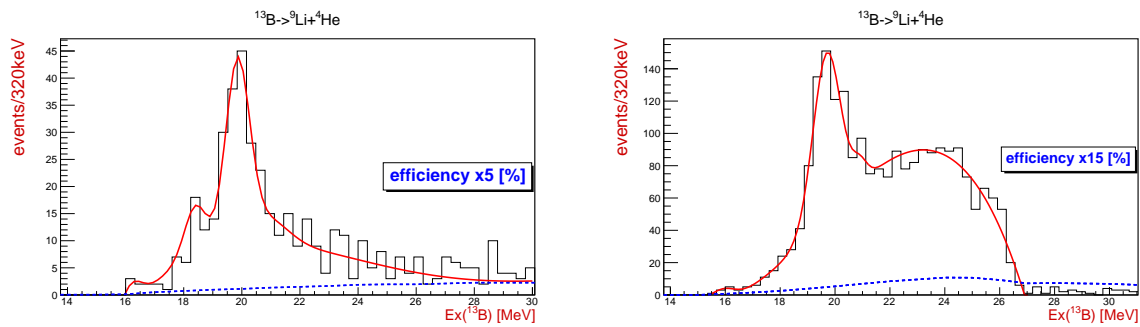
Figure 4.69: Excitation energy spectra for the ^{13}B from the ^{19}F(^{9}Li, ^{9}Li^{4}He)^{15}N (left) and ^{19}F(^{9}Li, ^{9}Li^{4}He)^{15}N$_{6.32}$ (right) reactions. The ^{9}Li+^{4}He pair was detected in the dT=3 combination. The results of the fit are listed in Table 4.44 for both cases.

Observation of the strong 19.7 MeV state in ^{13}B for both cases, where the recoil ^{15}N was in either ground or 6.32 MeV excited state, justifies the data selection for the latter exit

channel, skipping possible contributions from the neighbouring excited states based on the relative Q value difference from the ground state.

Ex [MeV]	(16.1)/[(15.9)]	(18.4)	19.9/[19.7]	(20.9)/[(20.9)]	background
norm [events]	(5.5)/[(6.0)]	(9)	32.6/[101.1]	(4.4)/[(12.1)]	pol4
σ [MeV]	(0.4)/[(0.5)]	(0.4)	0.4/[0.4]	(0.7)/[(0.3)]	[pol4]

Table 4.44: Results of the fit for the ^{13}B excited states from the ^{19}F(^{9}Li, ^{9}Li^{4}He)$_{\mathrm{dT}=3}$^{15}N and ^{19}F(^{9}Li, ^{9}Li^{4}He)$_{\mathrm{dT}=3}$^{15}N$_{6.32}$ ([] brackets) reactions, both presented on Fig. 4.69. The undetected ^{15}N was either in the ground $(1/2^-)$ state or 6.32 MeV excited $(3/2^-)$ state.

As a result of large uncertainty in the relative $\Delta\phi_{12}$ angle between detected particles, the data from the reaction on the ^{19}F target for the dT=2 case, seen in Fig. 4.60, remained unresolved from the dominant reactions on the ^{7}Li target. Explained in the previous section, the ^{19}F data were treated as a background in the relative energy spectra (Fig. 4.61) and in the projections for the ^{13}B excited states (Fig. 4.64). Being able to reproduce the background shape with the simulated 20 MeV excited state, treated as coming from the reaction on the ^{7}Li target, led to conclusion that the strong 19.7 MeV state is also produced in the reaction on the ^{19}F target for the dT=2 case. Due to the overall experimental uncertainty, it is not possible to estimate contributions from other states observed in reaction on the ^{7}Li target.

For the dT=1 case and the reaction on the ^{19}F target, the state at ~ 13.5 MeV is observed and although very low in statistics, higher excitation energy range (15-20 MeV) was fitted in search of contributions from already observed states in previous datasets. The background was modeled to the shape of the efficiency curve, shown on Fig. 4.70, and fitted with Gaussians to describe the overall shape of the spectra.
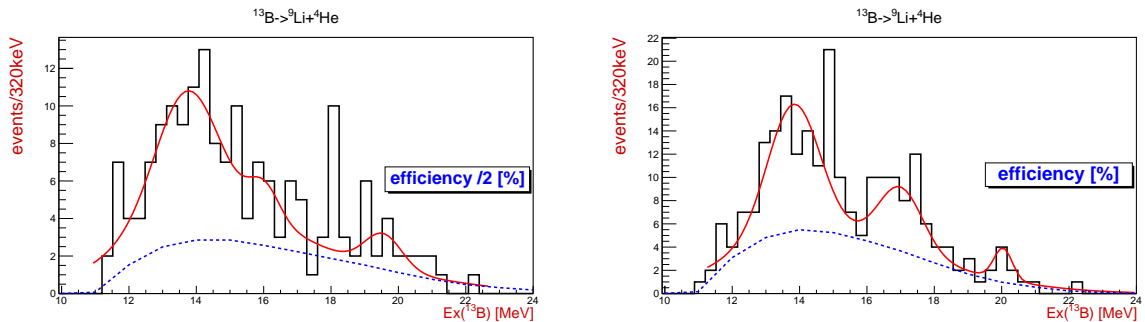
Figure 4.70: Excitation energy spectra for the ^{13}B from the ^{19}F(^{9}Li, ^{9}Li^{4}He)^{15}N (left) and ^{19}F(^{9}Li, ^{9}Li^{4}He)^{15}N$_{6.32}$ (right) reactions. The ^{9}Li+^{4}He pair was detected in the dT=1 combination. The results of the fit are listed in Table 4.45 for both cases.

Ex [MeV]	13.7/[13.8]	(15.9)	[17.0]	(18.5)	(20.2)/[(20.0)]	background
norm [ev.]	6.5/[11.0]	(1.8)	[5.5]	(1.8)	(2.2)/[(2.7)]	pol3
σ [MeV]	0.8/[0.8]	(0.5)	[0.7]	(0.5)	(0.9)/[(0.3)]	[gaus(13.8)+gaus(16.0)]

Table 4.45: Results of the fit for the ^{13}B excited states from the ^{19}F(^{9}Li, ^{9}Li^{4}He)$_{dT=1}$^{15}N and ^{19}F(^{9}Li, ^{9}Li^{4}He)$_{dT=1}$^{15}N$_{6.32}$ ([] brackets) reactions, both presented on Fig. 4.70. The undetected ^{15}N was either in the ground $(1/2^-)$ or 6.32 MeV excited $(3/2^-)$ state.

Due to the low data statistics for both reactions on ^{7}Li and ^{19}F targets, as seen in the data selection spectra for dT=0 case on Fig. 4.65, results for the dT=0 case are not shown separately here. Results from the ^{19}F target show a weak indication of the peak at ~ 12 MeV and more clearly the peak at 13.5 MeV, as observed previously in the ^{13}B excitation energy comparison spectra shown on Fig. 4.66.

Summary table of the observed states:^{13}B$\rightarrow$^{9}Li+^{4}He

^{9}Li+^{4}He ↓ || Ex [MeV] →	(12.3)	13.5	16.5	(18.5)	19.7	(21.2)
^{7}Li(^{9}Li, ^{9}Li^{4}He)$_{dT=3}$^{3}H			○	○	●	●
^{7}Li(^{9}Li, ^{9}Li^{4}He)$_{dT=2}$^{3}H			●	○	●	○
^{7}Li(^{9}Li, ^{9}Li^{4}He)$_{dT=1}$^{3}H	×	●				
^{7}Li(^{9}Li, ^{9}Li^{4}He)$_{dT=0}$^{3}H	○	●				
^{19}F(^{9}Li, ^{9}Li^{4}He)$_{dT=3}$^{15}N			○	○	●	×
^{19}F(^{9}Li, ^{9}Li^{4}He)$_{dT=3}$^{15}N*			×	○	●	○
^{19}F(^{9}Li, ^{9}Li^{4}He)$_{dT=1}$^{15}N	×	●	○	○		
^{19}F(^{9}Li, ^{9}Li^{4}He)$_{dT=1}$^{15}N*	×	●	●			
^{19}F(^{9}Li, ^{9}Li^{4}He)$_{dT=0}$^{15}N	○	○				
^{19}F(^{9}Li, ^{9}Li^{4}He)$_{dT=0}$^{15}N*	○	○				

Table 4.46: Results for the ^{9}Li+^{4}He decay of the ^{13}B excited states from the observed reactions on the LiF target. Clear peaks with good statistics are shown with ● symbol, while peaks with lower statistics and/or background interference are shown with ○ symbol. Low quality peaks observed in other data sets, but not seen clearly and/or are at the edge of the phase space are shown with × symbol.

4.3.2 ^{7}Li+^{6}He decay channel

In this subsection, study of the ^{7}Li+^{6}He decays of the ^{13}B excited states, produced in the reactions of the ^{9}Li beam on LiF target, are presented. Due to the fact that kinematical phase space covered, in most cases, by the ^{7}Li+^{6}He+^{3}H, ^{7}Li+^{6}He, ^{7}Li+^{3}H and ^{6}He+^{3}H coincidences corresponds only to the highest excitation energy range (>25 MeV) in ^{13}B, these results are insufficient to provide strong conclusion on the existence of this decay mode. A major disadvantages are low data statistics and the obtained experimental resolution at these energies, further affected by the inability to separate contributions from the ground ($3/2^-$) and the first excited (0.48 MeV, $1/2^-$) state of the ^{7}Li nuclei produced in the reactions of interest. Fortunately, for the ^{7}Li+^{6}He coincidences in the dT=2 and dT=1 cases, a lower excitation energy range from 16 to 22 MeV is covered. Results for the latter cases are directly comparable to the results obtained for the ^{9}Li+^{4}He decay channel. Particle decay threshold for the ^{7}Li+^{6}He decay is at 15.94 MeV.

^{7}Li(^{9}Li, ^{7}Li^{6}He^{3}H)

For the coincident detection of the ^{7}Li+^{6}He+^{3}H triple events, clean identification is obtained by imposing cuts on the Q value spectrum, similar to the ^{10}Be case presented on Fig. 4.1. As the real Q value for the ^{7}Li(^{9}Li, ^{7}Li^{6}He^{3}H) reaction is -7.59 MeV, the Q value of -7.8 MeV ($\sigma = 0.5$ MeV), obtained from the fit on the projection indicates the shift of -200 keV total energy. Even though this value is small on the scale of the total energy available in the exit channel (~ 70 MeV) and it's comparable to previously observed shifts of ~ 100 keV for coincident detection of all particles in the exit channel, it may be due to the contribution of the detection of the first excited state of the ^{7}Li at 0.48 MeV. As the ground state contribution is expected to dominate the data and taking low experimental resolution into account, all of the data was treated as coming from the ground state of detected ^{7}Li.

Even though obtained statistics is very low, an indication for the ^{13}B excited state at ~ 26.3 MeV, decaying to ^{7}Li+^{6}He pair, is observed in the data (Fig. 4.71). Direct comparison to the ^{9}Li*+^{4}He data, presented on Fig. 4.59, can be made as the peak at ~ 26.5 MeV, observed in that spectrum, remained the only candidate for the real state in ^{13}B decaying to ^{9}Li* channel, as it didn't fit the picture of missidentified ^{9}Li ground state data. It is possible that these peaks are coming from the same state in ^{13}B, although

obtained statistics is very low for both cases, so the existence of either peak can not be claimed. Unfortunately, the same state is not observed clearly in neither of the ^{7}Li+^{6}He, ^{7}Li+^{3}H or ^{6}He+^{3}H coincidences to have any additional confirmation of the existence of this state.
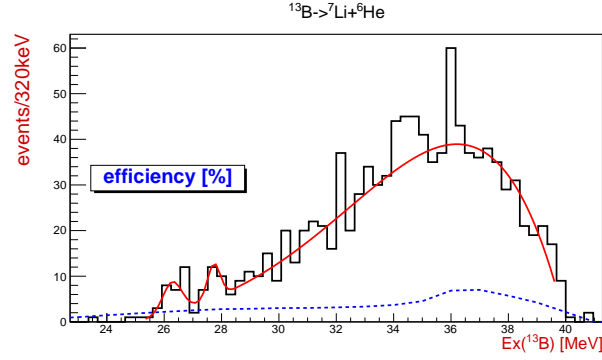
Figure 4.71: Excitation energy spectrum for the ^{13}B$_{12}$ from the ^{7}Li(^{9}Li, ^{7}Li^{6}He^{3}H) reaction. The results of the fit are listed in Table 4.47.

As already mentioned in text before, not all peaks that are fitted are considered as states and this can be said for the peak at 27.7 MeV (Table 4.47) which is not observed clearly in the relative energy spectra and has σ of the Gaussian fit of 200 keV, much smaller than expected experimental resolution of $\sim$ 400-500 keV (σ) in that energy range.

Ex [MeV]	26.3	27.7*	background
norm [events]	6.7	7.5	pol6
σ [MeV]	0.3	0.2	

Table 4.47: Results of the fit for the ^{13}B excited states from the ^{7}Li(^{9}Li, ^{7}Li^{6}He^{3}H) reaction, presented on Fig. 4.71. See text for details on the *.

^{7}Li(^{9}Li, ^{7}Li^{6}He)^{3}H

For the coincident detection of the ^{7}Li+^{6}He events, a major contribution to the overall experimental resolution is the inability to separate the 0.48 MeV ($1/2^-$) excited state of the detected ^{7}Li from the ($3/2^-$) ground state. Even though no significant contributions from the reactions on the ^{19}F and ^{6}Li targets were found, and the data selected in the final analysis is dominantly coming from the reaction on the ^{7}Li target, this inability to exclude the contributions from the excited state of the detected ^{7}Li greatly affects the resolution obtained in the reconstruction of the relative $\Delta\phi_{12}^{\text{reco.}}$ angle, and consequently

the excitation energy, as systematic error is included in the calculation whenever the excited state is detected instead of the ground state. The same observation can be made for the ^{7}Li+^{3}H and the ^{6}He+^{3}H coincidences, where ^{7}Li is undetected reaction product.

reaction	^{7}Li(^{9}Li, ^{7}Li^{6}He)^{3}H	^{19}F(^{9}Li, ^{7}Li^{6}He)^{15}N	^{6}Li(^{9}Li, ^{7}Li^{6}He)^{2}H
Q [MeV]	-7.59	-9.14	-6.60
color	red	blue	no color

Table 4.48: The Q values and color coding used for the three-body reaction channels observed in the data for the ^{7}Li+^{6}He coincident events in all detector combinations. The data is dominated by the reactions on the ^{7}Li target and no significant contributions from the reactions on the ^{19}F and ^{6}Li targets were observed.

Since the dT=3 and dT=2 cases lack the resolution to study the ^{7}Li+^{6}He decays of the 26.5 MeV and 19.5 MeV states, only the dT=1 case is presented here.

Figure 4.72: Catania plot and Q value spectrum for the ^{7}Li+^{6}He coincident events in the dT=1 combination, with identified and labeled exit channel from the reaction on the ^{7}Li target marked in red. On the right side of the figure ^{13}B excitation energy comparison spectrum is shown.

Even though systematic shift is observed in the data selection spectra for the dT=1 case, presented on Fig. 4.72, caused by the use of nominal $\Delta\phi_{12}^{\text{nom.}} = 60°$ value in the momentum reconstruction, it is plausible to expect that selected data is most likely coming solely from the reaction on the ^{7}Li target, as no contribution from the ^{19}F or ^{6}Li targets were observed in the dT=3, or any other, case where the resolution in Q value and Catania plot is acceptable. Although, one should expect contributions from the ^{7}Li excited state (0.48 MeV) to affect the final resolution.

To make comparison of the data from the ^{7}Li+^{6}He decay channel possible, with the states observed in the ^{9}Li+^{4}He decay channel (Tables 4.40 and 4.42), spectrum on the Fig. 4.73 was fitted with three Gaussian functions on top of the smooth background described by
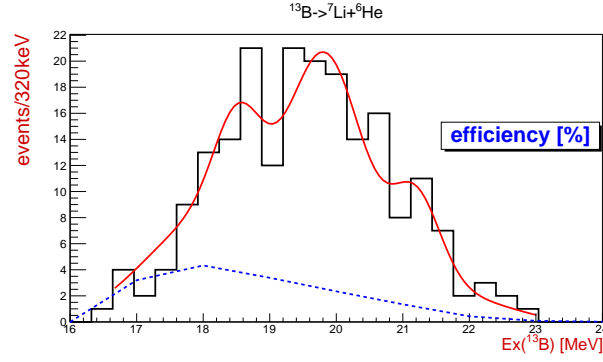
Figure 4.73: Excitation energy spectrum for the $^{13}B_{12}$ from the $^7Li(^9Li, {}^7Li^6He)_{dT=1}{}^3H$ reaction. The results of the fit are listed in Table 4.49.

the general shape of the detection efficiency curve. Although there is large uncertainty in the fitted spectrum, due to the resolution and unresolved contribution from the excited state of the detected ^7Li nucleus, peaks in Table 4.49 indicate that same states as in the $^9Li+^4He$ decay channel are observed here.

Ex [MeV]	(18.5)	19.5	(21.2)	background
norm [events]	18.5	19.8	21.2	gaus(18)+gaus(19.7)
σ [MeV]	0.4	0.5	0.4	

Table 4.49: Results of the fit for the ^{13}B excited states from the $^7Li(^9Li, {}^7Li^6He)_{dT=1}{}^3H$ reaction, presented on Fig. 4.73.

For the dT=0 case, in the ^{13}B excitation energy comparison spectrum a weak locus at $\sim$ 16.5 MeV in $^{13}B_{12}^{nom.}$ is observed. This characteristic behaviour in the excitation energy comparison spectrum is usually seen in many-body reactions (^2H+n and $^1H+n+n$ as "recoil"), when the assumption of the three-body reaction is not valid, but the nominal $\Delta\phi=0°$ yields correct excitation energy, with systematic error due to the use of the nominal $\Delta\phi$ value. Due to the low quality of dT=0 data, this case is not presented here. Observed states in the $^7Li+^6He$ and $^{10}Be+^3H$ channels are summarized in Table 4.52.

4.3.3 ^{10}Be+^{3}H decay channel

To round up comprehensive study of the ^{13}B excited states, decays to the ^{10}Be+^{3}H channel, observed in reactions on ^{7}Li and ^{19}F targets, are presented in this subsection. It's interesting to note that the detected ^{10}Be was observed in the ground (0^+), 3.37 MeV (2^+) and a mixture of excited states centered at ~ 6 MeV. The latter contains unresolved contributions from the states at 5.96 MeV (2^+), 5.96 MeV (1^-), 6.18 MeV (0^+) and 6.26 MeV (2^-). For both targets best results were obtained when ^{10}Be was detected in the ground state and presented results will be focus on this. The particle decay threshold for the ^{10}Be+^{3}H decay is 10.99 MeV.

^{7}Li(^{9}Li, ^{10}Be^{3}H)^{3}H

Data selection spectra, presented on Fig. 4.74, show clean selection of the ^{10}Be+^{3}H data for the dT=3 case and ^{7}Li target, while the selection for the ^{19}F target data is made accordingly. Some contamination of the latter can be expected in the ^{7}Li data, due to the inability to resolve close channel in Q value spectrum (see Table 4.50). Contamination from the ^{19}F target is treated as the background in the ^{13}B excitation energy spectra (Fig. 4.76).

reaction	^{7}Li(^{9}Li, ^{10}Be^{3}H)^{3}H	^{7}Li(^{9}Li, ^{10}Be*^{3}H)^{3}H	^{7}Li(^{9}Li, ^{10}Be**^{3}H)^{3}H
Q [MeV]	-2.64	-6.01	-8.60
color	red	blue	pink
reaction	^{19}F(^{9}Li, ^{10}Be^{3}H)^{15}N	^{19}F(^{9}Li, ^{10}Be*^{3}H)^{15}N	^{6}Li(^{9}Li, ^{10}Be^{3}H)^{2}H
Q [MeV]	-4.19	-7.56	-1.65
color	black	purple	no color

Table 4.50: The Q values and color coding used for the three-body reaction channels observed in the data for the ^{10}Be+^{3}H coincident events in all detector combinations. Since there is no contribution to the data from the reaction on the ^{6}Li target, it wasn't labeled.

For the projections of the ^{13}B excitation energy spectra, seen in Fig. 4.76, graphical cuts on ^{6}He-^{13}B$_{12}$ (example in Fig. 4.75-center) and ^{6}He-^{13}B$_{1*2}$ relative energy spectra were made respectively for each case, to exclude prominent off-diagonal data locus. This locus is most likely due to the unresolved combination of the ^{6}He excited states, background contributions and possible contaminations from the ^{19}F target. Results were compared
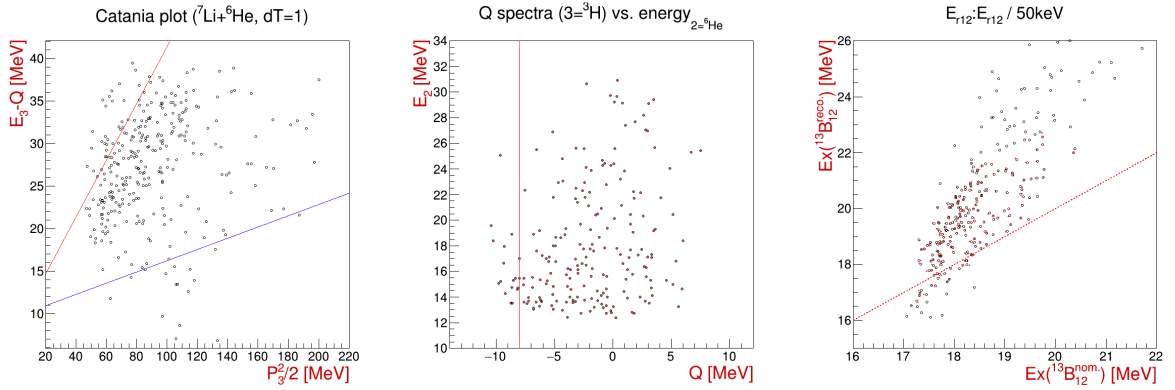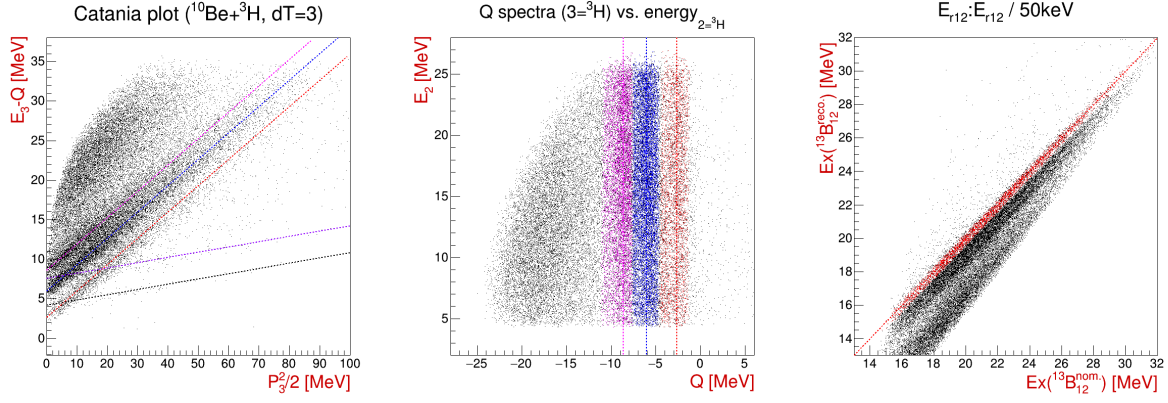
Figure 4.74: Catania plot and Q value spectrum for the ^{10}Be+^{3}H coincident events in the dT=3 detector combination, with identified and labeled exit channel from the reactions on the ^{7}Li target marked in red, blue and pink for the ground, 3.37 MeV (2^+) and $\sim$ 6 MeV states of detected ^{10}Be. Reactions on the ^{19}F target are labeled with black and purple dashed lines, as indicated in Table 4.50. The ^{13}B excitation energy comparison spectrum is shown on the right side, for the reaction on ^{7}Li target with ^{10}Be (g.s.) in the exit channel.

with the projections made by imposing simple linear cuts on the ^{6}He excitation energy and, apart from obvious change in statistics, they didn't differ in general shape of the spectrum. Graphical cuts were taken into account in the MC calculations for the detection efficiency. Due to low resolution of the data from the ^{10}Be**+^{3}H events, this case is not presented.
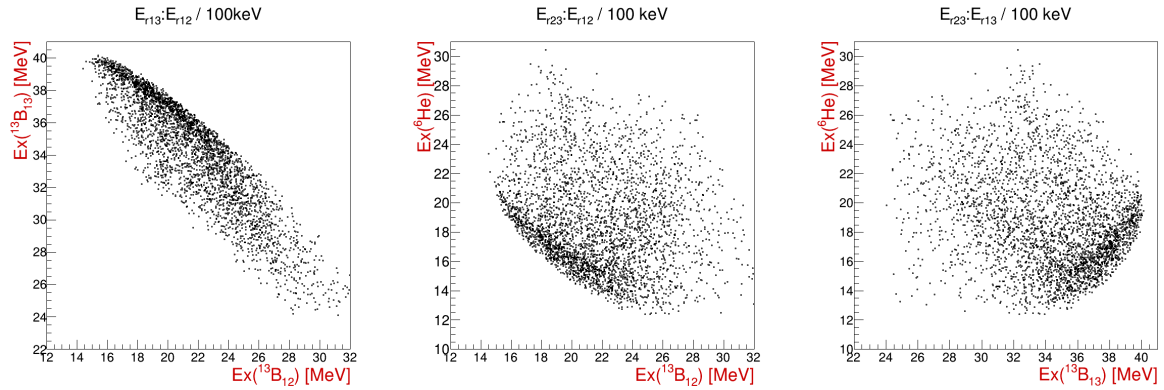
Figure 4.75: Excitation energy spectra for the ^{13}B$_{12}$, ^{13}B$_{13}$ and ^{6}He$_{23}$ from the ^{7}Li(^{9}Li, ^{10}Be^{3}H)$_{dT=3}$^{3}H reaction.

Even though no clear peaks are observed from the ^{10}Be*+^{3}H or ^{10}Be**+^{3}H coincident events, it's interesting to note that in the search for possible state at $\sim$ 26 MeV, a weak loci were observed in ^{13}B at that excitation energy in the 1^*-3 and $1^{**}-3$ combinations. Due to the low resolution, statistics and influence of background contributions clear conclusion cannot be made, especially since the corresponding peaks were not observed clearly, but the possible grouping of the data around $\sim$ 26 MeV can be pointed out. As this possible state was not observed strongly in ^{9}Li*+^{3}H or ^{7}Li+^{6}He data set, it's existence is not

clear from the present results. A better separation and resolution was achieved for the ^{10}Be ground state data (Fig. 4.75), thus the excitation energy spectrum was fitted to describe the shape of the data and possible states. Due to the limited resolution and large background, the ^{10}Be*+^{3}H (1-2 combination), and ^{10}Be**+^{3}H (1-2 combination) which is not presented, spectra are mostly structureless. The first one is presented here for the consistency, although it is not fitted.
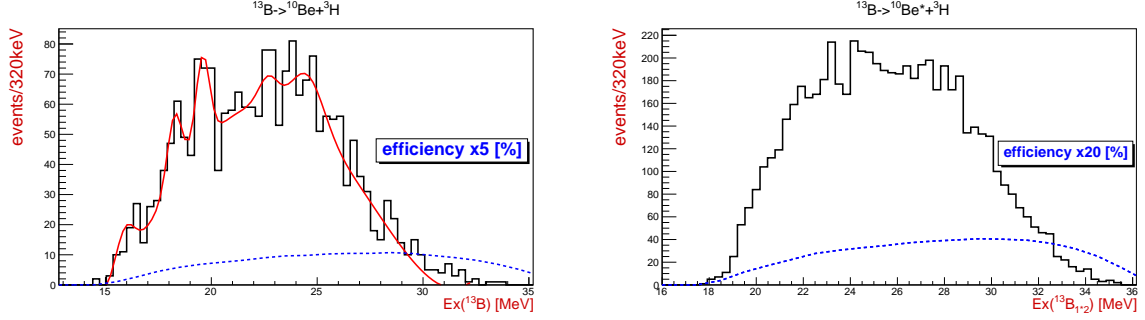
Figure 4.76: Excitation energy spectrum for the ^{13}B$_{12}$ and ^{13}B$_{1*2}$ from the ^{7}Li(^{9}Li, ^{10}Be^{3}H)^{3}H and ^{7}Li(^{9}Li, ^{10}Be*^{3}H)^{3}H reactions respectively. The ^{10}Be+^{3}H pairs were detected in the dT=3 combination. The results of the fit are listed in Table 4.51.

Comparing the obtained results (Table 4.51) with the results for the ^{9}Li+^{4}He and ^{7}Li+^{6}He cases, it is possible that either the same or close group of states are observed in all three cases, which will be discussed in the following chapter.

Ex [MeV]	15.9	18.3	19.6/[19.4]	22.7/[23.3]	24.6	background
norm [events]	12.6	22.9	29.7/[4.3]	9.0/[4.5]	16.2	pol4
σ [MeV]	0.44	0.34	0.32/[0.52]	0.45/[0.6]	0.77	[gaus(23.6)-gaus(14.0)]

Table 4.51: Results of the fit for the ^{13}B excited states from the ^{7}Li(^{9}Li, ^{10}Be^{3}H)$_{dT=3}$^{3}H and ^{19}F(^{9}Li, ^{10}Be^{3}H)$_{dT=3}$^{15}N ([] brackets) reactions, presented on Fig. 4.76 and 4.77 respectively.

^{19}F(^{9}Li, ^{10}Be^{3}H)^{15}N

Data selection for the ^{19}F reaction is made on "if(^{7}Li)-else if(^{19}F)" basis, since majority of the data is coming from the reaction on the ^{7}Li target, as seen in Fig. 4.74. Even though obtained statistic is low, an indication that the same states, seen in Fig. 4.76 for the ^{7}Li data, are observed also in the ^{19}F data presented on Fig. 4.77, with the results of the fit for both listed in Table 4.51. The fit was made to describe the general shape

of the spectrum, for the comparison with previous results. Due to the lack of obtained statistics, results for the $^{10}\text{Be}^*$ data are not presented here.
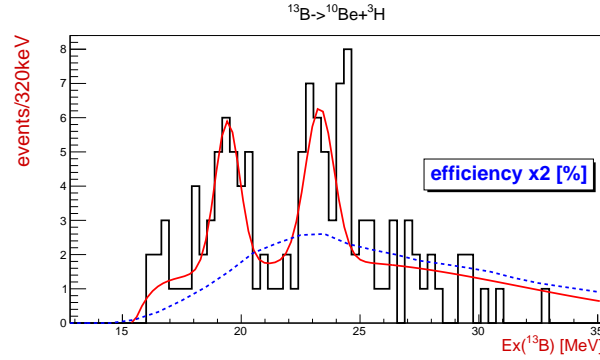
Figure 4.77: Excitation energy spectrum for the $^{13}\text{B}_{12}$ from the $^{19}\text{F}(^{9}\text{Li}, ^{10}\text{Be}^{3}\text{H})_{\text{dT}=3}^{15}\text{N}$ reaction. The results of the fit are listed in Table 4.51.

Summary table of the observed states: $^{13}\text{B} \rightarrow {}^{7}\text{Li}+{}^{6}\text{He}, {}^{10}\text{Be}+{}^{3}\text{H}$

$^{7}\text{Li}+^{6}\text{He}_{\downarrow} \parallel$ Ex [MeV] $_{\rightarrow}$			18.5	19.5	(21.2)		
$^{7}\text{Li}(^{9}\text{Li}, ^{7}\text{Li}^{6}\text{He})_{\text{dT}=1}^{3}\text{H}$			●	●	○		
$^{10}\text{Be}+^{3}\text{H}_{\downarrow} \parallel$ Ex [MeV] $_{\rightarrow}$	(16)		18.5	19.5	(21.2)	(23)	(24.6)
$^{19}\text{F}(^{9}\text{Li}, ^{10}\text{Be}^{3}\text{H})_{\text{dT}=3}^{3}\text{H}$	○		●	●	○	○	○
$^{19}\text{F}(^{9}\text{Li}, ^{10}\text{Be}^{3}\text{H})_{\text{dT}=3}^{15}\text{N}$				○		○	

Table 4.52: Results for the $^{7}\text{Li}+^{6}\text{He}$ and $^{10}\text{Be}+^{3}\text{H}$ decays of the ^{13}B excited states from the observed reactions on the LiF target. Clear peaks with good statistics are shown with ● symbol, while peaks with lower statistics and/or background interference are shown with ○ symbol.

5 Discussion

In this chapter an overview of the results obtained for the decays of the ^{10}Be, ^{12}Be and ^{13}B excited states will be given, with the focus on the cluster decays of these excited states and comparison with the previous measurements and theoretical expectations. For the reference on the tabulated values of the known states: energy, width and spin of the states, TUNL database [106] will be used, expanded with recent articles on the relevant states. Also, a brief discussion on the implication of these results on underlying cluster and molecular-like structure of these nuclei will be given.

5.1 ^{10}Be nucleus

Evolution of the clustering phenomena in neutron-rich beryllium isotopes has been in spotlight of both experimental and theoretical research in past three decades and prevails to be just as relevant to this day. With wider availability of the radioactive ion beam facilities and advances in computing power, new research methods are searched for and being applied to shed a light on the clustering phenomenon in neutron-rich light nuclei. While the α clustering is widely recognized phenomenon in Nα conjugate systems, with the ^{8}Be ground state [34] and ^{12}C Hoyle's state [32, 33, 81] serving as a prime examples of 2α and 3α structures, there are still unanswered questions like weather the α clustering prevails as nucleons are being added or in some cases subtracted [1] from cluster structures. Latter being the case with the removal of a proton in ^{11}B compared to ^{12}C [41] and the addition of neutrons in ^{13}B [25], which will be discussed in text following the discussion on the beryllium isotopes.

The ground state of ^{8}Be is particle unstable with large moment of inertia, indicating a well separated α-α structure [34], which is stabilized by addition of neutron in ^{9}Be, making

it not only stable, but a perfect example of the nuclear molecule [60], where α-α core is bound by a valence neutron. With additional two and four neutrons, proposed molecular α-Xn-α structure of ^{10,12}Be is even more diversified and serves as an important benchmark for the development of the theory to describe such exotic structure [10, 20], as was previously described in Chapter 2. Two arrangements of valence neutrons in molecular orbitals are being recognized: π orbital with neutron(s) in out-of-plane motion perpendicular to the α-α core and σ orbital with neutron(s) having in-plane motion with density distribution containing the α-α core [20]. These orbitals give rise to different intrinsic structures whose signatures are experimentally searched for. Although firm confirmation is not achieved on all of the members, three rotational bands are proposed to exist in ^{10}Be with band heads being $K^{\pi} = 0_1{}^+$ ground state at 0.0 MeV for π^2 structure (with the proposed members 2^+ = 3.37 MeV and 4^+ = 11.78 MeV), $K^{\pi} = 0_2^+$ 6.18 MeV state with σ^2 structure (2^+ = 7.54 MeV, 4^+ = 10.15 MeV) and $K^{\pi} = 1^-$ 5.96 MeV state with $\pi\sigma$ structure (with the proposed members 2^- = 6.26 MeV, 3^- = 7.37 MeV and 4^- = 9.27 MeV). All three bands follow simple linear energy dependence on the spin $\sim$ J(J+1) of the states with slope $(a(K^{\pi}) = \hbar^2/2I)$ inversely proportional to the moment of inertia for particular band structure. All three band heads have well developed α-α structure with $a(K^{\pi}) \sim$ 200-550 keV, similar to the ^{8}Be ground state rotational band ($\sim$ 500 keV), while the band built on σ^2 molecular orbital with $a(K^{\pi})$ = 200 keV indicates quite exotic and very deformed structure with very large α-α separation ($\sim$ 5.9 fm) [1]. For example, see Fig. 7 in [108] for systematization of the bands, based on what most of the results indicate, while the details on observed states (Table 5.2) and recent advancements (or disputes) in understanding of ^{10}Be nuclei will be given in the following text.

Experimental study of such exotic structures proves to be quite a challenging task, which largely depends on the sensitivity on the reaction mechanism on the structure of nuclei and the energy available in the entrance channel. As an example, in 2p pickup reaction, the ^{12}C+^{12}C used in [108], none of the members of positive-parity σ^2 band were observed, while all of the members from negative-parity $\pi\sigma$ band were observed, owing most likely to the structure of the nuclei in the entrance channel and high beam energy used. On the other hand Zagreb group [16–19] has successfully used triton and α pickup reactions to populate both members of the ground state π^2 and highly deformed σ^2 band. While

the full three-body kinematic measurement of the exit channel largely reduces the detection efficiency and thus the observed statistics, direct observation of the cluster decay for particular state is a clear indication of pronounced cluster structure of that state due to structural overlap with the strong decay channels.

^{4}He+^{6}He	(7.54)*		9.6	10.2		11.8	16.5	18.5	20.5	22.3
^{4}He+^{6}He*			9.6	10.2		11.8	(16.0)			(21.2)
^{9}Be+n	7.37	9.3	9.6		10.6	11.8	(16.1)	(18.1)		
^{8}Be+nn					10.6*	12.7*	(16.3)		(19.6)	

Table 5.1: Summary table of the observed decays of the ^{10}Be excited states. Tentative states are in parenthesis. New states observed in present work are indicated in red, while * is explained in the text.

^{4}He+^{6}He		ref.	^{4}He+^{6}He*		ref.
7.5	(✓*)	[19, 38, 109–111]			
9.6	✓	[16, 23, 27, 38, 108–113]	**9.6**	(✓)	[18]
10.2	✓	[16, 17, 19, 23, 27, 38, 109–112, 114], [21]*	**10.2**	✓	[18]
11.8	✓	[13, 16, 19, 23, 27, 38, 108, 110–113]	**11.8**	✓	[18]
[13.5]		[13, 23, 38, 110, 111, 113]			
[14.7]		[13]			
16.5	✓	[13]	16.0	✓	
[17.8]/**18.5**	✓	[112]*, [38, 110, 111]*, [13]			
20.5	✓		21.2	(✓)	
22.3	✓				

Table 5.2: Summary table for the ^{4}He+^{6}He and ^{4}He+^{6}He* decays of the ^{10}Be excited states. Observed states are in **bold** with brackets indicating the tentative states, while red are the newly observed states. States which appear in reported literature, but are not observed in present experiment are in the square brackets. For the references with *, further clarification is given in text.

In the present experiment main reaction mechanism expected to populate highly clustered states in ^{10}Be is proton pickup by the ^{9}Li beam, triton transfer to the ^{7}Li target and also a more complex reaction mechanisms. Simplistic analysis of the excitation energy spectra (like the one presented for ^{13}B in Fig. 5.4), made by imposing conditions on the momentum of the undetected recoil in the ^{7}Li(^{9}Li, ^{4}He^{6}He)^{6}He and ^{7}Li(^{9}Li, ^{6}He^{6}He)^{4}He

reactions seems to indicate that direct reaction mechanism, proton pickup, is dominating the production of ^{10}Be α clustered states. Unfortunately, due to limited data statistics, resolution and the non-zero spin of the target and beam, spin and parity of the states was not determined in the present experiment. Nevertheless, these results still present important step forward in understanding of the complex structure of the ^{10}Be excited states. To elaborate on these results summarized in Table 5.2, and put them in the context of previous measurements in time period from Hamada et al. in '94 [112] to Jiang et al. in '20 [109]), following excitation energy ranges will be discussed: 7.41< Ex(^{10}Be)<13 MeV, 13 <Ex(^{10}Be)< 20 MeV and Ex(^{10}Be)> 20 MeV, where 7.41 MeV is the threshold for the decay of ^{10}Be to ^{4}He+^{6}He$_{\text{g.s.}}$. For the ^{9}Be+n and ^{8}Be+nn channels, decay thresholds are 6.81 and 8.48 MeV respectively.

In the low excitation energy region strong population of the 2^+ state at 3.37 MeV is observed from the analysis of the two-body coincident and single spectra for the ^{10}Be*+^{6}He exit channel, alongside weaker population of 0^+ ground state and unresolved group of states centered at $\sim$ 6 MeV. Although these results are not presented in the thesis, since they were well studied in the past, they enable the estimate of the systematical offset for the excitation energy of the ^{10}Be states calculated from the detected ^{6}He nuclei, which is particularly important in the neutron and rarely studied two-neutron channel. Offset of 250-300 keV was observed in these spectra, which agrees well to estimate from the three-body reactions (uncertainty of $\sim$ one bin of 320 keV).

Starting of just above ($\sim$ 130 keV) the ^{6}He decay threshold 2^+ member of the σ^2 band is located at 7.54 MeV. Although it is not observed directly in any spectra with confidence, an indication of this state can be seen in Fig. 5.1, for the coincident detection of the ^{4}He+^{6}He pair in the dT=0 combination. Since the $\Delta\phi_{12}^{\text{nom.}} = 0°$ used to calculate the excitation energy Ex(^{10}Be$_{12}^{\text{nom.}}$) is not dependent on the correct exit channel identification as Ex(^{10}Be$_{12}^{\text{reco.}}$) is, plotting all of the data in excitation energy correlation spectra enables one to simultaneously see all of the contribution from different reaction exit channels. Since this state was not observed clearly in the reaction on ^{7}Li target, but it is observed in Fig. 5.1, means that the reaction proceeded through many-body exit channel and "recoil" particles could have been ^{5}He+n and ^{4}He+n+n, as it is shown for MC simulated spectra for the 10.5 MeV state. In similar manner Jiang et al. [109] have recently observed

this state in ^{9}Be(^{9}Be,^{4}He^{6}He)^{8}Be reaction and deduced large α cluster-decay partial width for this state, confirming it to be 2^+ member of the σ^2 band, as previously indicated by Milin et al. [19] and Liendo et al. [111].
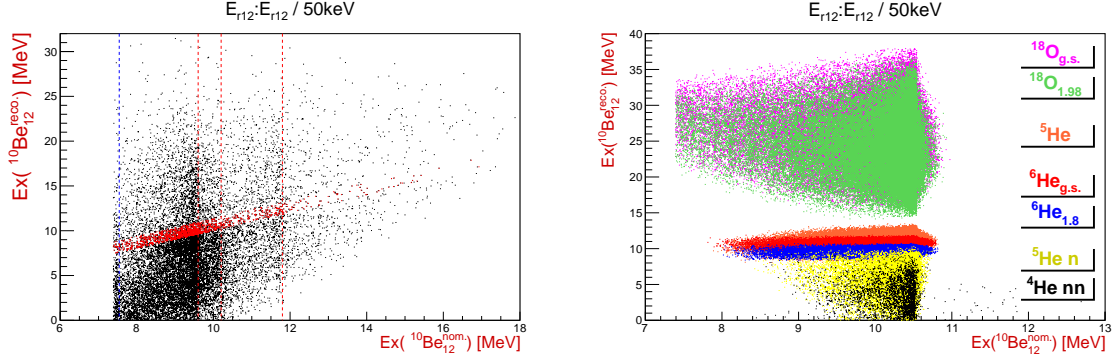
Figure 5.1: Excitation energy correlation spectra for ^{10}Be$_{12}$ calculated using $\Delta\phi_{12}^{\text{nom.}} = 0°$ or $\Delta\phi_{12}^{\text{reco.}}$ (assumption for the reaction on ^{7}Li target) value for the coincident detection of the ^{4}He+^{6}He pair in the dT=0 combination, with no data selection. Lines indicate observed states at 9.6, 10.2 and 11.8 MeV in red and 7.54 MeV in blue. Identified reaction on ^{7}Li target is shown with red markers. Simulated MC spectrum for 10.5 MeV excitation is shown on the right, for guidance on how different reaction exit channels, indicated by undetected particle, are differentiated in these kind of correlation spectra.

In the ^{9}Be+n decay channel observed peak at 7.4 MeV corresponds to 1^- 7.37 MeV state, while the peak at 8.9 MeV most likely corresponds to (4^-) 9.27 MeV state. It is highly unlikely that the latter peak is newly observed state, rather the statistical fluctuation of the data making it appear one bin (320 keV) below the correct energy. Next two peaks observed as 9.9 and 10.8 MeV have offset of ~ 300 keV, as expected from the analysis of the two-body reaction ^{7}Li(^{9}Li, ^{6}He)^{10}Be* and they correspond to the 2^+ state at 9.6 MeV and (3^-) 10.6 MeV state. Together with observed 4^+ state at 11.8 MeV, these n-decay results in overlapping excitation energy region correspond very well with the results from Soić et al. [16], where similar reaction entrance channel was used and the inclusive results from Bohlen et al. [108], where members of the σ^2 band were not populated at all, owing most likely to stronger excitation of single-particle states at high beam energy used in that experiment.

Coming back to α-decay channel, 2^+ state at 9.6 MeV, 4^+ state at 10.2 MeV and 4^+ state at 11.8 MeV were observed to decay both to the ^{6}He 0^+ ground state and 2^+ (1.8 MeV) excited state. Latter being quite important result as decay to the 2^+ state of ^{6}He was previously observed only in work by Zagreb group [18]. For low excitation energy states, lowering of the centrifugal barrier and required smaller momentum transfer for

the decay to 2^+ state, from the observed yield, seems to favor and enhance the decay to that channel (Fig. 4.10-right) compared to the ground state (Fig. 4.8 - right) channel, as calculated detection efficiency is similar in both cases ($\sim$ 3-4 %). It is also interesting to note that in the results from inelastic scattering to ^{4}He+^{6}He* channel by Suzuki et al. [21] there was a small peak in the cross section right at 11.8 MeV in the excitation energy and even though authors didn't claim that this peak corresponds to a strong resonance in ^{10}Be, in the light of the present results one can argue that indeed the same state is observed in both experiments. In the elastic channel they observe a strong resonance which corresponds to 10.2 MeV state, in agreement with present results.

Before the discussion on the structure of these states, ^{8}Be+nn decay has to be considered, as very little is know for this channel, with exception of α+^{6}He scattering by Suzuki et al. [21]. In present experiment two wide structures at $\sim$ 10.6 and 12.7 MeV are observed. Taking into account the offset of $\sim$ 300 keV observed in the two-body reaction analysis and for the neutron decays in this region it is likely that the real energy of corresponding peaks are $\sim$ 10.3 and 12.4 MeV. On closer inspection (Fig. 4.34) one can also notice that each peak has two smaller peaks contributing: 10 + 11 MeV for $\sim$ 10.6 MeV and 12.6 + 13.6 for $\sim$ 12.7 MeV peak. There are two possible explanations of these result; first one is that the 4^+ member of σ^2 band at 10.2 MeV and new state at $\sim$ 12.4 MeV are observed, while the other suggests that first peak is superposition of the 2^+ state at 9.6 MeV and (3^-) state at 10.6 MeV and the second peak is superposition of newly observed state at 12.6 MeV and the state at 13.6 MeV, which has been observed in previous measurements and will be discussed in text below in detail. Results by Suzuki et al. [21] are just as ambiguous and show peak at $\sim$ 10 MeV in cross section, with possible minor peaks at $\sim$ 11 and 12.4 MeV in energy region measured. While [21] concluded that the peak likely corresponds to 10.2 MeV state, one cannot exclude the possibility that if the data has offset of $\sim$ 300-400 keV, due to reconstruction of the energy losses within gas target, and that observed states are really 9.6+10.6 MeV together and possibly new $\sim$ 12.4 MeV state. Based on simple consideration about the density distribution of σ neutrons (see [20] for e.g.) and microscopic cluster model results [36], which suggest that 4_2^+ state at 10.2 MeV is dominated by strong α+^{6}He(0^+, 2^+) clustering, it is highly unlikely that 10.2 MeV states decays to ^{8}Be+nn channel. In the light of present results it's likely that in both experiments the sum of 9.6 and 10.6 MeV states is observed. For sure more experimental

data with better resolution is needed to clarify this case and a dedicated theoretical study for the decay to ^{8}Be ground state.

For previously mentioned states it's clear that 2^+ 9.6 MeV state has peculiar structure, which doesn't fit into any molecular band, with observed decays to ^{4}He+^{6}He, ^{4}He+^{6}He*, ^{9}Be+n and possibly ^{8}Be+nn channel. The 10.2 MeV state was proposed by Soić et al. [16] to be 4^+ member of σ^2 band, which was later confirmed by Milin et al. [19], and experiments that followed [21, 22, 114] to name a few, and very recently by Jiang et al. [109]. Present results support the claim [16] that this state does not decay (strongly) through neutron channel due to it's intrinsic α-2n-α structure with pronounced α+^{6}He(0^+), and now one may add α+^{6}He(2^+) clustering, observed in the work by Zagreb group [18]. Another important result in support of the molecular structure of the σ band is that the neutron decays of the $2_4{}^+$ state at 7.54 MeV were also not observed in present experiment. If they exist, neutron decays of these two states are for sure hindered by strong α-^{6}He clustering, as is indicated in microscopic cluster model [36]. The last state in this group, the 4^+ at 11.8 MeV, is believed to be the 4^+ member of the ground state rotational band, where two valence neutrons are located in π orbital. In the classical shell model this space is occupied by the p shell (-) neutrons, unlike the sd shell (+) for σ neutrons. Just like the 2^+ 9.6 MeV state, in the present experiment the 11.8 MeV state is observed to decay to ^{4}He+^{6}He, ^{4}He+^{6}He* and ^{9}Be+n channels. Based on the analogy with the ^{8}Be ground state rotational band (0^+ 0 MeV, 2^+ 3.04 MeV and 4^+ 11.4 MeV), the 11.8 MeV state still remains the best candidate for the 4^+ member of the ^{10}Be ground state rotational band, even though early AMD studies [20] have already pointed out the possibility of dissociation of the strong α-α clustering by spin-orbit force as neutron number increases toward the neutron dripline. This argument was pointed out in article by Suzuki et al. [21], since the results for elastic channel didn't indicate a strong resonance in this region. On contrary, Miljanić et al. [18] have observed decay of this state to ^{6}He (2^+) channel and Suzuki et al. [21] have an increase in the cross section at this energy in the inelastic (^{6}He 2^+) channel, as the existence of a resonance would suggest. Interestingly enough this state doesn't decay to the ^{8}Be+nn channel, like the 9.6 MeV state which likely does, but is not a member of any molecular band. This would indicate that, in the neutron decay channel, it only decays to the ^{9}Be ground state and not to the ^{9}Be* excited states, which can sequentially decay to the ^{8}Be ground state. If this structure is considered to

be a signature of π molecular band, as 80 % of the single-particle strength of two valence neutrons is found in negative parity component [20], than the results from the present experiment can help to finally close the case weather this state is really the 4^+ member of the ground state band. A dedicated theoretical study to single out this peculiar decay property of the 11.8 MeV state is suggested, while the present results support this state to be the best candidate for the 4^+ member of the ^{10}Be ground state rotational band.

In the excitation energy region around $\sim$ 13.5 MeV there is ongoing search for the possible 6^+ member of the deformed σ^2 band. Rogachev et al. [22] propelled the search with observed high-spin resonance in that region, followed by Dell' Aquila et al. [23], who have assigned the spin of 6^+ to that state, implying possible α-2n-α band structure. While the states have been observed in that region in the past [13, 110, 113], most measurements which had clearly seen the 4^+ band member of σ^2 band, and have covered that excitation energy, did not observe this state [19, 27, 38]. Recent dedicated experiment by Upadyuyala et al. [24] found no evidence of strong resonance in elastic or inelastic channel in that region, placing the upper limit on the partial width for hypothetical 6^+ state. From the excitation energy and $\sim$ J(J+1) spin systematics follows that the 6^+ member of the σ^2 band should be at slightly higher energy, at $\sim$ 15 MeV. In the present experiment no evidence was found for presence of that state in ^{6}He* nor in ^{6}He$_{\text{g.s.}}$ channel, in agreement with recent results by [24]. Only in one spectrum (Fig. 4.8) peak at $\sim$ 14 MeV had been observed for decay to ^{6}He$_{\text{g.s.}}$. Since it was not confirmed in any other spectrum clearly, likely due to the drop in detection efficiency, nor in ^{6}He* channel, one can only assume that the peak belongs to the misidentified data from the reaction on the ^{19}F target with ^{18}O* as recoil (see green line in Catania plot on Fig. 4.4). Misidentification could have shifted the 11.8 MeV state, which is strongly populated in reaction on ^{19}F target, by $\sim$ 2 MeV making the false peak appear in reaction on the ^{7}Li target. Only a tentative indication on existence of a state in this region is seen in ^{8}Be+nn channel at $\sim$ 13.3 MeV. Above the 15 MeV in Ex(^{10}Be) very little is know about the cluster structure of the ^{10}Be excited states and exclusive measurements for the decay to ^{4}He+^{6}He(0^+, 2^+) are almost non-existent. In the present experiment there are two group of states observed, first group at energies of 16.5 MeV (^{4}He+^{6}He (0^+)), 16.0 MeV (^{4}He+^{6}He (2^+)), 16.1 MeV (^{9}Be+n) and 16.3 MeV (^{8}Be+nn) and the second group at energies of 18.5 MeV (^{4}He+^{6}He (0^+)), 18.2 MeV (^{9}Be+n) and 18.0 MeV (^{8}Be+nn). With present experimental resolution ($\sim$ 800

keV) and energy uncertainty ($\sim$ 400 keV) it's hard to say weather these groups of states belong to two same states or these are different states with different intrinsic structures, indicative of respective decay channel observed. If one remembers the systematical offset of $\sim$ 200-300 keV for the neutron decay channel, it's likely that the observed energies in the n and nn channels are really $\sim$ 16 MeV and 17.8 MeV. For the states at $\sim$ 16.5 MeV, only Freer et al. [13] in 2n-transfer reaction and Bohlen et al. [108] in 2p-transfer reaction have observed states in this region at 16.1+17.1 MeV and 16.9 MeV respectively. Observed states at $\sim$ 17.8-18.5 MeV are just above the ^{7}Li+t decay threshold at 17.25 MeV. In the early measurement by Hamada et al. [112], using the ^{7}Li(α,p)^{10}Be reaction, two strong states with large cluster spectroscopic factors were observed at 17.78 and 18.55 MeV. These are believed to be important in astrophysical scenarios where in some cases they could be responsible for ^{7}Li depletion. Since their cross section have similar distribution, these are believed to have the same spin and parity. It is possible that in the present experiment the sum of these states, or just the 18.5 MeV state is observed in the α+^{6}He channel, while in the n and nn channels only 17.8 MeV state is observed. Interestingly enough, Curtis et al. [110] have observed state at 17.8 MeV and possibly also at $\sim$ 16-16.5 MeV (peak was attributed to maximum of detection efficiency at that exact energy) in the ^{7}Li(^{7}Li, α^{6}He)α reaction, where similar reaction mechanism of producing ^{10}Be excited states is expected. Liendo et al. [111] have observed the states of Hamada et al. [112] to decay to ^{7}Li+t (17.8 MeV) and ^{7}Li*+t (18.5 MeV) channels. Even though the ^{7}Li+t decay channel is omitted from presentation in the thesis, for the current discussion it's important to mention that a strong peak at $\sim$ 19 MeV (likely has an offset) is observed in this channel, which likely corresponds to the observations from [112] and [111]. Present experimental results indicate that these state(s) are indeed strong resonances in ^{10}Be with well developed cluster structure and many open decay channels: α, n, nn and t.

Before the discussion on the next observed state, a connecting mechanism for the excitation of set of rotational states can be mentioned. Based on rigid triaxial rotor model of ^{10}Be, Curtis et al. ([110] and references therein) have performed calculations for collective excitations based on rotations of a triaxially shaped ground state which reproduce quite nicely the gap in the existence of these kind of states between 11-17 MeV and give prediction of two set of states with different kind of deformation at 17.5 and 18.5 + 21.0 MeV (see Fig. 1 in [110]). Interestingly enough, the next set of states observed in the present

experiment are 20.5 MeV (^{4}He+^{6}He (0^+)), 21.2 MeV (^{4}He+^{6}He (2^+)), weakly 20.4 MeV (^{9}Be+n) and 19.6 MeV (^{8}Be+nn). It's quite possible that this simple model can roughly describe observed spectra for set of states seen in α+^{6}He (0^+, 2^+) channel at 18.5 and $\approx$ 20.8 MeV and the other set of states at $\sim$ 17.8-18 MeV seen in ^{9}Be+n and ^{8}Be+nn channels. The observed state at 19.6 MeV in the ^{8}Be+nn channel seems to far off to be included in these considerations and may be a newly observed state with special intrinsic structure, which needs to be treated carefully in theoretical calculation for any kind of conclusion. The last observed state is found in the ^{4}He+^{6}He (0^+) channel at 22.3 MeV, where previously no measurement has seen this mode of decay. Not presented here, but the strong peaks are also found in the ^{7}Li+t and ^{8}Li+d decay channel in this region ($\sim$ 22.5 MeV), while in the ^{9}Li+p channel peaks are found at $\sim$ 21.5 and 23 MeV.

It is evident, from the experimental results presented here, that the ^{10}Be nucleus has wide variety of structures appearing in the excited states. Even though experimental data lacks the resolution and statistics to determine the partial widths of the observed states, which could help to link observed states to the rotational bands with molecular α-nn-α structure, still valuable spectroscopic information are obtained. In summary, two of the most important observations obtained from the present experiment are the states decaying to the ^{4}He+^{6}He (2^+) and ^{8}Be+nn channel, for which the previous result were really scarce [18, 21]. Present result suggest that proposed 4^+ member of σ^2 band at 10.2 MeV doesn't undergo decay to the ^{9}Be+n and ^{8}Be+nn channels, which is in support of its deformed α-2n-α molecular structure. Another important result is that neutron decays of the proposed 4^+ member of π^2 ground state molecular band were observed, while the decay to ^{8}Be+nn channel was not. Detailed theoretical treatment of the obtained result is needed to clarify if this observation could finally wage on the existence of high-spin member of this band or the α clustering is hindered by strong spin-orbit force. Also, in the present experiment no evidence was found for existence of 6^+ member of σ^2 band in $\sim$ 13.5-15 MeV energy range. For the high-energy excited states, the state at $\sim$ 16.2 MeV was found to decay, just like the 2^+ 9.6 MeV state, within present experimental resolution, to all channels studied here: ^{4}He+^{6}He (0^+, 2^+), ^{9}Be+n and ^{8}Be+nn. Based on the analysis of the momentum of undetected recoil in the ^{7}Li(^{9}Li, ^{4}He^{6}He)^{6}He reaction one can claim that the states at 16.5 and 18.5 MeV in ^{4}He+^{6}He channel were produced by direct proton pickup from the ^{7}Li target, alongside more complex processes. States at

22.3 (^{4}He+^{6}He (0^+)), 21.2 (^{4}He+^{6}He (2^+)), 20.5 MeV (^{4}He+^{6}He (0^+)), and 19.6 MeV (^{8}Be+nn) are observed for the first time in respective decay channels. There is also an indication of the new state, observed only in ^{8}Be+nn decay channel at ~ 12.3 MeV, with the smaller peak at 13.3 MeV which could correspond to states in that region observed by [13, 23, 110, 113].

As the lookahead for the future studies, an interesting quasi three-center mode of clustering and thus corresponding decay channel, proposed to exist at high-excitation energies in AMD studies [20], is the α+t+t which is aligned with interest to study similar quasi three-center (α-2n)+t+α structure in ^{13}B [25]. For such studies highly segmented telescope array with large angular coverage is required and may be utilized in the future studies of complex cluster structures in neutron-rich light nuclei.

5.2 ^{12}Be nucleus

The ^{12}Be is one of the quintessential nuclei to understand the evolution of clustering and molecular-like α-Xn-α structure, with addition of neutrons, in weakly bound neutron-rich light nuclei. Quenching of the N=8 neutron shell closure and the intruder ($2\hbar\omega$) structure of the ground state is perhaps best understood in terms of molecular structure, where σ-orbit influences the development of $\alpha - \alpha$ clustering in the ground state, as indicated in the AMD study [10]. More recent study, using unlocalised clustering model (THSR wavefunctions) [39], found that the strong mixing of the π: 2α+2n(π)+2n(π^*) molecular orbit and α+^{8}He binary configuration could explain the breaking of the N=8 shell. Although, in latter study σ-orbit configuration was found to be redundant, as it was already included in model space when the THSR bases of the α+^{8}He configuration were superposed [39]. In that sense, both models agree on the influence of the α cluster development on the properties of the ground state. Looking at the next two 0^+ states, the $0_2{}^+$ excited state has "normal" ($0\hbar\omega$) configuration restored, while the $0_3{}^+$ state has well developed ^{6}He-^{6}He deformed cluster structure based on newly proposed δ'-orbit configuration [10]. Similarly to σ-orbit, neutrons are contained in $2\hbar\omega$ space, but with different linear combination of the single p orbits of valence nucleons, which is perpendicular to those in σ-orbit. All of these states are proposed to be the band-heads of rotational bands, together with 2_1^+ and 1_1^- with dominating $2\hbar\omega$ and $1\hbar\omega$ configurations [10], respectively.

Compared to the ^{10}Be, four valence neutrons in ^{12}Be give rise to even more rich and complex structural phenomena which are still not fully understood. Here the correlations among valence nucleons and covalent exchange among $\alpha - \alpha$ cluster core plays an important role and experimental data on low-lying and highly excited states are much needed to benchmark and improve theoretical models. In aforementioned example of AMD [10] versus unlocalised microscopic clustering (THSR) [39] approach, conclusion, even though they to great extent agree, are somewhat model dependent and are largely influenced by the choice of the wave-functions in which the many-body problem is solved. As the emergence of clustering is strongly related to the fine details of nuclear force, modern ab initio calculation can provide great insights in structure of the ^{12}Be, and other neutron-rich light nuclei, starting from the first principles [80].

From the experimental side, inelastic breakup of the ^{12}Be beam and resonant elastic scattering on ^{4}He gas target have been used to study molecular-like structures in ^{12}Be nucleus. In the early measurement Freer et al. [12, 13] have proposed the existence of the molecular rotational bands built on the ^{6}He+^{6}He and ^{4}He+^{8}He clustering. This finding was contradicted in later experiment [14], where strong structures corresponding to aforementioned decay channels were not found. While both experiment suffered from the limited experimental resolution ($\sim$ 800-1000 keV) due to the use of composite CH$_2$ target, in the latter experiment higher beam energy was used, which could be responsible for the discrepancies in the observed result. Recently, Yang et al. [15] have performed inelastic breakup measurement on carbon target with zero-degree detector, which enabled observation of the states in both ^{6}He+^{6}He and ^{4}He+^{8}He decay channels, close to the corresponding decay thresholds due to large efficiency in that region. In the ^{4}He+^{8}He channel, new 0_3^+ state was observed at 10.3 MeV, together with 2^+ state at 12.1 MeV and 4^+ at 13.6 MeV, which supports the existence of the rotational band proposed by Freer et al. [12, 13]. In the ^{6}He+^{6}He channel, new 2^+ state at 11.7 MeV was observed, together with 4^+ state at 13.6 MeV. Both results agree with Freer et al. [12, 13], in the small overlapping region, but results from [12, 13] need strong confirmation at higher excitation energies.

The use of multi-nucleon transfer reactions in the present experiment, to populate cluster and molecular structures in ^{12}Be, is novel approach and even though present results are by themselves inconclusive of the molecular structure, the direct observation of the ^{6}He+^{6}He, ^{6}He+^{6}He (2^+) and ^{4}He+^{8}He decaying states [115], listed in Table 5.3, is quite indicative of the underlying structure and together with the aforementioned results support the existence of strong clustering in ^{12}Be nucleus and proposed molecular α-Xn-α structure. The fact that neutron decay, together with proton or triton decays in the limited range of excitation energies covered by latter two cases, were not observed in the present experiment goes to support the persistence of strong $\alpha - \alpha$ clustering, even in neutron-rich ^{12}Be nucleus. It's also interesting to point out that none of helium-helium decaying states were observed in the two-neutron transfer reaction [38]. Here the selectivity of transfer reactions to the structure of nuclei in the entrance channel and it's structural overlap with the nuclei in the exit channel leads to conclusion that neutron transfer reaction are more suitable for the observation of the single-particle states. As these states were not

observed, most plausible explanation would be the peculiar structural properties of the ^{12}Be nucleus. Another important result from the present measurement is the first experimental observation of the ^{12}Be excited states decaying to the ^{6}He+^{6}He (2^+) channel [115].

The obtained results, summarized in Table 5.3, will be discussed in terms of the observed helium-helium cluster decays and will be put into the context of previous measurements where direct helium cluster decays where observed, in time period from Freer et al. [12] in '99 to Yang et al. [15] in '15. In some cases, inclusive results obtained from the detection of the recoil nuclei in "two-body" reaction, will be included in the discussion. To elaborate the results, excitation energy is divided into three ranges: from the respective decay thresholds to Ex(^{12}Be)<14 MeV, 14< Ex(^{12}Be)< 19 MeV and Ex(^{12}Be)> 19 MeV. Particle decay threshold for the decay of the ^{12}Be excited states to the ^{6}He+^{6}He ground state channel is 10.16 MeV and 9.0 MeV for ^{4}He+^{8}He channel. It's also important to note that the neutron decay threshold is only 3.2 MeV, thus all of the observed states are embedded deeply in the neutron continuum.

^{6}He+^{6}He		11.7	13.5		(16.5)	18.5	(20.0)	22.5	25.4
^{6}He+^{6}He*				15.4	16.5	17.8		22.1	24.0
^{4}He+^{8}He	10.3	(12.1)	13.8	15.6		17.5	(19.8)	(22.3)	

Table 5.3: Summary table of the observed decays of the ^{12}Be excited states. Tentative states are in parenthesis. New states observed in present work are indicated in red.

Starting with lower part of the excitation energy spectra, in the ^{4}He+^{8}He channel states are observed at 10.3, (12.1) and 13.8 MeV. These states correspond to the 0^+ (10.3 MeV), 2^+ (12.1 MeV) and 4^+ (13.6 MeV) states, respectively, observed by Yang et al. [15] and the latter two, 12.1 MeV and likely 14.1 MeV, by Freer et al. [12, 13]. In the work by Charity et al. [14], observed states have large uncertainty due to background influences, but state at $\sim$ 10.2 MeV is seen and very wide bump centered at $\sim$ 14 MeV. In the ^{6}He+^{6}He channel, in the same energy range, two states are observed, the first one being tentative assignment at (11.7) MeV and the second one at 13.5 MeV. Again, the observed states correspond very well to the ones observed by Yang et al. [15] at 11.7 and 13.3 MeV with very few counts in the spectrum. Spin and parity of 2^+ and 4^+ was assigned to these states, respectively. Since the Freer et al. [12, 13] had very low efficiency in this

^{6}He+^{6}He			^{6}He+^{6}He*	^{4}He+^{8}He		
				[9.8]		[93], [116, 117]*
				10.3	✓	[15]
[10.9]/[11.3]		[93], [116, 117]*				[93], [116, 117]*
11.7	✓	[116, 117], [15]		**12.1**	✓	[15], [12, 13]
13.5	✓	[15], [12, 13], [14]		**13.8**	✓	[15], [12, 13], [14]*
[14.7]/[15.5*]		[116, 117], [12, 13], [14]*	15.4	**15.6**/[14.5]	✓	[116, 117], [12, 13], [37]
16.5	✓	[12, 13], [14]*	16.5			
[17.8]/**18.5**/[19.3]	✓	[116, 117], [12, 13]]	17.8	**17.5**/[18.2]	✓	[12, 13]]
20.0	✓			**19.8**/[19.2/20.7]	✓	[116, 117], [12, 13]
[20.9]/[21.7]		[12, 13] [116, 117]				[116, 117]
22.5	✓	[12, 13]	22.1	22.3	✓	
[24.0]/**25.4**	✓	[12, 13]	24			

Table 5.4: Summary table for the helium decays of the ^{12}Be excited states. Observed states are in **bold** with brackets indicating the tentative states, while red are the newly observed states. States which appear in reported literature, but are not observed in present experiment are in the square brackets. For the references with *, further clarification is given in text.

region, only the 13.2 MeV state was observed in that measurement. Present experiment agrees with results from Yang et al. [15] and Freer et al. [12, 13] in this energy region and confirms the existence of two newly observed states at 10.3 and 11.7 MeV by [15]. In the work by Charity et al. [14], peak is observed at $\sim$ 13.5 MeV. The 0^+ state at 10.3 MeV is proposed to be a band-head of molecular rotational band built on ^{4}He-^{8}He cluster structure, while the 2^+ state at 11.7 MeV and 4^+ state at $\sim$ 13.5 MeV are proposed to be members of highly deformed molecular rotational band built on ^{6}He-^{6}He clustering. There are few other experiments [93, 116–118] available, with states observed in this energy region, but are inconclusive on the structure of these states, as the ^{12}Be excitation energy was deduced only from the recoiling particle. However, Bohlen et al. [116] have proposed molecular band built on the ^{6}He-^{6}He clustering, with the states at $\sim$ 10.7 and 14.6 MeV which are not observed in the present measurement, nor agree with [15], although if systematic shift is taken into account could respond to 10.3 MeV and $\sim$13.6 MeV. In full fairness to historical accuracy, it has to be mentioned that the state at 10.3 MeV was first weakly observed in experiment by Korsheninnikov et al. [118] at $\sim$ 10.0 MeV in '95.

In the excitation energy range from 15 to 20 MeV in the ^{4}He+^{8}He decay channel, two states at 15.6 and 17.5 MeV were observed in present experiment. Comparison with

the literature here is not straightforward as both Freer et al. [13] (improved analysis over [12]) and Charity et al. [14] have large uncertainty and observed peaks lie on large unresolved background due to mixture of events from C and H components of the CH_2 target. Nevertheless, if we consider the first peak at 15.6 MeV, state at 16 MeV (^{1}H target) and 15.1+16.5 MeV (^{12}C target) were observed in [13], and a wide structure at $\sim$ 15.5 MeV in [14]. For the next set of the observed states, there are 17.4+18.2 MeV in [13] for ^{1}H target and already mentioned state at 16.5 MeV on ^{12}C target, while [14] have one unresolved structure above the background at $\sim$ 17-18 MeV. Thorough analysis of 7 different spectra in which the peaks at 15.6 MeV and 17.5 were observed on [7]Li target and 2 different spectra on well separated reaction on ^{19}F target, with position uncertainty of $\sim$ 400 keV for both, lead to conclusion that these are indeed two main structures in the [4]He+[8]He decay channel, which coincide with unresolved structures observed in [14] and, if the states at 15.1+16 MeV and 16.5+17.4+18.2 MeV are grouped, to structures observed in [12, 13].

In the same excitation energy range, two states at (16.5) and 18.5 MeV were observed in the [6]He+[6]He decay channel and 15.4, 16.5 and 17.8 MeV in the [6]He+[6]He (2^+) decay channel. For the latter case, the state at 16.5 MeV decays to both [6]He ground (0^+) and excited (1.8 MeV, 2^+) states, while the states at 15.4 and 17.8 MeV decay also to the [4]He+[8]He channel. This quite astonishing feature of helium-helium cluster decays may be a indicative sign of the observed molecular resonances of underlying α-4n-α molecular structure. Results for the decay to the [6]He+[6]He ground state channel, correspond well to the state 16.1 MeV and a group of states 17.8+18.6+19.3 MeV, centered at $\sim$ 18.5 MeV by Freer et al. [12, 13], who had suggested spin and parity assignment of 6^+ for both. In the work by Charity et al. [14], the [6]He+[6]He spectrum is largely structureless, if spectra from ^{1}H and ^{12}C targets are not considered separately. In that case peaks can be found around the energies observed in present experiment. As this is very inconsistent way to compare the data, one has to mention that the result of [14] are considered in such way, because the interpretation of the original work was quite refutable towards the results by Freer et al. [12, 13]. In the light of present results, it is shown that these two experiments to large extent agree, but the unresolved background contributions from different constituents of the CH_2 target, in both experiments, have caused contradiction and inconsistent interpretation of the data.

The final set of states which are going to be discussed are highly excited states ~ 10 MeV and more above the particle decay threshold, in the excitation energy range from 19 - 25 MeV. These are the states at (20.0), 22.5 and 25.4 MeV in the ^{6}He+^{6}He decay channel, (19.8) and (22.3) MeV in ^{4}He+^{8}He decay channel and finally 22.1 and 24.0 MeV in the newly observed ^{6}He+^{6}He (1.8 MeV, 2^+) decay channel. The states at ~ 20 and ~ 22.5 are observed in both ^{8}He and ^{6}He (0^+) decay channels, with the latter one observed also in the ^{6}He (1.8 MeV, 2^+) channel. The states at 24.0 and 25.4 MeV are individually observed in the ^{6}He (2^+) and ^{6}He (0^+) decay channels, respectively. This intricate decay scheme of ^{12}Be excited states requires careful theoretical consideration, but simple qualitative conclusion can be made. Observation of the states at ~ 19.9 and 22.3 MeV in two and three helium cluster decay channels, may indicate observation of the resonances with underlying α-4n-α structure. Another support to this claim is that neutron decays of these states were not observed in the present experiment, even though the spectrum produced from the ^{11}Be+^{4}He coincidences in the dT=3 telescope combination has enough statistics in this region for the "neutron peak" to appear, if existing. There are only two available experimental results in this energy region. One of the results is by Bohlen et al. [116], with states observed at 19.2 and 21.7 MeV, which are in general disagreement with present study if systematic shift of ~ 700-800 keV is not applied to either of the results. One plausible reason, apart from the systematic shift, may be that different set of states were produced in 3n-transfer reaction to ^{9}Be beam, and since the excitation energy is reconstructed only from the recoiling particle, results are inconclusive on the populated decay channel. The other result is by Freer et al [12, 13], which have states observed at 19.4 and 20.7 MeV in the ^{4}He+^{8}He decay channel and at 19.3, 20.9, 22.8, (24.0) and (25.1) in the ^{6}He+^{6}He channel. State at ~ 19.3 MeV likely corresponds to ~ 19.9 MeV state observed in the present experiment, as it is observed in both decay channels in both experiments. Apart from the state at ~ 20.8 MeV which is not observed in the present experiment, corresponding peaks can be found in [12, 13], but the reader is referred to original articles for conclusion, as the quality of these peaks, due to lower statistics and large background, is generally very low.

Simple consideration of the momentum of the third undetected particle in the ^{7}Li(^{9}Li, ^{6}He^{6}He)$_{dT=3}$^{4}He and ^{7}Li(^{9}Li, ^{4}He^{8}He)$_{dT=3}$^{4}He reactions may indicate underlying reaction mechanism used to populate the cluster states in the ^{12}Be nuclei. If the condition $P_3{}^2/2m_u$

< 15 MeV is set, meaning very low momentum of recoil ^{4}He (see Catania plot on Fig. 4.24), one can select the events which were produced in direct reaction, transfer of the triton to the ^{9}Li beam. In the excitation energy range covered by this case (Fig. 4.36), states at 18.5, 20.0, 22.5 and 25.4 MeV are clearly populated in the ^{6}He+^{6}He decay channel, owing to the direct reaction mechanism. For direct pickup reaction of one constituent (t) of the target (^{7}Li), the other (^{4}He) remains almost at rest, if direct reaction happened. For the same ^{6}He+^{6}He coincidences, large momentum of undetected ^{4}He yields clear and well separated peaks at (9.6), 10.2 and (11.8) in ^{10}Be nuclei, since one of the detected ^{6}He is recoil, indicating that population of these states have proceeded through complex reaction mechanisms. On the other hand, if the same condition is applied to the ^{4}He+^{8}He decay channel and coincidences, results does not indicate strong population of these states through direct reaction mechanism. This indicates that ^{12}Be excited states in both "1-2" and "2-3" combination of reaction products, have proceeded dominantly through more complex process. Thus, for the $P_3{}^2/2m_u > 15$ MeV, states at 17.5, 19.8 and 22.3 MeV were populated for "1-2" combination, and strong state at 13.8 MeV in "1-3" combination. For the other combination of the telescopes momentum distribution of the undetected reaction product is largely dominated by the phase space covered, thus these considerations are not fully applicable and if anything would indicate complex reaction mechanism. It is important to note that the states which were observed in the direct reaction were also populated by other reaction mechanisms in other data sets, which is expected for the transfer reactions at energies of few MeV/A. The ^{6}He nucleus in which the ^{12}Be decays, in the microscopic clustering model is dominantly described with the ^{4}He+2n configurations, but has sizable and important t+t contribution [119, 120]. This structural overlap in the ^{9}Li+t$\rightarrow$ ^{12}Be* $\rightarrow$ ^{6}He+^{6}He direct reaction may explain differences observed in population of the ^{6}He+^{6}He decay channel, compared to the ^{4}He+^{8}He channel. There are studies which have considered t+t+2n structure in ^{8}He [120], but this seems rather complex structure to be produced in triton pickup reaction and these consideration would be perhaps more suitable for the complex reaction mechanism.

These results, for the helium-helium cluster decays of the ^{12}Be excited states, produced in the reaction on the ^{7}Li target were published recently in [115]. Although spin and parity of the states were not determined and in most cases peaks were observed with low statistics and resolution, a thorough analysis of the same set of reactions in different

telescope segments and particle combinations in the exit channel gives confidence that the states observed in the present experiment are indeed the ones which undergo strong helium cluster decays. As most of the experiments referenced in the text suffer from influence of unresolved background from reactions on different constituents of the composite targets, present observation provide a major step forward in understanding of the ^{12}Be structure. One of the most important result is the observation of several states which decay to the ^{6}He (1.8 MeV, 2^+) excited state, along the decay to ^{6}He (0^+) and/or ^{8}He decay channels. This may be a direct evidence of the observed molecular resonances of underlying α-4n-α molecular structure. A new tentative state is observed at (20.0) MeV in the ^{6}He+^{6}He channel, which also decays to the ^{4}He+^{8}He decay channel, and a state at 24.0 MeV which decay solely to ^{6}He+^{6}He (2^+) channel. Also, a new tentative state is observed at (22.3) MeV in the ^{4}He+^{8}He channel, which decays also to the ^{6}He+^{6}He and newly observed ^{6}He+^{6}He (2^+) channel. New states at 15.4, 16.5 and 17.8 MeV observed in the ^{6}He+^{6}He (2^+) channel decay either to ^{6}He (0^+) or ^{4}He decay channel, in support of the underlying α-4n-α molecular structure. A great advantage of the present experimental results is that the whole excitation energy range, from the respective particle decay threshold up to $\sim$ 30 MeV, is covered in single experiment and thoroughly analyzed in consistent manner, which has helped to resolve inconsistencies in the observed states and provided a major leap forward in understanding of the structure of the ^{12}Be excited states using a novel approach of many-nucleon and cluster transfer reactions.

As an outlook of the result obtained in the present experiment, it is evident that a lot of work, both experimentally and theoretically is required to fully understand all of the details in emergence of rich structural phenomena found in ^{12}Be nucleus and other neutron-rich beryllium isotopes. A similar experiment is proposed, the measurement of the ^{6}He+^{7}Li reaction can be used to populate the ^{12}Be excited states. This reaction, like the ^{9}Li+^{7}Li used here, accounts for the sensitivity of transfer reaction to the structure of the nuclei in the entrance and exit channel. The use of large and highly segmented array of silicon telescopes and even gamma and/or neutron detectors is required, to explore possible decays to molecular resonances in the excited states of neutron-rich beryllium nuclei.

5.3 ^{13}B nucleus

Intruder configuration of the ^{11}Be ground state and quenching of the N=8 neutron shell in ^{12}Be ground state [1, 80] illustrates the importance of the clustering in nuclei, with neutron-rich light nuclei serving as important benchmark for understanding of the nuclear structure and the evolution of the clustering phenomena with addition of neutrons and/or protons [25, 66, 90]. Latter being the case for the neutron-rich boron isotopes, especially the ^{13}B, where additional proton, compared to the neighbouring ^{12}Be, stabilizes the shell structure in the ground state restoring N=8 magic number with closure of the neutron p-shell [25]. While the theory suggests that neutron-rich boron isotopes do exhibit various cluster structures both in ground (^{15,17}B) and excited states [25], experimental results, especially for the higher excitation energies in ^{13}B, studied here, are scarce. While various cluster and molecular structures, studied by AMD method [90, 121–123], are proposed to exist in the paper by Kanada En'yo et al. [25], three rotational bands with large deformations are outlined: $K^{\pi} = 3/2^{-}$, $K^{\pi} = 1/2^{+}$ and $K^{\pi} = 1/2^{-}$, with predicted band-head states at energies of 5-8, 8-11 and 10-13 MeV respectively, where range depends on the interaction used. The $K^{\pi} = 3/2^{-}$ band has dominant $2\hbar\omega$ configuration, the band head state $1/2_1^+$ in the $K^{\pi} = 1/2^+$ band is the proton intruder state with large deformation and the $K^{\pi} = 1/2^{-}$ band has pronounced ^{9}Li-α cluster structure.

As seen in Fig. 5.2 (b) $3/2^{-}$ ground state has the most spherical shape due to the neutron p-shell closure. In the $1/2_1^{-}$ state three-center cluster core structure appears, clusters being α with two valence neutrons, triton and α. For the $3/2_2^{-}$ and $5/2_1^{-}$ states (Fig. 5.2) (c) and (d)), deformed structure with developed cluster cores appears as part of $3/2^{-}$ band just ~ 5 MeV above the ground state. Even larger deformation is found in the $1/2^{+}$ band (Fig. 5.2) (e) and (f)) with well developed ^{9}Li-α cluster structure. It is interesting to note that the final wave functions indicate mixing of both (e) and (f) structures in the $K^{\pi}=1/2^+$ band. These results indicate existence of both molecular and well developed two and three center cluster structures in the excited states of ^{13}B (Fig. 5.2). There are only few experimental results available, resonant-decay spectroscopy experiment by Charity et al. [27] indicates the existence of 13.6 MeV state, which was also seen by Fletcher et al. [26], with FWHM of < 320 keV. In more comprehensive resonant elastic scattering experiment done with the ^{9}Li beam by Di Pietro et al. [2], using the Thick
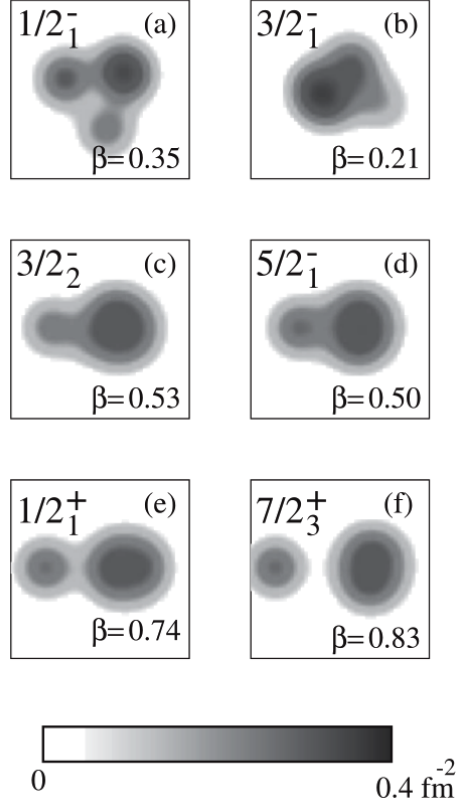
Figure 5.2: Density distribution of the ground ($3/2_1^-$) and excited states of ^{13}B. The intrinsic density of the dominant AMD wave function in the $|J_n^\pi>$ is shown. The density is integrated along the axis perpendicular to the plane. The deformation parameter β of matter density for the intrinsic state is also given. The box size is 10 fm. Taken from [25].

Target Inverse Kinematics Technique [124] on the ^{4}He gas target, broad resonances were observed in the ^{13}B excitation energy spectrum at 16.5, 18.5 and 19.5 MeV. None of the experiments did employ the use of the transfer reactions to populate cluster structures in ^{13}B excited states.

After comprehensive analysis presented in Sections 4.3.1 (^{9}Li+α), 4.3.2 (^{7}Li+^{6}He) and 4.3.3 (^{10}Be+t), a better insight in the structure of these excited states can be given. Starting with the ^{9}Li+α decays, all of the states observed by Charity et al. [27], Fletcher et al. [26] and Di Pietro et al. [2] are observed here, alongside newly observed state at (21.2) MeV and indication for state at (12.3) MeV. For the 13.6 MeV state the FWHM was deduced (details can be found in Section 3.3.7) to be $\sim$ 330 keV, which is in agreement with the value of $<$ 320 keV found by Charity et al. For the other states the FWHM values were deduced to be: $<$ 1450 keV for 16.5 MeV, $<$ 600 keV for 18.5 MeV, $<$ 510 keV for 19.5 MeV and $<$ 980 keV for 21.2 MeV state. Although low in statistics an indication of new state at $\sim$ 12.3 MeV was observed in the data, even though the σ of the Gaussian fit

on the data is smaller ($\sim$ 300 keV) than expected experimental resolution ($\sigma \sim$ 450 keV), making the observation unreliable. Estimate was based on the results from the ^{19}F data, where this state is best seen. Previously, only a doublet of states at 11.7 and 12.2 MeV was observed in n and n+n decay channel by Wuosamaa et al. [125] and one could speculate whether the state observed here is part of this doublet, undergoing also the α decay, or a new state. As discussed in the text before (Section 4.3.1), data presented in Fig. 4.59, for decay to the first excited state of ^{9}Li (2,69 MeV, 1/2$^-$) can be explained by the systematic shift of $\sim$ 3 MeV added to the peaks observed in the ^{9}Li ground state channel: 18.5 MeV (unresolved from the background) and two pronounced peaks: 19.5 MeV and 21.2 MeV, seen in Fig. 4.59 at 21.3, 22.7 and 24.4 MeV. Only remaining candidate for the decay to the first excited state of ^{9}Li is the state at 26.5 MeV. Possible reaction mechanism for the production of these states will be discussed at the end of this chapter.

In the ^{7}Li+^{6}He decay channel experimental resolution is affected by the inability to separate the ground (3/2$^-$) from the first excited state (0.48 MeV, 1/2$^-$) of detected ^{7}Li. Due to the higher particle decay threshold of 15.94 MeV, only the states seen by Di Pietro et al. [2] could be observed here. While only the 19.5 MeV state is observed clearly in the dT=1 case, deduced FWHM of 880 keV is not in agreement with the value of $\sim$ 500 keV deduced from the ^{9}Li+^{4}He decay channel. One possible explanation is the underestimate of the experimental resolution due to all uncertainties contributing to the final result, including the estimate of the background in Fig. 4.73 and contributions from unresolved first excited state, which was taken into account in MC simulations for the estimate of the width of the state. Other explanation could be that these are indeed two different states with different internal structure. Article by Kanada En'yo et al. [25] leaves space for such interpretation as interplay of well developed two-center cluster and molecular like structures are predicted. More detailed study, both theoretically and experimentally, is needed to clarify the result. For the 16.5, 18.5 and 21.2 MeV states not enough evidences were found to claim that these undergo ^{7}Li+^{6}He decay, even though indications are found in the results. The problem with latter two is that the σ's of the Gaussian fit to the data are smaller than estimated experimental resolution (from MC simulations) and the 16.5 MeV state is not observed clearly in dT=0 case due to low statistics and many-body contributions. Also, it's interesting to note that in the three-body coincidences (^{7}Li+^{6}He+^{3}H) peak in the ^{13}B excitation energy spectrum is observed at 26.3 MeV (Fig. 4.71), which

coincides with the peak at 26.5 MeV observed in the ^{9}Li*+^{4}He channel (Fig. 4.59). Although not shown in the results (Section 4.3.2), due to the low statistic and edge of the kinematic phase space effects, same peak (+/- 300 keV) is observed in the ^{7}Li+^{6}He and ^{7}Li+^{6}He* channels with very low statistics, when the ^{7}Li+^{3}H coincidences were studied. The same peak was searched for in the ^{10}Be+^{3}H, ^{10}Be$^*_{3.37}$+^{3}H and ^{10}Be$^{**}_{\sim 6}$+^{3}H decays (Section 4.3.3), but was not observed clearly in any spectrum. This leaves the space for speculation on the existence of this state, and certainly more experimental data is needed in the future to confirm this result.

^{9}Li+^{4}He	$\sim$(12.3)*	13.5	16.5	(18.5)	19.7	(21.2)		
^{9}Li*+^{4}He								$\sim$(26.5)*
^{7}Li+^{6}He				18.5	19.5	(21.2)		$\sim$(26.5)*
^{10}Be+^{3}H			$\sim$(16)	18.5	19.5	(21.2)	$\sim$(23.0)	$\sim$(24.6)*

Table 5.5: Summary table of the observed decays of the ^{13}B excited states. Tentative states are in parenthesis. New states observed in present work are indicated in red. Due to resolution and statistics, states indicated with $\sim$ have approximate excitations. Possible observation of states indicated by * is discussed in the text.

In the ^{10}Be+^{3}H channel (Section 4.3.3), due to strong contributions from the first (3.37 MeV, 2$^+$) excited state and the mixture of the excited states at $\sim$ 6 MeV of detected ^{10}Be, clear identification was achieved only for the dT=3 case. For the ^{13}B decay to the ^{10}Be ground state, with decay threshold of 10.99 MeV, a number of peaks were observed. While it is hard to give any strong conclusion solely on these result (Fig. 4.76 and 4.77), there are indications of existence of the states at energies of 16 MeV with deduced FWHM of 725 keV, 18.5 MeV with FWHM of 100 keV (σ of Gaussian fit comparable to the experimental resolution), 19.5 MeV with FWHM of 850 keV, $\sim$ 23 MeV with FWHM of $\sim$ 800 keV and 24.6 MeV with FWHM of 1.5 MeV. For the reaction on the ^{7}Li target, σ of the Gaussian fit for the 19.5 MeV peak was comparable, but smaller than expected experimental resolution of 350 keV. Combined with the small statistics of the ^{19}F data for the same peak, with deduced FWHM of 850 keV, question remains whether these observations provide enough evidence of the decay of the 19.5 MeV state to the ^{10}Be+^{3}H channel. These results, if confirmed, would indicate very different structure to that of lithium-helium two-center clustering for the state in question. Similar conclusion can be made for the 18.5 MeV peak, which is in this case observed with very small width (at the

edge of the experimental resolution). Peak at 16 MeV could be connected with the state at 16.5 MeV observed in the ^{9}Li+^{4}He channel, but considering the other known states are observed at correct energies, shift of $\sim$ 500 keV seems unlike and this could be an independent state observed solely in the ^{10}Be+^{3}H channel. For the tentative states at $\sim$ (23) MeV and (24.6) MeV, indication of the decay to the first excited state (3.37 MeV, 2^+) of detected ^{10}Be nuclei were searched for, but due to strong unresolved background contributions, clear evidence was not found. While it is out of scope of the analysis presented here, ^{13}B decay to highly excited states of ^{10}Be nuclei, with pronounced α+^{6}He cluster structure (10.2 MeV state as example) would be an interesting study to present in the future as it would link together molecular-like α-α-t structure (found in ^{11}B [42, 44]) with two valence neutrons, as proposed to exist by Kanada En'yo et al. [25] and possible α-^{6}He-t three-center cluster structure.
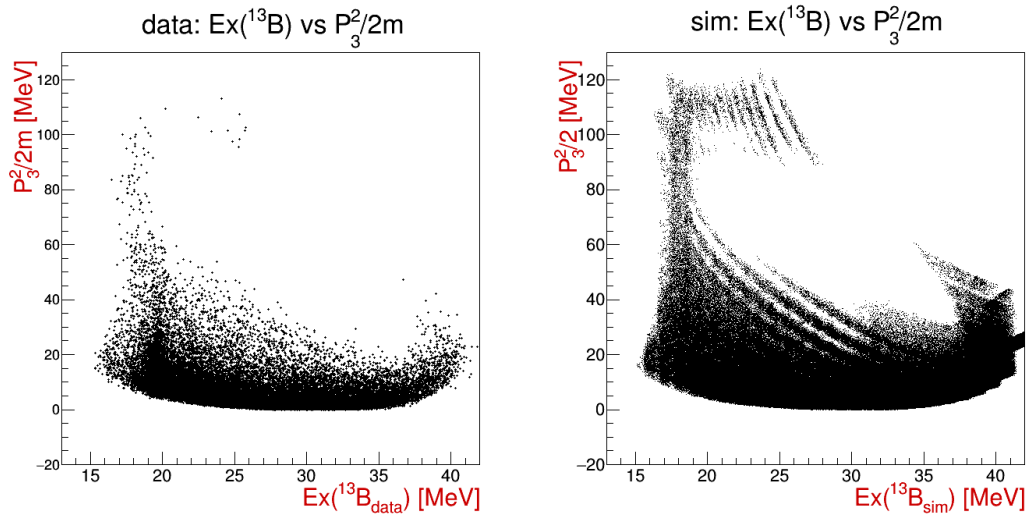
Figure 5.3: Excitation energy of ^{13}B in the ^{9}Li+^{4}He exit channel, for the reaction on the ^{7}Li target, versus the modified momentum variable ($P_3^2/2m_u$ [MeV]) of the third, undetected reaction product (^{3}H).

The reaction mechanism for the ^{9}Li+^{4}He channel was studied in more detail for the dT=3 case. As seen in Fig. 5.3, when ^{13}B excitation energy is plotted versus the modified momentum variable ($P_3^2/2m_u$ [MeV]) of the third, undetected reaction product (^{3}H), better separation of the observed states is achieved, most likely owing to different reaction mechanisms involved in the production of these states. As a control test, data from the MC simulations, produced isotropically is space (without any assumptions on the spin), were treated in the same way. One can notice that general shape of the data distribution is reproduced in the simulations, due to the effects of geometrical efficiency, with some

key differences. One can notice that the 19.5 MeV state is dominantly produced when undetected triton has very low momentum after the interaction (Fig. 5.4), indicating a direct process where ^{9}Li beam picks up α from the ^{7}Li target, leaving ^{3}H with very low momentum. The 16.5 MeV is seen with low statistics for the "middle momentum case", most likely due to the detection efficiency, while the 18.5 MeV state is not clearly seen in present case (Fig. 5.4).
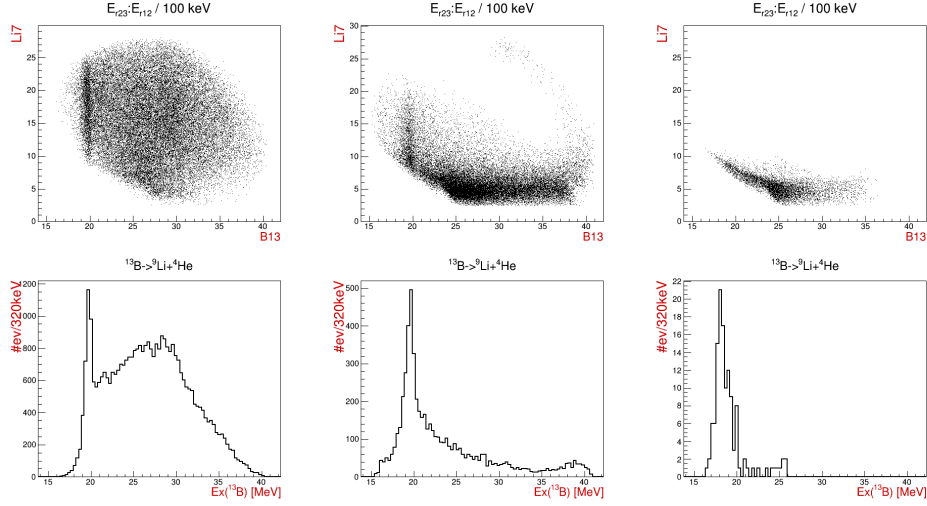
Figure 5.4: Excitation energy spectra for the ^{13}B decay to the ^{9}Li+^{4}He channel, for the reaction on the ^{7}Li target and dT=3 case. Spectra are differentiated by the modified momentum variable: $P_3^2/2m_u < 15$ (left), $15 <= P_3^2/2m_u < 60$ (center), and $P_3^2/2m_u >= 60$ (right). $P_3^2/2m_u$ is measured in MeV, where $m_u = 931.5$ MeV. As previously (Fig. 4.59), cut to exclude events below 9 MeV in ^{7}Li excitation energy is applied for the ^{13}B projection.

When similar analysis is applied to the dT=2 case (Fig. 5.5), momentum distribution is dominated by the geometrical efficiency of the LAMP setup. Still, the results are presented, as better separation of the states is achieved with different momentum intervals, especially the 16.5, 18.5 and 21.5 MeV states for "medium" momentum interval (Fig. 5.5 - center). Comparing the results in dT=2 case for 19.5 MeV state with the results for the dT=3 case, it seems that this prominent state is produced not only in direct processes, but also more complicated ones.

In the recent article by Di Pietro et al. [2], where ^{9}Li beam and ^{4}He gas target were used, it is suggested that transient orbital rotation model for the incoming reaction product could, with good agreement, describe general data shape and the observed states. In this model, a rolling process happens, where the reacting nuclei encounter each other at an impact parameter near the sum of their radii. After attachment and rolling, they break apart, often resulting in an enhancement of cross-section at backward angles [2], which
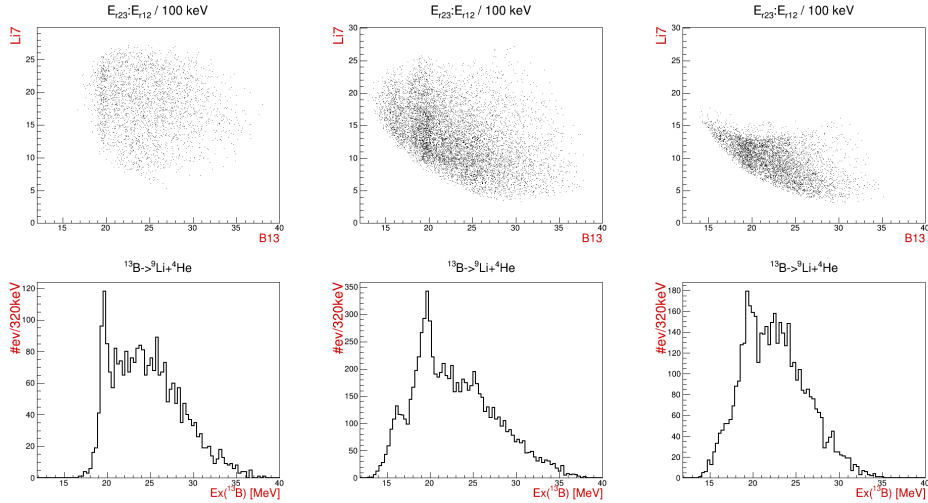
Figure 5.5: Excitation energy spectra for the ^{13}B decay to the ^{9}Li+^{4}He channel, for the reaction on the ^{7}Li target and dT=2 case. Spectra are differentiated by the modified momentum variable: $P_3^2/2m_u < 15$ (left), $15 <= P_3^2/2m_u < 50$ (center), and $P_3^2/2m_u >= 50$ (right). $P_3^2/2m_u$ is measured in MeV, where $m_u = 931.5$ MeV. As previously (Fig. 4.64), cut to exclude events below 9 MeV in ^{7}Li excitation energy is applied for the ^{13}B projection.

is indeed observed in the experiment. In their interpretation, a complex process through compound nucleus would yield narrow resonances which are not observed. In the case of the transfer reaction presented here, for sure the structure of the target nucleus (either ^{7}Li or ^{19}F) in the entrance channel plays an important role. From what is observed in the data, taking limited experimental resolution into account, it seems indeed that direct processes (α pick up) dominate the production of the ^{13}B excited states with pronounced ^{9}Li+^{4}He structure, but more complex processes can't be discarded as being a major contributor in the observed results, especially for the ^{7}Li+^{6}He and ^{10}Be+^{3}H channels.

Due to limited phase space covered by the LAMP setup and in most cases limited statistics and resolution, the partial widths of the observed states was not determined. Still, present measurement provides important spectroscopic information for the structure of the ^{13}B nucleus in the excited states and agrees well with the proposed existence of strong α clustering [25], in agreement with previous measurements [2, 26, 27]. Observation of the states which decay to all three channels may be an indication of underlying α-$2n$-t-α molecular structure proposed to exist alongside strong ^{9}Li+^{4}He clustering in the excited states. The measurement of the ^{10}Be+^{7}Li reaction is proposed for the study of cluster and molecular-like structure of the ^{13}B excited states.

6   Conclusion

The results for the cluster decays of the excited states of the neutron-rich ^{10,12}Be and ^{13}B nuclei were obtained in thorough analysis of the data from the S1620 experiment: "Examining the helium cluster decays of the ^{12}Be excites states by triton transfer to the ^{9}Li beam", performed at the ISAC-II accelerator facility at TRIUMF in Vancouver, Canada. The multi-nucleon and cluster transfer reactions of the ^{9}Li beam of 74.8 MeV energy on the $\approx$ 1mg/cm^2 LiF target were used to populate many interesting cluster states in neutron-rich light nuclei, with the focus on ^{10,12}Be and ^{13}B nuclei. Alongside carbon and oxygen, beryllium and boron isotopes present the key light nuclei to benchmark and test the development of theoretical models [1], due to the sensitivity of the nuclear force on nucleon-nucleon correlations, which are most prominent in weakly bound light systems and exotic structures such as nuclear molecules [28].

For the detection of the reaction products, large silicon strip detector array, arranged in the so called lampshade geometry was used, covering 16-48° in polar and 360° in azimuth angle. Each of the six telescopes was comprised of $\sim$ 70 μm thin ΔE and $\sim$ 1500 μm thick E detector, which were used to unambiguously identify isotopes from hydrogen to boron via standard ΔE-E method. Many useful and some novel techniques and approaches were established in the geometrical matching and classification of the events, as well as methods for the analysis of the three-body reactions. The developed routines and half-automatic procedures are well documented and will be of great help in future work with similar detection setups.

The use of transfer reactions and resonant particle spectroscopy method in the present experiment is quite novel approach in the study of the cluster and molecular-like struc-

tures in the excited states of the ^{12}Be and ^{13}B nuclei, as the most of previous research was done using the resonant elastic scattering and inelastic breakup reactions [2, 12–15]. This method had successfully been applied to the study of the cluster and molecular-like structure of the ^{10}Be nucleus in the seminal work by Zagreb nuclear physics group [16–19]. Although full study of the reaction dynamics was not possible in the present experiment, a simple consideration on the momentum of undetected reaction product revealed that a number of excited states in ^{10}Be, ^{12}Be and ^{13}B nuclei had been produced in the direct transfer reactions. These respectively include proton, triton and alpha transfer to the ^{9}Li beam, all of which have proceed through reactions with very large positive Q value. The same states observed in these direct reactions are also observed in reactions which have proceeded through more complex reaction mechanisms.

The successful use of the transfer reactions to study cluster and molecular-like structures even in the neutron-rich light nuclei, owes to the sensitivity of the transfer reactions to the structure of the nuclei in the entrance channel and the total energy available to the system [96]. Thus, enhanced clustering in the entrance channel and the use of neutron-rich ^{9}Li beam was correctly expected to enhance the observation of highly clustered states in the exit channel. It has to be mentioned that these reactions have very small cross-sections and consequently observation of strong cluster decays far above the neutron decay threshold in these nuclei is an evidence of peculiar intrinsic structure of these states [1].

Before listing the most important results and scientific contributions from the present thesis, some general remarks can be made. The first one would be that most of the states observed in the present experiment were previously observed in other measurements, but even for these states current experimental data will help to resolve part of the inconsistencies and contradictory results, especially in the case of the ^{12}Be nucleus. The present data is rare one to span the entire excitation energy region, from respective particle decay thresholds up to ~ 20 MeV above the thresholds, within the single experiment and analysis. Consequently, in ^{12}Be and ^{13}B, presented data are first experimental confirmations of initial observations for number of states close to the respective particle decay thresholds and in the high excitation energy region. The second important remark is that a number of new states in all three nuclei have been observed, with the first experimental observa-

tion of the ^{6}He+^{6}He* (1.8 MeV) decay of the ^{12}Be excited states and the ^{13}B decays to the ^{10}Be+^{3}H and ^{7}Li+^{6}He channels. Also, in the case of ^{10}Be nucleus, first experimental confirmation of the observed ^{4}He+^{6}He* (1.8 MeV) decays, since the initial observation of this decay channel by Zagreb group [18], and ^{8}Be+nn decay channel, for which there was only a single measurement available [21]. The third general remark is that the present results remain inconclusive on the existence of the molecular structure in these three nuclei, as the spin and parity of the states cannot be deduced from the current data. Still, the observation of strong cluster decays in the continuum of the single-particle neutron states, agreement with previous measurements which do indicate molecular structure of the observed states and observation of the number of these states in new decay channels agree well with the proposed molecular α-Xn-α structure in the ^{10,12}Be [10, 20] nuclei and possible underlying molecular α-2n-t-α structure proposed to exist in the highly excited states of the ^{13}B nucleus [25].

The results for the decays of the ^{10}Be excited states were obtained in thorough analysis of the ^{4}He+^{6}He, ^{6}He+^{6}He, ^{9}Be+^{6}He and ^{8}Be+^{6}He coincidences for all possible telescope and particle combinations in the exit channel separately. In the ^{4}He+^{6}He decay channel new states have been observed at 20.5 and 22.3 MeV and in the ^{4}He+^{6}He* (2^+) channel at (16.0) and (21.2) MeV, alongside the states at (9.6), 10.2 and 11.8 MeV, which were previously only observed in the latter channel by Zagreb group [18]. The state at $\sim$ 16.0 MeV is observed in all decay channels studied and the one at 20.5 MeV is observed also in the ^{9}Be+n channel. In the ^{8}Be+nn decay channel, for which previously only one measurement had existed [21], new states are observed at 12.7 and 19.6 MeV. Unlike the state at 10.6 MeV which strongly decays through one-neutron decay, the new state at 12.7 MeV was not previously observed in any other channel and may correspond to new structure in the ^{10}Be excited states proposed to exist in this energy range [85], but dedicated theoretical study and another experimental confirmation are needed. All other neutron decaying states were also observed in the ^{4}He+^{6}He decay channel and aforementioned $\sim$ 16 MeV state in all channels. Although present results are inconclusive on the molecular structure of the ^{10}Be excited states, observation of the 4^+ member of deformed σ molecular band in ^{4}He+^{6}He (0^+, 2^+) decay channels, but not in neutron ones, supports proposed molecular structure of this state [16–19]. Contrary to the observations in [22, 23], the 6^+ member of σ molecular band is not observed in the present results, in agreement with

recent dedicated measurement [24].

The results for the decays of the ^{12}Be excited states were obtained in thorough analysis of the ^{4}He+^{6}He, ^{6}He+^{6}He, ^{4}He+^{4}He and ^{4}He+^{8}He coincidences for all possible telescope and particle combinations in the exit channel separately. Close to respective particle decay thresholds, in the ^{6}He+^{6}He decay channel states were observed at (11.7) MeV and in ^{4}He+^{8}He channel at 10.3 and (12.1) MeV, in agreement with the results of recent experiment by Yang et al. [15], where zero-degree detector was used. The state at $\sim$ 13.5 MeV is observed in both channels, as well as highly excited state at $\approx$ 20 MeV, which is observed in the ^{6}He+^{6}He channel for the first time. Present results provide first experimental observation of the ^{6}He+^{6}He* (2$^+$) decay channel with the states at 15.4, 16.5, 17.8, 22.1 and 24.0 MeV, out of which the latter is observed only in this channel. The state at 16.5 MeV is also observed to decay to the ground state of ^{6}He, while the states at 15.4 and 17.8 MeV decay also to the ^{8}He channel. The state at $\approx$ 22.3 MeV is decaying to all three channels. Additionally, in the ^{6}He+^{6}He decay channel, at high excitation energies, the state is observed at 25.2 MeV, which was previously only seen in [12, 13]. The obtained results are in general agreement with those by Freer et al. [12, 13] and Yang et al. [15], and provide important spectroscopic information for the classification of these states, especially with newly observed ^{6}He+^{6}He*(2$^+$) decay channel [115]. Even though the present results do not provide direct evidence of the molecular structure and the existence of rotational bands built on these structures, obtained spectroscopic information surely improve understanding of the ^{12}Be structure and have helped to weight on the contradictory results from the past [14]. The fact than neutron decays of these states were not observed and that many of the states share decay modes is indicative of the underlying α-4n-α molecular structure and successful use of the transfer reactions in the study of these structures in neutron-rich ^{12}Be nucleus.

The results for the decays of the ^{13}B excited states were obtained in thorough analysis of the ^{9}Li+^{4}He, ^{7}Li+^{6}He and ^{10}Be+^{3}H coincidences for the detected particle pair and all possible telescope combinations in the exit channel separately. In the ^{9}Li+^{4}He channel previously known state at 13.5 MeV, seen in [26, 27], is observed together with the states at 16.5, 18.5 and 19.7 MeV, which agree very well with very recent results from

the ^{9}Li+^{4}He resonant elastic scattering by Di Pietro et al. [2]. Indication for two new states at (12.0) and (21.2) MeV are observed in this channel. The present experiment provides for the first time evidence of the ^{13}B decays to the ^{7}Li+^{6}He and ^{10}Be+t decay channels, with the states at 18.5, 19.5 MeV and tentatively (21.2) MeV observed in both cases. In the ^{10}Be+t decay channel additionally there are indications for the states at (16.0), (22.9) and (24.7) MeV, where the first one could correspond to the same state observed in the ^{9}Li+^{4}He decay channel. Present measurement provides important spectroscopic information for the structure of the ^{13}B nucleus in the excited states and agrees well with the proposed existence of strong α clustering [25], in agreement with previous measurements [2, 26, 27]. Observation of the states which decay to all three channels may be an indication of underlying α-2n-t-α molecular structure, proposed to exist alongside strong ^{9}Li+^{4}He clustering in the excited states of the ^{13}B nucleus. As the spin and parity is not know for any of these states, further dedicated experimental studies are needed to understand the structure of the ^{13}B excited states.

The successful use of the transfer reactions of the ^{9}Li beam on the LiF target in the present experiment, to populate cluster and molecular-like structures in the excited states of ^{10,12}Be and ^{13}B, presents transfer reactions as a valuable tool for the study of the structure of neutron-rich light nuclei. As an outlook for the future studies it is evident that highly segmented detection setups with large angular coverage are needed for the structure studies of these exotic nuclei and valuable information could be obtained with additional use of neutron and/or gamma detectors. Proposed study of the ^{10}Be+^{7}Li and ^{8,9}Li+^{9}Be reactions, with high efficiency, high resolution detection setup could provide a pathway to understanding of the molecular structure of the beryllium, boron and carbon isotopes and the evolution of the two-center molecular clustering found in Be isotopes to three-center one found in C isotopes, with addition of valence nucleons. Simultaneous study of the molecular $\alpha - 2n - t - \alpha$ structure of the ^{13}B nucleus and $\alpha - 2n - \alpha - \alpha$ structure of the ^{14}C nucleus, by triton and alpha transfer reactions of the ^{10}Be beam on the ^{7}Li target, could highlight the ^{13}B as a gateway nucleus in the understanding of the evolution from two- to three-center molecular-like clustering in the neutron-rich light nuclei.

Bibliography

[1] M. Freer, H. Horiuchi, Y. Kanada-En'yo, D. Lee, and Ulf-G Meißner. Microscopic clustering in light nuclei. *Reviews of Modern Physics*, 90(3):035004, 2018. doi: https://doi.org/10.1103/RevModPhys.90.035004. URL https://link.aps.org/doi/10.1103/RevModPhys.90.035004.

[2] A. Di Pietro, A.C. Shotter, J.P. Fernández-García, P. Figuera, M. Fisichella, A.M. Moro, M. Alcorta, M.J.G. Borge, T. Davinson, F. Ferrera, A.M. Laird, M. Lattuada, N. Soić, O. Tengblad, D. Torresi, and M. Zadro. Hints of quasi-molecular states in ^{13}B via the study of ^{9}Li $-^{4}$He elastic scattering. *Physics Letters B*, 832:137256, 2022. ISSN 0370-2693. doi: https://doi.org/10.1016/j.physletb.2022.137256. URL https://www.sciencedirect.com/science/article/pii/S0370269322003902.

[3] Y. Kanada-En'yo and H. Horiuchi. Structure of Light Unstable Nuclei Studied with Antisymmetrized Molecular Dynamics. *Progress of Theoretical Physics Supplement*, 142:205–263, 03 2001. ISSN 0375-9687. doi: 10.1143/PTPS.142.205.

[4] N. Itagaki, S. Aoyama, S. Okabe, and K. Ikeda. Cluster-shell competition in light nuclei. *Phys. Rev. C*, 70:054307, Nov 2004. doi: 10.1103/PhysRevC.70.054307. URL https://link.aps.org/doi/10.1103/PhysRevC.70.054307.

[5] J.-P. Ebran, E. Khan, T. Nikšić, and D. Vretenar. How atomic nuclei cluster. *Nature*, 487(7407):341–344, 2012. doi: 10.1038/nature11246. URL https://doi.org/10.1038/nature11246.

[6] A. C. Dreyfuss, K. D. Launey, T. Dytrych, J. P. Draayer, R. B. Baker, C. M. Deibel, and C. Bahri. Understanding emergent collectivity and clustering in nuclei from a symmetry-based no-core shell-model perspective. *Phys. Rev. C*, 95:044312,

Apr 2017. doi: 10.1103/PhysRevC.95.044312. URL `https://link.aps.org/doi/10.1103/PhysRevC.95.044312`.

[7] T. Otsuka, T. Abe, T. Yoshida, Y. Tsunoda, N. Shimizu, N. Itagaki, Y. Utsuno, J. Vary, P. Maris, and H. Ueno. α-Clustering in atomic nuclei from first principles with statistical learning and the Hoyle state character. *Nature Communications*, 13, 04 2022. doi: https://doi.org/10.1038/s41467-022-29582-0.

[8] Y. Kanada-En'yo and H. Horiuchi. Coexistence of cluster and shell-model aspects in nuclear systems. *Frontiers of Physics*, 13(6):1–25, 2018. doi: https://doi.org/10.1007/s11467-018-0830-y.

[9] Y. Kanada-En'yo, M. Kimura, and A. Ono. Antisymmetrized molecular dynamics and its applications to cluster phenomena. *Progress of Theoretical and Experimental Physics*, 2012(1), 08 2012. ISSN 2050-3911. doi: 10.1093/ptep/pts001. URL `https://doi.org/10.1093/ptep/pts001`. 01A202.

[10] Y. Kanada-En'yo and H. Horiuchi. Cluster structures of the ground and excited states of ^{12}Be studied with antisymmetrized molecular dynamics. *Phys. Rev. C*, 68:014319, Jul 2003. doi: 10.1103/PhysRevC.68.014319. URL `https://link.aps.org/doi/10.1103/PhysRevC.68.014319`.

[11] M. Ito, N. Itagaki, H. Sakurai, and K. Ikeda. Coexistence of Covalent Superdeformation and Molecular Resonances in an Unbound Region of ^{12}Be. *Phys. Rev. Lett.*, 100:182502, May 2008. doi: 10.1103/PhysRevLett.100.182502. URL `https://link.aps.org/doi/10.1103/PhysRevLett.100.182502`.

[12] M. Freer, J. C. Angélique, L. Axelsson, B. Benoit, U. Bergmann, W. N. Catford, S. P. G. Chappell, N. M. Clarke, N. Curtis, A. D'Arrigo, E. de Goes Brennard, O. Dorvaux, B. R. Fulton, G. Giardina, C. Gregori, S. Grévy, F. Hanappe, G. Kelly, M. Labiche, C. Le Brun, S. Leenhardt, M. Lewitowicz, K. Markenroth, F. M. Marqués, M. Motta, J. T. Murgatroyd, T. Nilsson, A. Ninane, N. A. Orr, I. Piqueras, M. G. Saint Laurent, S. M. Singer, O. Sorlin, L. Stuttgé, and D. L. Watson. Exotic Molecular States in ^{12}Be. *Phys. Rev. Lett.*, 82:1383–1386, Feb 1999. doi: 10.1103/PhysRevLett.82.1383. URL `https://link.aps.org/doi/10.1103/PhysRevLett.82.1383`.

[13] M. Freer, J. C. Angélique, L. Axelsson, B. Benoit, U. Bergmann, W. N. Catford, S. P. G. Chappell, N. M. Clarke, N. Curtis, A. D'Arrigo, E. de Góes Brennard, O. Dorvaux, B. R. Fulton, G. Giardina, C. Gregori, S. Grévy, F. Hanappe, G. Kelly, M. Labiche, C. Le Brun, S. Leenhardt, M. Lewitowicz, K. Markenroth, F. M. Marqués, J. T. Murgatroyd, T. Nilsson, A. Ninane, N. A. Orr, I. Piqueras, M. G. Saint Laurent, S. M. Singer, O. Sorlin, L. Stuttgé, and D. L. Watson. Helium breakup states in ^{10}Be and ^{12}Be. *Phys. Rev. C*, 63:034301, Jan 2001. doi: 10.1103/PhysRevC.63.034301. URL `https://link.aps.org/doi/10.1103/PhysRevC.63.034301`.

[14] R. J. Charity, S. A. Komarov, L. G. Sobotka, J. Clifford, D. Bazin, A. Gade, Jenny Lee, S. M. Lukyanov, W. G. Lynch, M. Mocko, S. P. Lobastov, A. M. Rogers, A. Sanetullaev, M. B. Tsang, M. S. Wallace, S. Hudan, C. Metelko, M. A. Famiano, A. H. Wuosmaa, and M. J. van Goethem. Particle decay of ^{12}Be excited states. *Phys. Rev. C*, 76:064313, Dec 2007. doi: 10.1103/PhysRevC.76.064313. URL `https://link.aps.org/doi/10.1103/PhysRevC.76.064313`.

[15] Z. H. Yang, Y. L. Ye, Z. H. Li, J. L. Lou, J. S. Wang, D. X. Jiang, Y. C. Ge, Q. T. Li, H. Hua, X. Q. Li, F. R. Xu, J. C. Pei, R. Qiao, H. B. You, H. Wang, Z. Y. Tian, K. A. Li, Y. L. Sun, H. N. Liu, J. Chen, J. Wu, J. Li, W. Jiang, C. Wen, B. Yang, Y. Liu, Y. Y. Yang, P. Ma, J. B. Ma, S. L. Jin, J. L. Han, and J. Lee. Helium-helium clustering states in ^{12}Be. *Phys. Rev. C*, 91:024304, Feb 2015. doi: 10.1103/PhysRevC.91.024304. URL `https://link.aps.org/doi/10.1103/PhysRevC.91.024304`.

[16] N. Soić, S. Blagus, M. Bogovac, S. Fazinić, M. Lattuada, M. Milin, Đ. Miljanić, D. Rendić, C. Spitaleri, T. Tadić, and M. Zadro. ^{6}He $+ \alpha$ clustering in ^{10}Be. *Europhysics Letters (EPL)*, 34(1):7–12, 1996. doi: 10.1209/epl/i1996-00407-y. URL `https://doi.org/10.1209/epl/i1996-00407-y`.

[17] M. Milin, M. Aliotta, S. Cherubini, T. Davinson, A. Di Pietro, P. Figuera, W. Galster, D. Miljanić, A. Ninane, A. N. Ostrowski, A. C. Shotter, N. Soić, C. Spitaleri, and M. Zadro. The ^{6}He $+^6$Li reactions and exotic states of ^{10}Be. *Europhysics Letters*, 48(6):616, 1999. doi: 10.1209/epl/i1999-00528-3. URL `https://dx.doi.org/10.1209/epl/i1999-00528-3`.

[18] Đ. Miljanić, N. Soić, S. Blagus, S. Cherubini, M. Lattuada, M. Milin, A. Mussumara, R.G. Pizzone, D. Rendić, S. Romano, C. Spitaleri, A. Tumino, and M. Zadro. ^{10}Be and molecular states. *Fizika B*, 10(4):235–246, 2001. ISSN 1330-0016.

[19] M. Milin, M. Zadro, S. Cherubini, T. Davinson, A. Di Pietro, P. Figuera, Đ. Miljanić, A. Musumarra, A. Ninane, A.N. Ostrowski, M.G. Pellegriti, A.C. Shotter, N. Soić, and C. Spitaleri. Sequential decay reactions induced by a 18 MeV ^{6}He beam on ^{6}Li and ^{7}Li. *Nuclear Physics A*, 753(3):263–287, 2005. ISSN 0375-9474. doi: https://doi.org/10.1016/j.nuclphysa.2005.02.154. URL `https://www.sciencedirect.com/science/article/pii/S0375947405003398`.

[20] Y. Kanada-En'yo, H. Horiuchi, and A. Doté. Structure of excited states of ^{10}Be studied with antisymmetrized molecular dynamics. *Phys. Rev. C*, 60:064304, Oct 1999. doi: 10.1103/PhysRevC.60.064304. URL `https://link.aps.org/doi/10.1103/PhysRevC.60.064304`.

[21] D. Suzuki, A. Shore, W. Mittig, J. J. Kolata, D. Bazin, M. Ford, T. Ahn, F. D. Becchetti, S. Beceiro Novo, D. Ben Ali, B. Bucher, J. Browne, X. Fang, M. Febbraro, A. Fritsch, E. Galyaev, A. M. Howard, N. Keeley, W. G. Lynch, M. Ojaruega, A. L. Roberts, and X. D. Tang. Resonant α scattering of ^{6}He: Limits of clustering in ^{10}Be. *Phys. Rev. C*, 87:054301, May 2013. doi: 10.1103/PhysRevC.87.054301. URL `https://link.aps.org/doi/10.1103/PhysRevC.87.054301`.

[22] G. V. Rogachev, M. L. Avila, A. N. Kuchera, L. T. Baby, J. Belarge, J. Blackmon, V. Z. Goldberg, E. D. Johnson, K. W. Kemper, E. Koshchiy, L. Linhardt, K. Macon, D. Santiago-Gonzalez, and I. Wiedenhöver. Clustering in non-self-conjugate nuclei ^{10}Be and ^{18}O. *Journal of Physics: Conference Series*, 569:012004, dec 2014. doi: 10.1088/1742-6596/569/1/012004. URL `https://doi.org/10.1088/1742-6596/569/1/012004`.

[23] D. Dell'Aquila, I. Lombardo, L. Acosta, R. Andolina, L. Auditore, G. Cardella, M. B. Chatterjiee, E. De Filippo, L. Francalanza, B. Gnoffo, G. Lanzalone, A. Pagano, E. V. Pagano, M. Papa, S. Pirrone, G. Politi, F. Porto, L. Quattrocchi, F. Rizzo, E. Rosato, P. Russotto, A. Trifirò, M. Trimarchi, G. Verde, and M. Vigilante. New experimental investigation of the structure of ^{10}Be and ^{16}C by

means of intermediate-energy sequential breakup. *Phys. Rev. C*, 93:024611, 2016. doi: 10.1103/PhysRevC.93.024611. URL `https://link.aps.org/doi/10.1103/PhysRevC.93.024611`.

[24] S. Upadhyayula, G. V. Rogachev, J. Bishop, V. Z. Goldberg, J. Hooker, C. Hunt, H. Jayatissa, E. Koshchiy, E. Uberseder, A. Volya, B. T. Roeder, and A. Saastamoinen. Search for the high-spin members of the $\alpha : 2n : \alpha$ band in ^{10}Be. *Phys. Rev. C*, 101:034604, Mar 2020. doi: 10.1103/PhysRevC.101.034604. URL `https://link.aps.org/doi/10.1103/PhysRevC.101.034604`.

[25] Y. Kanada-En'yo, Y. Kawanami, Y. Taniguchi, and M. Kimura. Cluster States in ^{13}B. *Progress of Theoretical Physics*, 120(5):917–935, 11 2008. ISSN 0033-068X. doi: 10.1143/PTP.120.917. URL `https://doi.org/10.1143/PTP.120.917`.

[26] N. R. Fletcher, D. D. Caussyn, F. Maréchal, N. Curtis, and J. A. Liendo. New highly excited states of ^{10}Be observed in charged particle decay. *Phys. Rev. C*, 68:024316, Aug 2003. doi: 10.1103/PhysRevC.68.024316. URL `https://link.aps.org/doi/10.1103/PhysRevC.68.024316`.

[27] R. J. Charity, S. A. Komarov, L. G. Sobotka, J. Clifford, D. Bazin, A. Gade, Jenny Lee, S. M. Lukyanov, W. G. Lynch, M. Mocko, S. P. Lobastov, A. M. Rogers, A. Sanetullaev, M. B. Tsang, M. S. Wallace, R. G. T. Zegers, S. Hudan, C. Metelko, M. A. Famiano, A. H. Wuosmaa, and M. J. van Goethem. Investigation of particle-unbound excited states in light nuclei with resonance-decay spectroscopy using a ^{12}Be beam. *Phys. Rev. C*, 78:054307, Nov 2008. doi: 10.1103/PhysRevC.78.054307. URL `https://link.aps.org/doi/10.1103/PhysRevC.78.054307`.

[28] W. von Oertzen, M. Freer, and Y. Kanada-En'yo. Nuclear clusters and nuclear molecules. *Physics Reports*, 432(2):43–113, 2006. ISSN 0370-1573. doi: https://doi.org/10.1016/j.physrep.2006.07.001. URL `https://www.sciencedirect.com/science/article/pii/S0370157306002626`.

[29] K. Ikeda, N. Takigawa, and H. Horiuchi. The Systematic Structure-Change into the Molecule-like Structures in the Self-Conjugate 4n Nuclei. *Progress of Theoretical Physics Supplement*, E68:464–475, 1968. ISSN 0375-9687. doi: 10.1143/PTPS.E68.464. URL `https://doi.org/10.1143/PTPS.E68.464`.

[30] F. Hoyle. On Nuclear Reactions Occuring in Very Hot STARS. I. the Synthesis of Elements from Carbon to Nickel. *The Astrophysical Journal Supplement Series*, 1: 121, 1954. doi: 10.1086/190005.

[31] D.N.F. Dunbar, R.E. Pixley, W.A. Wenzel, and W. Whaling. The 7.68MeV state in ^{12}C. *Physical Review*, 92(3):649 – 650, 1953. doi: 10.1103/PhysRev.92.649.

[32] M. Freer and H.O.U. Fynbo. The Hoyle state in ^{12}C. *Progress in Particle and Nuclear Physics*, 78:1–23, 2014. ISSN 0146-6410. doi: https://doi.org/10.1016/j.ppnp.2014.06.001. URL `https://www.sciencedirect.com/science/article/pii/S0146641014000453`.

[33] H.O.U. Fynbo, C.A. Diget, U.C. Bergmann, M.J.G. Borge, J. Cederkäll, P. Dendooven, L.M. Fraile, S. Franchoo, V.N. Fedosseev, B.R. Fulton, et al. Revised rates for the stellar triple-α process from measurement of ^{12}C nuclear resonances. *Nature*, 433(7022):136–139, 2005. doi: https://doi.org/10.1038/nature03219.

[34] R. B. Wiringa, Steven C. Pieper, J. Carlson, and V. R. Pandharipande. Quantum Monte Carlo calculations of A = 8 nuclei. *Phys. Rev. C*, 62:014001, Jun 2000. doi: 10.1103/PhysRevC.62.014001. URL `https://link.aps.org/doi/10.1103/PhysRevC.62.014001`.

[35] M. Lyu, K. Yoshida, Y. Kanada-En'yo, and K. Ogata. Manifestation of α clustering in ^{10}Be via α-knockout reaction. *Phys. Rev. C*, 97:044612, Apr 2018. doi: 10.1103/PhysRevC.97.044612. URL `https://link.aps.org/doi/10.1103/PhysRevC.97.044612`.

[36] K. Arai. Structure of the excited states of ^{10}Be in a microscopic cluster model. *Phys. Rev. C*, 69:014309, Jan 2004. doi: 10.1103/PhysRevC.69.014309. URL `https://link.aps.org/doi/10.1103/PhysRevC.69.014309`.

[37] M. Freer, N.I. Ashwood, N.L. Achouri, W.N. Catford, N. Curtis, F. Delaunay, H. Al Falou, F.M. Marques, T. Munoz-Britton, N.A. Orr, R. Raabe, N. Soić, J.S. Thomas, C. Wheldon, and V.A. Ziman. Elastic scattering of ^{8}He+^{4}He and two$-$neutron transfer and the influence of resonances in ^{12}Be. *Physics Letters B*, 775:58–62, 2017. ISSN 0370-2693. doi: https://doi.org/10.1016/j.physletb.2017.10.063. URL `https://www.sciencedirect.com/science/article/pii/S0370269317308754`.

[38] N. Curtis, N. I. Ashwood, L. T. Baby, T. D. Baldwin, T. R. Bloxham, W. N. Catford, D. D. Caussyn, M. Freer, C. W. Harlin, P. McEwan, D. L. Price, D. Spingler, and I. Wiedenhover. α-decaying states in ^{10,12}Be populated in the ^{10}Be(^{14}C,^{10,12}Be) reaction. *Phys. Rev. C*, 73:057301, 2006. doi: 10.1103/PhysRevC.73.057301. URL `https://link.aps.org/doi/10.1103/PhysRevC.73.057301`.

[39] M. Lyu, K. Yoshida, Y. Kanada-En'yo, and K. Ogata. Direct probing of the cluster structure in ^{12}Be via the $\alpha-$knockout reaction. *Phys. Rev. C*, 99:064610, Jun 2019. doi: 10.1103/PhysRevC.99.064610. URL `https://link.aps.org/doi/10.1103/PhysRevC.99.064610`.

[40] Y. Kanada-En'yo. The Structure of Ground and Excited States of ^{12}C. *Progress of Theoretical Physics*, 117(4):655–680, 04 2007. ISSN 0033-068X. doi: 10.1143/PTP.117.655. URL `https://doi.org/10.1143/PTP.117.655`.

[41] Y. Kanada-En'yo. Negative parity states of ^{11}B and ^{11}C and the similarity with ^{12}C. *Phys. Rev. C*, 75:024302, Feb 2007. doi: 10.1103/PhysRevC.75.024302. URL `https://link.aps.org/doi/10.1103/PhysRevC.75.024302`.

[42] N. Soić, M. Freer, L. Donadille, N. M. Clarke, P. J. Leask, W. N. Catford, K. L. Jones, D. Mahboub, B. R. Fulton, B. J. Greenhalgh, D. L. Watson, and D. C. Weisser. Three-centre cluster structure in ^{11}C and ^{11}B. *Journal of Physics G: Nuclear and Particle Physics*, 31(10):S1701–S1704, sep 2005. doi: 10.1088/0954-3899/31/10/057. URL `https://doi.org/10.1088/0954-3899/31/10/057`.

[43] N. Curtis, N. I. Ashwood, W. N. Catford, N. M. Clarke, M. Freer, D. Mahboub, C. J. Metelko, S. D. Pain, N. Soić, and D. C. Weisser. $\alpha + \mathrm{Li}$ and $\mathrm{H} + \mathrm{Be}$ decay of ^{10,11,12}B. *Phys. Rev. C*, 72:044320, Oct 2005. doi: 10.1103/PhysRevC.72.044320. URL `https://link.aps.org/doi/10.1103/PhysRevC.72.044320`.

[44] T. Kawabata, H. Akimune, H. Fujita, Y. Fujita, M. Fujiwara, K. Hara, K. Hatanaka, M. Itoh, Y. Kanada-En'yo, S. Kishi, K. Nakanishi, H. Sakaguchi, Y. Shimbara, A. Tamii, S. Terashima, M. Uchida, T. Wakasa, Y. Yasuda, H.P. Yoshida, and M. Yosoi. $2\alpha+$t cluster structure in ^{11}B. *Physics Letters B*, 646(1):6–11, 2007. ISSN 0370-2693. doi: https://doi.org/10.1016/j.physletb.2006.11.079. URL `https://www.sciencedirect.com/science/article/pii/S0370269307000706`.

[45] D. D. Zhang, Z. X. Ren, P. W. Zhao, D. Vretenar, T. Nikšić, and J. Meng. Effects of rotation and valence nucleons in molecular α-chain nuclei. *Phys. Rev. C*, 105: 024322, Feb 2022. doi: 10.1103/PhysRevC.105.024322. URL `https://link.aps.org/doi/10.1103/PhysRevC.105.024322`.

[46] H. Yamaguchi, D. Kahl, S. Hayakawa, Y. Sakaguchi, K. Abe, T. Nakao, T. Suhara, N. Iwasa, A. Kim, D.H. Kim, S.M. Cha, M.S. Kwag, J.H. Lee, E.J. Lee, K.Y. Chae, Y. Wakabayashi, N. Imai, N. Kitamura, P. Lee, J.Y. Moon, K.B. Lee, C. Akers, H.S. Jung, N.N. Duy, L.H. Khiem, and C.S. Lee. Experimental investigation of a linear-chain structure in the nucleus ^{14}C. *Physics Letters B*, 766:11–16, 2017. ISSN 0370-2693. doi: https://doi.org/10.1016/j.physletb.2016.12.050. URL `https://www.sciencedirect.com/science/article/pii/S0370269316307961`.

[47] D.R. Tilley, H.R. Weller, and G.M. Hale. Energy levels of light nuclei A = 4. *Nuclear Physics A*, 541(1):1–104, 1992. ISSN 0375-9474. doi: https://doi.org/10.1016/0375-9474(92)90635-W.

[48] M. Freer. Clustering in Light Nuclei; from the Stable to the Exotic. In C. Scheidenberger and M. Pfützner, editors, *The Euroschool on Exotic Beams, Vol. IV*, pages 1–37. Springer Berlin Heidelberg, 2014. ISBN 978-3-642-45141-6. doi: 10.1007/978-3-642-45141-6_1.

[49] A. Poves and F. Nowacki. The nuclear shell model. In J. M. Arias and M. Lozano, editors, *An Advanced Course in Modern Nuclear Physics*, pages 70–101. Springer Berlin Heidelberg, 2001. ISBN 978-3-540-44620-0. doi: 10.1007/3-540-44620-6_3. URL `https://doi.org/10.1007/3-540-44620-6_3`.

[50] J. Dobaczewski, N. Michel, W. Nazarewicz, M. Płoszajczak, and J. Rotureau. Shell structure of exotic nuclei. *Progress in Particle and Nuclear Physics*, 59(1):432–445, 2007. ISSN 0146-6410. doi: https://doi.org/10.1016/j.ppnp.2007.01.022. URL `https://www.sciencedirect.com/science/article/pii/S0146641007000233`. International Workshop on Nuclear Physics 28th Course.

[51] T. Otsuka, A. Gade, O. Sorlin, T. Suzuki, and Y. Utsuno. Evolution of shell structure in exotic nuclei. *Rev. Mod. Phys.*, 92:015002, Mar 2020. doi:

10.1103/RevModPhys.92.015002. URL `https://link.aps.org/doi/10.1103/RevModPhys.92.015002`.

[52] L. R. Hafstad and E. Teller. The Alpha-Particle Model of the Nucleus. *Phys. Rev.*, 54:681–692, Nov 1938. doi: 10.1103/PhysRev.54.681. URL `https://link.aps.org/doi/10.1103/PhysRev.54.681`.

[53] W. Nazarewicz and J. Dobaczewski. Dynamical symmetries, multiclustering, and octupole susceptibility in superdeformed and hyperdeformed nuclei. *Phys. Rev. Lett.*, 68:154–157, Jan 1992. doi: 10.1103/PhysRevLett.68.154. URL `https://link.aps.org/doi/10.1103/PhysRevLett.68.154`.

[54] M. Freer, R.R. Betts, and A.H. Wuosmaa. Relationship between the deformed harmonic oscillator and clustering in light nuclei. *Nuclear Physics A*, 587(1):36–54, 1995. ISSN 0375-9474. doi: https://doi.org/10.1016/0375-9474(94)00820-D. URL `https://www.sciencedirect.com/science/article/pii/037594749400820D`.

[55] T. Yukawa and S. Yoshida. An alpha-cluster model calculation of ^{12}C. *Physics Letters B*, 33(5):334–336, 1970. ISSN 0370-2693. doi: https://doi.org/10.1016/0370-2693(70)90246-7. URL `https://www.sciencedirect.com/science/article/pii/0370269370902467`.

[56] A. Tohsaki, H. Horiuchi, P. Schuck, and G. Röpke. Alpha Cluster Condensation in ^{12}C and ^{16}O. *Phys. Rev. Lett.*, 87:192501, Oct 2001. doi: 10.1103/PhysRevLett.87.192501. URL `https://link.aps.org/doi/10.1103/PhysRevLett.87.192501`.

[57] Y. Funaki, H. Horiuchi, W. von Oertzen, G. Röpke, P. Schuck, A. Tohsaki, and T. Yamada. Concepts of nuclear α-particle condensation. *Phys. Rev. C*, 80:064326, Dec 2009. doi: 10.1103/PhysRevC.80.064326. URL `https://link.aps.org/doi/10.1103/PhysRevC.80.064326`.

[58] Fujiwara, Y. and Horiuchi, H. and Ikeda, K. and Kamimura, M. and Katō, K. and Suzuki, Y. and Uegaki, E. Chapter II. Comprehensive Study of Alpha-Nuclei. *Progress of Theoretical Physics Supplement*, 68:29–192, 01 1980. ISSN 0375-9687. doi: 10.1143/PTPS.68.29. URL `https://doi.org/10.1143/PTPS.68.29`.

[59] J. A. Wheeler. On the Mathematical Description of Light Nuclei by the Method of Resonating Group Structure. *Phys. Rev.*, 52:1107–1122, Dec 1937. doi: 10.1103/PhysRev.52.1107. URL `https://link.aps.org/doi/10.1103/PhysRev.52.1107`.

[60] P. Descouvemont. Microscopic study of α clustering in the ^{9,10,11}Be isotopes. *Nuclear Physics A*, 699(3):463–478, 2002. ISSN 0375-9474. doi: https://doi.org/10.1016/S0375-9474(01)01286-6. URL `https://www.sciencedirect.com/science/article/pii/S0375947401012866`.

[61] M. Ito and K. Ikeda. Unified studies of chemical bonding structures and resonant scattering in light neutron-excess systems, ^{10,12}Be. *Reports on Progress in Physics*, 77(9):096301, sep 2014. doi: 10.1088/0034-4885/77/9/096301. URL `https://doi.org/10.1088/0034-4885/77/9/096301`.

[62] Y. Ogawa, K. Arai, Y. Suzuki, and K. Varga. Microscopic four-cluster description of ^{10}Be and ^{10}C with the stochastic variational method. *Nuclear Physics A*, 673(1):122–142, 2000. ISSN 0375-9474. doi: https://doi.org/10.1016/S0375-9474(00)00133-0. URL `https://www.sciencedirect.com/science/article/pii/S0375947400001330`.

[63] B. Zhou, M. Kimura, Q. Zhao, and S. Shin. Microscopic calculations for Be isotopes within real-time evolution method. *The European Physical Journal A*, 56:298, 2020. ISSN 1434-601X. doi: 10.1140/epja/s10050-020-00306-6. URL `https://doi.org/10.1140/epja/s10050-020-00306-6`.

[64] N. Itagaki and S. Okabe. Molecular orbital structures in ^{10}Be. *Phys. Rev. C*, 61:044306, Mar 2000. doi: 10.1103/PhysRevC.61.044306. URL `https://link.aps.org/doi/10.1103/PhysRevC.61.044306`.

[65] N. Itagaki, S. Okabe, and K. Ikeda. Important role of the spin-orbit interaction in forming the $1/2^+$ orbital structure in Be isotopes. *Phys. Rev. C*, 62:034301, Jul 2000. doi: 10.1103/PhysRevC.62.034301. URL `https://link.aps.org/doi/10.1103/PhysRevC.62.034301`.

[66] H. Furutani, H. Kanada, T. Kaneko, S. Nagata, H. Nishioka, S. Okabe, S. Saito, T. Sakuda, and M. Seya. Chapter III. Study of Non-Alpha-Nuclei Based on the

Viewpoint of Cluster Correlations. *Progress of Theoretical Physics Supplement*, 68:193–302, 01 1980. ISSN 0375-9687. doi: 10.1143/PTPS.68.193. URL `https://doi.org/10.1143/PTPS.68.193`.

[67] M. Bender, P.-H. Heenen, and P.-G. Reinhard. Self-consistent mean-field models for nuclear structure. *Rev. Mod. Phys.*, 75:121–180, Jan 2003. doi: 10.1103/RevModPhys.75.121. URL `https://link.aps.org/doi/10.1103/RevModPhys.75.121`.

[68] D. Vretenar, A.V. Afanasjev, G.A. Lalazissis, and P. Ring. Relativistic Hartree–Bogoliubov theory: static and dynamic aspects of exotic nuclear structure. *Physics Reports*, 409(3):101–259, 2005. ISSN 0370-1573. doi: https://doi.org/10.1016/j.physrep.2004.10.001. URL `https://www.sciencedirect.com/science/article/pii/S0370157304004545`.

[69] P. Arumugam, B. K. Sharma, S. K. Patra, and Raj K. Gupta. Relativistic mean field study of clustering in light nuclei. *Phys. Rev. C*, 71:064308, Jun 2005. doi: 10.1103/PhysRevC.71.064308. URL `https://link.aps.org/doi/10.1103/PhysRevC.71.064308`.

[70] H. Feldmeier. Fermionic molecular dynamics. *Nuclear Physics A*, 515(1):147–172, 1990. ISSN 0375-9474. doi: https://doi.org/10.1016/0375-9474(90)90328-J. URL `https://www.sciencedirect.com/science/article/pii/037594749090328J`.

[71] H. Feldmeier, K. Bieler, and J. Schnack. Fermionic molecular dynamics for ground states and collisions of nuclei. *Nuclear Physics A*, 586(3):493–532, 1995. ISSN 0375-9474. doi: https://doi.org/10.1016/0375-9474(94)00792-L. URL `https://www.sciencedirect.com/science/article/pii/037594749400792L`.

[72] Y. Kanada-En'yo. Isovector and isoscalar dipole excitations in ^{9}Be and ^{10}Be studied with antisymmetrized molecular dynamics. *Phys. Rev. C*, 93:024322, Feb 2016. doi: 10.1103/PhysRevC.93.024322. URL `https://link.aps.org/doi/10.1103/PhysRevC.93.024322`.

[73] Y. Kanada-En'yo. Isoscalar monopole and dipole excitations of cluster states and giant resonances in ^{12}C. *Phys. Rev. C*, 93:054307, May 2016. doi: 10.1103/PhysRevC.93.054307. URL `https://link.aps.org/doi/10.1103/PhysRevC.93.054307`.

[74] W. Leidemann and G. Orlandini. Modern ab initio approaches and applications in few-nucleon physics with A ≥4. *Progress in Particle and Nuclear Physics*, 68:158–214, 2013. ISSN 0146-6410. doi: https://doi.org/10.1016/j.ppnp.2012.09.001. URL `https://www.sciencedirect.com/science/article/pii/S014664101200110X`.

[75] R. Machleidt and D.R. Entem. Chiral effective field theory and nuclear forces. *Physics Reports*, 503(1):1–75, 2011. ISSN 0370-1573. doi: https://doi.org/10.1016/j.physrep.2011.02.001. URL `https://www.sciencedirect.com/science/article/pii/S0370157311000457`.

[76] E. Epelbaum, H.-W. Hammer, and Ulf-G. Meißner. Modern theory of nuclear forces. *Rev. Mod. Phys.*, 81:1773–1825, Dec 2009. doi: 10.1103/RevModPhys.81.1773. URL `https://link.aps.org/doi/10.1103/RevModPhys.81.1773`.

[77] J. Carlson, S. Gandolfi, F. Pederiva, Steven C. Pieper, R. Schiavilla, K. E. Schmidt, and R. B. Wiringa. Quantum Monte Carlo methods for nuclear physics. *Rev. Mod. Phys.*, 87:1067–1118, Sep 2015. doi: 10.1103/RevModPhys.87.1067. URL `https://link.aps.org/doi/10.1103/RevModPhys.87.1067`.

[78] B. R. Barrett, P. Navrátil, and J. P. Vary. Ab initio no core shell model. *Progress in Particle and Nuclear Physics*, 69:131–181, 2013. ISSN 0146-6410. doi: https://doi.org/10.1016/j.ppnp.2012.10.003. URL `https://www.sciencedirect.com/science/article/pii/S0146641012001184`.

[79] G. Hagen, T. Papenbrock, D. J. Dean, A. Schwenk, A. Nogga, M. Włoch, and P. Piecuch. Coupled-cluster theory for three-body Hamiltonians. *Phys. Rev. C*, 76: 034302, Sep 2007. doi: 10.1103/PhysRevC.76.034302. URL `https://link.aps.org/doi/10.1103/PhysRevC.76.034302`.

[80] P. Maris, M. A. Caprio, and J. P. Vary. Emergence of rotational bands in ab initio no-core configuration interaction calculations of the Be isotopes. *Phys. Rev. C*, 91: 014310, Jan 2015. doi: 10.1103/PhysRevC.91.014310. URL `https://link.aps.org/doi/10.1103/PhysRevC.91.014310`.

[81] E. Epelbaum, H. Krebs, D. Lee, and U.-G. Meißner. Ab Initio Calculation of the Hoyle State. *Phys. Rev. Lett.*, 106:192501, May 2011. doi:

10.1103/PhysRevLett.106.192501. URL https://link.aps.org/doi/10.1103/PhysRevLett.106.192501.

[82] S. Elhatisari, N. Li, A. Rokash, J. M. Alarcón, D. Du, N. Klein, B. Lu, U.-G. Meißner, E. Epelbaum, H. Krebs, T. A. Lähde, D. Lee, and G. Rupak. Nuclear Binding Near a Quantum Phase Transition. *Phys. Rev. Lett.*, 117:132501, Sep 2016. doi: 10.1103/PhysRevLett.117.132501. URL https://link.aps.org/doi/10.1103/PhysRevLett.117.132501.

[83] N. Itagaki, M. Ito, M. Milin, T. Hashimoto, H. Ishiyama, and H. Miyatake. Coexistence of $\alpha + \alpha + n + n$ and $\alpha + t + t$ cluster structures in ^{10}Be. *Phys. Rev. C*, 77:067301, Jun 2008. doi: 10.1103/PhysRevC.77.067301. URL https://link.aps.org/doi/10.1103/PhysRevC.77.067301.

[84] V. S. Vasilevsky, Yu. A. Lashko, and G. F. Filippov. Two- and three-cluster decays of light nuclei within a hyperspherical harmonics approach. *Phys. Rev. C*, 97:064605, Jun 2018. doi: 10.1103/PhysRevC.97.064605. URL https://link.aps.org/doi/10.1103/PhysRevC.97.064605.

[85] F. Kobayashi and Y. Kanada-En'yo. A New Approach to Investigate Dineutron Correlation and Its Application to ^{10}Be. *Progress of Theoretical Physics*, 126(3): 457–482, 09 2011. ISSN 0033-068X. doi: 10.1143/PTP.126.457. URL https://doi.org/10.1143/PTP.126.457.

[86] M. Lyu, Z. Ren, B. Zhou, Y. Funaki, H. Horiuchi, G. Röpke, P. Schuck, A. Tohsaki, C. Xu, and T. Yamada. Investigation of ^{10}Be and its cluster dynamics with the nonlocalized clustering approach. *Phys. Rev. C*, 93:054308, May 2016. doi: 10.1103/PhysRevC.93.054308. URL https://link.aps.org/doi/10.1103/PhysRevC.93.054308.

[87] M. Takashina and Y. Kanada-En'yo. Inelastic proton scattering and neutron quadrupole transitions of ^{12}Be. *Phys. Rev. C*, 77:014604, Jan 2008. doi: 10.1103/PhysRevC.77.014604. URL https://link.aps.org/doi/10.1103/PhysRevC.77.014604.

[88] C. Romero-Redondo, E. Garrido, D. V. Fedorov, and A. S. Jensen. Three-body structure of low-lying ^{12}Be states. *Phys. Rev. C*, 77:054313, May 2008. doi: 10.1103/

PhysRevC.77.054313. URL `https://link.aps.org/doi/10.1103/PhysRevC.77.054313`.

[89] M. Seya, M. Kohno, and S. Nagata. Nuclear Binding Mechanism and Structure of Neutron-Rich Be and B Isotopes by Molecular-Orbital Model. *Progress of Theoretical Physics*, 65(1):204–223, 01 1981. ISSN 0033-068X. doi: 10.1143/PTP.65.204. URL `https://doi.org/10.1143/PTP.65.204`.

[90] Y. Kanada-En'yo and H. Horiuchi. Neutron-rich B isotopes studied with antisymmetrized molecular dynamics. *Phys. Rev. C*, 52:647–662, Aug 1995. doi: 10.1103/PhysRevC.52.647. URL `https://link.aps.org/doi/10.1103/PhysRevC.52.647`.

[91] D. Robson. Nuclear reactions with resonant-particle production. *Nuclear Physics A*, 204(3):523–528, 1973. ISSN 0375-9474. doi: https://doi.org/10.1016/0375-9474(73)90392-8. URL `https://www.sciencedirect.com/science/article/pii/0375947473903928`.

[92] G.G. Ohlsen. Kinematic relations in reactions of the form $A + B \rightarrow C + D + E$. *Nuclear Instruments and Methods*, 37:240–248, 1965. ISSN 0029-554X. doi: https://doi.org/10.1016/0029-554X(65)90368-X. URL `https://www.sciencedirect.com/science/article/pii/0029554X6590368X`.

[93] A. Saito, S. Shimoura, S. Takeuchi, T. Motobayashi, T. Minemura, Y. U. Matsuyama, H. Baba, H. Akiyoshi, Y. Ando, N. Aoi, et al. Molecular states in neutron-rich beryllium isotopes. *Nuclear physics. A, Nuclear and hadronic physics*, 738: 337–341, 2004.

[94] J. Gómez Camacho and A. Moro. A pedestrian approach to the theory of transfer reactions: Application to weakly-bound and unbound exotic nuclei. In C. Scheidenberger and M. Pfützner, editors, *The Euroschool on Exotic Beams, Vol. IV*, pages 39–66. Springer Berlin Heidelberg, 2014. ISBN 978-3-642-45140-9. doi: 10.1007/978-3-642-45141-6_2.

[95] F. Hammache and N. de Séréville. Transfer Reactions As a Tool in Nuclear Astrophysics. *Frontiers in Physics*, 8, 2021. ISSN 2296-424X. doi: 10.3389/fphy.2020.602920. URL `https://www.frontiersin.org/articles/10.3389/fphy.2020.602920`.

[96] W. N. Catford. What Can We Learn from Transfer, and How Is Best to Do It? In C. Scheidenberger and M. Pfützner, editors, *The Euroschool on Exotic Beams, Vol. IV*, pages 67–122. Springer Berlin Heidelberg, 2014. ISBN 978-3-642-45141-6. doi: 10.1007/978-3-642-45141-6_3.

[97] E. Costanzo, M. Lattuada, S. Romano, D. Vinciguerra, and M. Zadro. A procedure for the analysis of the data of a three-body nuclear reaction. *Nuclear Instruments and Methods in Physics Research Section A: Accelerators, Spectrometers, Detectors and Associated Equipment*, 295(3):373–376, 1990. ISSN 0168-9002. doi: https://doi.org/10.1016/0168-9002(90)90715-I. URL `https://www.sciencedirect.com/science/article/pii/016890029090715I`.

[98] U. Köster. Intense radioactive-ion beams produced with the ISOL method. *The European Physical Journal A*, 15:255.265, 2002. ISSN 1434-601X. doi: 10.1140/epja/i2001-10264-2. URL `https://doi.org/10.1140/epja/i2001-10264-2`.

[99] Micron Semiconductor Ltd. YY1, 2022. URL `http://www.micronsemiconductor.co.uk/product/yy1/`.

[100] O. Kirsebom, M. Munch, et al. AUSALIB, 2022. URL `https://gitlab.au.dk/ausa/ausalib`.

[101] J. Riegel, Werner Mayer, Y. van Havre, et al. FreeCAD, 2022. URL `https://www.freecadweb.org/`.

[102] H. Spieler. *Semiconductor Detector Systems*, volume v.12 of *Semiconductor Science and Technology*. Oxford University Press, Oxford, 2005. ISBN 978-0-19-852784-8.

[103] V. Pucknell, C. Unsworth, et al. Multi Instance Data Acquisiton System (MIDAS), 2022. URL `http://npg.dl.ac.uk/MIDAS/`.

[104] R. Brun, F. Rademakers, et al. ROOT Data Analysis Framework, 2022. URL `https://root.cern.ch/`.

[105] J.F. Ziegler et al. Stopping and Range of Ions in Matter (SRIM), 2022. URL `http://www.srim.org/`.

[106] D.R. Tilley, C.M. Cheves, J.L. Godwin, G.M. Hale, H.M. Hofmann, J.H. Kelley, G. Sheu, and H.R. Weller. Energy Levels of Light Nuclei, A = 4−20, 2022. URL `https://nucldata.tunl.duke.edu/nucldata/ELTables.shtml`.

[107] D. Dell' Aquila. UNISim − tool, 2022. URL `https://github.com/dellaquilamaster/UNISim-tool`.

[108] H. G. Bohlen, T. Dorsch, Tz. Kokalova, W. von Oertzen, Ch. Schulz, and C. Wheldon. Structure of ^{10}Be from the ^{12}C(^{12}C,^{14}O)^{10}Be reaction. *Phys. Rev. C*, 75: 054604, May 2007. doi: 10.1103/PhysRevC.75.054604. URL `https://link.aps.org/doi/10.1103/PhysRevC.75.054604`.

[109] W. Jiang, Y. L. Ye, C. J. Lin, Z. H. Li, J. L. Lou, X. F. Yang, Q. T. Li, Y. C. Ge, H. Hua, D. X. Jiang, D. Y. Pang, J. Li, J. Chen, Z. H. Yang, X. H. Sun, Z. Y. Tian, J. Feng, B. Yang, H. L. Zang, Q. Liu, P. J. Li, Z. Q. Chen, Y. Liu, Y. Zhang, J. Ma, H. M. Jia, X. X. Xu, L. Yang, N. R. Ma, and L. J. Sun. Determination of the cluster-decay branching ratio from a near-threshold molecular state in ^{10}Be. *Phys. Rev. C*, 101:031304, 2020. doi: 10.1103/PhysRevC.101.031304. URL `https://link.aps.org/doi/10.1103/PhysRevC.101.031304`.

[110] N. Curtis, D. D. Caussyn, N. R. Fletcher, F. Maréchal, N. Fay, and D. Robson. Decay angular correlations and spectroscopy for ^{10}Be $\rightarrow ^{4}$He+^{6}He. *Phys. Rev. C*, 64:044604, 2001. doi: 10.1103/PhysRevC.64.044604. URL `https://link.aps.org/doi/10.1103/PhysRevC.64.044604`.

[111] J. A. Liendo, N. Curtis, D. D. Caussyn, N. R. Fletcher, and T. Kurtukian-Nieto. Near threshold three-body final states in ^{7}Li+^{7}Li reactions at $E_{lab} = 34$MeV. *Phys. Rev. C*, 65:034317, 2002. doi: 10.1103/PhysRevC.65.034317. URL `https://link.aps.org/doi/10.1103/PhysRevC.65.034317`.

[112] S. Hamada, M. Yasue, S. Kubono, M. H. Tanaka, and R. J. Peterson. Cluster structures in ^{10}Be from the ^{7}Li (α, p) ^{10}Be reaction. *Physical Review C*, 49(6):3192, 1994.

[113] N. I. Ashwood, N. M. Clarke, M. Freer, B. R. Fulton, R. J. Woolliscroft, W. N. Catford, V. A. Ziman, R. P. Ward, C. J. Bickerton, C. E. Harrison, and V. F. E.

Pucknell. ^{10}Be excited states populated in the ^{9}Be(^{9}Be,^{8}Be)^{10}Be reaction. *Phys. Rev. C*, 68:017603, Jul 2003. doi: 10.1103/PhysRevC.68.017603. URL `https://link.aps.org/doi/10.1103/PhysRevC.68.017603`.

[114] M. Freer, E. Casarejos, L. Achouri, C. Angulo, N. I. Ashwood, N. Curtis, P. Demaret, C. Harlin, B. Laurent, M. Milin, N. A. Orr, D. Price, R. Raabe, N. Soić, and V. A. Ziman. α:$2n$:α Molecular Band in ^{10}Be. *Phys. Rev. Lett.*, 96:042501, Jan 2006. doi: 10.1103/PhysRevLett.96.042501. URL `https://link.aps.org/doi/10.1103/PhysRevLett.96.042501`.

[115] N. Vukman, N. Soić, M. Freer, M. Alcorta, D. Connolly, P. Čolović, T. Davinson, A. Di Pietro, A. Lennarz, A. Psaltis, C. Ruiz, M. Uroić, and M. Williams. Cluster decays of ^{12}Be excited states. *Frontiers in Physics*, 10, 2022. ISSN 2296-424X. doi: 10.3389/fphy.2022.1009421. URL `https://www.frontiersin.org/articles/10.3389/fphy.2022.1009421`.

[116] H. G. Bohlen, W. Von Oertzen, A. Blažević, B. Gebauer, S. M. Grimes, R. Kalpakchieva, T. N. Massey, and S. Thummerer. Structure studies of ^{11}Be and ^{12}Be: Observation of molecular rotational bands. *Physics of Atomic Nuclei*, 65 (4):603–606, 2002.

[117] H.G. Bohlen, R. Kalpakchieva, W. Von Oertzen, T.N. Massey, B. Gebauer, T. Kokalova, A.A. Ogloblin, Ch. Schulz, and S. Thummerer. Structure of neutron-rich beryllium and carbon isotopes. *Nuclear Physics A*, 738:333–336, 2004. ISSN 0375-9474. doi: https://doi.org/10.1016/j.nuclphysa.2004.04.056. URL `https://www.sciencedirect.com/science/article/pii/S0375947404005974`. Proceedings of the 8th International Conference on Clustering Aspects of Nuclear Structure and Dynamics.

[118] A.A. Korsheninnikov, E.Yu. Nikolskii, T. Kobayashi, D.V. Aleksandrov, M. Fujimaki, H. Kumagai, A.A. Ogloblin, A. Ozawa, I. Tanihata, Y. Watanabe, and K. Yoshida. Spectroscopy of ^{12}Be and ^{13}Be using a ^{12}Be radioactive beam. *Physics Letters B*, 343(1):53–58, 1995. ISSN 0370-2693. doi: https://doi.org/10.1016/0370-2693(94)01435-F. URL `https://www.sciencedirect.com/science/article/pii/037026939401435F`.

[119] L. Giot, P. Roussel-Chomaz, S. Pita, N. Alamanos, F. Auger, M.-D. Cortina-Gil, Ch.-E. Demonchy, J. Fernandez, C. Jouanne, A. Gillibert, V. Lapoux, L. Nalpas, E.C. Pollacco, A. Rodin, A. Pakou, K. Rusek, H. Savajols, J.-L. Sida, S. Stepantsov, G. Ter-Akopian, and R. Wolski. Search for t+t clustering in ^{6}He. *Nuclear Physics A*, 738:426–430, 2004. ISSN 0375-9474. doi: https://doi.org/10. 1016/j.nuclphysa.2004.04.079. URL `https://www.sciencedirect.com/science/article/pii/S0375947404006165`. Proceedings of the 8th International Conference on Clustering Aspects of Nuclear Structure and Dynamics.

[120] S. Aoyama, N. Itagaki, K. Arai, K. Katō, and M. Oi. $t+t$ clustering in He-isotopes. *Modern Physics Letters A*, 21:2499–2502, 2006. ISSN 1793-6632. doi: https://doi. org/10.1142/S021773230602216X. Special Issue: Proceedings of the RCNP Osaka Spring Workshop on Cluster Condensation and Nucleon Correlation in Nuclei.

[121] Y. Kanada-En'yo, H. Horiuchi, and A. Ono. Structure of Li and Be isotopes studied with antisymmetrized molecular dynamics. *Phys. Rev. C*, 52:628–646, Aug 1995. doi: 10.1103/PhysRevC.52.628. URL `https://link.aps.org/doi/10.1103/PhysRevC.52.628`.

[122] Y. Kanada-En'yo. Variation after Angular Momentum Projection for the Study of Excited States Based on Antisymmetrized Molecular Dynamics. *Phys. Rev. Lett.*, 81:5291–5293, Dec 1998. doi: 10.1103/PhysRevLett.81.5291. URL `https://link.aps.org/doi/10.1103/PhysRevLett.81.5291`.

[123] Y. Kanada-En'yo, M. Kimura, and H. Horiuchi. Antisymmetrized Molecular Dynamics: a new insight into the structure of nuclei. *Comptes Rendus Physique*, 4(4):497–520, 2003. ISSN 1631-0705. doi: https://doi.org/10. 1016/S1631-0705(03)00062-8. URL `https://www.sciencedirect.com/science/article/pii/S1631070503000628`.

[124] J. Walshe, M. Freer, C. Wheldon, L. N. Achouri, N. I. Ashwood, W. N. Catford, I. C. Celik, N. Curtis, F. Delaunay, B. Fernández-Domínguez, L. Grassi, T. Kokalova, M. Marqués, N. A. Orr, L. Prepolec, V. Scuderi, N. Soić, and V. Tokić. The thick target inverse kinematics technique with a large acceptance silicon detector array. *Jour-*

nal of Physics: Conference Series, 569:012052, dec 2014. doi: 10.1088/1742-6596/569/1/012052. URL `https://doi.org/10.1088/1742-6596/569/1/012052`.

[125] A. H. Wuosmaa, J. P. Schiffer, S. Bedoor, M. Albers, M. Alcorta, S. Almaraz-Calderon, B. B. Back, P. F. Bertone, C. M. Deibel, C. R. Hoffman, J. C. Lighthall, S. T. Marley, R. C. Pardo, K. E. Rehm, and D. V. Shetty. Stretched states in ^{12,13}B with the (d,α) reaction. *Phys. Rev. C*, 90:061301, Dec 2014. doi: 10.1103/PhysRevC.90.061301. URL `https://link.aps.org/doi/10.1103/PhysRevC.90.061301`.

Biography

Nikola Vukman was born on 27th of January, 1992 in Split, Croatia. He obtained master degree in Physics at Faculty of Science, University of Zagreb in 2015, with thesis subject "Measurement of e^+e^- pairs in Au+Au collisions in PHENIX experiment", under supervision of Dr. Mihael Makek. During his master thesis he was an active part of PHENIX collaboration and got the opportunity to participate in high-energy nuclear physics experiment at RHIC in Brookhaven. This research sparked an interest in nuclear physics and in 2016 he got an opportunity to start his research career in Laboratory for Nuclear Physics at Ruđer Bošković Institute and started working on his PhD thesis under supervision of Dr. Neven Soić. At Ruđer Bošković he found his love for the study of cluster and molecular-like structures in light nuclei and got the opportunity to participate in number of experiments, out of which the experiment performed at TRIUMF, Vancouver remains his favorite, as it has provided the data for his thesis subject. Collaboration with different experimental groups in the international environment gave him the opportunity to participate in more than fifteen experiments in diverse range of topics within the field of nuclear physics. These experiments were performed with various experimental setups at accelerator facilities such as TRIUMF in Vancouver, INFN-LNS in Catania, INFN-LNL in Legnaro, GANIL in Caen and his home institution Ruđer Bošković in Zagreb. His research interests span diverse range of topics, from both technical and fundamental knowledge side of things, but the primary interest remains the study of cluster and molecular-like structures in neutron-rich light nuclei where he would like to contribute scientifically in the future as there are still many puzzles to be solved.

Bibliography of published work:

1. N. Vukman, N. Soić, M. Freer, M. Alcorta, D. Connolly, P. Čolović, T. Davinson, A. Di Pietro, A. Lennarz, A. Psaltis, C. Ruiz, M. Uroić, M. Williams
   "Cluster decays of ^{12}Be excited states", Front. Phys. **10** (2022) 1009421
   `https://www.frontiersin.org/articles/10.3389/fphy.2022.1009421`

2. G. Provatas, S. Fazinić, N. Soić, N. Vukman et al. *"Systematic study of the $^{12}C(^{3}He,p)^{14}N$ reaction for NRA applications"*, Nucl. Instrum. Methods Phys. Res. **B 500-501** (2021) 57-67
   `https://doi.org/10.1016/j.nimb.2021.03.005`

3. G. Provatas, S. Fazinić, N. Soić, N. Vukman et al. *"Differential cross section measurements of the $^{9}Be(^{3}He,p)^{11}B$ reaction for NRA applications"*, Nucl. Instrum. Methods Phys. Res. **B 472** (2020), 36-45
   `https://doi.org/10.1016/j.nimb.2020.03.039`

4. C. Spitaler et al. *"The ^{3}He $+^{5}$He $\rightarrow \alpha + \alpha$ reaction below the Coulomb barrier via the Trojan Horse Method"*, Eur. Phys. J. A **57** (2021) 20
   `https://doi.org/10.1140/epja/s10050-020-00324-4`

5. C. Spitaler et al. *"Study of the quasi-free ^{3}He$+^{9}$Be$\rightarrow 3\alpha$ reaction for the Trojan Horse Method"*, Eur. Phys. J. A **56** (2020), 1; 18, 14
   `https://doi.org/10.1140/epja/s10050-020-00026-x`

6. G. Colucci, G. Montagnoli, A. M. Stefanini et al. *"Sub-barrier fusion involving odd mass nuclei: the case of ^{36}S $+^{50}$Ti,^{51}V"*, Eur. Phys. J. A **55** (2019), 111, 6
   `https://doi.org/10.1140/epja/i2019-12796-0`

7. L. Corradi, S. Szilner et al. *"Probing Nucleon–Nucleon Correlations in Heavy Ion Transfer Reactions Using Large Solid Angle Magnetic Spectrometers"*, JPS Conf. Proc. **32**, (2020) 010043
   `https://doi.org/10.7566/JPSCP.32.010043,`

8. G. Colucci, G. Montagnoli, A. M. Stefanini et al. *"Effects of Non-Zero Spin in Sub-Barrier Fusion Involving Odd Mass Nuclei: The Case of ^{36}S $+^{50}$Ti,^{51}V"*, JPS Conf. Proc. **32**, (2020) 010010
   `https://doi.org/10.7566/JPSCP.32.010010`

9. G. Colucci, G. Montagnoli, A. M. Stefanini et al.
   "Study of sub-barrier fusion of ^{36}S $+^{50}$Ti,^{51}V", EPJ Web of Conferences **223**, (2019)

01013

https://doi.org/10.1051/epjconf/201922301013

10. T. Mijatović, S. Szilner, L. Corradi et al. *"Multinucleon transfer reactions and proton transfer channels"*, EPJ Web of Conferences **223**, (2019) 01039

https://doi.org/10.1051/epjconf/201922301039

11. N. Vukman, N. Soić, M. Freer et al. *"Examining the Helium Cluster Decays of the ^{12}Be Excited States by Triton Transfer to the ^9Li Beam"*, RÁBIDA 2018, Springer Proceedings in Physics, **225** (2019) 257-258

https://doi.org/10.1007/978-3-030-22204-8_43

12. PHENIX Collaboration *"Transverse-single-spin asymmetries of charged pions at midrapidity in transversely polarized $p+p$ collisions at $\sqrt{s} = 200$GeV "*, Phys. Rev. D **105**, (2022) 032003

https://doi.org/10.1103/PhysRevD.105.032003

13. PHENIX Collaboration *"Transverse single spin asymmetries of forward neutrons in $p+p$, $p+$Al, and $p+$Au collisions at $\sqrt{s_{NN}} = 200$GeV as a function of transverse and longitudinal momenta"*, Phys. Rev. D **105**, (2022) 032004

https://doi.org/10.1103/PhysRevD.105.032004

14. PHENIX Collaboration *"Kinematic dependence of azimuthal anisotropies in $p+$Au, $d+$Au, and ^{3}He$+$Au at $\sqrt{s_{NN}} = 200$ GeV "*, Phys. Rev. C **105**, (2022) 024901

https://doi.org/10.1103/PhysRevC.105.024901

15. PHENIX Collaboration *"Probing Gluon Spin-Momentum Correlations in Transversely Polarized Protons through Midrapidity Isolated Direct Photons in $p^\uparrow+p$ Collisions at $\sqrt{s} = 200$GeV "*, Phys. Rev. Lett. **127**, (2021) 162001

https://doi.org/10.1103/PhysRevLett.127.162001

16. PHENIX Collaboration *"Transverse momentum dependent forward neutron single spin asymmetries in transversely polarized $p+p$ collisions at $\sqrt{s} = 200$GeV "*, Phys. Rev. D **103**, (2021) 032007

https://doi.org/10.1103/PhysRevD.103.032007

17. PHENIX Collaboration *"Measurement of J/ψ at forward and backward rapidity in $p+p$, $p+$Al, $p+$Au, and ^{3}He$+$Au collisions at $\sqrt{s_{NN}} = 200$ GeV"*, Phys. Rev. C **102**, (2020) 014902

https://doi.org/10.1103/PhysRevC.102.014902

18. PHENIX Collaboration *"Nuclear-modification factor of charged hadrons at forward and backward rapidity in $p + $ Al *and* $p + $ Au *collisions at* $\sqrt{s_{NN}} = 200\,\mathrm{GeV}$ "*, Phys. Rev. C **101**, (2020) 034910

    https://doi.org/10.1103/PhysRevC.101.034910

19. PHENIX Collaboration *"Nuclear Dependence of the Transverse Single-Spin Asymmetry in the Production of Charged Hadrons at Forward Rapidity in Polarized $p+p$, $p+$Al, and $p+$Au Collisions at* $\sqrt{s_{NN}} = 200\mathrm{GeV}$ "*, Phys. Rev. Lett. **123**, (2019) 122001

    https://doi.org/10.1103/PhysRevLett.123.122001

20. PHENIX Collaboration *"Measurement of charm and bottom production from semileptonic hadron decays in $p+p$ collisions at* $\sqrt{s} = 200\mathrm{GeV}$ "*, Phys. Rev. D **99**, (2019) 092003

    https://doi.org/10.1103/PhysRevD.99.092003

21. PHENIX Collaboration *"Nonperturbative-transverse-momentum broadening in dihadron angular correlations in* $\sqrt{s_{NN}} = 200\,\mathrm{GeV}$ *proton-nucleus collisions"*, Phys. Rev. C **99**, (2019) 044912

    https://doi.org/10.1103/PhysRevC.99.044912

22. PHENIX Collaboration *"Measurements of $\mu\mu$ pairs from open heavy flavor and Drell-Yan in $p+p$ collisions at* $\sqrt{s} = 200\mathrm{GeV}$ "*, Phys. Rev. D **99**, (2019) 072003

    https://doi.org/10.1103/PhysRevD.99.072003

23. PHENIX Collaboration *"Creation of quark–gluon plasma droplets with three distinct geometries"*, Nature Phys.

    15, (2019) 214–220

    https://doi.org/10.1038/s41567-018-0360-0

24. PHENIX Collaboration *"Nuclear dependence of the transverse-single-spin asymmetry for forward neutron production in polarized $p+A$ collisions at* $\sqrt{s_{NN}} = 200\ GeV$"*, Phys. Rev. Lett. **120** (2018), 022001

    https://doi.org/10.1103/PhysRevLett.120.022001

25. PHENIX Collaboration *"Measurements of multiparticle correlations in $d+Au$ collisions at 200, 62.4, 39, and 19.6 GeV and $p+Au$ collisions at* $\sqrt{s_{NN}} = 200\ GeV$ *and implications for collective behaviour"*, Phys. Rev. Lett. **120** (2018), 062302

    https://doi.org/10.1103/PhysRevLett.120.062302

26. PHENIX Collaboration *"Measurements of mass-dependent azimuthal anisotropy in central p+Au, d+Au, and ^3He+Au collisions at $\sqrt{s_{NN}} = 200\ GeV"$*, Phys. Rev. C **97** (2018), 064904

    https://doi.org/10.1103/PhysRevC.97.064904

27. PHENIX Collaboration *"Single-spin asymmetry of J/ψ production in p+p, p+Al, and p+Au collisions with transversely polarized proton beams at $\sqrt{s_{NN}} = 200\ GeV"$*, Phys. Rev. D **98** (2018), 012006

    https://doi.org/10.1103/PhysRevD.98.012006

28. PHENIX Collaboration *"Nonperturbative transverse-momentum-dependent effects in dihadron and direct photon-hadron angular correlations in p+p collisions at $\sqrt{s_{NN}} = 200\ GeV"$*, Phys. Rev. D **98** (2018), 072004

    https://doi.org/10.1103/PhysRevD.98.072004

29. PHENIX Collaboration *"Pseudorapidity Dependence of Particle Production and Elliptic Flow in Asymmetric Nuclear Collisions of p+Al, p+Au, d+Au, and ^3He+Au at $\sqrt{s_{NN}} = 200\ GeV"$*, Phys. Rev. Lett. **121** (2018), 222301

    https://doi.org/10.1103/PhysRevLett.121.222301

30. PHENIX Collaboration *"Measurement of relative yields of $\psi(2S)$ to $\psi(1S)$ mesons produced at forward and backward rapidity in p+p, p+Au, and $^3He + Au$ collisions at $\sqrt{s_{NN}} = 200\ GeV"$*, Phys. Rev. C **95** (2017), 34904

    https://doi.org/10.1103/PhysRevC.95.034904

31. PHENIX Collabo *"Nonperturbative-transverse-momentum effects and evolution in dihadron and direct photon-hadron angular correlations in p+p collisions at $\sqrt{s_{NN}} = 510\ GeV"$*, Phys. Rev. D **95** (2017), 072002

    https://doi.org/10.1103/PhysRevD.95.072002ration

32. PHENIX Collaboration *"Angular decay coefficients of J/ψ mesons at the forward rapidity from p+p collisions at $\sqrt{s_{NN}} = 510\ GeV"$*, Phys. Rev. D **95** (2017), 092003

    https://doi.org/10.1103/PhysRevD.95.092002

33. PHENIX Collaboration *"B-meson production at forward and backward rapidity in p+p and Cu+Au collisions at $\sqrt{s_{NN}} = 200\ GeV"$*, Phys. Rev. C **96** (2017), 064901

    https://doi.org/10.1103/PhysRevC.96.064901